The mechanism of action of a mutant mitochondrial fission protein

Vincenzo Carlo Leo

Submitted in accordance with the requirements for the degree of
Doctor of Philosophy

University of Leeds
Faculty of Medicine & Health

December 2012

The candidate confirms that the work submitted is his own and that appropriate credit has been given where reference has been made to the work of others.

Acknowledgements

A huge thank you to Professor Neil Dear for his excellent advice, commitment and supervision during this project. I would also like to thank Dr. John Boyle, Professor Chris Peers and David Myers of the University of Leeds for their contribution to the work on oxidative phosphorylation and membrane potential and also Dr. Houman Ashrafian and Dr. Tom Cahill of the University of Oxford for supplying the MEF cell model and for their work in parallel to this project. Thank you to Professor Gillian Bates of King's College London for supplying the R6/2 mouse line. Thanks also to Dr. Pam Jones for her support and Dr. Narcis Fernandez-Fuentes for a valuable piece of homology modelling. Finally, thank you to all the staff in the section of experimental therapeutics, LIMM, the staff in St. James biological sciences for maintaining the mouse lines and thank you to LIMM for the funding, making this PhD project a possibility.

Abstract

Cardiovascular disease is the most common cause of morbidity and mortality worldwide, of which cardiomyopathies account for a proportion. One of the hallmarks of progressive heart disease is diminished energy metabolism associated with cardiac mitochondrial dysfunction. Recent evidence directly implicates malfunctioning mitochondria and altered mitochondrial dynamics in the development of heart disease. Yet, little is known about mitochondrial remodelling changes that might contribute to the development of heart failure.

A recently identified mouse mutant in the *Dnm1l* gene, Python, leads to the development of dilated cardiomyopathy at specific ages. The work reported herein focussed on understanding the mechanisms responsible for the development of cardiomyopathy in this model. Evidence was obtained of alteration in mitochondria, peroxisome and endoplasmic reticulum (ER) morphology in various cell types. There was a suggestion of altered physical interaction between the mitochondria and the ER. Increased cytosolic calcium levels and reduced mitochondrial uptake of calcium were also observed in Python fibroblasts. Mitochondrial membranes were also depolarised. These changes resulted in reduced oxidative phosphorylation activity in the hearts of Python mice, which showed a progressive reduction with age. Ultimately a decrease in ATP levels occurred, which was unsustainable with normal heart function. DNM1L expression was found to increase with age in hearts of wild type mice, but not other tissues. This may be suggestive of an increase in the importance for the DNM1L protein in the ageing heart, though the exact reasons for this remain elusive.

Fragmented mitochondria have been postulated to contribute to the development of Huntington's disease. However, a reduction in fragmentation through introduction of the Python mutation did not alleviate the progressive development of symptoms in these animals.

We hypothesize that the Python mutation impairs the ability of mitochondrial-ER tethering. Subsequent dysfunctional mitochondrial calcium uptake and altered mitochondrial membrane potential, leads to a progressive decline in oxidative phosphorylation activity and ATP production.

Table of contents

Acknowledgements **2**

Abstract **3**

Table of contents **4**

List of Figures **7**

List of Tables **9**

Abbreviations **10**

Chapter 1 : Introduction **17**

1.1 Mitochondrial Dynamics **17**

1.1.1 The role of mitochondrial fusion and fission 18

1.1.2 Mitochondrial fusion and fission proteins 19

1.1.3 DNM1L structure 23

1.1.4 Regulation of DNM1L activity 29

1.2 The role of mitochondria in physiological processes **31**

1.2.1 Cell metabolism 31

1.2.2 Mitochondria-ER cooperation 33

1.2.3 Maintenance of the mitochondrial membrane potential 33

1.2.4 Autophagy and Mitophagy 34

1.2.5 Apoptosis 38

1.3 Association of altered mitochondrial morphology with disease processes **41**

1.3.1 Parkinson's disease 41

1.3.2 Alzheimer's disease 42

1.3.3 Huntington's disease 43

1.4 Alterations in expression of fusion / fission factors lead to disease **44**

1.4.1 Charcott-Marie-Tooth Type 2A (CMT2A) 44

1.4.2 Optic Atrophy 45

1.4.3 The *DNM1L*^{A401D} mutation 46

1.4.4 The *Dnm1l* Python mutation 46

1.5 Familial Dilated Cardiomyopathy **50**

1.6 Mouse models of heart failure **58**

1.7 Overview of project **64**

1.8 Hypotheses and aims **65**

1.8.1 Hypotheses 65

1.8.2 Aims 66

Chapter 2 : Methods **67**

2.1 List of mouse strains: **67**

2.2 Home office licenses that experiments were carried out under: **67**

2.3 Genotyping **68**

2.3.1 DNA extraction 68

2.3.2 PCR amplification 68

2.3.3 Restriction assay with XapI for *Dnm1l*^{Py} 69

2.4 Western blot analyses **69**

2.5 His-tag protein purification **71**

2.6 Protein extraction & renaturation 71
2.7 GTPase activity....72
2.8 RNA isolation....73
2.9 Reverse transcription 73
2.10 Pyrosequencing 74
2.11 PCR cDNA amplification of cardiomyocyte markers 76
2.12 Site-directed Mutagenesis....77
2.13 DNA isolation from bacterial cells 78
2.14 Cell culture....78
2.14.1 Mouse skin fibroblasts....79
2.14.2 Mouse embryonic fibroblasts (MEFs)....79
2.14.3 Embryonic stem (ES) cells 80
2.14.4 Embryoid body formation 80
2.14.5 Cardiomyocyte-induced differentiation of ES cells 81
2.14.6 Adult mouse cardiomyocyte culture 82
2.14.7 Neuron culture....83
2.14.8 HeLa cell transfection....83
2.15 Mitochondria labelling 84
2.16 ER labelling....84
2.17 Immunocytochemistry 85
2.18 Mitochondrial isolation 86
2.18.1 Mitochondrial protein extraction. 86
2.18.2 Mitochondrial DNA extraction....86
2.19 Mitochondrial DNA amplification....87
2.20 Yeast-2-hybrid 88
2.20.1 Yeast-2-Hybrid Analysis of DNM1L self interactions....88
2.20.2 Yeast-2-Hybrid Library screen for Dnm1l interactions....89
2.20.3 Yeast-2-Hybrid analysis of DNM1L interactions....91
2.21 Calcium concentration....93
2.21.1 Cytoplasmic calcium concentration measurement....93
2.21.2 Mitochondrial calcium concentration measurement 93
2.22 Oxidative phosphorylation measurement....94
2.22.1 Oxidative phosphorylation in cells 94
2.22.2 Oxidative phosphorylation in tissues 95
2.23 ATP determination 96
2.23.1 Cell lines....96
2.23.2 Tissues 96
2.24 Mitochondrial membrane potential (MMP) measurement 97
2.25 Behavioural analyses....97
2.26 Statistical analyses 97

Chapter 3 : The effect of the Python mutation on DNM1L function 98
3.1 Results 98
3.1.1 The Python mutation impairs DNM1L intramolecular interactions ..98
3.1.2 DNM1L protein levels are reduced in Python....103
3.1.3 The Python and wild type alleles are equally expressed....105
3.1.4 The DNM1L^{Py} protein has reduced GTPase activity 108
3.1.5 Python can act in a dominant-negative fashion....109
3.1.6 The *Dnm1l*^{Py} and *Dnm1l*^{A401D} mutations impair DNM1L Interactions with UBC9 and MFF. 111

3.1.7 Decreased DNM1L^{Py} stability on the OMM 117
3.2 Discussion 120

Chapter 4 : DNM1L^{Py} and organelle morphology.... 125
4.1 Results 125
4.1.1 The Python mutation alters mitochondrial, peroxisomal and ER morphology....125
4.1.2 Highly abnormal mitochondria in fibroblasts homozygous for the Python mutation 131
4.2 Discussion 132

Chapter 5 : Investigation of the effects of the Python mutation on other aspects of cellular physiology.... 134
5.1 Results 134
5.1.1 Mitophagy is not altered by DNM1L^{Py}....134
5.1.2 Reduced ER-Mitochondrial Tethering 140
5.1.3 Calcium signalling is perturbed in Python cells 143
5.1.4 Age-related decrease in oxidative phosphorylation in Python heart tissue. 147
5.1.5 Python ES cells fail to differentiate into cardiomyocytes 156
5.1.6 ATP levels are reduced in differentiated Python cell lines 159
5.1.7 Dnm1l protein levels in the heart increase with age....160
5.2 Discussion 162

Chapter 6 : Introduction of the Python mutation into R6/2 mice does not ameliorate progressive development of Huntington's disease.... 168
6.1 Introduction 168
6.2 Results 170
6.2.1 Introduction of the Python mutation into R6/2 mice corrects the mitochondrial morphology defect. 170
6.2.2 Introduction of the Python mutation does not alter HD symptoms. 173
6.2.3 HTT aggregation remains in R6/2 x Python cortex 178
6.2.4 ATP levels are reduced in R6/2 and R6/2 x Python striata 179
6.2.5 The R6/2 transgene does not increase DNM1L levels in Python mice. 181
6.3 Discussion 183

Chapter 7 : General discussion 186
7.1 How the Python mutation leads to energy dysregulation 186
7.2. How dilation might result from energy dysregulation 189
7.3 DNM1L^{Py} does not appear to ameliorate the symptoms of Huntington's disease in R6/2 mice 189
7.4 Future for the Python model of DCM....194

References.... 195

Appendices.... 219
Appendix I. Amino acid reference sequence for DNM1L....219
Appendix II. Primers for Python genotyping. 220
Appendix III. Python genotyping result.....221
Appendix IV. pET101 222

Appendix V. primers for pyrosequencing.....223
Appendix VI. Primers for mouse cDNA cardiomyocyte markers.....224
Appendix VII. pLd11 construct.....225
Appendix VIII. The mouse mtDNA C3H/HEH genome.....226
Appendix IX. pDEST32 & pDEST22 vectors.....227
Appendix X. pAS2-1 and pACT2 vectors 229
Appendix XI. mitochondrial aequorin vector.....230
Appendix XII. R6/2 genotyping.....231
Appendix XIII. Strain specific onset of CHF.....232
Appendix XIV. Subcloning to derive ES cell models 233
Appendix XV. Growth rates of *+/Py* and +/+ ES cell lines 234
Appendix XVI. Publication.....235

List of Figures

Figure 1.1. Mitochondrial compartments. 17
Figure 1.2. Structures of the mitochondrial fusion and fission proteins..20
Figure 1.3. A schematic diagram illustrating the proteins involved in mitochondrial fusion and fission.. 22
Figure 1.4. Dynamin (DPRD) structure. 25
Figure 1.5. Membrane curvature induced by dynamin structural rearrangements. 26
Figure 1.6. BDLP mechanism of action. 27
Figure 1.7. BDLP Vs Dnm1l homology models. 28
Figure 1.8. ATP production via oxidative phosphorylation.....32
Figure 1.9. Pathway of Autophagy regulation by Ca^{2+} transfer.. 37
Figure 1.10. DNM1L-induced membrane remodeling in apoptosis.. 40
Figure 1.11. The Python phenotype.....47
Figure 1.12. Sequence and homology surrounding the Python mutation. 49
Figure 1.13. The amino acid substititution resuting from the Python mutation.. 49
Figure 1.14. Ca^{2+} transport in ATP production and EC coupling. 54
Figure 1.15. Hypotheses to explain the development of HCM. 57
Figure 2.1. Sequence of events during pyrosequencing analysis. 75
Figure 2.2. ES cell differentiation.....82
Figure 2.3. A schematic representation of the Yeast-2-Hybrid system.....91
Figure 3.1. DNM1L domain interactions. 100
Figure 3.2. Python abrogates some DNM1L domain interactions. 102
Figure 3.3. Cellular DNM1L levels are reduced in Python mice. 104
Figure 3.4. The *Dnm1l*^{Py} allele is expressed in heterozygotes. 107
Figure 3.5. GTPase activity of Python DNM1L is reduced.....109
Figure 3.6. Python reduces the GTPase activity of wild type DNM1L. ...110
Figure 3.7. Overall GTPase activity within Python brains is not altered.111
Figure 3.8. Y2H library screen showing positive clones. 113
Figure 3.9. DNM1L interactions with UBC9 and MFF are severely impaired by the introduction of Python or $A_{401}D$ mutations. 116
Figure 3.10. DNM1L localisation within the cell. 117

Figure 3.11. A decrease in the level of DNM1L associated with mitochondria of Python mice. 119
Figure 3.12. Ribbon representation of a homology model of the dimeric form of DNM1L protein in the extended conformation and embedded in a lipid membrane. 121
Figure 4.1. Mitochondrial elongation in cultured Python cell lines. 126
Figure 4.2. Mitochondrial morphology in adult cardiomyocytes. 127
Figure 4.3. Altered peroxisome and ER morphology in cultured Python cells 128
Figure 4.4. Transfection of HeLa cells with DNM1L expression constructs 130
Figure 4.5. Mitochondrial perinuclear aggregation in *Py/Py* fibroblasts.131
Figure 5.1. Analysis of mtDNA deletions. 136
Figure 5.2. LC3-mitochondria colocalisation. 137
Figure 5.3. Degree of mitochondria-LC3 colocalisation 138
Figure 5.4. Python tissues do not demonstrate evidence of increased mitophagy.. 139
Figure 5.5. Reduced ER protein in mitochondrial preparations from Python tissues. 141
Figure 5.6. Reduced mitochondrial-ER colocalisation in skin fibroblasts. 142
Figure 5.7. Decreased mitochondrial Ca^{2+} uptake in Python cells. 145
Figure 5.8. Increased cytosolic Ca^{2+} in Python fibroblasts is a result of dysfunctional mitochondria. 146
Figure 5.9. Mitochondrial membrane depolarisation in Python cells. 147
Figure 5.10. OXPHOS efficiency is not compromised in Python ES cells and fibroblasts. 149
Figure 5.11: Direct comparison between Python and wild type OXPHOS in the heart. 151
Figure 5.12. Age-related decrease of OXPHOS efficiency in Python hearts. 153
Figure 5.13. OXPHOS activity in wild type hearts. 155
Figure 5.14. Python ES cells fail to differentiate into cardiomyocytes. ..158
Figure 5.15. ATP levels in cell lines. 159
Figure 5.16. Mitochondrial fusion/fission protein levels increase in the heart with age.. 161
Figure 6.1. Mitochondrial morphology in 5-week-old R6/2 mice is restored by the introduction of the Python mutation. 171
Figure 6.2. Mitochondrial morphology in 15-week-old R6/2 mice is restored by the introduction of the Python mutation. 172
Figure 6.3. Mitochondrial elongation and nuclear aggregation in Python neurons 173
Figure 6.4. A progressive decrease in body weight for R6/2 mice is not rescued by the presence of Python. 175
Figure 6.5. Decline in grip strength in R6/2 mice is not improved by the presence of Python. 176
Figure 6.6. Brain weights severely reduced in the presence of the R6/2 transgene. 177
Figure 6.7. HTT aggregation in the cortex of R6/2 and R6/2 x Python mice. 179

Figure 6.8. ATP is reduced in the striata of R6/2 and R6/2 x Python mice. 180
Figure 6.9. Lower cellular DNM1L levels in R6/2 x Python. 182
Figure 7.1. The effect of myocyte hypertrophy. 190
Figure 7.2. Summary of a possible pathway in which the Python mutation leads to DCM. 192

List of Tables

Table 1.1. Table of genes in which DCM-predisposing mutations have been identified in humans. 52
Table 2.1. PCR conditions for the amplification of DNA for the identification of the Python mutation and the R6/2 transgene 68
Table 2.2. Table of antibodies used for Western blots. 70
Table 2.3. PCR conditions for the amplification of the cardiomyocyte markers. 76
Table 2.4. Primer pairs for site-directed mutagenesis 77
Table 2.5. Cell culture reagents 78
Table 2.6. Table of antibodies used for immunocytochemistry 85
Table 2.7. PCR conditions for the amplification of the mtDNA. 87
Table 3.1. List of proteins that were used in interaction experiments with DNM1L 114
Table 3.2. Chemical properties of the amino acids involved in the $C_{452}F$ and $A_{401}D$ substitutions. 122
Table 5.1. Statistical analyses of OXPHOS between wild type and Python cell lines. 149
Table 5.2. Statistical analyses of OXPHOS between wild type and Python heart tissue. 152
Table 5.3. Statistical analyses comparing Python OXPHOS values between time points for each substrate added. 154
Table 6.1. Statistical analyses for mitochondrial length. 173
Table 6.2. Statistical analyses for brain weights. 178

Abbreviations

Diseases

- AD: Alzheimer's disease
- ARVD: Arrythmogenic right ventricular dysplasia
- CHF: Congestive heart failure
- CMT2A: Charcott-Marie-Tooth Type 2A
- DCM: Dilated cardiomyopathy
- DOA: Dominant optic atrophy
- HCM: Hypertrophic cardiomyopathy
- HD: Huntington's disease
- PD: Parkinson's disease
- RCM: Restrictive cardiomyopathy
- SCD: Sudden cardiac death

Proteins

- AC3-1: Autocamtide-3 derived inhibitory peptide
- Acetyl coA: Acetyl coenzyme A
- AMPK: AMP-activated protein kinase
- ANT: Adenine nucleotide translocator
- BAK: Bcl-2 homologous antagonist
- BAX: Bcl-2-associated X protein
- BCL-2: B-cell lymphoma 2
- BCL-X: Bcl-2-like 1
- BDLP: Bacterial dynamin-like protein
- Caf4p: Caffeine-resistant 4
- CaMKII: Calcium-calmodulin-dependent protein kinase II
- COX7A1: Cardiac-specific subunit 7a mouse cytochrome c oxidase
- DNM1L: Dynamin-like protein 1
- FBP1: Far upstream element-binding protein 1
- FIS1: Mitochondrial fission protein 1

- GATA4: GATA binding protein 4
- GSK3β: Glycogen synthase kinase-3 beta
- HTT: Huntingtin
- IGF-1: Insulin-like growth factor 1
- IP_3: Inositol-1,2,4-triphosphate
- IP_3R: Inositol-1,2,4-triphosphate receptor
- LC3-I: MAP1 light chain 3 isoform I
- LC3-II: MAP1 light chain 3 isoform II
- MARCHV: Membrane-associated RING-CH V
- Mdv1p: Mitochondrial division 1
- MEF2: Myocyte enhancer factor-2
- MFF: Mitochondrial fission factor
- MFN1: Mitofusin 1
- MFN2: Mitofusin 2
- MIEF1: Mitochondrial elongation factor 1
- MnSOD2: Manganese superoxide dismutase
- mTOR: Mammalian target of rapamycin
- NFAT: Nuclear activator of activated T-cells
- OPA1: Optic atrophy 1
- P-AMPK: Phosphorylated AMP-activated protein kinase
- PDH: Pyruvate dehydrogenase
- Pex19: Peroxisomal biogenesis factor 19
- PINK1: PTEN-induced kinase 1
- PKCa: Protein kinase C alpha
- PLN: Phospholamban
- RYR1: Ryanodine receptor
- RYR2: Heart-specific isoform of ryanodine receptor
- SERCA: Sarcoplasmic/endoplasmic reticulum calcium ATPase
- SUMO-1: Small ubiquitin-related modifier 1
- T-cap: Telethonin
- tBid: Truncated BH3 interacting-domain death agonist
- TFAM: Transcription factor A, mitochondrial
- TGF-β1: Transforming growth factor β1
- TIM23: Mitochondrial import inner membrane subunit TIM23

- UBC9: E2 ubiquitin ligase
- ULPs: Ubiquitin-like proteases
- βAR: β-adrenergic receptor

Protein domains

- AD: Activation domain
- BD: Binding domain
- GED: GTPase effector domain
- HR1: Heptad repeat 1
- HR2: Heptad repeat 2
- M: Middle domain
- NTE: NH_2-terminal extension
- PHD: Pleckstrin homology domain
- PRD: Proline-rich domain
- R1: N-terminus amino acid repeat 1
- R2: N-terminus amino acid repeat 2
- SH3: SRC homology domain 3
- TM: Transmembrane domain
- TPR: Tetratricopeptide repeats
- VD: Variable domain
- ΔPRD: Minus the proline-rich domain

Amino acids

- A: Alanine
- C: Cysteine
- D: Aspartic acid
- F: Phenylalanine
- K: Lysine

Molecules

- ADP: Adenosine diphosphate
- AMP: Adenosine monophosphate
- APS: Adenosine 5' phosphate
- ATP: Adenosine triphosphate
- Aβ: β-amyloid plaques
- Ca^{2+}: Calcium ion
- cDNA: Complementary DNA
- DNA: Deoxyribonucleic acid
- dNTPs: Deoxynucleotide triphosphate
- GTP: Guanosine triphosphate
- mtDNA: Mitochondrial DNA
- NADH: Nicotineamide adenine dinucleotide
- NO: Nitric oxide
- O_2: Oxygen
- P_i: Inorganic phosphate
- PPi: Pyrophosphate
- Q: Ubiquinone
- RNA: Ribonucleic acid
- ROS: Reactive oxygen species

Terms

- CAC: Citric acid cycle
- CCV: Clathrin coated vesicle
- CICR: Calcium-induced calcium release
- CMV: Cytomegalovirus
- cryoTEM: Cryo-transmission electron microscopy
- *Dnm1l*^{Py}: Python mutation
- E14.5: 14.5-day-old embryos
- E9.5: 9.5-day-old embryos
- ER: Endoplasmic reticulum
- ES cells: Embryonic stem cells

- ETC: Electron transport chain
- ETS: Electron transport system
- IMM: Inner mitochondrial membrane
- iPSCs: Induced pluripotent stem cells
- IRES: Internal ribosome entry site
- LTCC: L-type calcium channel
- MEFs: Mouse embryonic fibroblasts
- MMP: Mitochondrial membrane potential
- MOMP: Mitochondrial outer membrane permeability
- OMM: Outer mitochondrial membrane
- OXPHOS: Oxidative phosphorylation
- PTPC: Permeability transition pore complex
- RGCs: Retinal ganglion cells
- ROX: Residual oxygen consumption
- SR: Sarcoplasmic reticulum
- SRC: Sarcoma

Genotypes

- *+/+*: Wild-type
- *+/Py*: Python heterozygote
- *Py/Py*: Python homozygote
- *0/0 +/+* : Wild type for the R6/2 transgene, wild type for the Python mutation
- *0/0 +/Py*: Wild type for the R6/2 transgene, positive for Python heterozygous mutation
- *0/T +/+* : Positive for the R6/2 transgene, wild type for the Python mutation
- *0/T +/Py*: Positive for the R6/2 transgene, positive for Python heterozygous mutation

Reagents

- 3-AT: 3-amino-1,2,4-triazole
- APS: Ammonium persulfate
- BDM: 2,3-butanedione monoxime
- BMP4: Bone morphogenic protein 4
- BSA: Bovine serum albumin
- DMEM: Dulbecco's modified eagle medium
- EDTA: Ethylenediaminetetraacetic acid
- EGTA: Ethylene glycol tetraacetic acid
- EtBr: Ethidium bromide
- FCCP: Carbonyl cyanide-4-(trifluoromethoxy)phenylhydrazone
- FCS: Foetal calf serum
- FGF2: Fibroblast growth factor 2
- GFP: Green fluorescent protein
- HBSS: Hank's balanced salt solution
- KRB: Krebs-Ringer modified buffer
- LB: Luthia broth
- LiAc: Lithium acetate
- LIF: Leukaemia inhibitory factor
- ONPG: Ortho-Nitrophenyl-β-D-galtactopyranoside
- PBS: Phosphate buffered saline
- PEG: Polyethylene glycol
- PFA: Paraformaldehyde
- PIC: Protease inhibitor cocktail
- PVA: Polyvinyl alcohol
- SC: Synthetic complete
- SDS: Sodium dodecyl sulphate
- tBuBHq: TertButylHydroquinone
- TEMED: N,N,N',N'-Tetramethylethylenediamine

Experimental procedures

- ENU: *N*-ethyl-*N*-nitrosourea
- PAGE: Polyacrylamide gel electrophoresis
- PCR: Polymerase chain reaction
- Y2H: Yeast-2-hybrid

Chapter 1 : Introduction

1.1 Mitochondrial Dynamics

Mitochondria are found in most eukayotic cell types (Henze and Martin, 2003) and produce the majority of ATP within the cell. Aside from a source of energy production, mitochondria are also involved in other cellular processes such as apoptosis, autophagy, cell signalling and control of the cell cycle and growth. Compartments within the mitochondria include the outer mitochondrial membrane (OMM), intermembrane space, inner mitochondrial membrane (IMM), cristae and matrix (Fig. 1.1). They also contain their own genome, with each mitochondrion containing multiple copies. Mitochondrial dysfunction is implicated in a number of diseases including neuropathies and cardiac dysfunction. Mitochondrial morphology differs between cell types, but a balance between mitochondrial fusion and fission is common to most cells containing mitochondria (Nunnari *et al*., 1997). Their dynamic nature is thought to be essential for function, and disease may be a consequence of alterations in their morphology.

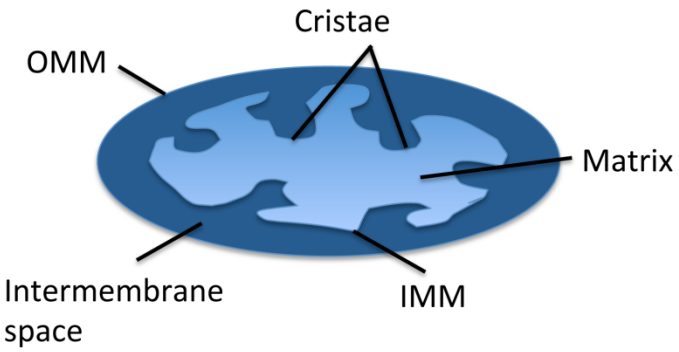

Figure 1.1. Mitochondrial compartments. Mitochondria consist of the following compartments: outer mitochondrial membrane (OMM), intermembrane space, inner mitochondrial membrane (IMM), cristae and matrix.

1.1.1 The role of mitochondrial fusion and fission

Mitochondria are dynamic organelles, constantly undergoing fusion and fission in most cell types (Nunnari *et al*., 1997). This dynamic nature of mitochondria is thought to serve multiple purposes, though the exact role of fusion and fission remains unclear. Fusion is required for mitochondrial growth and fission for cell division (Hoffmann and Avers, 1973), but the latter also contributes to other processes such as removing damaged mitochondrial regions for subsequent degradation (De Meyer *et al*., 2010, Gomes *et al*., 2011, Westermann, 2010). A number of cellular functions have been associated with mitochondrial fission. Morphometric analysis of mitochondria during the cell cycle provides evidence that mitochondrial fission is required for the distribution of mitochondria into daughter cells (Taguchi *et al*., 2007). A reduction in fission was shown to decrease cell proliferation (Lee *et al*., 2007), as was a hyperfused state in vascular smooth muscle cells (Guo *et al*., 2007b, Zhang and Chan, 2007).

Fusion may also help maintain mitochondrial function. Imaging studies of mutant fibroblasts in which fusion proteins had been knocked down revealed most cells contain dysfunctional mitochondria as indicated by a decrease in membrane potential within small regions of a single mitochondrial tubule (Chen *et al*., 2003, Chen *et al*., 2005, Olichon *et al*., 2003). It has since been postulated that fusion protects mitochondria by ensuring that membrane potential – critical to ion exchange across the mitochondrial membrane – is only ever transiently compromised. Fusion facilitates intermitochondrial cooperation, allowing the mitochondrial contents to mix, and thus, may rectify mitochondrial function (Nakada *et al*., 2001).

Mitochondria contain their own genome of mitochondrial DNA (mtDNA), which encodes twelve out of the eighty subunits that make up the complexes of the electron transport chain (ETC) essential for mitochondrial function (Andersson and Kurland, 1999). It was through analysis of the deleterious effect of accumulating mtDNA mutations that the first evidence of a protective effect of mitochondrial fusion was observed (Guan *et al*., 1993, Hermann *et al*., 1998, Jones and Fangman, 1992, Rapaport *et al*., 1998, Shepard and Yaffe, 1999). Measuring enzyme activity across the ETC in human skin fibroblasts revealed that cells only contain defective mitochondria when more than 60% of

mtDNA is mutated, supporting the protective role for mitochondrial fusion (Miyabayashi *et al*., 1992).

Fragmented mitochondria have also been detected in cellular processes such as apoptosis (Martinou *et al*., 1999) and autophagy (Mouli *et al*., 2009), which will be explained in more detail below (Section 1.2). The mitochondria of senescing human umbilical vein endothelial cells have also been shown to display an elongated phenotype. It has been hypothesised that mitochondria in ageing cells conserve energy by reducing the dynamic processes of fusion and fission, yet maintain sufficient energy production for cell survival (Mai *et al*., 2010).

1.1.2 Mitochondrial fusion and fission proteins

The fusion and fission processes are controlled by different sets of proteins. Three large GTPases in the dynamin family are known to participate in mitochondrial fusion: mitofusin 1 (MFN1), mitofusin 2 (MFN2) (Chen *et al*., 2003, Rojo *et al*., 2002, Santel and Fuller, 2001) and optic atrophy 1 (OPA1) (Olichon *et al*., 2003). Recently, mitochondrial elongation factor 1 (MIEF1) (also known as Mid51, (Palmer *et al*., 2011)) has also been shown to participate in the fusion process (Zhao *et al*., 2011). The GTPase dynamin-like protein 1 (DNM1L, previously called DRP1) mediates mitochondrial fission (Chen and Chan, 2005, Frank *et al*., 2001), with the assistance of the docking proteins, mitochondrial fission protein 1 (FIS1) (Chen and Chan, 2005) and mitochondrial fission factor (MFF) (Otera *et al*., 2010). The basic domain structures of fusion and fission proteins are shown in Figure 1.2.

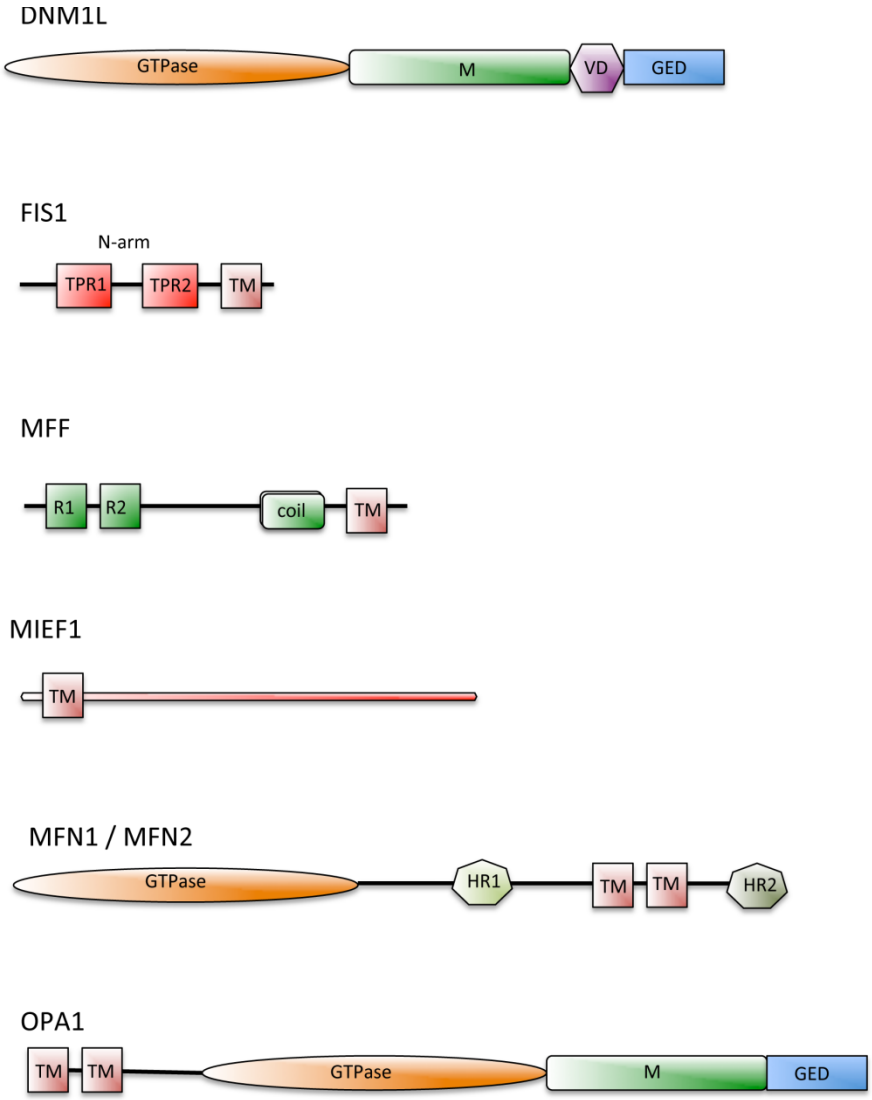

Figure 1.2. Structures of the mitochondrial fusion and fission proteins. The protein structures are shown from the N-terminus (left) to the C-terminus. DNM1L (736 amino acids) is composed of a GTPase domain, a middle domain (M), a variable domain (VD) and a GTPase effector domain (GED). FIS1 (152 amino acids), a non-dynamin protein, comprises an N-arm of six α-helices, where the first is required for oligomerisation and the other five make up two tetratricopeptide repeats (TPR), thought to be essential for DNM1L recruitment. A transmembrane (TM) domain is also necessary for anchorage to the OMM. MFF (342 amino acids) is anchored to the OMM via its C-terminal TM domain, located downstream of a coiled coil domain. MFF also contains two N-terminus amino acid repeats (R1 and R2). MIEF1 (463 amino acids) contains an N-terminus TM domain. MFN1 (741 amino acids) and MFN2 (757 amino acids) both contain a GTPase domain, heptad repeat 1 (HR1), two TM domains and heptad repeat 2 (HR2). OPA1 (997 amino acids) is made up of two TM domains, a GTPase domain, an M domain and a GED. Sizes indicated are of the human proteins.

The mitofusin proteins MFN1 and MFN2 are members of the dynamin family, depicted in Figure 1.2. MFN1 and MFN2 are capable of forming homo- and heterotypic dimers (Koshiba *et al*., 2004, Rojo *et al*., 2002). The proteins are anchored in the OMM via the transmembrane (TM) domains, with the C-terminus, containing the HR2 domain exposed to the cytosol (Koshiba *et al*., 2004, Santel and Fuller, 2001). Interactions between the HR2 domains of mitofusins on adjacent mitochondria mediate mitochondrial docking (Fig. 1.3A). While the mitochondria are tethered, mitochondrial fusion of the inner membranes is then mediated by the dynamin-like protein OPA1, anchored to the cristae on the IMM via its TM domains. The exact mechanism by which OPA1 induces IMM fusion is unknown. It has been postulated that it may mediate tubulation of the IMM, forming protrusions and bringing into contact membranes of adjacent mitochondria (Olichon *et al*., 2003).

A recent discovery suggests MIEF1 is also involved in fusion. Its overexpression in 293T cells resulted in hyperfused mitochondria, while its knockdown by RNAi leads to mitochondrial fragmentation. Interestingly MIEF1 was found to be colocalised with DNM1L on the mitochondria (Zhao *et al*., 2011). Paradoxically, MIEF1 is implicated in the recruitment of DNM1L to the OMM, independent of interactions with FIS1 or MFF. Yet it is apparent that MIEF1 decreases the GTP-binding capability of DNM1L, hence, decreases GTPase activity, rendering the fission protein inactive, thereby promoting fusion. Evidence also suggests that MIEF1 may directly facilitate the fusion process, bringing mitochondrial membranes into close apposition (Zhao *et al*., 2011). The role of this protein was also confirmed in an independent study by Palmer *et al* (2011), by overexpression in HeLa cells.

FIS1 is a small protein comprised of a TM domain, which allows anchorage to the OMM, and six α-helices located at the N-terminus (designated N-arm) (Fig.1.2) (Suzuki *et al*., 2003). The helices form an arrangement that bears some similarity to a tandem arrangement of tetratricopeptide repeats (TPR), a structural motif known to be involved in protein-protein interactions (Blatch and Lassle, 1999). The docking protein, MFF, anchored to the OMM via its TM domain, assists the recruitment of

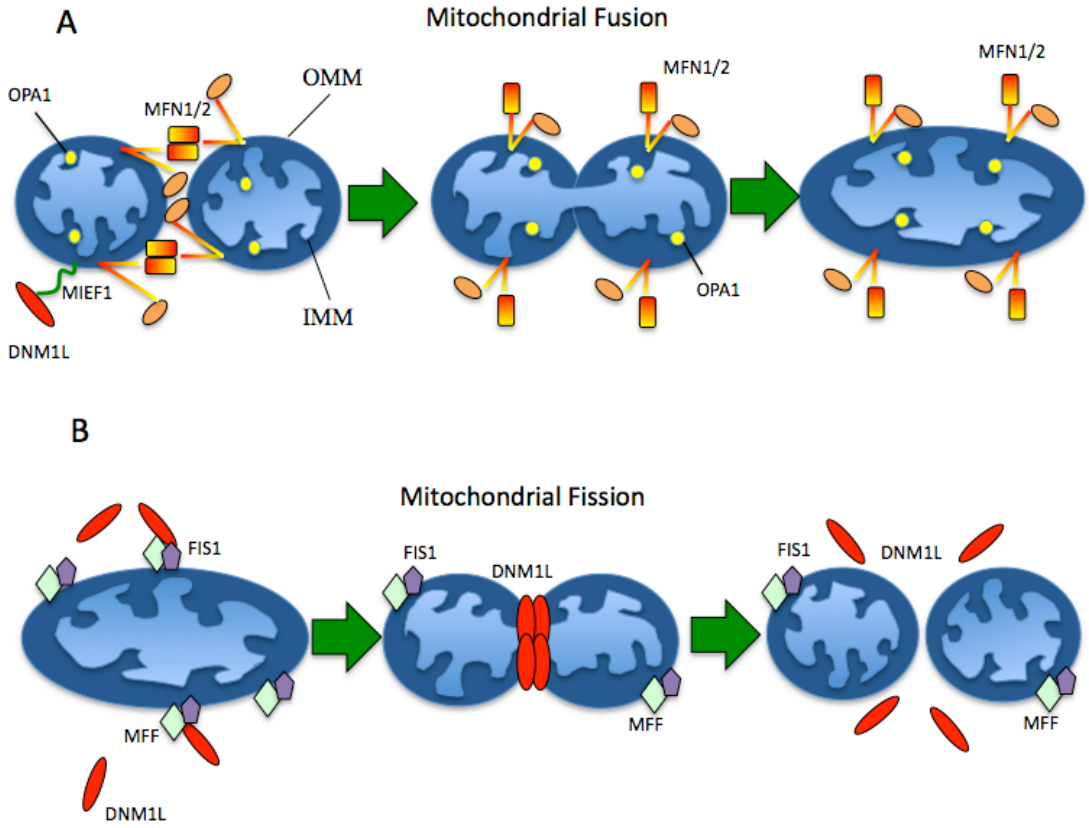

Figure 1.3. A schematic diagram illustrating the proteins involved in mitochondrial fusion and fission. (A) While DNM1L is maintained inactive through interactions with MIEF1, mitochondrial fusion begins with the homo- or heterodimerisation of the mitofusin proteins MFN1 and MFN2 joining the OMMs of two adjacent mitochondria via their HR2 domains. The IMMs then fuse with the help of OPA1. (B) In mitochondrial fission, DNM1L translocates to the OMM surface, where docking is mediated by interactions with FIS1 and MFF. The DNM1L oligomer rearranges, constricting the membranes, resulting in two separate mitochondria.

DNM1L to the OMM to facilitate the process of mitochondrial fission (Fig. 1.3B). MFF directly interacts with DNM1L, independent of FIS1. Knockdown of MFF in CKO human colon tumour cells results in DNM1L remaining in the cytosol and unable to form higher order structures (Otera *et al*., 2010).

The yeast homologue of DNM1L, Dnm1, utilizes two further docking proteins, for which there appear to be no mammalian homologues, mitochondrial division 1 (Mdv1p) and Caffeine-resistant 4 (Caf4p). These proteins mediate the interaction between Dnm1 and Fis1p (the yeast orthologue of FIS1). The docking proteins possess similar domain architectures with an NH_2-terminal extension (NTE), which mediates oligomerisation and association with Fis1p, and a WD40 domain at the C-terminus, which facilitates interactions with Dnm1 (Griffin *et al*., 2005, Tieu and Nunnari, 2000). Crystallographic analysis of complexes containing Fis1p reveal the two adapter proteins bind to Fis1p via the TPR domains (Zhang and Chan, 2007).

1.1.3 DNM1L structure

DNM1L is a member of the dynamin family of proteins. Much of what has been intimated about the structure of DNM1L comes from analysis of other members of the dynamin family. Dynamins are involved in a variety of cellular processes such as vesicle budding (Henley *et al*., 1998, Gold *et al*., 1999), organelle fission (Fukushima *et al*., 2001, Labrousse *et al*., 1999, Pitts *et al*., 1999, Smirnova *et al*., 1998), cytokinesis (Feng *et al*., 2002, Thompson *et al*., 2002, Lukowitz *et al*., 1996) and pathogen resistance (Kochs and Haller, 1999a, Kochs and Haller, 1999b). The main members of the classical dynamin family (dynamin 1, dynamin 2 and dynamin 3) contain GTPase, middle (M), pleckstrin homology (PHD), GTPase effector (GED) and proline-rich (PRD) domains (Fig. 1.4A). The PRD enables the dynamins to interact with proteins that contain a SRC homology domain 3 (SH3) in order to perform vesicle scission functions, including clathrin coated vesicle (CCV) scission, caveolae budding and phagocytosis (Gold *et al*., 1999, Henley *et al*., 1998, Oh *et al*., 1998). DNM1L was first identified as a homologue of the yeast golgi dynamin-like protein,

Vps1p (Imoto *et al*., 1998). DNM1L was soon after shown to associate with mitochondria and to be involved in mitochondrial fission (Otsuga *et al*., 1998, Smirnova *et al*., 1998).

A defining feature of dynamins is their ability to constrict membranes (Sweitzer and Hinshaw, 1998). By way of oligomerisation, dynamins are able to form a helical polymer, made of many dynamin assembly units, around a lipid bilayer, which is essential to induce membrane destabilisation (Praefcke and McMahon, 2004). Due to regions of high flexibility and the tendency to self assemble, the dynamin proteins have proven difficult to crystallise (Low *et al*., 2009) and, therefore, there is a relative paucity of structural detail available. Most information has come from using electron cryomicroscopy reconstructions. A three-dimensional map of a mutant dynamin missing the PRD (ΔPRD) was obtained using electron cryomicroscopy and revealed a T-shaped sub-unit consisting of three distinct regions designated the leg, stalk and head (Fig. 1.4B), with heads being shared by neighbouring dimers. It is evident that interactions also exist within each monomeric subunit; the GED domain folds back to interact with the M domain, which within the dimer, together comprise the stalk region. The strongest interactions between repeat units lie within this stalk region on which oligomerisation is dependent upon (Zhang and Hinshaw, 2001).

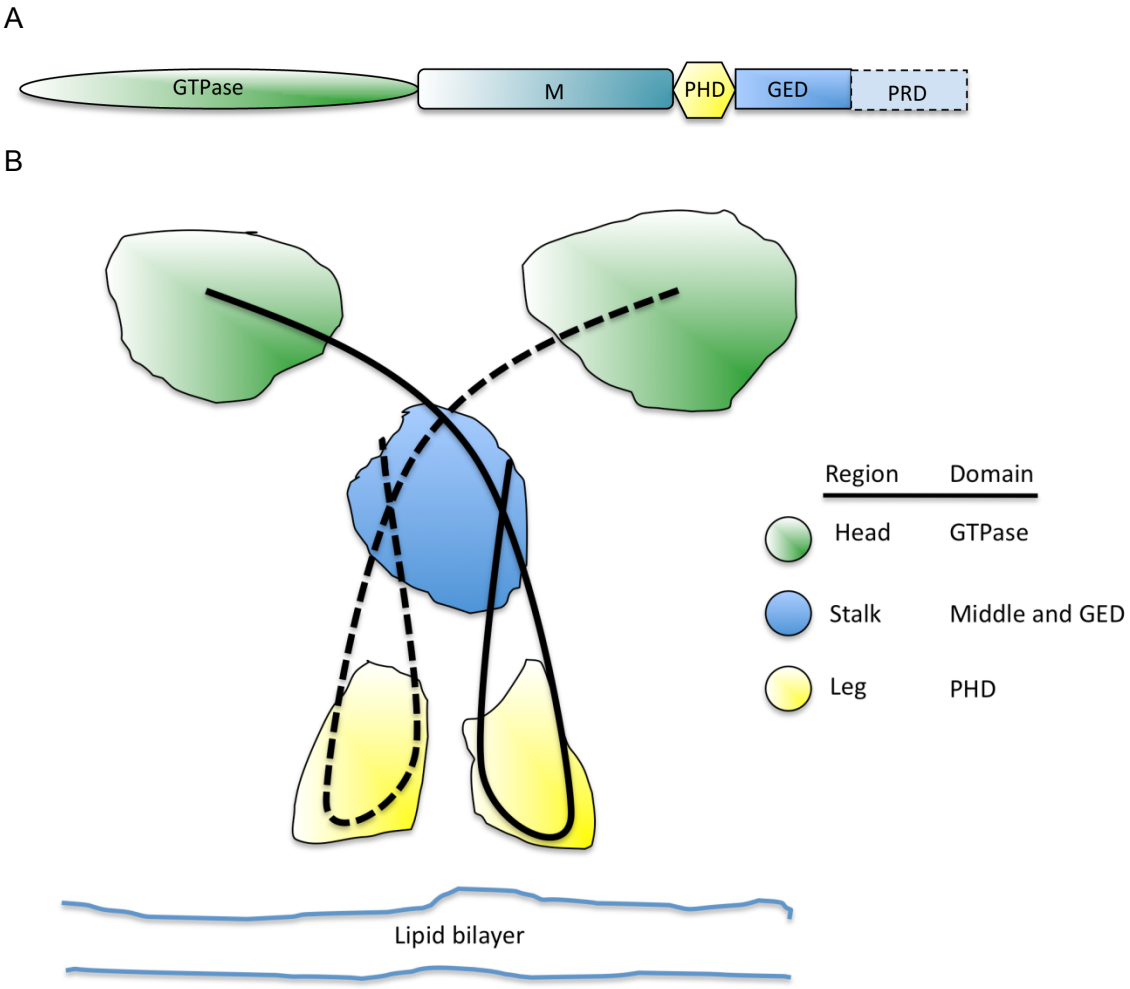

Figure 1.4. Dynamin (ΔPRD) structure. (A) The dynamin protein structure is shown from the N-terminus (left) to the C-terminus. Dynamin is composed of a GTPase domain, an M domain, a pleckstrin homology domain (PHD), a GED and a proline-rich domain (PRD). (B) A schematic diagram of the T-shaped dynamin (ΔPRD) dimer obtained using cryoelectron microscopy. The legs of the sub-unit indicated in yellow represent the PHD, which binds to the lipid bilayer. The stalk region, in blue, contains the M and GED domains. The head region, indicated in green contains the GTPase domain. The dotted and full lines represent two separate monomers of the dimer interacting at the stalk region (Zhang and Hinshaw, 2001).

Upon GTP hydrolysis, the dynamin (ΔPRD) polymer exerts a force, leading to lipid rearrangement and membrane constriction, in which the diameter of the spiral polymer narrows from 50nm to 40nm and the distance between assembly units also shortens from 132 amino acids to 94 amino acids (Fig. 1.5) (Zhang and Hinshaw, 2001).

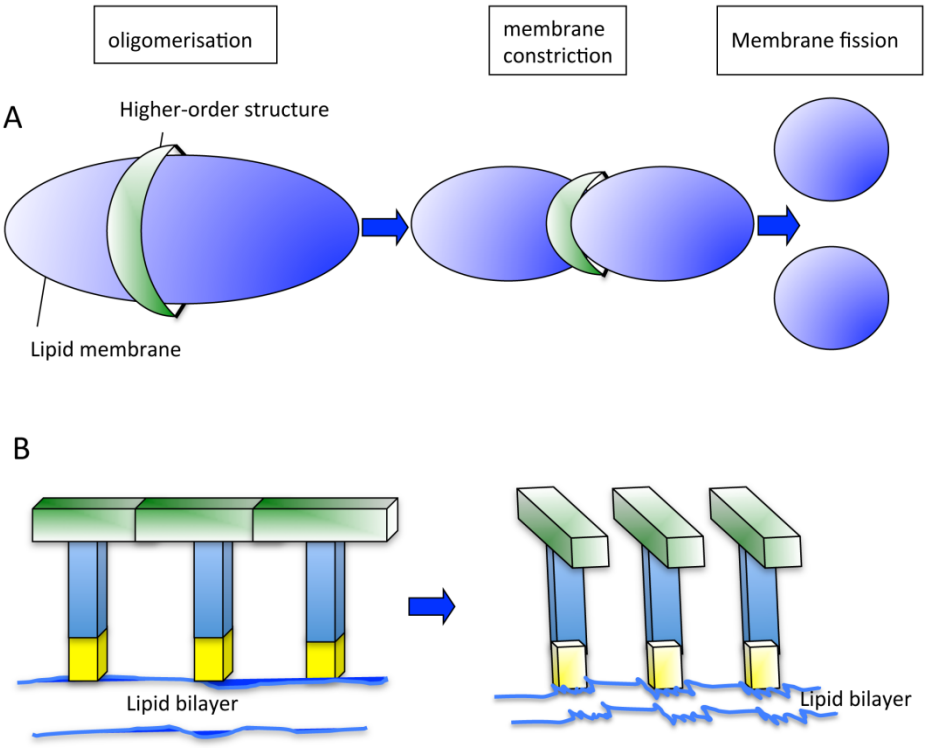

Figure 1.5. Membrane curvature induced by dynamin structural rearrangements. (A) Oligomerisation of the dynamin subunits at the lipid membrane surface induces membrane constriction. The high curvature of the membrane results in fission to regain membrane stability. (B) A possible mechanism by which the dynamin oligomer induces membrane constriction. A twisting motion of each subunit allows tighter packing of the molecules inflicting stress upon the membrane and subsequent curvature.

Cryo-transmission electron microscopy (cryoTEM) of bacterial dynamin-like protein (BDLP) provided further structural data, proposing that the dimer is folded and compact until GTP-binding and lipid association triggers the conformational change to the extended T-shaped repeat (Fig. 1.6A) (Low and Lowe, 2006, Low *et al*., 2009). It is unclear whether BDLP participates in membrane fission, fusion or both. It has been hypothesised that GTPase activity depolymerises the spiral, leaving the lipid membrane in an energetically unfavourable state, which may result in the formation of two separate membranes or if two separate membranes in such state are within close proximity, may lead to their fusion (Fig. 1.6B). Either situation may also result in the membrane returning to its original state (Low and Lowe, 2006, Low *et al*., 2009).

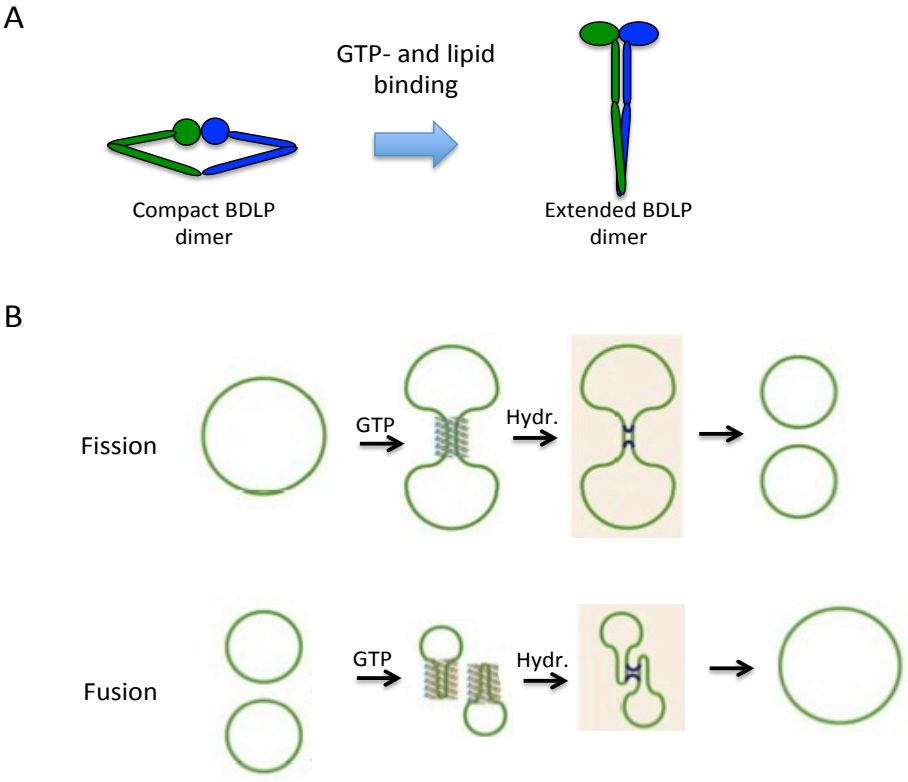

Figure 1.6. BDLP mechanism of action. (A) The compact form of the BDLP dimer undergoes a conformational change upon GTP-binding and lipid association into the extended form required for oligomerisation. Different colours have been used to show individual monomers of the dimer. (B) Polymerisation of the BDLP units creates a coat around the lipid bilayer. GTPase activity leads to membrane rearrangement and depolymerisation of BDLP, resulting in an energetically unfavourable state. This state can cause a single membrane to divide into two or two membranes in close proximity to fuse into one. Modified from Low *et al* (2009).

The mechanism of BDLP polymerisation is likely to be conserved throughout the dynamin family. In agreement with this, the yeast homologue of DNM1L, Dnm1 was also shown to form a filament around the membrane and a change in conformation that accompanies GTP hydrolysis leads to membrane constriction and separation of mitochondria (Ingerman *et al*., 2005). A structural model of mouse DNM1L has also been generated by comparative sequence homology to BDLP, showing similarities in structure to that of the Dynamin (ΔPRD) dimer and the BDLP dimer (Fig. 1.7) (Ashrafian *et al*., 2010).

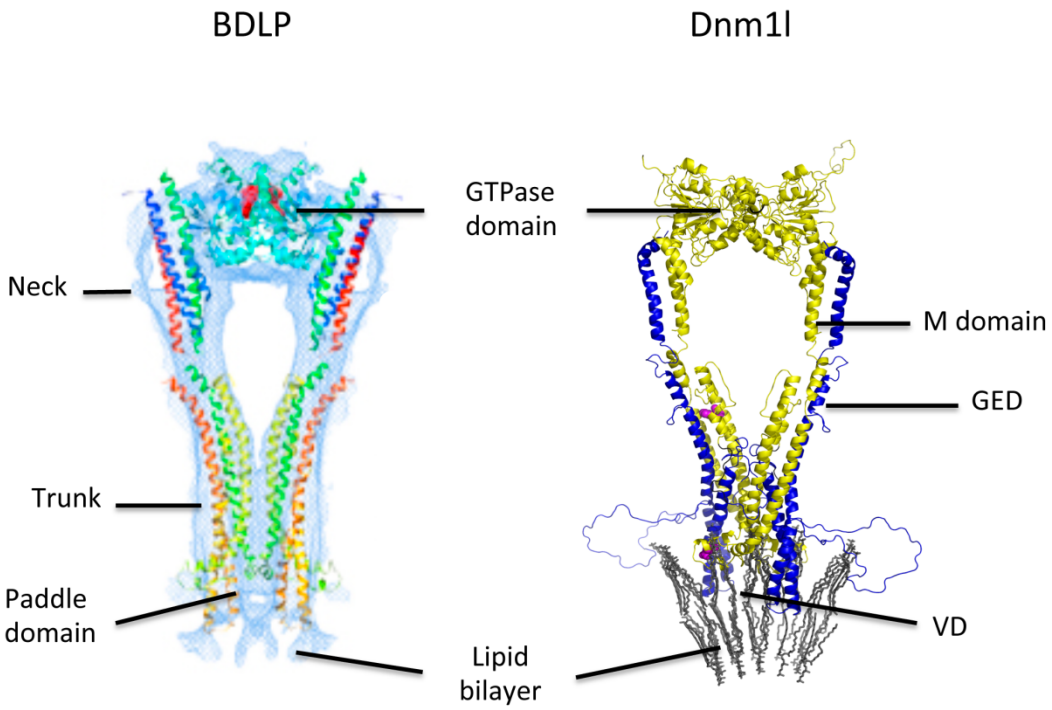

Figure 1.7. BDLP Vs Dnm1l homology models. Homology model of the BDLP dimer (Low *et al*., 2009) displaying the conserved GTPase domain and neck and trunk domains, which correspond to the M and GED domains of Dnm1l shown in the homology model by (Ashrafian *et al*., 2010). The paddle domain of BDLP is thought to mediate lipid binding, as is the VD or PHD in eukaryotes.

In contrast to reports that suggest the DNM1L basic unit *in vivo* is a dimer, other evidence suggests that a tetramer DNM1L unit exists. Cross-linking analysis revealed a molecular mass of ~320KDa for the eluted protein; equal to four DNM1L monomers of ~80KDa (Shin *et al*., 1999). The same method of analysis with dynamin also showed its existence as a tetramer, displaying a molecular mass of ~400KDa (four times the ~100KDa dynamin monomer) (Muhlberg *et al*., 1997). Following size exclusion chromatography, eluted protein from the mouse DNM1L pool was shown to consist of three different molecular masses: ~180KDa, representing the dimer; ~360KDa, indicative of the tetramer; and a mass of over 16MDa, which is likely to represent the higher order structure (Chang *et al*., 2010). Therefore it is likely that DNM1L exists as both dimers and tetramers before forming higher order structures.

1.1.4 Regulation of DNM1L activity

DNM1L exists largely as a cytoplasmic protein, with only 3% bound to the mitochondrial membrane at any one time (Smirnova *et al*., 1998). DNM1L activity is known to be regulated, at least in part, by a number of post-translational modifications. Ubiquitination involved in processes such as protein degradation, DNA repair (Nakamura *et al*., 2006) and membrane protein trafficking (Staub and Rotin, 2006) is one such example. The mitochondrial E3 ubiquitin ligase, MARCHV, was co-immunoprecipitated with the ubiquitinated form of DNM1L (Nakamura *et al*., 2006), suggesting a physical interaction between the proteins. Expressing mutant MARCHV in HeLa cells led to mitochondrial elongation and perinuclear localisation of DNM1L, implying MARCHV may facilitate the translocation of DNM1L to the mitochondria, possibly by mediating self-assembly at sites of mitochondrial fission (Karbowski *et al*., 2007). Through a yeast-two-hybrid screen, SUMO-1 and the sumo-conjugating enzyme (UBC9) were revealed as strong interacting partners of DNM1L, which was also confirmed by pull-down experiments in mammalian cell lines co-expressing both proteins (Harder *et al*., 2004). Fluorescence microscopy also revealed co-localisation of SUMO-1 with DNM1L at sites of fission in many mitochondria indicating DNM1L activity may

also be regulated by sumoylation. In support of this, overexpression of SUMO-1 in Cos7 cells increases mitochondrial fission. It has been postulated that sumoylation may protect against degradation by inhibiting ubiquitin-like proteases (ULPs) (Harder *et al*., 2004). Excess nitric oxide (NO) was reported to induce dimerisation and increase GTPase activity of DNM1L through S-nitrosylation of a cysteine residue at position 644 (Cys_{644}) in the GED (Cho *et al*., 2009). This report is, however, directly contradicted by subsequent work by another research group (Bossy *et al*., 2010) and so its significance remains unknown. Three serine residues within the GED have been identified as regulation sites by phosphorylation. Phosphorylation of Ser_{616} in human DNM1L cells by cyclin-dependent kinase 1 bound to cyclinB induces mitochondrial fission during mitosis (Taguchi *et al*., 2007). Ser_{637} is a target for a number of regulatory proteins. Phosphorylation of this residue by protein kinase A inhibits fission (Chang and Blackstone, 2007), while phosphorylation by calmodulin dependent kinase 1a or dephosphorylation by calcineurin induce mitochondrial fission (Cereghetti *et al*., 2008, Han *et al*., 2008). Similarly, Ser_{656} dephosphorylation by calcineurin results in fission (Cereghetti *et al*., 2008), as does phosphorylation by cyclic AMP-dependent protein kinase (Cribbs and Strack, 2007). The effect of phosphorylation or dephosphorylation therefore appear to have contradicting effects on the activity of DNM1L, depending on the residue modified and the protein, which brings about the modification. It may be that post-translational modifications influence the different steps in the fission process, from DNM1L translocation to the mitochondria, assembly of DNM1L into higher-order structures, GTP hydrolysis, membrane disruption, and finally resulting in the detachment and separation of the DNM1L molecules (Chang and Blackstone, 2010).

1.2 The role of mitochondria in physiological processes

Mitochondria are key organelles, playing a part in a number of cellular processes. The maintenance of mitochondrial morphology through the action of fusion and fission proteins has been shown to be crucial for some processes. The roles of fusion/fission proteins in the impact of mitochondrial biology and physiology are described below.

1.2.1 Cell metabolism

A major role of mitochondria is ATP production, achieved through oxidative phosphorylation (OXPHOS), which takes place in the IMM. The process of OXPHOS can be initiated by glucose, which upon glycolysis, produces pyruvate and subsequently acetyl coenzyme A (acetyl coA) via pyruvate dehydrogenase (PDH). Alternatively fatty acids are also used as substrate to produce acetyl coA. Acetyl coA is transported into the mitochondrial matrix where it provides the carbon atoms necessary for a series of oxidation reactions in the citric acid cycle (CAC). The transfer of electrons from nicotineamide adenine dinucleotide (NADH) and succinate, produced in the CAC, are used by the enzymes of the respiratory chain to pump protons into the intermembrane space creating a proton gradient, also known as the mitochondrial membrane potential (MMP). These protons then re-enter the matrix via ATP synthase with the resulting energy being used to drive ATP synthesis (Fig. 1.8). Enzymes involved in the CAC (pyruvate dehydrogenase, alpha-ketoglutarate dehydrogenase and isocitrate dehydrogenase) and the F_0F_1 ATP synthase are regulated by the mitochondrial uptake of calcium ions (Ca^{2+}) (Balaban, 2009, McCormack and Denton, 1980).

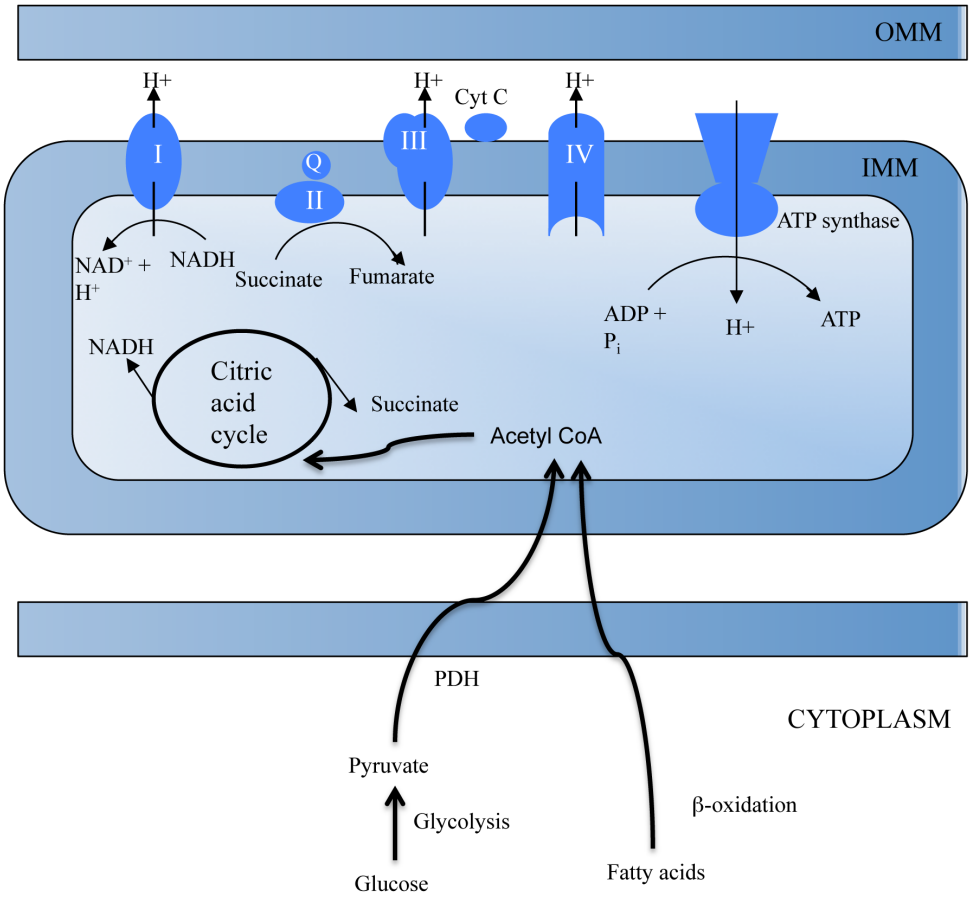

Figure 1.8. ATP production via oxidative phosphorylation. Glucose or fatty acids are used to provide acetyl coA to the CAC in the mitochondrial matrix. NADH and succinate are 2 key substrates produced in the CAC. Complex I (NADH dehydrogenase) removes electrons from the NADH molecules passed from the CAC. These electrons are transferred to a lipid soluble carrier, ubiquinone (Q) while protons translocate across the membrane into the intermembrane space, producing a proton gradient. Complex II (succinate dehydrogenase) delivers more electrons into the quinone pool from succinate. These electrons are important to reduce cytochrome C molecules by complex III (cytochrome BC_1 complex). Complex IV (cytochrome C oxidase) then oxidizes Cytochrome C, pumping more protons across the membrane. This proton gradient proves to be very important in ATP synthesis, as it is required for the F_0F_1 ATP synthase complex to produce ATP. The F_0 component of ATP synthase acts as an ion channel that provides a proton flux back into the mitochondrial matrix, which releases free energy produced during the generation of oxidized forms of electron carriers NAD^+ and Q. The free energy from this proton flux is used to drive ATP synthesis, catalysed by the F_1 component.

1.2.2 Mitochondria-ER cooperation

A proportion of mitochondrial membrane is directly tethered to the endoplasmic reticulum (ER). This is believed to be of central importance as it allows for very rapid uptake of Ca^{2+} released from the ER at these sites into mitochondria (Rizzuto *et al*., 2004). MFN2 has been shown to be important in this tethering process (de Brito and Scorrano, 2008). The presence of MFN2 on the ER surface forms homo- or heterotypic complexes with MFN1 or MFN2 present on the mitochondria, tethering the two organelles. This close positioning between the organelles facilitates efficient mitochondrial Ca^{2+} uptake required for the subsequent activation of key enzymes of the CAC in order to supply succinate and NADH to the respiratory complexes (de Brito and Scorrano, 2008).

Aside from this important role in mitochondrial Ca^{2+} uptake, ER-mitochondrial tethering may be important in mitochondrial fission. Independently of DNM1L and MFF, the ER is able to interact with mitochondria. These sites later become occupied by DNM1L, and hence, become sites of fission. It has since been postulated that the ER interacts with the mitochondria in order to initiate the constriction of the OMM, allowing the DNM1L oligomer to spiral around and further constrict the mitochondria until fully divided (Friedman *et al*., 2011). Defective ER morphology has also been reported in association with *DNM1L* mutants, demonstrating up to an 80% decrease in total ER volume (Pitts *et al*., 1999).

1.2.3 Maintenance of the mitochondrial membrane potential

Maintenance of the MMP is essential for ATP production via OXPHOS. MMP not only drives ATP synthesis, but also stimulates mitochondrial Ca^{2+} uptake via the mitochondrial Ca^{2+} uniporter (MCU) (Hansford and Zorov, 1998). This is achieved through an electrochemical gradient across the mitochondrial membrane, provided by the MMP. Evidence has shown that a reduction in MMP significantly reduces mitochondrial Ca^{2+} uptake (Szanda *et al*., 2010). Therefore MMP maintenance is fundamental for survival of cells.

The fusion factors MFN1 and MFN2 have been shown to be important in the maintenance of MMP. Disruption of mitochondrial morphology by knockdown of MFN1 or MFN2 in mouse embryonic fibroblasts was shown to result in the complete dissipation of membrane potential, increased mtDNA instability and decreased ATP production (Chen *et al*., 2010). This might be a direct result of a reduction in fusion, for example, the lack of a repair mechanism for mitochondria, in which fusion facilitates mitochondrial content sharing (Nakada *et al*., 2001). Alternatively, it might be a related function of MFN1 or MFN2, for example, given MFN2's involvement in ER-mitochondrial tethering, knockdown of MFN2 will reduce the efficiency of ER-mitochondrial contact, leading to defective uptake of Ca^{2+} into the mitochondria, and associated decrease in the number of protons pumped across the inner membrane, thereby significantly reducing the MMP. It has been postulated that fission might also be important for maintaining the MMP, for instance, fission can segregate depolarized mitochondria, allowing them to be removed by autophagy (Mouli *et al*., 2009, Twig *et al*., 2008).

1.2.4 Autophagy and Mitophagy

Autophagy is the process by which damaged or excess organelles are removed by lysosomal degradation. This occurs under normal conditions to maintain cell function, and may be upregulated as a result of nutrient deprivation. During the process of autophagy, mammalian target of rapamycin (mTOR) activity is often suppressed. The process is then initiated by autophagy-related proteins, which mediate the formation of a double-membrane (also known as an isolation membrane) that surrounds the organelle to be degraded forming the so-called autophagosome. The autophagosome marker MAP1 light chain 3 isoform I (LC3-I) is localised to the cytosol. Upon C-terminal cleavage and lipidation LC3-I is converted into the LC3-II isoform. LC3-II becomes localised to the autophagosome membrane to complete the formation of the lipid bilayer of the isolation membrane (Xie and Klionsky, 2007) It is unknown whether the modification of LC3-I occurs before translocation to the autophagic membrane or after (Kabeya *et al*., 2000).

Fusion of autophagosomes with lysosomes allows degradation of the components engulfed by the autophagosome (Nakatogawa *et al*., 2009, Yang and Klionsky, 2010).

Cardenas *et al* (2010) report that autophagy can be a cellular response to defective inositol-1,2,4-triphosphate receptor (IP_3R) Ca^{2+} release from the ER and subsequent signalling between the ER and mitochondria. When IP_3 binds to the IP_3R on the ER, Ca^{2+} is released from the ER allowing uptake by mitochondria. As stated previously (Section 1.2.1), Ca^{2+} is required for the activity of specific enzymes involved in ATP production. ATP maintains the inactivation of AMP-activated protein kinase (AMPK), a sensor of energy insufficiency (Hardie, 2007). Reduced mitochondrial Ca^{2+} uptake leads to a reduction in ATP production via OXPHOS. Upon ATP depletion, AMPK is activated through phosphorylation (P-AMPK). This response to a reduction in ATP enables the cell to recycle metabolites by the synthesis of new raw materials for the production of acetyl coA, which kick-starts the CAC, and so increasing the production of ATP. Autophagy in the case of defective IP_3R Ca^{2+} release from the ER was, however, shown to occur via a pathway independent of mTOR, as nutrition within cells was still sufficient (Fig. 1.9) (Cardenas *et al*., 2010). It has also been proposed that this IP_3R-mediated autophagic response is targeted specifically for defective ER removal (Green and Wang, 2010).

Mitophagy is the term given to the removal of mitochondria by autophagy. This is a cellular maintenance mechanism in which damaged mitochondria are removed (Mouli *et al*., 2009). The inability to remove damaged organelles such as mitochondria may result in the accumulation of non-functional organelles, eventually leading to oxidative stress and decreased ATP production (De Meyer *et al*., 2010). It has been demonstrated that dissipation of the inner membrane potential prevents mitochondrial fusion (Twig *et al*., 2008, Legros *et al*., 2002) and mitochondria exhibiting this defect are targeted by autophagosomes for digestion and elimination (Elmore *et al*., 2001). The mechanism by which membrane potential facilitates fusion is thought to involve the proteolytic cleavage of OPA1. During fusion, OPA1 exists in the large (L)-isoform. It has been postulated that membrane potential is required to maintain the mechanical coupling of the fusion machinery on the outer and inner membranes. Upon dissipation of the membrane potential,

fusion is inhibited due to the translocation of the OPA1 L-isoform across the IMM into the matrix, where it is processed to produce the short (S)-isoform, observed in fragmented mitochondria (Ishihara *et al*., 2006). Depolarised membranes have also been shown to cause mitophagy through the recruitment of PARKIN (Yang *et al*., 2006, Park *et al.,* 2006, Greene *et al.,* 2003). When PTEN-induced kinase 1 (PINK1) is imported into mitochondria, the protein is usually cleaved by voltage-sensitive proteolysis. When the membrane potential dissipates, PINK1 cleavage is inhibited, leading to the recruitment of PARKIN. Increasing the expression of PARKIN leads to ubiquitination of proteins on the OMM and thought to initiate mitohphagy through the recruitment of factors that activate autophagy such as LC3 and cortactin (Narenda *et al*,, 2010, Jin & Youle, 2012).

It has been postulated that mitochondrial fission precedes mitophagy in order to create smaller fragments to enable engulfment and selective removal by the autophagosome (Westermann, 2010). In support of this, it has been observed that during starvation, elongated mitochondria are spared from mitophagy (Gomes *et al*., 2011). It is hypothesized the combination between fusion and fission segregates dysfunctional mitochondria and identifies them for removal by autophagy (Twig *et al*., 2008, Mouli *et al*., 2009).

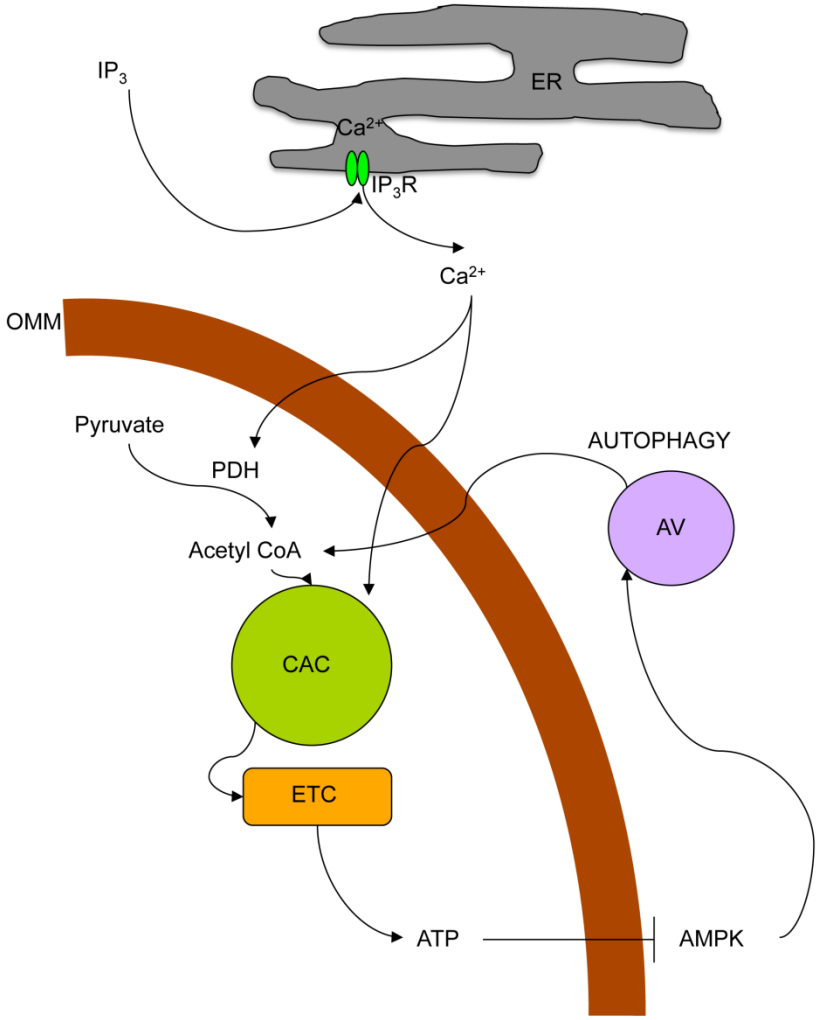

Figure 1.9. Pathway of Autophagy regulation by Ca^{2+} transfer. Upon binding of IP_3 to the IP_3R, Ca^{2+} is released from the ER, which then enters the mitochondria, activating PDH and dehydrogenases of the CAC. The production of ATP via the ETC blocks the phosphorylation of AMPK. When phosphorylated, in the absence of ATP, it is able to stimulate autophagosomal growth, leading to autophagy (Green and Wang, 2010).

1.2.5 Apoptosis

Apoptosis is the term given to programmed cell death, a critical function in the development and maintenance of tissues and organs (Meier *et al*., 2000). Apoptosis also ensures the accurate elimination of damaged and potentially harmful cells. The process can be induced by various stimuli that all converge to induce activation of the caspase complex and subsequent cell death (Kerr *et al*., 1972). The BCL-2 protein family mediates the regulation of apoptosis. Some members, known as anti-apoptotic proteins e.g. BCL-2 and BCL-X, inhibit apoptosis by inhibiting the activation of the pro-apoptotic proteins, BAX and BAK. (Yang *et al*., 1997, Rosse *et al*., 1998, Kluck *et al*., 1997, Eskes *et al*., 1998). The family known as BH3-only proteins also contributes to the pathway by blocking the activity of the anti-apoptotic proteins, allowing the activation of BAX and BAK (Shimizu and Tsujimoto, 2000). In response to apoptotic stimuli, BAX translocates from the cytosol to the mitochondria, while BAK is already present at the mitochondrial membrane. Oligomerisation of these proteins contributes to mitochondrial outer membrane permeability (MOMP). This mitochondrial destruction leading to leakage of toxic components (primarily cytochrome c) from the OMM is a crucial aspect of the process.

In addition to its role in fission, DNM1L is required for apoptosis, mediating mitochondrial cristae remodelling and cytochrome c release leading to cell death. It has been postulated that DNM1L associates with the fusion protein MFN2, initiates tethering of the OMM and promotes oligomerisation of the pro-apoptotic factor BAX (Karbowski *et al*., 2002, Montessuit *et al*., 2010). Inhibition of DNM1L GTPase activity (by expression of a dominant negative mutant) impairs both fission and apoptosis (Frank *et al*., 2001) supporting a role for DNM1L in both processes.

The translocation of BAX to the mitochondria in response to apoptotic stimuli also mediates an increase in DNM1L translocation to the mitochondria (Frank *et al*., 2001). However the precise role of DNM1L and mitochondrial fission in apoptosis remains elusive. It has been postulated that DNM1L and MFN2 colocalise with BAX at scission foci, inducing MOMP (Karbowski *et al*., 2002). In a recent report, DNM1L was shown to be capable of stimulating BAX

oligomerisation by promoting membrane remodelling. In response to apoptotic stimuli, BAX undergoes a conformational change and translocates to the OMM, recruited by tBID, a receptor protein for BAX to integrate into the OMM. At the same site, membrane remodelling, facilitated by DNM1L, induces BAX oligomerisation, causing MOMP and subsequent apoptosis. Remodelling may provide the appropriate membrane curvature and lipid composition, explaining the preference of BAX localisation to the mitochondrial fission sites in apoptotic cells (Fig. 1.10) (Montessuit *et al*., 2010).

In marked contrast, DNM1L-mediated mitochondrial fission has also been reported to have a protective role against apoptosis by protecting mitochondria from elevated Ca^{2+} uptake (Ong *et al*., 2010, Szabadkai *et al*., 2004). During the process of OXPHOS, electrons passed through the ETC can leak out and react with molecular oxygen, which triggers a sequence of reduction reactions eventually leading to the production of reactive oxygen species (ROS) (Brookes *et al*., 2004, Takimoto and Kass, 2007). Normally, ROS are chemically reduced, however at elevated levels they can become detrimental to the cell. While mitochondrial Ca^{2+} uptake is a crucial element in ATP production, an overload of mitochondrial Ca^{2+} increases respiratory output, therefore increasing ROS generation. The switch of Ca^{2+} from being a physiological stimulus to a pathological stimulus is known as the 'two-hit hypothesis' (Brookes *et al*., 2004). Increased leakage of mitochondrial contents including ROS and cytochrome c have been reported in association with mitochondrial Ca^{2+} overload, ultimately resulting in apoptosis (Szalai *et al*., 1999). This is also supported by the formation of the mitochondrial permeability transition pore (mPTP), which opens in response to a high mitochondrial Ca^{2+} concentration. The mPTP permeabilises the inner membrane usually leading to mitochondrial swelling and subsequent necrosis (Choi *et al.*, 1999). However it has also been shown that the resulting dissipation of the membrane potential activates Calpain, a protein that cleaves BID into its truncated form, tBID, enabling the recruitment and oligomerisation of BAX, leading to MOMP formation and apoptosis (Chen *et al*., 2002).

Over expression of DNM1L in HeLa cells leads a highly fragmented mitochondrial network as a result of increased fission. It is thought that a greater degree of fragmentation will result in a greater distance between

mitochondria and sites of ER Ca^{2+} release, reducing the efficiency of mitochondrial Ca^{2+} uptake. Therefore DNM1L-mediated fission protects against mitochondrial Ca^{2+} overload during apoptosis, while ensuring sufficient Ca^{2+} is present in mitochondria to perform physiological functions (Szabadkai *et al*., 2004). Overexpression of the mitochondrial fusion protein MFN2 initiates apoptosis of vascular smooth muscle cells independently of its ability to mediate fusion (Guo *et al*., 2007a, Suen *et al*., 2008), which may indicate alternative roles for the fusion protein. The roles of mitochondrial fusion and fission proteins in apoptosis thus appear to be dissociable, at least in some contexts.

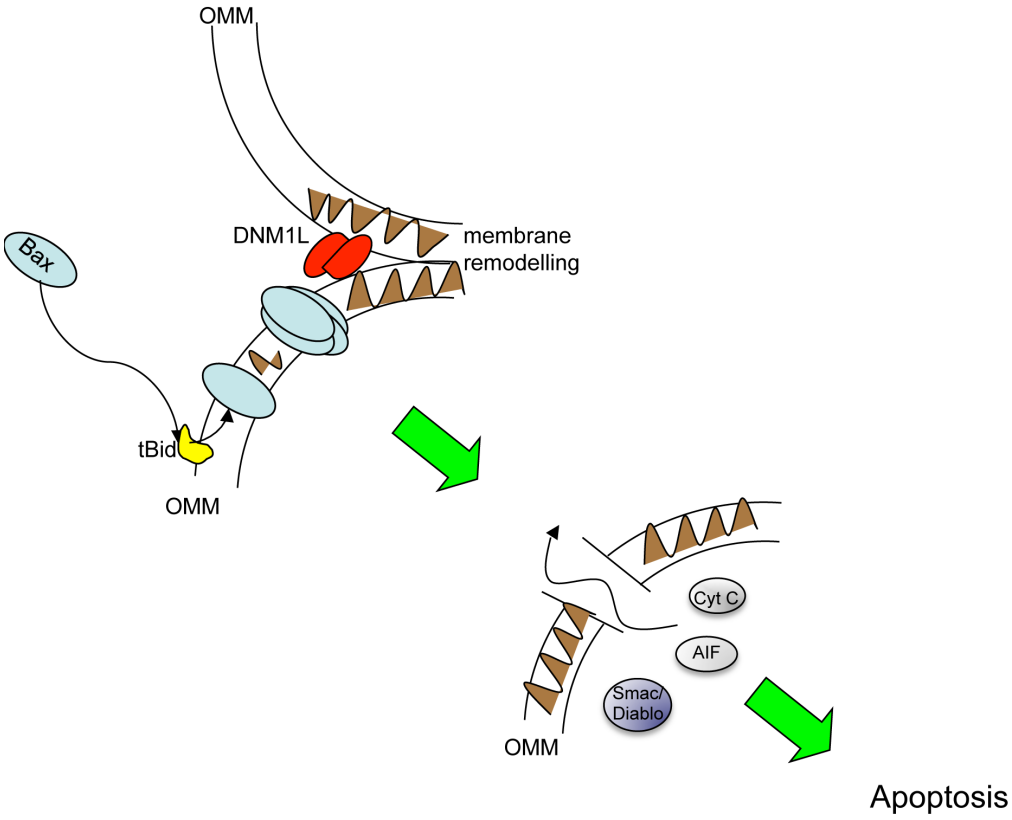

Figure 1.10. DNM1L-induced membrane remodelling in apoptosis. Apoptotic stimuli cause a conformational change in BAX, resulting in the translocation from the cytoplasm to the OMM with the help of tBID. DNM1l-induced membrane remodelling is required for BAX oligomerisation. This is, in turn, critical for mitochondrial outer membrane permeabilisation. Components of the intermembrane space, including cytochrome c, SMAC/DIABLO and apoptosis inducing factor (AIF), exit the mitochondria, leading to cell death. Remodelled OMM is indicated by the brown triangles. Modified from Montessuit *et al* (2010).

1.3 Association of altered mitochondrial morphology with disease processes

Alterations in mitochondrial morphology have been associated with a number of neurodegenerative diseases. The fusion/fission balance has proven very important in all cell types, however alterations in morphology in highly polarised cells such as neurons can result in restricted mitochondrial motility within the cell. Defective fission, resulting in larger mitochondrial networks prevents their translocation into small structures such as axons of neurons (Chen and Chan, 2009). How reduced fusion reduces mitochondrial motility is less clear, but may be due to increased swelling and aggregation (Chen *et al*., 2003). A gradual neurodegeneration may be a consequence of mitochondrial dysfunction.

1.3.1 Parkinson's disease

Parkinson's disease (PD) is characterized by the progressive loss of dopaminergic neurons in the substantia nigra. Symptoms include a resting tremor, rigidity, bradykinesia and an unsteady gait. Two proteins have been identified as key players in the development of PD: PINK1 and PARKIN. PINK1 is a serine/threonine kinase containing an N-terminal mitochondrial targeting sequence localised to cytosolic mitochondria. PINK1 interacts with PARKIN, an E3 ubiquitin ligase, which targets specific proteins for degradation by ubiquitination. Loss of PARKIN can lead to the accumulation of a number of targeted proteins such as the far upstream element (FUSE)-binding protein 1 (FBP1) and p38, as found in the brain of *Park2*-knockout mice (Ko *et al*., 2006, Ko *et al*., 2005). In knockout mouse models of *Park2* (Palacino *et al*., 2004) and *Pink1* (Gispert *et al*., 2009), the mitochondria were shown to exhibit defective respiration, oxidative stress and hyperfragmentation. PARKIN has been shown to interact with and regulate DNM1L turnover (Wang *et al*., 2011). Failure of this function will lead to increased DNM1L activity and excessive mitochondrial fragmentation. Similarly, stable knockdown of *PINK* in SH-SY5 cells also resulted in mitochondrial fragmentation. This is however in contrast to the *Drosophila Park* knockout model (Wang *et al*., 2011), and the loss-of-

function *Pink1* model (Poole *et al*., 2008, Yang *et al*., 2008), which claim mitochondrial elongation is increased. This variance may be in part due to the difference in system used for the experiments.

PARKIN has also been shown to mediate mitophagy, which requires mitochondrial fission (Dagda *et al*., 2009). PARKIN may function to keep DNM1L levels under control, but if recruited to depolarised mitochondria, may help to remove the damaged mitochondria. A mutated PARKIN protein might lead to dysregulated DNM1L maintenance and mitophagy. The resulting phenotype is that of mitochondrial fragmentation and accumulation of damaged mitochondria, a possible cause for neuronal cell death and progression of neurodegenerative disease.

1.3.2 Alzheimer's disease

The most common neurodegenerative disease, Alzheimer's disease (AD), is the result of the loss of neurons in the cerebral cortex causing cognitive dysfunction and memory loss. It is thought the accumulation of β-amyloid plaques (Aβ) leads to cell death (Dodart and May, 2005). Alterations in mitochondrial morphology have been identified in the brains of AD patients (Baloyannis, 2006). The ability of Aβs to localise to mitochondria may play a part in cellular toxicity (Manczak *et al*., 2006, Lustbader *et al*., 2004). It has been hypothesised that generation of NO from the excessive Aβs increases the activity of DNM1L via S-nitrosylation, leading to increased mitochondrial fission. This is supported by the increased levels of SNO-DNM1L found in the brains of AD patients (Cho *et al*., 2009) though the data are not entirely consistent as AD patient fibroblasts express decreased DNM1L levels and mitochondria exhibit the formation of a perinuclear network (Wang *et al*., 2008, Wang *et al*., 2009). However, this could be explained by differences between DNM1L functions in specific cell types.

1.3.3 Huntington's disease

Huntington's disease (HD) is caused by a polyglutamine expansion in exon 1 of the huntingtin protein (HTT). The polyglutamine length determines severity and age of onset, with longer repeats causing increased severity. The resulting striatal neuron degeneration causes symptoms such as cognitive decline and uncontrolled movement that progressively worsen with age (Perry *et al*., 1973). Mitochondria have long been regarded as central to the pathogenicity of HD, based on observations of mitochondrial dysfunction and oxidative stress in cells from HD patients. The striatum, in particular, is sensitive to alterations in energy metabolism, often resulting in degeneration (Beal, 1992). OXPHOS activity has been reported to be severely impaired in the striatum of HD patients, with reduced activity of complexes II, III and IV of the ETC (Brennan *et al*., 1985, Browne *et al*., 1997, Tabrizi *et al*., 1999). MMP (Sawa *et al*., 1999) and increased cytosolic Ca^{2+} due to defective signalling between the mitochondria and ER (Bezprozvanny and Hayden, 2004) also display alterations in the striata of HD patients. However, the underlying mechanisms in which mutant HTT triggers these pathological responses leading to striatal degeneration remains elusive (Damiano *et al*., 2010).

The mitochondrial fission protein, DNM1L, has been implicated by findings of increased translocation to the mitochondrial membrane and GTPase activity in neurons of HD patients (Song *et al*., 2011), which could potentially result in increased mitochondrial fission and subsequent leakage of apoptotic-inducing factors. An increase in the direct interaction between mutant HTT and DNM1L, which appears to increase GTPase activity of DNM1L, has been observed (Song *et al*., 2011, Giacomello *et al*., 2011). Mutant HTT also enhances mitochondrial fission through its stimulation of Ca^{2+} release from the ER by binding to the IP_3R. The increased Ca^{2+} release activates calcineurin, which in turn dephosphorylates DNM1L, stimulating its translocation to the mitochondrial membrane where it can effect fission (Costa *et al*., 2010, Giacomello *et al*., 2011). The fragmented mitochondrial network reduces the motility of mitochondria to the axons in neurons (Shirendeb *et al*., 2012). As a result of these findings it has been postulated that correcting mitochondrial morphological abnormalities in striatal neurons may ameliorate the symptoms

of HD (Shirendeb *et al*., 2012). The increased levels of mitochondrial fragmentation and neuronal apoptosis along with reduced mitochondrial motility and velocity displayed in cells from HD patients have all been reversed in cell lines by expression of a dominant-negative form of DNM1L (Costa *et al*., 2010, Song *et al*., 2011), though this has not yet been translated *in vivo* in animal models of HD.

1.4 Alterations in expression of fusion / fission factors lead to disease

Mutations in fusion/fission proteins have been shown to result in a number of severe disorders. Alterations in mitochondrial morphology also accompany such phenotypes; however, it is unknown whether disease is a result of altered morphology or is due to pleiotropic roles, and the resultant fusion/fission balance is therefore a secondary effect.

1.4.1 Charcott-Marie-Tooth Type 2A

Charcott-Marie-Tooth type 2A (CMT2A) is a neurodegenerative autosomal dominant disorder, characterised by the loss of sensation, predominantly in the lower limbs, although hands and arms eventually become affected as the disease progresses. Missense mutations have been identified in *MFN2*, an OMM fusion protein, responsible for the disease in the affected members of a single family (Zuchner *et al*., 2004). Immunofluorescence studies using cultured CMT2A motor neuron cells reveal the presence of mitochondrial clusters that are unable to translocate down the axon towards the synapses, preventing the synaptic function that is critical for nervous system communication (Detmer *et al*., 2008). Mouse knockout models of *Mfn1* or *Mfn2* result in embryonic lethality and mitochondrial dysfunction (Chen *et al*., 2003), implying an essential role in embryonic development.

1.4.2 Optic Atrophy

Mutations in *OPA1*, the inner membrane fusion protein, results in the neuropathy, dominant optic atrophy (DOA), characterised by the progressive loss of vision, with many cases leading to complete blindness due to damage to the optic nerve. As in CMT2A, mitochondria become highly fragmented as a result of decreased fusion along with abnormal mitochondrial distribution in cells harbouring putative *Opa1* gene mutations, clumping in discrete areas of the cytoplasm. It has been postulated that the mitochondrial defect is followed by decreased respiration and a loss of retinal ganglian cells (RGCs) (Delettre *et al*., 2000). The difference in tissues affected by *MFN2* and *OPA1* mutations regardless of the similar mitochondrial phenotypes, may be due to inner versus outer membrane fusion defects or due to unknown pleiotropic roles for each protein. The specificity of OPA1 defects in RGCs may be explained by its predominant expression in the high-energy demanding retina (Pesch *et al*., 2004)

Lack of OPA1 in mice leads to embryonic lethality (Alavi *et al*., 2009, Davies *et al*., 2007). Heterozygotes for the null mutation (*Opa1*$^{+/-}$) live normal lives up until the onset of optic atrophy (Alavi *et al*., 2009). Studies in the *Opa1*$^{+/-}$ mice have revealed that the effects spread further than the optic nerve; abnormal clutching of the hind limbs suggests defects in the brain, spinal cord and dorsal root ganglia. A third of mice also had a resting tremor of the upper limbs suggesting defects in the brain stem or cerebellum and performed worse in a Roterod test for motor skills suggesting neuromuscular coordination difficulties (Alavi *et al*., 2009). Using *N*-ethyl-*N*-nitrosourea (ENU) mutagenesis, an *Opa1*^{Q825STOP} exon 8 mutation was identified. The mutation truncates the protein immediately prior to the GTPase domain. These mice show reduced visual activity and muscle power and disrupted mitochondrial fusion upon onset of DOA symptoms, reminiscent of the *Opa1*$^{+/-}$ null mutant mouse (Davies *et al*., 2007). Dendritic pruning in RGCs from heterozygous animals is evident from ten months, preceding the onset of the optic atrophy symptoms (White *et al*., 2009). OPA1 may therefore be critical for communication between neurons. Given that mitochondrial fusion is impaired, mitochondrial morphology may also be a requirement for neuronal communication.

Over seventy mutations (missense, nonsense, insertions and deletions) have been reported in the *OPA1* gene in patients with a predisposition to DOA (Alavi *et al*., 2007, Baris *et al*., 2003, Delettre *et al*., 2000, Pesch *et al*., 2001, Thiselton *et al*., 2001, Thiselton *et al*., 2002). Two thirds of these mutations occur in the GTPase domain, which is highly conserved across species and orthologues, and this might reflect a crucial role for this particular domain in the function of OPA1.

1.4.3 The *DNM1L*^{A401D} mutation

An infant that died 37 days after birth exhibited severe neurological and metabolic abnormalities including microcephaly, optic atrophy, abnormal brain development, hyperplasia and elevated lactic acid concentrations in the blood and cerebral spinal fluid (Waterham *et al*., 2007). The metabolic features were suggestive of a defect in energetics and, thus, mitochondria were examined in cell lines from the patient. Both mitochondria and peroxisomes exhibited abnormal morphology and sequencing of *DNM1L* in this patient identified a single nucleotide substitution resulting in an alanine-aspartate substitution in domain M. The infant was heterozygous for the mutation and it was not carried by either parent (Waterham *et al*., 2007). The mutation results in defective DNM1L that shows a lower GTPase activity and an inability to form higher order oligomers (Chang *et al*., 2010).

1.4.4 The *Dnm1l* Python mutation

Large scale ENU mutagenesis in mice is a forward genetics approach to identify mutations that contribute to disease phenotypes (Cordes, 2005). In a dysmorphology screen at MRC Harwell for mutations with dominant effects, a male offspring from an ENU-mutagenised BALB/cCrlAnN male x C3H/HeH female exhibited rapid weight gain over several days (Fig. 1.11A), piloerection and shallow, rapid breathing. It became clear the underlying cause of these symptoms was cardiovascular in nature as the heart was grossly dilated (Fig. 1.11B). The heart also exhibited myocyte hypertrophy and fibrosis (Fig. 1.11C).

The rapid increase in the weight of the mouse was a result of substantial ascites and subcutaneous oedema (Fig. 1.11D). These phenotypes were consistent with dilated cardiomyopathy (DCM) resulting in congestive heart failure (CHF).

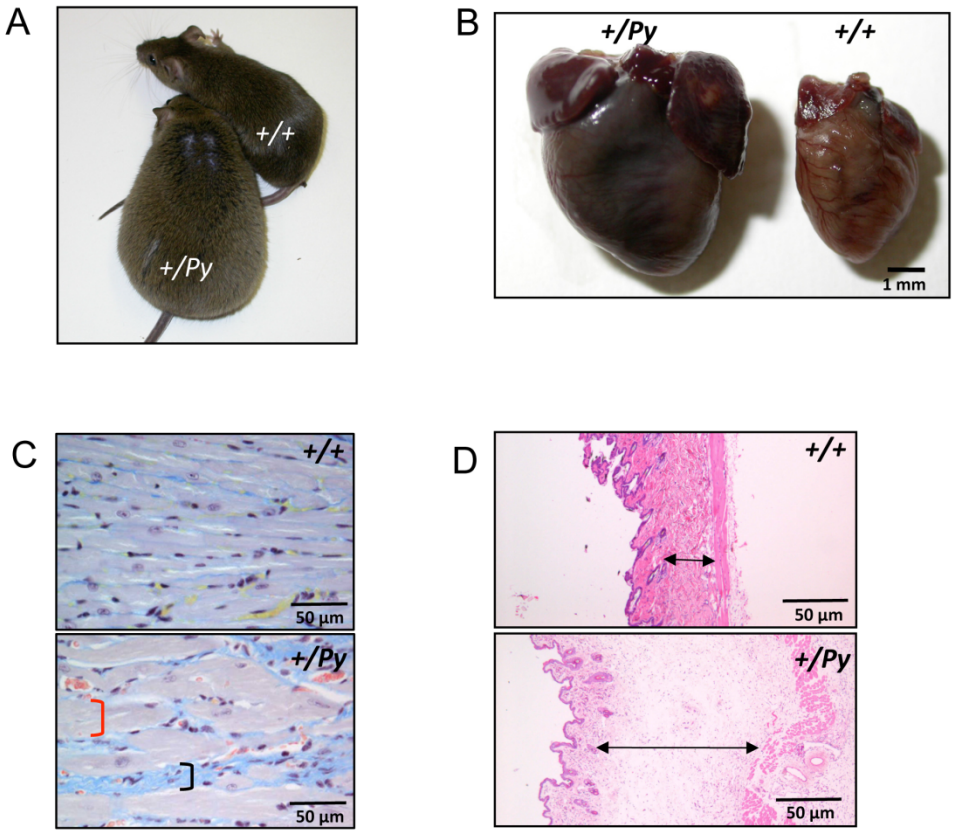

Figure 1.11. The Python phenotype. (A) A 13-week-old Python mouse and wild type control of the C3H/HeN strain, showing the grossly enlarged body size. (B) The hearts excised from the 13-week-old Python and wild type control mice, displaying bi-ventricular and bi-atrial dilation (C) MSB staining of heart sections from Python and wild type mice. Note the enlarged cardiomyocytes (indicated by the red bracket) and increased collagen deposition (indicated by the black bracket) (D) H&E stained dermal connective tissue of Python and wild type control mice; the Python mouse displays subcutaneous oedema (Ashrafian *et al*., 2010).

The phenotype was inherited in an autosomal dominant fashion and was fully penetrant in both males and females, though the onset of overt CHF symptoms occurs earlier in males (Ashrafian *et al*., 2010). Homozygosity for the mutation results in lethality midway through embryogenesis (Ashrafian *et al*., 2010). The

onset of overt CHF appears to be influenced by genetic background as CHF symptoms develop more rapidly when the Python mutation is on the C3H/HeN background compared to C57BL/6J (Ashrafian *et al*., 2010).

Genetic mapping defined a small region of 787kb on chromosome 16 from 16q15.9 to 16q16.7 in which the mutation resided. Sequencing of all exons and intron/exon junctions in the three genes in this region (*Pkp2*, *Fdge4* and *Dnm1l*) identified a single nucleotide substitution (T → G) that resulted in the substitution of a cysteine to a phenylalanine at amino acid position 452 ($C_{452}F$) of the DNM1L protein (Fig. 1.12A). The mutation is located within the M domain. The cysteine residue is highly conserved in DNM1L across species (Fig. 1.12B) suggesting that change in this residue is not well tolerated. The cysteine is not reported to participate in disulphide bonding (Faelber *et al*., 2011, Ford *et al*., 2011). Its location suggests that it is more likely to disrupt intramolecular interactions within the DNM1L monomer rather than affect interactions between monomers (Fig. 1.13A). This is supported by a helix-wheel projection of the region around the Python mutation that predicts the mutation is located within one face of the helix containing principally hydrophobic residues (Fig. 1.13B). The mutated site is therefore likely to be buried within the protein and unable to come into contact with another protein. This face may however be involved in an intramolecular interactions within the DNM1L monomer (Ashrafian *et al*., 2010).

As *Dnm1l* is ubiquitously expressed (Kamimoto *et al*., 1998) the mutant phenotype might manifest itself in all cells. Mitochondrial morphology is altered in fibroblasts isolated from neonatal Python mice. Yet, energy metabolism is severely affected in the heart, but not in other tissue type examined such as liver and brain (Ashrafian *et al*., 2010).

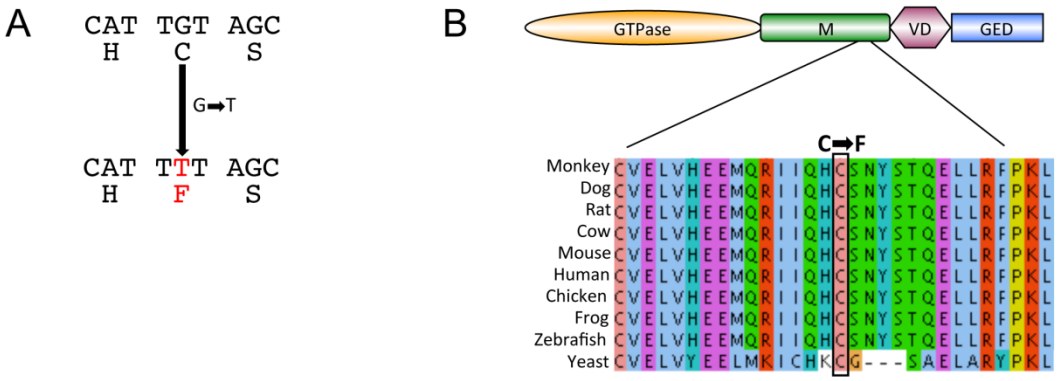

Figure 1.12. Sequence and homology surrounding the Python mutation. (A) The G to T substitution in Python leads to the replacement of a cysteine with a phenylalanine in exon 11 of *Dnm1l*. (B) Clustal alignment of a segment of the M domain in which the Python mutation is located, showing conservation of the mutated cysteine across all species examined (Ashrafian *et al*., 2010).

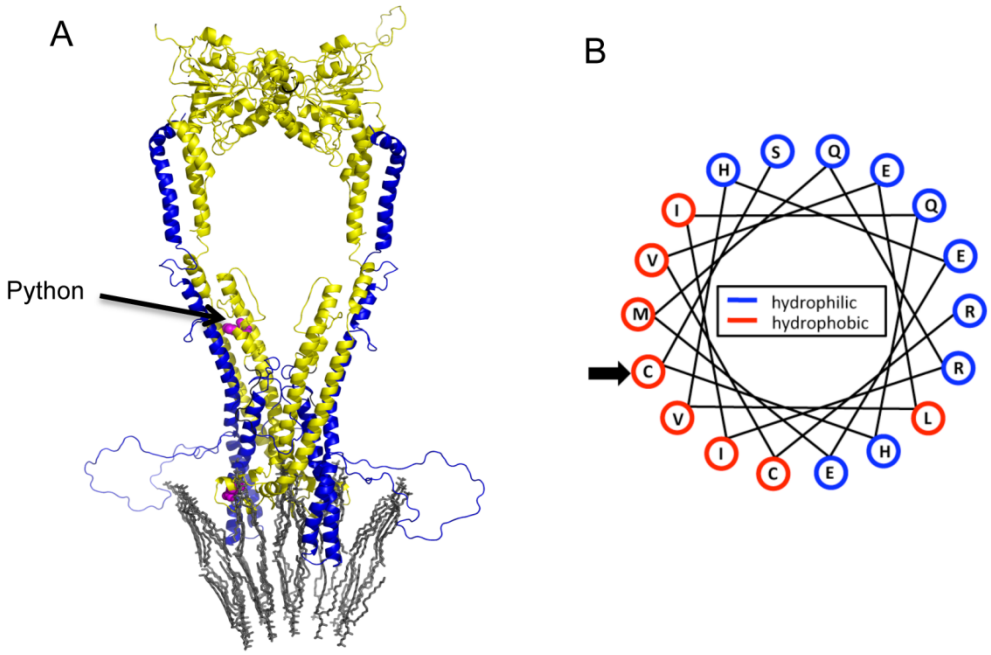

Figure 1.13. The amino acid substitution resulting from the Python mutation. (A) Ribbon representation of the homology model of the DNM1L dimer. The arrow indicates the position of the Python amino acid substitution, shown in pink. (B) A helix wheel projection, displaying the amino acid sequence around the Python containing region. The hydrophobicity indices of the amino acids reveals the cysteine residue that replaced by phenylalanine in Python (indicated by the arrow) is in a predominantly hydrophobic face of the protein (Ashrafian *et al*., 2010).

1.5 Familial Dilated Cardiomyopathy

Cardiovascular disease is a major cause of morbidity and mortality. It is responsible for almost 200,000 deaths each year in the UK, accounting for more than 20% of all hospital admissions in individuals over sixty-five years of age (Allender *et al*., 2008).

Cardiomyopathies are a subset of heart conditions, which specifically affect the heart muscle. From birth cardiomyocytes rely on hypertrophy for growth as hyperplasia becomes very limited. The closure of the ductus arteriosus blood vessel, which allows blood flow from the right ventricle to bypass the fluid filled lungs of the foetus, leads to a sudden increase in preload for the left side of the heart. This sudden increased demand is met with a hypertrophic response, activated about 3 days after birth.

Hypertrophic cardiomyopathy (HCM) occurs when cardiomyocytes exhibit a massive hypertrophic response, causing thickening of the ventricle walls. Despite this thickening, ventricle size often remains the same, and so may block blood flow out of the heart. This is known as obstructive HCM. Symptoms include chest pain, dizziness, shortness of breath and fainting as a result of increased workload put on the ventricles. If blood flow is not blocked, this is termed non-obstructive HCM. In both types of HCM the ventricles are able to hold less blood due to the increased thickness of walls and so less space inside the ventricles. The heart may also experience hypercontractility, in which the heart is unable to relax and fill with blood, leading to high blood pressure in the ventricles and vessels of the lung. Cardiomyocytes may become damaged and electrical signals may become disrupted causing arrhythmias. HCM is a common cause of sudden cardiac arrest during physical activity; on the other hand, some people with HCM may have no symptoms (Cohen *et al*., 1964).

Restrictive cardiomyopathy (RCM) mainly affects older adults. In RCM, normal tissue is replaced with scar tissue. This leads to ventricle rigidity and so the heart is unable to relax and fill with blood, as in HCM. This reduction in blood flow can lead to problems such as heart failure and arrhythmias. The atria also become enlarged (Hayashi *et al*., 1998).

Like RCM, arrythmogenic right ventricular dysplasia (ARVD) occurs when muscle tissue is replaced with scar tissue. In ARVD, however, this is specific to the right ventricle. This can disrupt electrical signals, causing arrhythmias and may cause symptoms such as palpitations and fainting after physical activity. ARVD is also a cause of sudden cardiac arrest in young athletes (Dalla Volta, 1989, Thiene *et al*., 1988).

Dilated cardiomyopathy (DCM) is the most common type of cardiomyopathy. The age in which people are likely to have DCM ranges from 20 to 60 years, males being more affected than females. DCM is characterised by systolic dysfunction and left ventricular dilation, often spreading to all four chambers as the disease progresses. As a result, force transduction is impaired often leading to arrhythmia and congestive heart failure (CHF) (Richardson *et al*., 1996). The molecular mechanisms underlying DCM remain to be elucidated. It is estimated that between 20-50% of cases are familial in nature. DCM-causing mutations have been identified in genes encoding sarcomeric, cytoskeletal, nuclear envelope, intermediary filament, sarcoplasmic reticulum and desmosomal proteins (Table 1.1).

The proteins listed in Table. 1.1 are common to a single pathway that links Ca^{2+} signalling, ATP production, contraction and transduction of the contractile force within a cardiomyocyte. Upon Ca^{2+} entry into the cell, the ryanodine receptor (RYR2) releases Ca^{2+} from the sarcoplasmic reticulum (SR) into the cytosol, a process known as Ca^{2+}-induced Ca^{2+} release (CICR). Ca^{2+} enters the sarcomere where it binds to and shifts the tropomyosin complex away from the myosin head. While some Ca^{2+} is taken back up into the SR via the sarcoplasmic/endoplasmic reticulum Ca^{2+} ATPase (SERCA), the mitochondria also take up Ca^{2+}, necessary for activating enzymes within the mitochondrial matrix required for ATP production. ATP is then transported out of the mitochondria via the adenine nucleotide translocator (ANT) and binds to the vacant myosin head in the sarcomere. The energy generated upon ATP hydrolysis leads to the movement of the actin filament to the centre of the sarcomere causing contraction. Desmin connects the contractile apparatus to other structural elements of the cell such as the nucleus and dystro-glycan complex, transducing the contractile force across the cell and between cells (Fig. 1.14). It therefore becomes plausible that an alteration in any of the

proteins involved in this pathway from ER Ca^{2+} release, mitochondrial Ca^{2+} uptake, ATP production, sarcomeric contraction to the transduction of the contractile force may lead to a similar phenotype (Knollmann and Roden, 2008).

Table 1.1. Table of genes in which DCM-predisposing mutations have been identified in humans.

Gene	Protein	Function	Reference
PLN	Phospholamban	Regulates SERCA Ca^{2+} uptake into ER.	(Haghighi *et al*., 2003, Schmitt *et al*., 2003)
ANT1	Adenine nucleotide translocator	ADP/ATP transport	(Jordens *et al*., 2002, Palmieri *et al*., 2005)
ABCC	SURA2A	Regulatory subunit of Kir6.2, an inwardly rectifying cardiac K_{ATP} channel	(Bienengraeber *et al*., 2004)
TTN	Titin	Sarcomere structure	(Gerull *et al*., 2002)
VCL	Metavinculin		(Olson *et al*., 2002)
ACTN2	α-actinin-2		(Mohapatra *et al*., 2003)
MLP	Muscle LIM protein	Sarcomere stretch sensor / Z disc	(Knoll *et al*., 2002)
ACTC	Cardiac actin	Sarcomeric protein; muscle contraction	(Olson *et al*., 1998)
MYH7	β-myosin heavy chain		(Daehmlow *et al*., 2002, Kamisago *et al*., 2000)
TNNT7	Cardiac troponin T		(Hanson *et al*., 2002, Kamisago *et al*., 2000, Li *et al*., 2001)

TPM1	α-tropomyosin		(Olson *et al*., 2001)
MYBPC	Myosin-binding protein C		(Daehmlow *et al*., 2002)
MYH6	α-myosin heavy chain		(Carniel *et al*., 2005)
TNN13	Cardiac troponin I		(Murphy *et al*., 2004)
DES	Desmin	Dystrophin-associated glycoprotein complex; transduces contractile forces	(Li *et al*., 1999a)
SGCD	δ-sarcoglycan		(Tsubata *et al*., 2000)
DMD	Dystrophin		(Muntoni *et al*., 1993, Towbin *et al*., 1993)
LBD3	Cypher / LIM binding protein domain 3	Cytoskeletal assembly; involved in targeting and clustering of membrane proteins	(Vatta *et al*., 2003)
LMNA	Lamin A/C	Nuclear membrane protein; confers stability to nuclear membrane	(Arbustini *et al*., 2002, Becane *et al*., 2000, Brodsky *et al*., 2000, Fatkin *et al*., 1999, Hershberger *et al*., 2002, Jakobs *et al*., 2001, Sebillon *et al*., 2003, Taylor *et al*., 2003)
TAZ	Tafazzin	Unknown	(Bione *et al*., 1996, D'Adamo *et al*., 1997)

Modified from Burkett *et al* (2005).

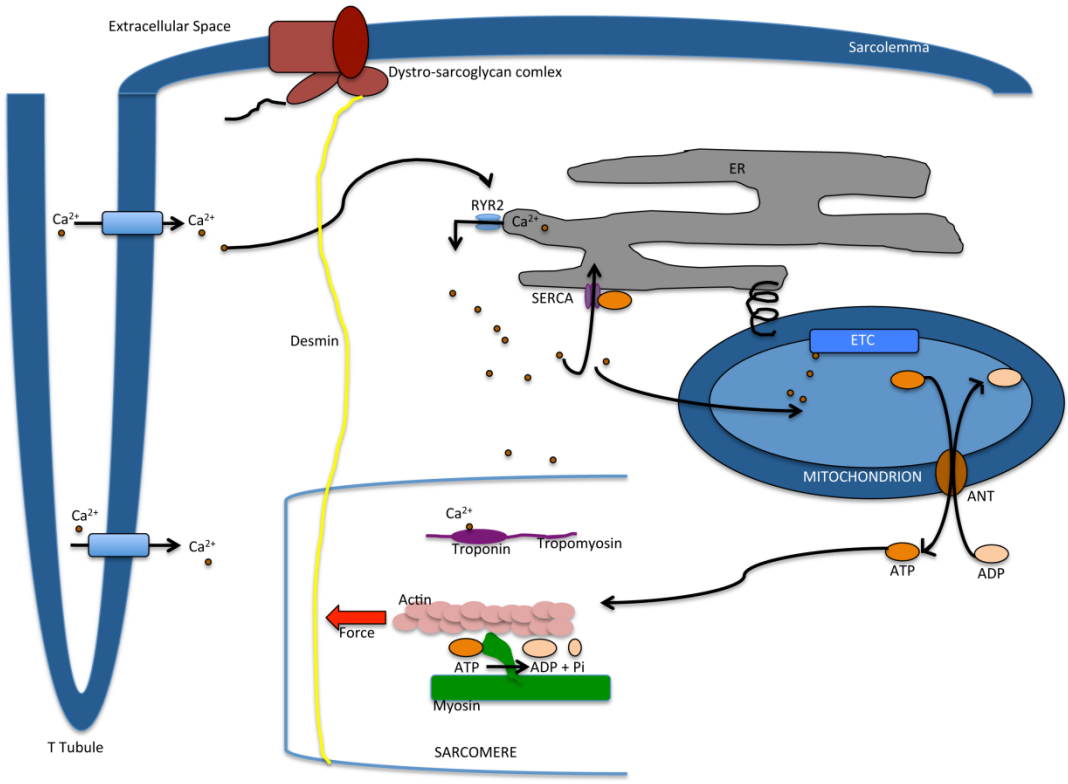

Figure 1.14. Ca^{2+} transport in ATP production and EC coupling. 1) Ca^{2+} influx into the cardiomyocyte triggers the RYR2 to open, allowing the release of intracellular Ca^{2+} from the SR. While some of the Ca^{2+} translocates directly to the sarcomere and binds to Troponin causing a shift away from the myosin head, a large proportion of the Ca^{2+} released from the SR is taken up by the mitochondria, which activates the necessary enzymes of the CAC and the ETC to produce ATP. 2) ATP is then transported out of the mitochondria at the same rate as ADP is transported in via the ANT. 3) Some ATP is hydrolysed by the SERCA in order to reuptake Ca^{2+} into the SR. 4) The majority of ATP is transported to the sarcomere, where it attaches to the myosin head and hydrolysed by ATPase releasing energy. 5) The myosin filament utilizes the energy pulling the actin filament to the centre of the sarcomere, leading to contraction. 6) Desmin then connects these contractile apparatus to other structural elements of the cell including the nucleus and the dystro-sarcoglycan complex, thereby transducing the contractile force across the cell.

Energy dysregulation is at the centre of many forms of heart disease (Tian and Barger, 2006). Mitochondria become highly organised in the adult cardiomyocyte, the reason for which remains unknown. Mitochondria are central to energy production within the cell (Chidsey *et al*., 1966), and constitute a significant proportion of a typical cardiomyocyte, so might be expected to be important in maintaining proper cardiomyocyte function. This is supported by recent evidence implicating mitochondrial dysfunction in the development of disease (Ashrafian *et al*., 2010, Chen *et al*., 2009, Ong *et al*., 2010).

At birth, the myocardium switches from the glycolytic pathway to fatty acid OXPHOS as the major source of ATP production. This provides the myocardium with the source of high-energy production, vital for the beating cardiomyocytes. As a comparison, fatty acids can provide up to 131 ATP molecules per fatty acid molecule, whereas glucose yields 38 and glycolysis yields just 2 (Tian and Barger, 2006).

Initially, a hypothesis to account for the development of HCM postulated that mutant sarcomeric proteins depressed contractility. In response to this stress, expression of stress-responsive factors are increased, such as insulin-like growth factor 1 (IGF-1), transforming growth factor β1 (TGF-β1) and angiotensin II leading to compensatory hypertrophy (Fig. 1.15A) (Marian, 2000). The problem, however, is that this hypothesis cannot explain those cases of HCM in which contractility is increased, nor can it explain the progressive decline in cardiac function, as the mutation is present from birth, but is not apparent until at least puberty.

An alternative theory was proposed based on energy dysregulation as the principle cause of HCM. With inefficient ATP utilisation, cardiomyocyte energy levels would become compromised, affecting SR Ca^{2+} uptake, leading to an increased prolonged cytosolic Ca^{2+} concentration, activating downstream pathways that resulted in HCM (Fig. 1.15B) (Ashrafian *et al*., 2003). During puberty the heart increases in size significantly and concomitantly increases in its demand for energy, while ATP levels decline with ageing due to mitochondrial dysfunction (Wallace, 1999). This would help to explain the progressive decline seen in HCM, as any energy dysregulation would be exacerbated in effect with time. In support of this theory, sudden cardiac death

(SCD) during competitive sports could be explained by energy compromise being most noticeable during strenuous exercise. Further support is provided when considering the range of gene mutations reported in HCM. A *MYH7* mutation leads to a greater proportion of detachment of the myosin head from actin before the power stroke is completed, thereby consuming ATP, but with a lower stroke volume. Similarly, mutant troponin-T increases contractile velocity, but shortens the power stroke, decreasing power output for each ATP hydrolysed (Ashrafian *et al*., 2003). It may be that mutations in genes involved in ATP utilisation, ATP production or calcium handling can result in HCM and similar cardiac conditions.

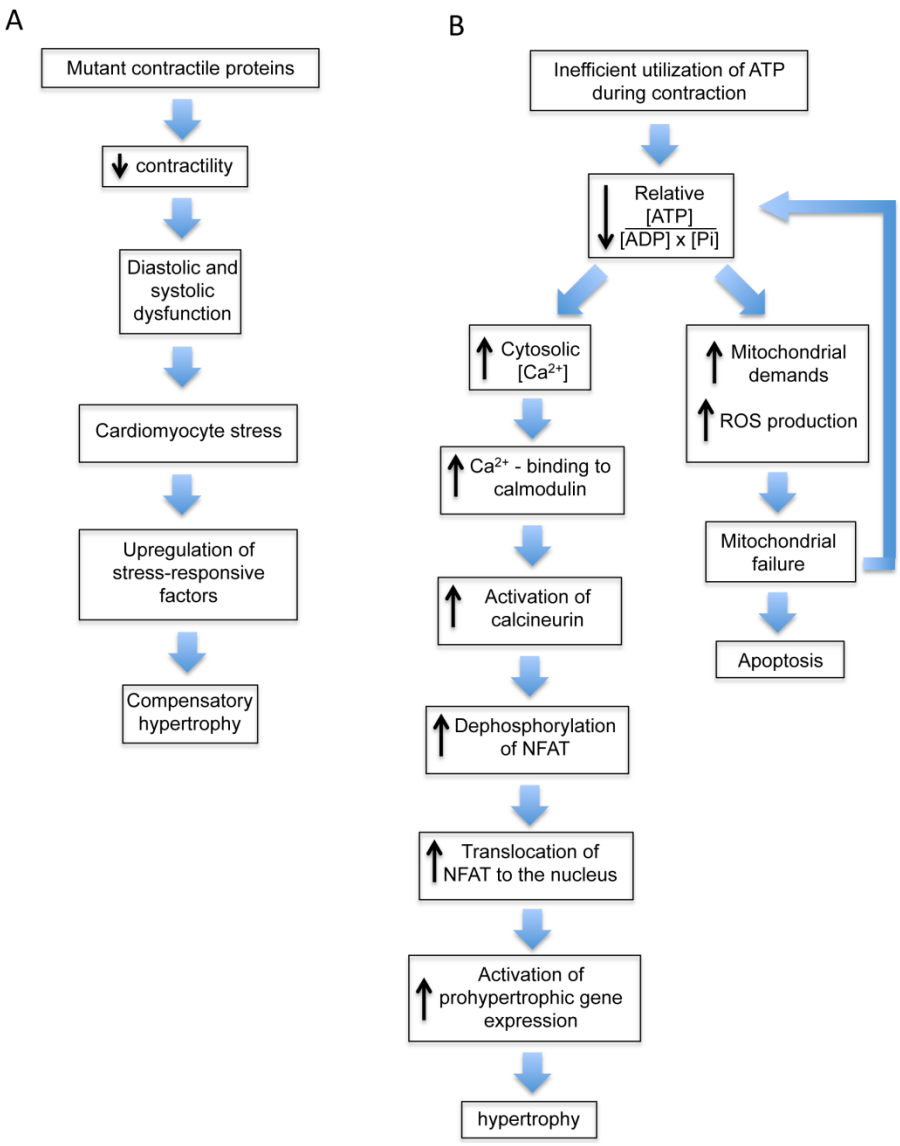

Figure 1.15. Hypotheses to explain the development of HCM. A) The hypothesis of compensatory hypertrophy whereby contractility is decreased due to mutant contractile proteins, leading to diastolic and systolic dysfunction. Subsequent activation of stress-responsive factors results in compensatory hypertrophy. B) The energy depletion model where inefficient utilization of ATP decreases the ATP:ADP ratio. This in turn increases cytosolic Ca^{2+}, leading to the increased activation of calcineurin via the activated Ca^{2+}-bound calmodulin. Calcineurin dephosphorylates nuclear activator of activated T-cells (NFAT), increasing its translocation to the nucleus and subsequent activation of prohypertrophic gene expression. The altered adenosine nucleotide ratio also increases demands on mitochondria and ROS production increases damaging the mitochondria. Mitochondrial failure can then lead to apoptosis or further reduce the ATP:ADP ratio progressively increasing cytosolic Ca^{2+}. Hypertrophy is the end result (Ashrafian *et al*., 2003, Heineke and Molkentin, 2006, Marian, 2000).

1.6 Mouse models of dilated cardiomyopathy

Several genes have been implicated in the development of heart failure through generation of mouse models.

Mlp

The first model of DCM established in a genetically modified organism was that of the muscle LIM protein (MLP) – deficient mouse (Arber *et al*., 1997). Initially generated to assess the role of MLP in muscle differentiation, this mouse model then provided a means to test theories of the effect of the disruption of cytoarchitecture on development of disease. MLP is a positive regulator of myogenic differentiation, associating with the actin-based cytoskeleton and proposed to function in muscle stretch sensing (Arber *et al*., 1994, Arber and Caroni, 1996). While the protein is highly expressed in all striated muscle in neonates, its expression declines in adult skeletal muscle, but remains high in adult cardiomyocytes (Arber *et al*., 1994). MLP has been shown to interact with telethonin (T-cap) and titin at the z-discs, which define the boundaries of the sarcomere (Knoll *et al*., 2002). The interaction between T-cap and titin is essential to sarcomeric function in coordinating contraction and force generation. MLP has been shown to mediate this interaction and is, thus, an important requirement for z-disc architecture (Knoll *et al*., 2002).

Mlp$^{-/-}$ mice develop DCM within the first month of life, with dilation of all four chambers and notable hypertrophy. After the onset of overt symptoms, the mice died 20-30 hours later and possessed a 2–4 fold increase in the size of the heart. However only 50% of *Mlp*$^{-/-}$ mice developed DCM and explanations as to why remain obscure (Arber *et al*., 1997). As in *Mlp*$^{-/-}$ mouse cardiac muscle, skeletal muscle also display swollen muscle fibres, however the phenotype in the heart appears more extreme. This may be due to increased workload of the heart and the higher number of membrane attachment sites per sarcomere (Arber *et al*., 1997).

Screening of over 1200 DCM patients revealed a mutation within the *MLP* gene, W4R, converting a tryptophan residue to an arginine residue. The mutation was found in nine individuals from different families, all of which displayed DCM symptoms similar to those of the *Mlp*$^{-/-}$ mouse (Knoll *et al*.,

2002). Mutations in the proteins T-cap (R87Q) and titin (V54M & A743V) (Itoh-Satoh *et al*., 2002) identified in DCM patients also showed impaired interactions between MLP, T-cap, titin and α-actinin, emphasising alterations in z-line architecture may be important in the development of DCM.

As the contractile machinery is dependent on ATP for energy, a defect in OXPHOS or in genes on which the process relies will lead to a decrease in fatty acid oxidation and shift ATP production back to anaerobic glycolysis. Although this will be a general effect on the whole organism, a much more severe impact in cardiomyocytes is predicted because of the increased energy demand of the heart (Schiff *et al*., 2011). This would explain why the later stages of heart failure often appear to be so tissue specific (Tian and Barger, 2006). This switch to glycolysis is accompanied with increased lactic acid production, which itself can result in damage to the heart and may trigger DCM (Huttemann *et al*., 2012). Similarly, increased ROS production as a result of mitochondrial Ca^{2+} overload may cause oxidative damage to components of the ETC or mtDNA, which encodes components of the ETC (Ide *et al*., 1999).

Cox7a1

A mouse knockout of the cardiac-specific subunit 7a mouse cytochrome c oxidase (COX7A1) was generated in order to provide insight into the role of the cardiac specific isoform. It was noticed that both *Cox7a1*$^{-/-}$ and *Cox7a1*$^{+/-}$ develop DCM at 6 weeks of age, despite the fact that ATP levels in the heart were notably higher in the mutants. It was postulated that a decrease in energy production per mitochondrion leads to increased mitochondrial proliferation, thereby increasing the net energy production in the heart tissue with dilation being an adaptive response to accommodate the increased number of mitochondria. This is, however, in contrast to the theory in which dilation is the result from failing cells.

Astonishingly, these mice recover from DCM from 6 months of age. The liver isoform, COX7A2 was found to be increased, approximately 5-fold in the hearts of the COC7A1-deficient mice, when compared to wild type controls. This increase may possibly compensate for the loss of the cardiac isoform and may explain how these mice recover from DCM (Huttemann *et al*., 2012).

Tfam

The enzymes of the ETC require a number of subunits encoded by the mitochondrial genome. Transcription factor A, mitochondrial (TFAM)-deficient mice (*Tfam*$^{-/-}$) provide evidence for the importance of the mitochondrial genome. Tfam activates mitochondrial transcription and has a role in mitochondrial genome replication. *Tfam*$^{-/-}$ mice do not survive past E10.5. The mitochondria of the hearts of these mice are grossly enlarged and display abnormal cristae formation and complex IV deficiency (Larsson *et al*., 1998). *Tfam*$^{+/-}$ mice are also affected. They are able to survive up to 20 days postnatally before developing DCM. As well as a 50% decrease in TFAM protein expression, they also exhibit a 34% reduction in mtDNA copy number and a 22% reduction in mitochondrial transcripts. Similarly, complex IV was shown to be reduced, with some cardiomyocytes being complex IV-deficient and complex II-hyperactive (Wang *et al*., 1999). Mitochondrial copy number and transcript level therefore prove to be very important in OXPHOS, in which a reduction is likely to lead to reduced ATP production and energy deficiency, critical for the high energy-demanding cardiomyoctes.

Ant1

Export of ATP out of the mitochondria relies on the transmembrane protein, ANT, which also transports ADP into the mitochondrial matrix at the same rate (Souverijn *et al*., 1973). ANT-1 is an isoform expressed in high energy-demanding cells such as heart, skeletal muscle and brain. ANT-1 recessive mutations were discovered in human patients exhibiting mitochondrial myopathy and cardiomyopathy, with exercise intolerance and hypertrophy (Palmieri *et al*., 2005). Before *ANT-1* mutations were found in humans, a mouse model of *Ant-1*$^{-/-}$ was created and reported to display mitochondrial myopathy, lactic acidemia and increased ROS production (Esposito *et al*., 1999). The hearts of these mice demonstrated myocyte hypertrophy, ventricular dilation and a decrease in cardiac output at an earlier age to that of wild type control mice (Narula *et al*., 2011).

Inhibition of the ADP/ATP exchange will deprive ATP synthase of substrate, blocking proton transport into the matrix via ATP synthase, thereby leading to a hyperpolarised MMP and a decrease in electron transfer. These

electrons then become redirected to O_2 molecules increasing the production of ROS, which has previously been shown to damage the mitochondrial genome. In accordance, mtDNA in the heart of 16-20-month-old *Ant1*$^{-/-}$ mice was shown to exhibit as much rearrangement of a 32-month-old wild type. This increased mtDNA rearrangement will further inhibit the ETC and so decrease ATP production as well as ATP transport, ultimately leading to DCM (Narula *et al*., 2011).

Sod2

The impact of increased ROS generation on OXPHOS has been further evidenced by mouse models lacking manganese superoxide dismutase (MnSOD2). MnSOD2 is known to be the first line of defence against ROS produced as a by-product of OXPHOS. In one mouse model, in which *Sod2* had been inactivated by the deletion of exon 3, mice die by 5 days of age from DCM. As a result of increased ROS levels, a reduction in complex II and aconitase (a CAC enzyme) was detected, most dramatically in the heart. This is probably due to the increased OXPHOS activity in cardiomyocytes (Benard *et al*., 2006), which requires an increased activity of antioxidant defences in order to prevent ROS build up. A reduction in fatty acid β-oxidation and glycolysis will therefore lead to energy starvation in the heart eventually leading to DCM and CHF (Li *et al*., 1995). A second mouse model, a knockout of *Sod2,* was also created and showed an increased survival period. Unlike the previous model, these mice display a number a pathologic phenotypes including neuronal degeneration in the basal ganglia and brainstem and rapid fatigue, with only 10% developing DCM (Lebovitz *et al*., 1996).

Fkbp12

Ca^{2+} cycling deficiencies leading to heart failure have been reported in a number of mouse models. The FK506 binding protein (FKBP12) modulates the activity of the ryanodine receptors, which release Ca^{2+} from the ER, and hence, are involved in Ca^{2+} signalling during contraction. An *Fkbp12*-deficient mouse model was developed in order to deduce the functions of the protein. The majority of these mice died between E14.5 and birth. It was noted that the hearts in these mice displayed diastolic and systolic dysfunction, and were

shown to exhibit 4-chamber dilation with thinner walls and ventricular septal defects. These defects are typical of DCM. The heart weight was also increased and some developed liver hepatopathy as a secondary effect to cardiac congestion of the liver (Shou *et al*., 1998).

FKBP12 controls the opening of the ryanodine receptor in skeletal muscle (RYR1) and in cardiac muscle (RYR2). In *Fkbp12*-deficient mice, RYR1 and RYR2 mostly existed in a sub conductance state, however the effect of abnormal gating properties was only seen in the heart, which displayed increased Ca^{2+} leak from the SR. This difference may be explained by the difference in control mechanisms of Ca^{2+} release between the tissues; CICR mainly controls that of the heart, whereas voltage-sensors are also used as well as CICR in skeletal muscle (Shou *et al*., 1998). This increase in cytosolic Ca^{2+} has been reproduced in other mouse models of heart failure and therefore may prove to be a principle cause of heart dysfunction.

Prkca

Protein kinase C alpha (PKCa) is activated by intracellular Ca^{2+}, which leads to the dephosphorylation of phospholamban (PLN). This in turn inactivates the SERCA, reducing SR Ca^{2+} uptake and consequently reduced contractile output. Hearts of *Prkca*-deficient mice exhibit increased contractility as a result of the increased SR Ca^{2+}uptake. Double knockout *Prkca*- and *Mlp*- deficient mice are protected from heart failure. The lack of PKCa enhances the contractility of the heart that is otherwise diminished in *mlp*$^{-/-}$ mice, restoring sufficient cardiac function (Braz *et al*., 2004).

Camk2a

Ca^{2+}-calmodulin-dependent protein kinase II (CaMKII) is a downstream target of the β-adrenergic receptor (βAR) signalling cascade, activated by cytosolic Ca^{2+} during contraction. Excessive βAR activation has been shown to increase cytosolic Ca^{2+} levels, leading to cardiac remodelling, myocardial dysfunction, hypertrophy and dilation (Zhang *et al*., 2005). Evidence suggests upregulation of CaMKII increases cytosolic Ca^{2+} causing an influx via the L-type Ca^{2+} channel (LTCC) and increase SR Ca^{2+} release via the RYR2. A genetic mouse model of cardiac CaMKII inhibition was created by encoding an inhibitory

peptide, autocamtide-3 derived inhibitory peptide (AC3-I) fused to the cardiac-specific *Myh6* promoter. CaMKII inactivation was shown to prevent cardiac dysfunction that can result from excessive βAR stimulation supporting the hypothesis that reducing cytosolic Ca^{2+} prevents heart failure (Zhang *et al*., 2005).

Ryr2

Duchenne muscular dystrophy (DMD) is a disorder of progressive muscle weakness, eventually affecting the heart, with a decline in cardiac output and ventricular dilation as a result of DCM (Muntoni *et al*., 1993, Towbin *et al*., 1993). In the mdx mouse model of DMD, which exhibit skeletal muscle degeneration and later, DCM, increased Ca^{2+} levels were found in the cytosol of cardiomyocytes, which may be the underlying cause of DCM in mdx mice (Bridges, 1986, Dunn and Radda, 1991).

Phosphorylation of RYR2 at serine 2808 (S2808) by PKA has been shown to be a significant event in heart failure development (Marx *et al*., 2000, Chen-Izu *et al*., 2007) and found to be increased in the mdx mouse. A knock-in mouse model preventing the activation of S2808 by substituting the serine for an alanine (S2808A) resulted in improved signs of cardiac output following myocardial infarction (Jiang *et al*., 2002). When mdx mice were crossed with *Ryr2*^{S2808A} mice to obtain double mutants, the cytosolic Ca^{2+} levels and SR Ca^{2+} leak were reduced. Subsequently, the development of age-related cardiomyopathy was almost completely prevented, with heart contractility greatly improved. (Sarma *et al*., 2010).

Casq2

A decrease in cytosolic Ca^{2+} has also been shown to cause heart failure. Calsequestrin binds to and sequesters Ca^{2+} in the SR lumen. Transgenic mice overexpressing calsequestrin in cardiomyocytes exhibit reduced Ca^{2+} release from the SR, down-regulation of RYR2, up-regulation of SERCA and cardiac hypertrophy (Jones *et al*., 1998). This may be due to less Ca^{2+} being available for mitochondrial uptake leading to a decrease in ATP production, and resultant energy deficiency within the heart (Limas *et al*., 1987).

1.7 Overview of project

The Python mouse develops CHF as a result of a point mutation in the gene *Dnm1l*. Overt symptoms become apparent at different ages on different congenic backgrounds and although *Dnm1l* is ubiquitously expressed, the mutation results in a heart-specific defect. Using Python as a mouse model for DCM and DNM1L biology, this project focuses on identifying the underlying mechanisms by which a defect in a mitochondrial fission protein leads to a decrease in energy production, and characterising the extent to which the mutant phenotype is manifest in different cell types. Experiments will aim to identify the affect of Python on DNM1L protein folding, intermolecular interactions, cellular localisation, mitochondrial morphology and Ca^{2+} signalling.

1.8 Hypotheses and aims

1.8.1 Hypotheses

1. The *Dnm1l*^{Py} mutation alters the intrinsic nature of the encoded protein, leading to one or more of:
    a. Failure of oligomerisation of DNM1L into higher order structures.
    b. Failure of stable assembly of, or dissociation from, a functional fission complex.
    c. Failure of cycling between the cytosol and the OMM.

2. The *Dnm1l*^{Py} mutation results in cardiac ATP deficiency via dysregulation of one or more of:
    a. Ca^{2+} regulation. Given the key role of Ca^{2+} in mitochondrial OXPHOS and known defects in Ca^{2+} cycling observed in cells with mutations in the mitochondrial fusion factor MFN2, *Dnm1l*^{Py} might alter ER-mitochondrial interactions and thus abrogate efficient Ca^{2+} signalling in mitochondria.
    b. Mitophagy: defective removal of senescent mitochondria with subnormal function may result in an abnormal accumulation of poorly functioning mitochondria.

3. The Python mutation is manifest in other tissue types and there are, as yet, unidentified phenotypic abnormalities in Python mice that affect other body systems.

1.8.2 Aims

1. Examining the biology of the DNM1L^{Py} protein by:
    a. Investigating self-interactions of DNM1L and interactions with other proteins.
    b. Identifying potential new protein partners of DNM1L.
    c. Assessing GTPase and mitochondrial fission activity of the mutant protein.

2. Examining the effect of Dnm1l^{Py} on cellular processes. Specifically:
    a. Mitochondria, peroxisomes and ER morphology.
    b. Activation and translocation of DNM1L to mitochondria.
    c. ER-mitochondrial interactions.
    d. Ca^{2+} homeostasis and OXPHOS in mitochondria.
    e. Levels of autophagy.

Chapter 2 : Methods

2.1 List of mouse strains:

All mice were housed in numbers no greater than 8, with *ad libitum* access to food and water. Colonies were maintained as described below.

Python- B61

The colony was maintained by breeding *Dnm1l*$^{+/Py}$ (hereafter referred to as *+/Py*) males with *Dnm1l*$^{+/+}$ (hereafter referred to as +/+) females on the background strain C57BL/6J. All animals were sacrificed by way of cervical dislocation.

Python-C3H

The colony was maintained by breeding *+/Py* males with +/+ females on the background strain C3H/HeN. All animals were sacrificed by way of cervical dislocation.

Python x R6/2

R6/2 mice were provided from Professor Gillian Bates of King's College London. R6/2 males were mated with Python females on the C57BL/6J background, with offspring of the following four genotypes: R6/2$^{0/0}$ *Dnm1l*$^{+/+}$ designates wild type; R6/2$^{0/0}$ *Dnm1l*$^{+/Py}$, indicates positive for the Python mutation; while R6/2$^{0/T}$ *Dnm1l*$^{+/+}$ means positive for the R6/2 transgene only, and R6/2$^{0/T}$ *Dnm1l*$^{+/Py}$ (hereafter referred to as R6/2 x Python) is positive for both the R6/2 transgene and the Python mutations, respectively.

2.2 Home office licenses that experiments were carried out under:

Work during this project was authorised by the University of Leeds' Animal Ethics Committee and under approval from the home office. Work was carried out under the following licenses, 40/3146 and 40/3991, held by Professor Neil Dear.

2.3 Genotyping

2.3.1 DNA extraction

DNA was extracted from mice ear biopsies by incubation at 55ºC in a total volume of 150µl tail lysis buffer (50mM Tris-HCl, pH8.5, 10mM EDTA and 0.5% Tween 20) containing 300µg/ml proteinase K. Following the incubation, the DNA was diluted by the addition of 600µl Millipore water.

2.3.2 PCR amplification

To identify Python mice, the DNA was subsequently amplified using primers designed to create a restriction site in the presence of the mutation, but not in wild type (Appendix II). R6/2 transgenic mice were identified by amplifying extracted DNA using primers, which produce a 170bp fragment in transgenic mice only (Appendix XII). The PCR reaction carried out for both mutations is shown in Table 2.1.

Table 2.1. PCR conditions for the amplification of DNA for the identification of the Python mutation and the R6/2 transgene

A. Reaction mixture (15µl)

Component	Volume (µl)	Final concentration
Template DNA	3	
5x Go Taq reaction buffer 1 (containing 7.5mM $MgCl_2$)	3	1x (1.5mM $MgCl_2$)
10x dNTPs (2mM each)	1.5	0.2mM each
Forward primer (10µM)	1.5	1µM
Reverse primer (10µM)	1.5	1µM
Go Taq polymerase (5u/µl)	0.2	1u
H_2O	4.3	
Total	**15**	

B. PCR cycling

Temperature (°C)	Time	
94	2 mins	
94	15s	X 35
55	15s	
72	30s	
72	10mins	

(A) Components and concentrations of the PCR reaction. (B) Optimum conditions for PCR cycling.

2.3.3 Restriction assay with XapI for *Dnm1l*^{Py}

5µl of the PCR reaction mix was incubated at 37°C for two hours, in a 20µl reaction containing 4U of XapI enzyme and 1x buffer tango (33mM Tris-acetate (pH7.9), 10mM magnesium acetate, 66mM potassium acetate, 0.1mg/ml BSA). The digested product was analysed by electrophoresis on a 4% agarose, TBE gel, containing 1µg/ml Ethidium Bromide (EtBr) at 10V/cm. The presence of bands of specific sizes indicates the genotype (See appendix III).

2.4 Western blot analyses

Brain and heart tissue samples were excised from mice and immediately snap frozen in liquid nitrogen. The tissue was then minced and homogenised in RIPA buffer (50mM Tris-HCl, 150mM NaCl, 2mM EDTA, 1% NP-40, 0.1% SDS, and 1% sodium deoxycholate) containing 1x protease inhibitor cocktail (PIC) (P8340, Sigma-Aldrich, Dorset, UK). Protein concentration was determined by means of a Bradford assay. Equal amounts of protein were loaded onto a sodium dodecyl sulphate (SDS) gel. The stacking gel composed of 4% acrylamide, 14mM Tris-HCl, pH 6.8, 0.1% SDS, 0.06% ammonium persulfate (APS) and 0.11% N,N,N',N'-Tetramethylethylenediamine (TEMED). Resolving gels contained 10% acrylamide/bisacrylamide were used for analysing DNM1L, OPA1, MFN2, calnexin, AMPK, P-AMPK and α-tubulin and 15% acrylamide/bisacrylamide for TIM23, LC3 and HTT analysis. Other resolving gel constituents common to both acrylamide concentrations were: 0.375M Tris-HCl, pH 8.8, 0.1% SDS, 0.05% APS and 0.05% TEMED. The gel was placed in a tank with enough SDS-polyacrylamide gel electrophoresis (PAGE) running buffer (2.5µM Tris, 0.5M glycine and 0.1% SDS) to cover the whole of the gel. Samples were boiled at 100ºC for 5 mins in loading buffer (12.5% glycerol, 2.5% SDS, 50mM Tris-HCl, pH 6.8, 0.625% bromophenol blue and 20% β-Mercaptoethanol) to separate into single protein molecules and subsequently electrophoresed at 12.5V/cm.

Proteins were transferred to a Hybond-P membrane (GE Healthcare, Little Chalfont, UK), by means of Western blot in transfer buffer (25mM Tris, 192mM glycine and 20% methanol, pH 8.3) for 1 hour at 100V.

Antibodies against Drp1, Tim23, α-tubulin, calnexin, AMPK, P-AMPK, LC3, Opa1 and Mfn2 were used to detect proteins. A secondary anti-mouse HRP-conjugated antibody was used for Drp1, Tim23, Opa1, Mfn2, HTT and α-tubulin, while a secondary anti-rabbit HRP-conjugated antibody was used for calnexin, AMPK, P-AMPK and LC3; in connection with ECL Western Blotting Detection Reagents (RPN2106, GE Healthcare, Little Chalfont, UK) to detect the individual proteins, which were developed using an SRX 1-1A developer (Photon Imaging, Swindon, UK) after an exposure of between 2 mins and 20 mins.

Table 2.2. Table of antibodies used for Western blots.

Antibody	Dilution	Company	Cat. No.
Anti-Drp1 antibody	1:1000	BD Biosciences, Oxford, UK	611112
Anti-Tim23 antibody	1:1000	BD Biosciences, Oxford, UK	611222
Anti-α-Tubulin antibody	1:20,000	Sigma-Aldrich, Dorset, UK	T6074
Anti-calnexin antibody	1:2000	Abcam, Cambridge, UK	ab10286
Anti-AMPK antibody	1:1000	Cell Signaling, Denvers, MA, USA	2532S
Anti-P-AMPK antibody	1:2000	Cell Signaling, Denvers, MA, USA	4188S
Anti-LC3 antibody	1:1500	Cell Signaling, Denvers, MA, USA	2775
Anti-OPa1 antibody	1:1000	Abnova, Taipei, Taiwan	Clone 8A8
Anti-Mfn2 antibody	1:2000	Abnova, Taipei, Taiwan	Clone 6A8
Anti-HTT (mEM48)	1:1000	Millipore, Billerica, MA, USA	MAB5374
Anti-mouse-HRP secondary antibody	1:1000	Cell Signaling, NEB, Hitchin, UK	7076
Anti-rabbit-HRP secondary antibody	1:3000	Abcam, Cambridge, UK	ab6721

2.5 His-tag protein purification

His-tag fusion constructs of *Dnm1l* were created containing either wild type *Dnm1l* or *Dnm1l*^{Py} using the vector pET101 (Appendix IV). These constructs were transformed into DH10β *E.coli* bacterial cells by resuspending cells in transformation buffer (LB medium containing 10% polyethylene glycol $(PEG)_{3350}$, 10mM $MgCl_2$ and 10mM $MgSO_4$) and mixing with 50ng DNA diluted in KCM (100μM KCl, 30μM $CaCl_2$ and 50μM $MgCl_2$). The DNA/cell mixture was incubated on ice for 20 mins then at room temperature for 10 mins, before being placed in a shaking incubator for 1 hour at 37ºC with 1ml LB. The cells were plated onto to LB-agar plates containing 100μg/ml Ampicillin. Positive clones were confirmed by sequencing of the fusion construct then selected for induction of fusion protein expression.

Growing a clone containing the pET101 vector in a 50ml culture at 37ºC for 5 hours containing 1mM IPTG induced fusion protein expression. The cells were then harvested and resuspended in 5ml lysis buffer (50mM Tris-HCl, pH8.0, 0.1M NaCl, 0.02% NaN_3, 100U/ml DNase, 0.2mg/ml lysozyme, 15mM 2-Mercaptoethanol, 0.1% NP-40, 1x PIC) and incubated on ice for 20 mins. Two passes through a TS 1.1 cell disrupter at 4ºC completed cell lysis. The resulting lysate was then mixed with equilibrated Ni-NTA agarose beads (Invitrogen Ltd., Paisley, UK), which binds to the his-tag, for 2 hours at 4ºC, followed by 2 washes in washing buffer (50mM Tris-HCl, pH8.0, 0.3M NaCl, 0.02% NaN_3). The fusion proteins were then eluted in 2 x 500μl elution buffer 1 (50mM Tris-HCl, pH8.0, 0.3M NaCl, 0.02% NaN_3, 100mM Imidazol) and a further 2 x 500μl elution buffer 2 (50mM Tris-HCl, pH8.0, 0.3M NaCl, 0.02% NaN_3, 300mM Imidazol). The eluted protein was verified by SDS PAGE and Western blot analysis using anti-Drp1 antibody as described in section 2.4.

2.6 Protein extraction & renaturation

Full-length protein was extracted from an SDS gel and soaked in 1mM DTT for 15 mins then homogenised using a Teflon homogeniser. 2.5 volumes of elution buffer (5mM DTT, 50mM Tris-HCl (pH 7.5), 0.1% SDS, 0.15M NaCl, 0.1mM EDTA) was added and incubated for 2 hours at 30ºC. The eluted protein was

collected by a 30s centrifugation at 5000rpm. 5 volumes of -20ºC methanol:acetone (1:1) were added to the eluted protein, gently vortexed and incubated overnight at -20ºC. The protein was then pelleted by centrifugation at 10,000rpm for 15 mins at -5ºC and washed in -20ºC methanol:acetone (1:1). In order to renature the proteins, the samples were gently resuspended in buffer A (100mM KCl, 1mM DTT, 12.5mM MgCl2, 6M Guanidine, 10% Glycerol, 25 mM HEPES-KOH, pH 7.6, 0.1 mM EDTA). The concentrations of proteins were determined by means of a Bradford assay. 60ng of wild type DNM1L and 60ng of Python DNM1L were renatured individually. 60ng of both samples were also renatured together in a third sample. 2 volumes of buffer B (1mM DTT, 0.1mM KCl, 0.01% IGEPAL, 12.5mM MgCl2, 10% Glycerol, 25 mM HEPES-KOH, pH 7.6, 0.1 mM EDTA) was then added to each sample and dialyzed at room temperature against 250ml buffer B. After 3 hours the protein samples were snap frozen in liquid nitrogen and stored at -80ºC.

2.7 GTPase activity

GTPase activity was measured by means of the PiColourLock™ system (303-0030, Innova Biosciences, Cambridge, UK). 60ng purified protein samples were prepared in a total volume of 400µl. Proteins were also extracted from the brains of 3 wild type and 3 Python C57BL/6J mice aged 5-weeks-old by homogenisation in NP-40 lysis buffer (100 mM NaCl, 1% NP-40, 10% glycerol, 2 mM $MgCl_2$, 1 mM NaF, 1 mM Na_3VO_4, 50 mM Tris-HCl, pH 7.4).

400µl of the substrate / buffer mix (100mM Tris-HCl (pH7.4), 5mM $MgCl_2$ and 1mM GTP) were then added to each sample. 200µl of Gold mix (99% PiColourLock™ Gold + 1% accelerator) was added to each sample and incubated at room temperature for 2 mins. A negative control was also prepared substituting the protein samples with water. 80µl of stabiliser (part of the P_i ColourLock Gold kit) was then added and further incubated for 30 mins at room temperature. The absorptions at wavelength 635nm were taken, using the negative control to calibrate the JENWAY 6305 spectrophotometer. The absorption readings were then converted to inorganic phosphate (P_i) concentration using a standard curve of absorption readings against known concentrations of P_i.

2.8 RNA isolation

RNA was isolated from heart and brain tissues and also ES cells and cardiomyocyte-induced ES cells. The tissues extracted from wild type and Python mice were homogenised in 1ml TRIzol reagent (Invitrogen Ltd., Paisley, UK) using a polytron. The homogenate was then incubated at room temperature for 5 mins. In order to isolate RNA from cells, they were first trypsinized and resuspended in 1ml TRIzol for 5 mins at room temperature. The following protocol applies to both tissues and cells. The tissue / cell lysate was pelleted by centrifugation at 13,000rpm for 1 min. 0.2ml chloroform was then added to the supernatant and vortexed vigorously for 15s. Following a 3-minute incubation at room temperature, the samples were centrifuged at 13,000rpm for 15 mins, separating the solution into different phases. The colourless upper aqueous phase was transferred to a fresh tube and combined with 0.5ml isopropanol. Following a 10-minute incubation the RNA was pelleted by centrifugation at 13,000rpm for 10 mins at 4ºC. After 2 washes in 70% ethanol, the pellet was air dried and resuspended in DEPC-treated water. RNA quantification was achieved using the NanoDrop ND-1000 3.3 system.

2.9 Reverse transcription

RNA isolated from cells / tissues was converted into cDNA using the QuaniTect® Reverse Transcription kit (205310, Qiagen, Crawley, UK). 1µg of RNA was incubated in 1 x gDNA wipeout buffer for 2 mins at 42ºC to remove any contaminated genomic DNA. The RNA sample was then incubated for 15 mins at 42ºC with 1µl quantiscript reverse transcriptase, 1 x reverse transcriptase buffer and 1µl reverse transcriptase random primers in a total volume of 14µl. The quantiscript reverse transcriptase was then inactivated with a 3-minute incubation at 95ºC. The cDNA product was stored at -20ºC for use in further experiments.

2.10 Pyrosequencing

Pyrosequencing analysis was carried out in collaboration with Dr. Phil Chambers, University of Leeds. PCR was performed on the cDNA samples of heart and brain of 2 wild type and 2 Python mice aged 5-6 weeks on the C57BL/6J background. Initially, a 286bp product within exon 11 of *Dnm1l*, surrounding the position of the mutation (Appendix V), was amplified. Primers for PCR amplification and Pyrosequencing analysis (Appendix V) were designed using proprietary Pyrosequencing assay design software version 2.0.1.15 (Qiagen, Crawley, UK). PCR reactions contained 12.5µl of Qiagen HotStarTaq Master Mix (Qiagen, Crawley, UK), $MgCl_2$ to a final concentration of 2mM, 200nM each of forward and reverse primers and 10ng of DNA in a final volume of 25µl. Thermal cycling conditions were 94°C for 12 minutes followed by 40 cycles of 94°C for 10 seconds, 55°C for 20 seconds and 72°C for 20 seconds. PCR products were sequenced by Pyrosequencing on a PyroMark ID system (Qiagen, Crawley, UK) following the manufacturer's protocols. Pyrosequencing data were analysed using PyroMark ID software in the "SNP" mode in order to quantify allelic expression.

During the process of pyrosequencing, as in PCR, deoxynucleotide triphosphates (dNTPs) are added sequentially to the complementary template, however dNTPs are labelled with pyrophosphate (PPi) in this reaction. As a dNTP is added, PPi is released in a quantity equimolar to the amount of nucleotide added. ATP sulfurase then converts PPi into ATP in the presence of adenosine 5' phosphate (APS). The ATP is then used in a reaction where luciferase catalyses the conversion of luciferin to oxyluciferin, generating light in proportion to the amount of ATP present. The detection of this light creates signal intensity in proportion to the amount of nucleotide incorporated, creating a visible peak as shown in Figure 2.1. Apyrase degrades any unicorporated dNTPs and ATP.

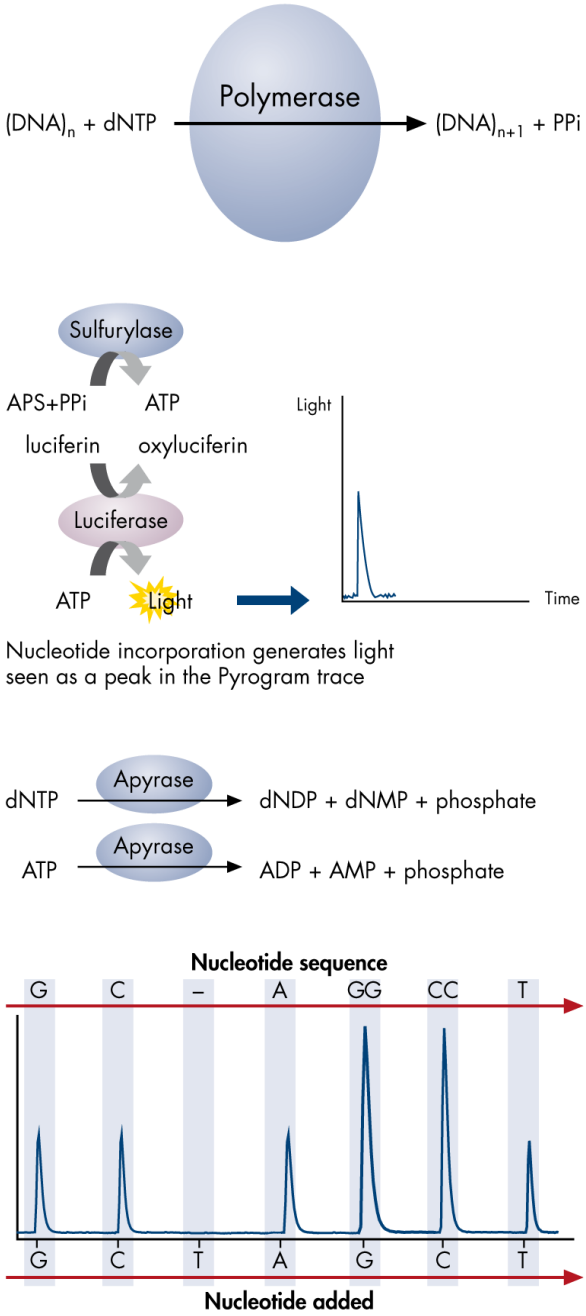

Figure 2.1. Sequence of events during pyrosequencing analysis. dNTPs are incorporated according to their complementary template. PPi is released during dNTP incorporation and is subsequently converted into ATP by sulfurase in the presence of APS. ATP is then converted into light by luciferase as luciferin is also converted into oxyluciferin. The resulting light intensity is in proportion to the amount of dNTP incorporated at that position providing a quantitative means for allelic expression. Any unicorporated dNTP or ATP is degraded by Apyrase. Image from QIAGEN.

2.11 PCR cDNA amplification of cardiomyocyte markers

After cardiomyocyte-induction of ES cells, PCR was used to determine the expression of a number of cardiomyocyte markers. Sequences within the coding regions of the following genes were tested for using RNA isolated from ES cells and induced-cardiomyocytes after reverse transcription: *Actb, Gapdh, Pou5f1, Gata4, Myl7* and *Myh7.* See Appendix VI for primer sequences. The PCR conditions were:

Table 2.3. PCR conditions for the amplification of the cardiomyocyte markers.

A. Reaction mixture (15µl)

Component	Volume (µl)	Final concentration
Template DNA	3	
5x Go Taq reaction buffer 1 (containing 7.5mM $MgCl_2$)	3	1x (1.5mM $MgCl_2$)
10x dNTPs (2mM each)	1.5	0.2mM each
Forward primer (10µM)	1.5	1µM
Reverse primer (10µM)	1.5	1µM
Go Taq polymerase (5u/µl)	0.2	1u
H_2O	4.3	
Total	**15**	

B. PCR cycling

Temperature (°C)	Time	
94	2 mins	
94	15s	X 35
55	15s	
72	30s	
72	10mins	

(A) Components and concentrations of the PCR reaction. (B) Optimum temperatures of PCR cycling.

2.12 Site-directed Mutagenesis

Table 2.4. Primer pairs for site-directed mutagenesis

Mutation	Primers	
C452F	5'-d(GCAGAGGATCATTCAGCATTTTAGCAA)3'	5'-d(AATGCTGAATGATCCGCATCTCCT)3'
A401D	5'-d(CACTATTGACATCCTGACTGACATCAGAAATG)3'	5'-d(CAGTCAGGATGTCAATAGTGTTAAGGCCACCTA)3'
K38A	5'-d(TGGGAACGCAGAGCAGTGGGGCGAGCTCAGTG)3'	5'-d(CCCACTGCTCTGCGTTCCCACTACGACGAT)3'

Mutagenesis was achieved using the GeneTailor™ Mutagenesis System (12397-014, Invitrogen, Paisley, UK). The primers above were designed based on the *Dnm1l* cDNA sequence surrounding mutation site. Primers pairs were designed to contain a 5' overlapping region of 15-20 nucleotides plus an extended region of over 10 nucleotides with 1 of the pair containing the mutation immediately after the overlapping region. The plasmid DNA to be mutated was first methylated in the following reaction: 50ng plasmid DNA, 0.8µl 10X Methylation buffer, 0.8µl 10X S-Adenosyl methionine (SAM) and 2U DNA methylase in a total volume of 8µl. The mixture was then incubated for 1 hour at 37ºC.

2µl of the methylation reaction (12.5ng plasmid DNA) was then amplified using the primer pairs displayed in Table 2.4 under the following conditions: 25µl reaction containing 12.5ng methylated DNA, 1U of AccuPrime™ *Taq* DNA polymerase High Fidlity (12346-086, Invitrogen, Paisley, UK), 1x AccuPrime™ PCR buffer 1 and 2µM of each primer. Thermal cycling conditions were 94°C for 15 seconds followed by 35 cycles of 94°C for 30 seconds, 55°C for 30 seconds and 68°C for between 6 and 8 minutes (1min / kb). A final step of 68ºC for 10 minutes was performed before completion of cycling.

The PCR product was then transformed into *DH10β E. Coli* bacterial cells as previously described in section 2.5. Upon transformation into *E.Coli*, the methylated DNA (which doesn't contain the mutation) is degraded by the *Mcr*BC enzyme activity within the bacteria, leaving the unmethylated, mutated DNA only.

2.13 DNA isolation from bacterial cells

Bacteria were cultured in LB containing the necessary antibiotic and 37ºC overnight. The cells were then pelleted by centrifugation at 13000g for 1 min and resuspended in ice-cold solution 1 (25mM Tris-HCl, 10mM EDTA). 2 volumes of solution 2 (0.2N NaOH, 1% SDS) is then added and mixed by inversion. Following a 5 minute incubation on ice 0.5 volumes of ice-cold solution 3 (3M Potassium acetate, 11.5% Glacial acetic acid) was added and centrifuged at 13000g for 5 mins. The supernatant was then transferred to a fresh tube and 2 volumes of absolute ethanol was added to precipitate the DNA out of solution. The DNA was then pelleted by centrifugation at 13000g for 5 mins and washed in 70% ethanol. Following a 10-min incubation at 13000g, all of the supernatant was removed and the DNA pellet was air-dried before dissolving in TE Buffer (pH 8) (1mM EDTA, 10mM Tris-HCl) containing 50µg/ml RNase A.

2.14 Cell culture

Table 2.5. Cell culture reagents

Reagent	Company	Cat. No.
DMEM	Invitrogen Ltd, Paisley, UK	11960044
DMEM – GlutaMAX	Invitrogen Ltd, Paisley, UK	31966021
m199	Sigma-Aldrich, Dorset, UK	M7528
DMEM/Ham's F12	Biochrom, Cambridge, UK	F0815
Neurobasal medium	Invitrogen Ltd, Paisley, UK	10888-022
Foetal Calf Serum (FCS)	Sera Laboratories International Ltd, Sussex, UK	EU-000-F (batch no: 239207)
PBS	Invitrogen Ltd, Paisley, UK	20012019
Penicillin : Streptomycin (500units/ml)	Invitrogen Ltd, Paisley, UK	15070063
Trypsin	Invitrogen Ltd, Paisley, UK	2530054
Chemically defined lipids	Gibco, Paisley, UK	11905
Lipofectamine	Invitrogen Ltd, Paisley, UK	18324-012

2.14.1 Mouse skin fibroblasts

Mouse skin fibroblasts were cultured from C57BL/6J or C3H/HeN neonates. A skin sample was removed from the mouse, washed in ethanol and cut into small pieces, which were then placed in a 10cm cell culture dish and incubated at 37ºC, 5% CO_2 in Dulbecco modified Eagle medium (DMEM)-glutaMAX, containing 10% foetal calf serum (FCS) and 100U/ml:100µg/ml penicillin : streptomycin. After 5 days in culture, a substantial number of fibroblasts grew from the tissue clumps. The cells were then trypsinized and passed through a cell strainer to remove the clumps of tissue for subsequent use.

2.14.2 Mouse embryonic fibroblasts (MEFs)

MEFs were isolated from E9.5 (performed by Professor Neil Dear) or E14.5 embryos. At E14.5 the embryos were removed from the uterus and placed in phosphate buffered saline (PBS) followed by decapitation and evisceration. The remaining tissue was cut up into small pieces and placed into a sterile conical flask containing 5mm glass beads (Sigma-Aldrich, Dorset, UK, 18406). At E9.5, the whole embryo was cut up into small pieces and placed into a conical flask containing 5mm glass beads. 10ml of trypsin was then added to the flask and incubated for 10 mins at 37ºC, 5% $C0_2$ with gentle stirring to aid in breaking up the tissue. The resulting supernatant was transferred to a fresh tube and more trypsin was added to the tissue and beads to replace the trypsin removed. The incubation was repeated twice. The three supernatants were pooled and cells counted using a haemocytometer. The cells were then seeded at 10^7 cells per T175 flask in DMEM-glutaMAX medium containing 10% FCS and 100U/ml:100µg/ml penicillin : streptomycin in order to expand by incubation at 37ºC, 5% CO_2. When cells reached a confluency of 80 – 90% they were passaged by incubation in 3ml Trypsin / T175 flask for 5 mins at 37ºC, 5% CO_2, diluted by 50% in culture medium and centrifuged at 1500rpm for 5 mins to pellet the cells. The supernatant was then removed and cells resuspended in culture medium before seeding into flasks / dishes for subsequent use.

Immortalized MEF cell lines: DR_MEF_wt and DR_MEF_Py were generated using viral transfection with Telomerase reverse transcriptase (TERT) performed by Dr. Houman Ashrafian and Dr. Tom Cahill of The Univeristy of Oxford.

2.14.3 Embryonic stem (ES) cells

ES cells were isolated from the inner cell mass of blastocysts (E3.5) from C57BL/6J mouse embryos, performed by Professor Neil Dear. ES cells are cultured on a feeder layer of MEFs. MEFs were prepared for feeder layer by incubation in DMEM, containing 10% FCS and 10µg/ml Mitomycin C at 37ºC and 5% CO_2 for 4 hours when the flasks reached 90% confluency. This leads to the arrest of the cell cycle of the MEFs therefore will not continue to divide when used as a feeder layer. Mitomycin C-treated MEFs are plated out at a density of 3 x 10^6 cells per 10cm dish and incubated at 37ºC, 5% CO_2 at least 4 hours prior to seeding ES cells to allow them to attach to the dish, in DMEM + glutaMAX containing 10% FCS and 100U/ml:100µg/ml penicillin : streptomycin. Before seeding ES cells, the medium was changed to DMEM containing 20% FCS, L-glutamine, 1% non-essential amino acids, 0.1mM 2-Mercaptoethanol and leukaemia inhibitory factor (LIF) (1:500 dilution). ES cells were seeded onto the feeder layer at a density of 3 x 10^6 cells per 10cm dish. Medium was changed daily when culturing ES cells and passaged after a maximum of 3 days in culture to prevent differentiation. ES cells were harvested by removing the medium on the cells, washing in PBS and trypsinizing for 5 mins at 37ºC, 5% CO_2.

2.14.4 Embryoid body formation

ES cells were plated out at a density of 3 x 10^6 cells in a 10cm non-adherent cell culture dish in 10ml DMEM containing 20% FCS, L-glutamine, 1% non-essential amino acids and 0.1mM 2-Mercaptoethanol and cultured at 37ºC and 5% CO_2 for up to 5 days. 5ml extra medium was added every 48 hours. The

embryoid bodies were then pelleted by centrifugation at 1000rpm for 5 mins. The supernatant was removed and cells resuspended in the same medium then plated out at 2 x 10^6 cells onto 0.1% gelatinized 10cm dishes. The medium was changed every 3-4 days.

2.14.5 Cardiomyocyte-induced differentiation of ES cells

Embryoid bodies were formed and seeded onto gelatinized plates as described above (section 2.14.4). After 7 days at 37ºC, 5% CO_2, medium was replaced with DMEM containing 4mg/ml polyvinyl alcohol (PVA), 400µM thioglycerol, 10µg/ml insulin, 25ng/ml bone morphogenic protein 4 (BMP4), 5ng/ml fibroblast growth factor 2 (FGF2) and 1x chemically defined lipids. The cells were incubated under hypoxic conditions at 37ºC, 5% CO_2, 5% O_2 for 72 hours. The medium was then replaced with DMEM containing 20% serum replacement, 400µM thioglycerol, 1x chemically defined lipids, 5mg/ml bovine serum albumin (BSA) and 280µM ascorbic acid and cultured at 37ºC, 5% CO_2 for 72 hours. The final phase consisted of replacing the medium with DMEM containing 400µM thioglycerol, 10µg/ml insulin and 1x chemically defined lipids and culturing at 37ºC, 5% CO_2 for up to 9 days, replacing the medium every 72 hours.

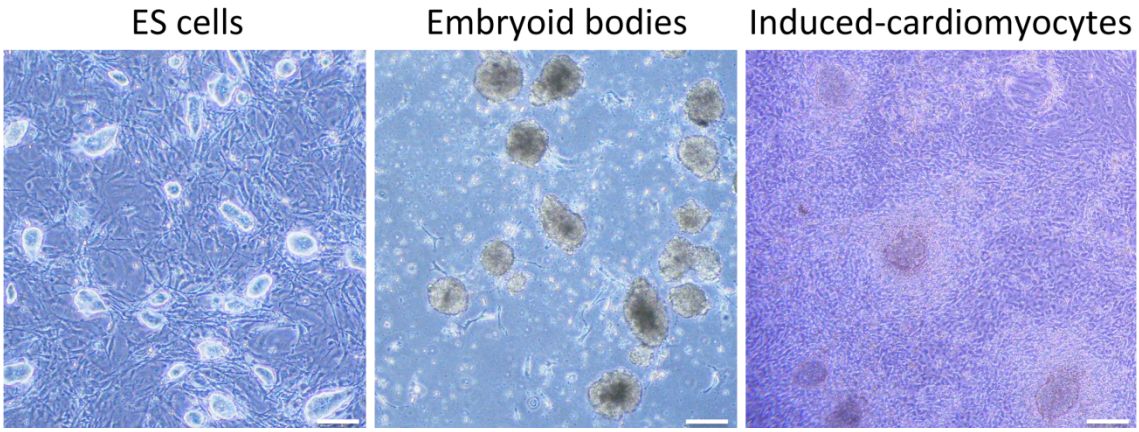

Figure 2.2. ES cell differentiation. ES cells are seeded onto non-adherent cell culture dishes allowing them to aggregate and form embryoid bodies, where they begin to differentiate. After being exposed to specific conditions, the cells differentiate into beating clumps of cardiomyocytes. Scale bars represent 100µm. Experimental protocols are detailed in sections 2.14.3, 2.14.4 and 2.14.5.

2.14.6 Adult mouse cardiomyocyte culture

Cardiomyocyte isolation was performed in collaboration with Professor Ed White and culture with Professor Michelle Peckham. Hearts were excised from adult mice at the age of 12 weeks. The hearts were cut at the aortic arch, to allow them to quickly be attached onto a needle via the aorta in preparation for perfusion. The hearts were flushed with isolation solution (130mM NaCl, 5.4mM KCl, 1.4mM $MgCl_2$, 0.4mM NaH_2PO_4, 5mM HEPES, 10mM glucose, 20mM taurine, 10mM creatine, 10mM 2,3-butanedione monoxime (BDM)), supplemented with 750µM Ca^{2+} and 1% heparin to prevent coagulation. The hearts were then attached to the perfusion pump with the needle attached to the aorta and perfused for 3 mins with isolation solution supplemented with 1µM EGTA. The perfusion fluid was then changed to isolation solution containing 1mg/ml collagenase and 0.1mg/ml protease (enzyme solution) and 40ml of the enzyme solution was allowed to pass through the hearts, prior to dissection of the ventricles, which were then cut into pieces. The small ventricle fragments were incubated in a shaking incubator at 37ºC in enzyme solution. Dissociated cells were then pelleted by centrifugation at 500rpm for 40s; the supernatant was removed and the cells were washed in isolation

buffer. The centrifugation step was repeated and the cells were resuspended in m199 medium, containing 10% FCS, 100U/ml:100µg/ml penicillin / streptomycin and 2mM L-glutamine, then seeded onto lamin-coated coverslips for 2 hours at 37ºC, 5% CO_2. Mitochondria were labelled and imaged as described in section 2.15.

2.14.7 Neuron culture

The brains of 2-day-old Python and wild type C57BL/6J mice were dissected and placed in ice cold PBS containing 3mg/ml BSA. The tissue was then cut up and digested in PBS containing 3mg/ml BSA and 0.08% trypsin at 37ºC for 20 mins. Non-dissociated tissue was removed by passing the digested tissue through a cell strainer. The supernatant was subsequently removed after centrifugation at 1000rpm for 7 mins and resuspended in 10ml plating medium (70% DMEM/Ham's F12 medium, 30% Neurobasal medium, 1% glucose, 2mM L-glutamine, 2% B27, 100U/ml:100µg/ml penicillin / streptomycin). The cells were then seeded onto poly-L-lysine coated coverslips at various densities and cultured overnight at 37ºC, 5% CO_2. Mitochondria were labelled as described in section 2.15.

2.14.8 HeLa cell transfection

HeLa cells were cultured on coverslips to a confluency of approximately 50%, in DMEM-glutaMAX containing 10% FCS. 2µg of pLD11 DNA (Appendix VII), containing the relevant Dnm1l version (wild type, Python or $K_{38}A$) was diluted in DMEM-glutaMAX to a final volume of 100µl and incubated with diluted lipofectamine (10µl lipofectamine + 90µl DMEM-glutaMAX) for 30 minutes at room temperature. Another 200µl DMEM-glutamMAX was then added to the DNA-lipofectamine mixture. The medium from the cells was then aspirated and replaced with 400µl DMEM-glutaMAX before adding the DNA-lipofectamine mixture. The cells were then incubated at 37°C, 5% CO_2 for 5 hours before adding 1.2ml DMEM-glutamax containing 17% FCS (final concentration of

10%) and incubated again at 37°C, 5% CO_2 overnight. Mitochondria were stained as described in section 2.15.

2.15 Mitochondria labelling

Mitochondria were labelled in mouse skin fibroblasts, mouse embryonic fibroblasts (MEFs) ES cells, cardiomyocyte-induced ES cells, HeLa cells, cardiomyocytes and neurons for visualization by fluorescence microscopy. Cells were cultured on glass coverslips and treated with 200nM MitoTracker™ Orange CMTMRos (M7510, Invitrogen Ltd., Paisley, UK) in culture medium for 45 mins at 37°C, 5% CO_2. After washing in PBS, cells were fixed in 4% paraformaldehyde (PFA) for 20 minutes at room temperature. The coverslips were then mounted onto slides in ProLong Gold mounting medium (Invitrogen Ltd., Paisley, UK) containing 10µg/ml Hoechst 33258. Mitochondria were then visualised using the Texas red filter and nuclei, using the Dapi filter of the Zeiss ApoTome AXIO Imager and the AxioVision Re. 4.7 software.

2.16 ER labelling

Mouse skin fibroblasts were cultured on glass coverslips in organelle lights ER-GFP transduction solution (O36212 component A, Invitrogen Ltd., Paisley, UK) diluted to 40% in PBS and incubated for 4 hours at room temperature, protected from light. The transduction solution was then replaced with the enhancer solution (O36212 component B, Invitrogen Ltd., Paisley, UK) and incubated at 37°C, 5% CO_2 for 2 hours. The cells were then incubated for over 16 hours in DMEM glutaMAX containing 10% FCS at 37°C, 5% CO_2. The cells were then washed in PBS and subsequently fixed in 4% PFA. The coverslips were mounted onto slides in ProLong Gold mounting medium (Invitrogen Ltd., Paisley, UK) containing 10µg/ml Hoechst 33258. The ER was then visualised using the FITC filter and nuclei, using the Dapi filter of the Zeiss ApoTome AXIO Imager and the AxioVision Re. 4.7 software.

2.17 Immunocytochemistry

Table 2.6. Table of antibodies used for immunocytochemistry.

	1º Antibody	Dilution	2º Antibody	Dilution
Peroxisomes	Rabbit anti-catalase IgG (ab16731, Abcam, Cambridge, UK)	1:100	Goat anti-rabbit FITC-conjugated IgG (ab6717, Abcam, Cambridge, UK)	1:150
DNM1L	Mouse anti-Drp1 (Clone 8; BD Biosciences, Oxford, UK)	1:100	Daylight 549-conjugated anti-mouse IgG (715-505-150, Jackson Immuno Research, Suffolk, UK)	1:150
LC3	Rabbit anti-LC3B IgG antibody (2775, Cell Signalling, Hitchin, UK)	1:67	Goat anti-rabbit FITC-conjugated IgG (ab6717, Abcam, Cambridge, UK)	1:67

Peroxisomes, DNM1L and LC3 were labelled using immunocytochemistry (ICC). Mouse skin fibroblasts or MEFs were cultured on glass coverslips in DMEM glutaMAX containing 10% FCS at 37°C, 5% CO_2. Following fixation in 4% PFA for 20 minutes, cells undergoing peroxisome labelling only were treated in antigen retrieval buffer (100mM Tris-HCl pH 9.5 and 5% Urea), for 10 minutes at 95°C. The cells were blocked for 1 hour in 95% PBS + 5% FCS. The cells were then permeabilised in 0.1% Triton X-100 for 30 minutes at 4°C. Peroxisomes were labelled using a primary rabbit anti-catalase IgG antibody and a secondary goat anti-rabbit FITC-conjugated IgG. DNM1L was labelled using an anti-Drp1 primary antibody with a Daylight 549-conjugated anti-mouse IgG secondary antibody. LC3 was labelled using a primary rabbit anti-LC3B IgG antibody and a secondary goat anti-rabbit FITC-conjugated IgG. All incubations with antibodies were performed at room temperature for 1 hour. The cells were washed and coverslips were mounted onto slides in ProLong Gold mounting medium (Invitrogen Ltd., Paisley, UK) containing 10µg/ml Hoechst 33258. Peroxisomes and LC3 were visualised using the FITC filter while Dnm1l was visualised under the Texas red filter of the Zeiss ApoTome AXIO Imager and the AxioVision Re. 4.7 software.

2.18 Mitochondrial isolation

Brain, heart and rectus femoris tissues were excised from mice and placed immediately in ice-cold isolation buffer (225nM mannitol, 75mM sucrose, 0.5% BSA, 0.5mM EGTA and 30mM Tris-HCl pH 7.4). The tissue was subsequently minced and homogenised on ice in 10ml isolation buffer. Differential centrifugation at 4ºC was used to obtain a mitochondrial pellet. An initial centrifugation at 740g was used to pellet nuclei and cell debris. The supernatant containing mitochondria was then transferred to a fresh tube and centrifuged at 9000g three times to pellet the mitochondria. After each centrifugation, the supernatant was removed and mitochondria were resuspended in ice-cold isolation buffer. After the final centrifugation, the supernatant was removed and the mitochondrial pellet was air-dried before mitochondrial proteins or mtDNA was extracted.

2.18.1 Mitochondrial protein extraction.

The mitochondrial pellet was resuspended in RIPA buffer (50mM Tris-HCl, 150mM NaCl, 2mM EDTA, 1% NP-40, 0.1% SDS, and 1% sodium deoxycholate) containing 1x PIC, incubated for 5 minutes on ice, then centrifuged at 10000g for 10 minutes at 4ºC. The supernatant containing extracted proteins was transferred to a fresh pre-chilled tube and stored at -80ºC.

2.18.2 Mitochondrial DNA extraction

Mitochondrial DNA was then isolated as described in section 2.13 starting by resuspension in cold solution 1 (25mM Tris-HCl & 10mM EDTA).

2.19 Mitochondrial DNA amplification

The Roche Expand Long Range kit (04829034001, Roche, Burgess Hill, UK) was used to amplify DNA across a 4.6kb region of mtDNA and the entire mtDNA genome (~16kb) (Appendix VIII).

Table 2.7. PCR conditions for the amplification of the mtDNA.

A. Reaction mixture (15µl)

Component	Volume (µl)	Final concentration
Template DNA	1	
5x Roche Expan Long Range buffer (containing 12.5mM $MgCl_2$)	3	1x (2.5mM $MgCl_2$)
dNTPs (10mM each)	0.75	500µM each
Forward primer (10µM)	3	2µM
Reverse primer (10µM)	3	2µM
DMSO	0.5	3.3%
Expand Long Range Enzyme mix (5U/µl)	0.2	1U
H_2O	3.55	
Total	**15**	

B. PCR cycling

Temperature (°C)	Time	
92	2 mins	
92	15s	cycle 1 x10
55	15s	
68	1min/kb	
92	15s	cycle 2 x25
55	15s	
68	1min/kb + 20s increment per cycle	
68	7mins	

(A) Components and concentrations of the PCR reaction using the Roche Expand Long Range kit. (B) Optimum temperatures of PCR cycling.

2.20 Yeast-2-hybrid

2.20.1 Yeast-2-Hybrid Analysis of Dnm1l self interactions

Regions of *Dnm1l* were cloned into the vectors pDEST32 (bait) and pDEST22 (prey) (Appendix IX) (Invitrogen Ltd., Paisley, UK) by Professor Neil Dear. The domain interactions were performed in the yeast strain MaV203, which contains *HIS3* and *GAL1* promoters driving the expression of *HIS3* and *LacZ* reporter genes respectively. The yeast cells were co-transformed with the bait and prey vectors by combining 100ng of each vector plus 100µg of Herring testes carrier DNA and adding to 100µl of yeast cells that have been cultured in 50ml liquid yeast peptone dextrose (YPD) at 30ºC overnight and resuspended in 1.5ml TE / lithium acetate (LiAc). This mixture was then added to 600µl PEG/LiAc and vortexed briefly at high speed. The cells were then heat-shocked in a water bath at 42ºC for 15 minutes followed by a 2 minute incubation on ice. Cells were pelleted by centrifugation for 5 secs at 13000rpm, resuspended in 500µl TE and plated on agar. Interactions were identified on the ability of transformants (in serial 10-fold dilutions) to grow on yeast drop-out medium agar lacking leucine, tryptophan and histidine supplemented with 100mM 3-amino-1,2,4-triazole. Interactions were semi-quantified by performing a β-galactosidase overlay assay: cells within the yeast colonies were first lysed with chloroform ($CHCl_3$) to expose the β-galactosidase that is expressed only in interactants. The plate was allowed to dry and then covered with a 0.1% low gelling temperature agarose gel made up in Z buffer (60mM $Na_2HPO_4.7H_2O$, 20mM $NaH_2PO_4.H_2O$, 10mM KCl, 1mM $MgSO_4$) containing 0.5mg/ml X-gal and 8mM 2-mercaptoethanol. Once the gel had set, the plate was incubated at 30ºC and monitored over 3 – 5 days for a blue colour to develop, indicating a positive interaction; the X-gal is colourless, turning blue when cleaved by β-galactosidase.

A more sensitive quantification method was used for mutated strains: the β-galactosidase liquid culture assay, based on the ability of β-galactosidase to cleave ortho-Nitrophenyl-β-D-galtactopyranoside (ONPG). Following an overnight growth of the yeast liquid culture at 30ºC, the cells were pelleted and resuspended in Z buffer (60mM $Na_2HPO_4.7H_2O$, 20mM $NaH_2PO_4.H_2O$, 10mM

KCl, 1mM $MgSO_4$), containing 38mM 2-mercaptoethanol. Cells were snap frozen in liquid nitrogen and thawed immediately, and this freeze / thaw was repeated twice more to lyse the cells. The cell lysate was then incubated overnight at 37ºC with 1mg/ml ONPG in Z buffer. Cleavage of ONPG is accompanied by the emission of light at 420nm, which was measured by a JENWAY 6305 spectrophotometer to quantify the level of β-galactosidase activity and hence, the strength of protein interaction.

2.20.2 Yeast-2-Hybrid Library screen for Dnm1l interactions

Dnm1l cDNA was cloned into the vector pAS2-1 (bait), using the following primer sequences:

Forward sequence	5'-d(ATAGAATTCGAGGCGCTGATCCCGGTCATC)3'
Reverse sequence	5'-d(TAGGGATCCTCACCAAAGATGAGTCTCTG)3'

Dnm1l cDNA was amplified by PCR under the following conditions: 50µl reaction containing 10ng DNA, 1U of AccuPrime™ *Taq* DNA polymerase High Fidlity (12346-086, Invitrogen, Paisley, UK), 1x AccuPrime™ PCR buffer 1 and 2µM of each primer. Thermal cycling conditions were 94°C for 15 seconds followed by 35 cycles of 94°C for 30 seconds, 55°C for 30 seconds and 68°C for 2 minute. A final step of 68ºC for 10 minutes was performed before completion of cycling. The PCR product was then double-digested with EcoRI and BamHI (NEB, Ipswich, UK) for 2 hours at 37ºC. pAS2-1 was also double digested using the same conditions. The restricted *Dnm1l* and pAS2-1 were then ligated using T4 DNA ligase (M0202, NEB, Ipswich, UK). 100ng of pAS2-1 plasmid and 75ng *Dnm1l* were ligated in a 10µl reaction containing 1x T4 DNA ligase reaction buffer and 1µl T4 DNA ligase and incubated overnight at 16ºC. The ligation product was subsequently transformed into *DH10β E. Coli* bacterial cells as previously described in section 2.5, plated out onto LB-agar plates containing 100µg/ml Ampicillin and incubated overnight at 37ºC. Colonies that grew were screened by colony PCR amplification using the primer sequences above and confirmed by sequencing using AS2-1 primers, which amplify the insert and flanking regions within the pAS2-1 plasmid:

AS2-1 forward	5'-d(GGAGACTGATATGCCTC)3'
AS2-1 reverse	5'-d(CCGGTAGAGGTGTGGTC)3'

A human placental cDNA library was previously cloned into pACT2 (prey) by Professor Neil Dear (Appendix X). The vectors were sequentially transformed into MaV203 yeast cells. Yeast cells were prepared by culture overnight at 30ºC in 50ml of YPD. The cells were pelleted by centrifugation at 2500rpm for 1 min and reuspended in 40ml TE. The centrifugation step was repeated and cells resuspended in 0.1M LiAc / 0.5x TE and incubated at room temperature for 10 minutes. 100ng of pAS2-1 containing *Dnm1l* was mixed with 100µg denatured sheared salmon sperm DNA and added to 100µl of yeast cells. 700µl 0.1M LiAc / 40% PEG-3350 / TE was added to the cells and incubated for 30 minutes at 30ºC. 88µl DMSO was added before heat shocking at 42ºC for 7 minutes. The cells were then pelleted and resuspended in TE, which was repeated twice to wash the cells. After the final wash, the cells were resuspended in 100µl TE and plated on yeast drop-out medium agar lacking tryptophan. Following incubation at 30ºC for 3-4 days, colonies that grew (hence contain the pAS2-1 plasmid) were cultured in 50ml synthetic complete (SC) medium lacking tryptophan. The same process of transformation was then repeated as above, replacing the 100ng pAS2-1 plasmid with 30µg pACT2 containing the human placental cDNA library and plated on yeast drop-out medium agar lacking leucine, tryptophan and histidine supplemented with 10mM 3-amino-1,2,4-triazole. After a 3-4 day incubation at 30ºC, any colonies that grew were picked and resuspended in SC medium lacking tryptophan and leucine, before being replated in serial 10-fold dilutions, on plates lacking leucine, tryptophan and histidine, but supplemented with 100mM 3-amino-1,2,4-triazole and semi-quantified by means of a β-galactosidase overlay assay (described in section 2.20.1).

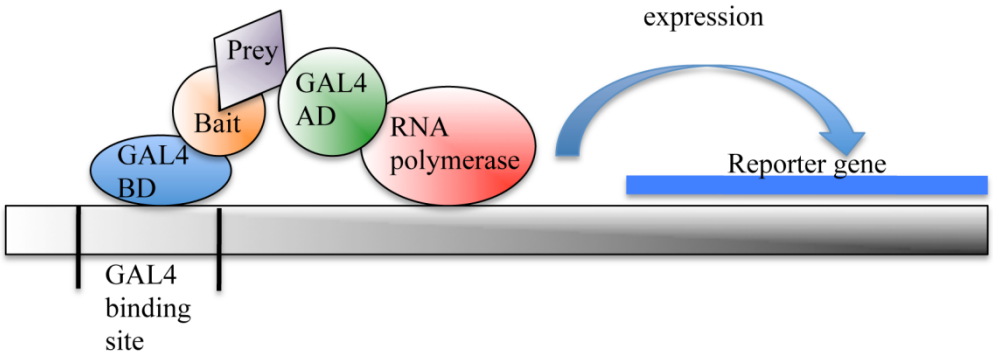

Figure 2.3. A schematic representation of the Yeast-2-Hybrid system. The GAL4 DNA binding domain (BD) is fused with the bait and GAL4 activation domain (AD) with the prey. An interaction between the bait and prey reconstitute a functional transcription factor of the reporter genes, activating the transcription of these genes.

2.20.3 Yeast-2-Hybrid analysis of DNM1L interactions

Mouse heart mRNA (7800, Invitrogen, Paisley, UK) was reverse transcribed into cDNA using the QuaniTect® Reverse Transcription kit (205310, Qiagen, Crawley, UK) as described in section 2.8. The following genes were cloned into pACT2:

Gene	Primer sequences	Restriction enzyme
MarchV (858bp)	5'-d(ATAGGCCATGGAGGCCCCGGACCAAGCCCTTCAACAG)3'	SfiI
	5'-d(ATAGGATCCTTATGCTTCTTCTTGCTCTGG)3'	BamHI
Mff (870bp)	5'-d(ATAGGATCCGAGCAGAAATTAGTCGAATTCAG)3'	BamHI
	5'-d(ATACTCGAGCTAGCGTCGAAACCAGAGCCA)3'	XhoI
Gsk3B (1021bp)	5'-d(ATAGGCCATGGAGGCCTCGGGGCGACCGAGAACCACC)3'	SfiI
	5'-d(ATACCCGGGTCAGGTGGAGTTGGAAGCTGA)3'	SmaI
Fis1 (462bp)	5'-d(ATAGAATTCGAGAGGCCGTGCTGAACGAGCTG)3'	EcoRI
	5'-d(ATACTCGAGTCAGGATTTGGACTTGGAGAC)3'	XhoI

The coding regions were amplified by PCR using the primer sequences designed above: 50µl reaction containing 10ng DNA, 1U of AccuPrime™ *Taq* DNA polymerase High Fidlity (12346-086, Invitrogen, Paisley, UK), 1x

AccuPrime™ PCR buffer 1 and 2μM of each primer. Thermal cycling conditions were 94°C for 15 seconds followed by 35 cycles of 94°C for 30 seconds, 55°C for 30 seconds and 68°C for 1 minute. A final step of 68ºC for 10 minutes was performed before completion of cycling. The PCR products were double-digested at 37ºC for 2 hours using the enzymes listed above (NEB, Ipswich, UK). The pACT2 plasmid was also double digested using the 4 different pairs of enzymes listed above and ligated with the corresponding DNA restriction product using T4 DNA ligase (M0202, NEB, Ipswich, UK). 100ng of pACT2 plasmid and 75ng insert DNA were ligated in a 10μl reaction containing 1x T4 DNA ligase reaction buffer and 1μl T4 DNA ligase and incubated overnight at 16ºC. The ligation product was subsequently transformed into *DH10β E. Coli* bacterial cells as previously described in section 2.5, plated out onto LB-agar plates containing 100μg/ml Ampicillin and incubated overnight at 37ºC. Colonies that grew were screened by colony PCR amplification using the primer sequences above and confirmed by sequencing using AD LD primers, which amplify the insert and flanking regions within the pACT2 plasmid:

AD LD forward	5'-d(ATGAAGATACCCCACCAAACCCA)3'
AD LD reverse	5'-d(GGGGTTTTTCAGTATCTACGAT)3'

The pAS2-1 vector containing mutant or wild type *Dnm1l* co-transformed with each version of pACT2 into MaV203 cells (as described in section 2.20.1) in which interactions were tested on yeast drop-out medium agar lacking leucine, tryptophan and histidine supplemented with 50mM 3-amino-1,2,4-triazole and by the β-galactosidase overlay assay. Yeast clones containing pACT2_*UBC9* identified from the human placental library screen in section 2.20.2 was also transformed with pAS2-1 containing mutant or wild type *Dnm1l.* After a 3-4 day incubation period at 30ºC, any colonies that grew were picked and resuspended in SC medium lacking tryptophan and leucine, before being replated in serial 10-fold dilutions, on the same drop-out agar plates and semi-quantified by means of a β-galactosidase overlay assay (described in section 2.20.1).

2.21 Calcium concentration

2.21.1 Cytoplasmic calcium concentration measurement

ES cells were cultured as described in section 2.14.3 in 10cm dishes. Once a confluency of 60-70% was reached, the cells were trypsinized and washed in Hanks' balanced saline solution (HBSS) (Thermo Scientific, Utah, USA) and resuspend in HBSS at 10^7 cells/ml. 100µl aliquots of cells (10^6 cells) were added to 900µl of labelling solution (5µM Fura-2 (Invitrogen Ltd., Paisley, UK) and 2.5mM Probenecid (Alfa Aezar, Heysha, UK), made up in HBSS containing 1mg/ml Bovine serum albumin (BSA) (Calbiochem., Darmstadt, Germany) and incubated at 37ºC, 5% CO_2 for 45 minutes, protected from light. After washing twice in 1ml HBSS, the cells were resuspended in 90µl HBSS and transferred to a white 96-well plate.

Fura-2 concentration was measured using the Berthold Mithras LB940 with Mikrowin 2000 software. Excitation was measured at 380nm (which measures Fura-2 bound to Ca^{2+}) and 340nm (which measures unbound Fura-2). Measurements were taken every 0.5s. After 30 seconds 10µl 1mM ATP (100µM ATP final concentration) was injected into the cells solution in each well to trigger the release of Ca^{2+} from the internal Ca^{2+} store, the ER. Measurements were taken for a further 13 minutes.

The ratio between unbound and bound Fura-2 (340nm/380nm) was calculated to normalise for cell number and then converted to Ca^{2+} concentration by means of a calibration curve in which known Ca^{2+} concentrations are plotted against Fura-2 concentrations.

2.21.2 Mitochondrial calcium concentration measurement using aequorin

Immortalized wild type and Python MEFs were cultured to 90% confluency in T75 flasks and subsequently transfected with a mitochondria-targeted aequorin vector (appendix XI) using Lipofectamine 2000 (Invitrogen Ltd, Paisley, UK). The mitochondrial aequorin DNA was incubated with lipofectamine 2000 for 20 minutes at room temperature then added to the growth medium on the MEFs.

The cells were then incubated at 37ºC, 5% CO_2 for 48 hours. 3 x 10^6 cells were then trypsinized and washed twice in Krebs-Ringer modified buffer (KRB) (125mM NaCl, 5mM KCl, 1mM Na_3PO4, 1mM $MgSO_4$, 5.5mM glucose, 20mM Hepes, pH7.4), containing 1mM $CaCl_2$, then incubated in KRB containing 1mM $CaCl_2$ and 5μM coelenterazine (Promega, Madison, USA) for 30 minutes on ice to reconstitute the aequorin protein. A final centrifugation was required to remove the supernatant and resuspend the cells in 90μl KRB containing 1mM $CaCl_2$ and 5μM coelenterazine. The cells were then transferred to a white 96-well plate. The luminescence was measured every 0.5s using the Berthold Mithras LB940 with Mikrowin 2000 software. After 30s, tertButylHydroquinone (tBuBHq) was added to the cells to a final concentration of 10mM. Subsequent conversion to Ca^{2+} concentration was achieved using a standard curve of known Ca^{2+} concentrations against luminescence.

2.22 Oxidative phosphorylation measurement

Oxidative phosphorylation (OXPHOS) was measured *in vitro* (MEFs and ES cells) and *in vivo* (heart and brain tissue) using the OROBOROS, high-resolution respirometry Oxygraph-2K, in collaboration with Professor Chris Peers and Dr. John Boyle.

2.22.1 Oxidative phosphorylation in cells

Cells were cultured as described in section 2.14, and then placed in the chamber of the OROBOROS Oxygraph-2K. Respiration was monitored from when the chamber is sealed. The initial measurement taken was that of 'routine', representing the total respiration of the cells. Oligomycin was then added to a final concentration of 4mg/ml to inhibit the activity of ATP synthase providing a measure of proton leak. The electron transport chain (ETC) was then completely uncoupled by a series of additions of Carbonyl cyanide-4-(trifluoromethoxy)phenylhydrazone (FCCP) from 0.5μM to 1.25μM until there was no further increase in O_2 consumption, therefore representing the maximum capacity of the electron transport system (E.T.S). Residual O_2 consumption (ROX) is a measure of non-mitochondrial respiration and was the

final measurement after shutting down OXPHOS with 4mg/ml oligomycin (F_1/F_0 ATPsynthase inhibitor), 0.5µM rotenone (complex I inhibitor) and 2.5µM antimycin A (complex III inhibitor).

2.22.2 Oxidative phosphorylation in tissues

Tissues were excised from the animal and placed directly in Mir05 solution (0.5mM EGTA, 3mM $MgCl_2.6H_2O$, 60mM K-lactibionate, 20mM taurine, 10mM KH_2PO_4, 20mM HEPES, 110mM sucrose and 1mg/ml BSA) on ice to preserve mitochondrial function. The tissues were then teased apart under the microscope into very fine segments and placed in 50µg/ml saponin on ice for 30 minutes to lyse cells and expose the mitochondria. The saponin was then removed by 3 subsequent washes in Mir05 and placed into the chamber of the OROBOROS Oxygraph-2K. While O_2 flux was constantly measured, appropriate substrates or inhibitors were added to deduce the efficiency of mitochondrial function. To the tissues, 10mM pyruvate, 2mM malate and 10mM glutamate were added to show total respiration. This was not necessary in intact cells as respiration was already taking place. 2.5mM ADP and subsequently 10mM succinate were added to measure the increase in O_2 consumption. FCCP was added gradually from 0.5 – 1.25µM to completely uncouple O_2 consumption and ATP production, emphasizing the maximum capacity of OXPHOS. The complex I inhibitor, rotenone was added at 0.5µM reducing the efficiency of mitochondrial function. Finally, the addition of 2.5µM antimycin A, a complex III inhibitor completely ceases the process of OXPHOS and any remaining O_2 consumption at this stage is as a result of non-mitochondrial respiration.

2.23 ATP determination

2.23.1 Cell lines

ATP was measured in MEFs, ES cells, embryoid bodies and cardiomocytes, which were cultured in 10cm plates as described in section 2.14. When cells reached an appropriate density, they were harvested by trypsinization and washed twice in 1ml incubation medium (140mM NaCl, 5mM KCl, 1mM $MgCl_2$, 1.2mM $CaCl_2$, 6mM glucose, 20mM Na-HEPES (pH7.4), 0.04% phenol red). After the final wash, the cell were resuspended in 70µl permeabilising solution (30µM digitonin, 140mM potassium glutamate, 1mM EGTA, 1mM $MgCl_2$, 6mM glucose, and 20mM K-PIPES (pH7.0) 0.04% phenol red) and subsequently incubated for 10 minutes at 30ºC. Volumes of 20µl were aliquoted into 3 wells of a white 96-well plate, therefore analysing each cell line in triplicate. 180µl of the standard reaction solution (1µM DTT, 0.5mM D-luciferin and 12.5µM firefly luciferase (Invitrogen Ltd., Paisley, UK)) was added to the cells in suspension. Luciferase activity was measured using the Berthold Mithras LB940 with Mikrowin 2000 software. A standard curve of known ATP concentrations against luminescence was used to deduce ATP concentrations.

2.23.2 Tissues

Whole brain or striatal tissue was lysed by homogenisation in NP-40 lysis buffer (100 mM NaCl, 1% Nonidet P-40, 10% glycerol, 2 mM $MgCl_2$, 1 mM NaF, 1 mM Na_3VO_4, 50 mM Tris-HCl, pH 7.4). Protein concentrations were subsequently deduced by means of a Bradford assay. Volumes of 20µl containing equal amounts of protein across samples were aliquoted into wells of a white 96-well plate. 180µl of the standard reaction solution (1µM DTT, 0.5mM D-luciferin and 12.5µM firefly luciferase (Invitrogen Ltd., Paisley, UK)) was added to the tissue lysate. Luciferase activity was measured using the Berthold Mithras LB940 with Mikrowin 2000 software. A standard curve of known ATP concentrations against luminescence was used to deduce ATP concentrations.

2.24 Mitochondrial membrane potential (MMP) measurement

Immortalized MEFs were cultured on coverslips in growth medium until 80% confluent. The cells were then incubated in a final concentration of 2μM JC-1 (Invitrogen Ltd., Paisley, UK) for 30 minutes at 37ºC, 5% CO_2. Images were captured using the Zeiss LSM 5.10 confocal microscope. Fluorescence was quantified using the ImageJ 1.42q software. This experiment was performed by Dr. John Boyle.

2.25 Behavioural analyses

In a cohort of 71 Python x R6/2 mice (males: 10 wt, 11 Py, 10 R6/2, 4 R6/2 x Py; females: 11 wt, 8 Py, 7 R6/2, 10 R6/2 x Py), males and females were housed in single sex, mixed genotypes up to the onset of Huntington's disease at approximately 15 weeks. They were weighed twice a week from the age of 3-weeks-old until disease onset. Grip strength (grams) was recorded from 7-weeks-old using a force metre containing a grid providing a means of forelimb grasping. Clasping was also monitored based upon how quickly a mouse clasps after being handled by the tail tip and how severe the clasping is in terms of hind limb, forelimb or all 4 limb clasping.

2.26 Statistical Anaylses

Statistical analyses were carried out to evaluate significance of experiments using GraphPad Prism 6 software. Comparisons between two sets of data were performed using a paired Student's t-test. Multiple comparisons were analysed by a One-Way ANOVA and Bonferroni post-test correction. Significance between compared data is denoted by an asterisk and given where $P<0.05$, unless stated otherwise. Error bars represent standard error of the mean in all analyses.

Chapter 3 : The effect of the Python mutation on DNM1L function

3.1 Results

The replacement of cysteine with phenylalanine in DNM1L^{Py} has in some way altered DNM1L function. Consequently, a series of experiments were performed to investigate whether DNM1L structure or activity might be altered by the Python mutation. Initial investigations on the effect of the Python mutation focused on determining whether the mutation altered basic aspects of DNM1L biology such as cellular protein levels, subcellular localisation, GTPase activity and ability of the DNM1L protein to self-interact and interact with other proteins.

3.1.1 The Python mutation impairs DNM1L intramolecular interactions

There is no evidence to suggest that the cysteine residue mutated in Python is involved in the formation of disulphide bonds, as determined by X-ray crystallography of dynamin, and so likely to be replicated in DNM1L (Faelber *et al*., 2011, Ford *et al*., 2011). Regardless it might influence folding of the monomer or interaction between monomers. Indeed, other mutations in the middle (M) domain have been shown to affect higher order structures (Chang *et al*., 2010, Ramachandran *et al*., 2007, Zhu *et al*., 2004). As discussed in Section 1.4.4, a structural homology model of DNM1L indicates that the Python mutation is located in a region that might affect intramolecular interactions (Ashrafian *et al*., 2010).

To investigate if interactions were compromised by the $C_{452}F$ mutation, a yeast-2-hybrid (Y2H) experiment was performed using the Pro-Quest™ system. This system allows measurement of interactions by expressing a GAL4 DNA binding domain fusion protein expressed in the pDEST32 vector and a GAL4 activation domain fusion protein expressed in the pDEST22 (Appendix IX). Initially, a test was done to confirm what regions of the DNM1L protein are able to interact. The DNM1L domains used were based on previous studies that had demonstrated an interaction between the N-terminal (amino

acids 1-459) and C-terminal (506-742) parts of the protein (Smirnova *et al*., 1998), as well as reports of an association between the M and GTPase effector (GED) domains (Smirnova *et al*., 1998, Zhu *et al*., 2004). The plasmid vectors containing cloned cDNA fragments to express the above domains were supplied by Professor N Dear. They were then transfected into yeast cells in appropriate combinations. The DNM1L domains in the fusion proteins tested are indicated in Figure 3.1A. All domains were tested for interactions with one another in the yeast strain MaV203. If two fusion proteins expressed from the pDEST22 and pDEST32 expression vectors interact, this will be reflected in activation of reporter cassettes in the MaV203 yeast strain leading to histidine auxotrophy and β-galactosidase activity. Plasmids were co-transfected into yeast, cultured on -leu -trp plates to select for colonies containing both plasmids, then plated on -trp -leu -his + 100 mM 3-amino-1,2,4-triazole (3-AT) plates to detect interactions. Only a few positive interactions were detected: (i) the full-length (1-742) protein with itself, (ii) the reported N-terminal (1-495) and C-terminal (506-742) domains, and (iii) the N-terminal (1-495) and GED (641-742) (Fig. 3.1B). However M domain self-interactions have also been reported, which were not reproduced in this system. Interestingly, some of the interactions worked much better in one plasmid combination e.g. the 1-495:506-742 and 1-495:641-742 interactions worked far more efficiently when 1-495 was in the pDEST32 plasmid.

A β-galactosidase plate assay was also carried out to confirm these interactions. It is evident, however, that this method is less sensitive than assessing for histidine auxotrophy, identifying the stronger interactions only. For example, the strong interaction control Krev1:RalGDS shows up strongly positive in the β-galactosidase assay, whereas the control for the weak interactor, Krev1:RalGDSm1 is barely detectable. This is despite both the strong and the weak interactor growing well on –trp –leu –his + 100 mM 3-AT plates (Fig.3.1B).

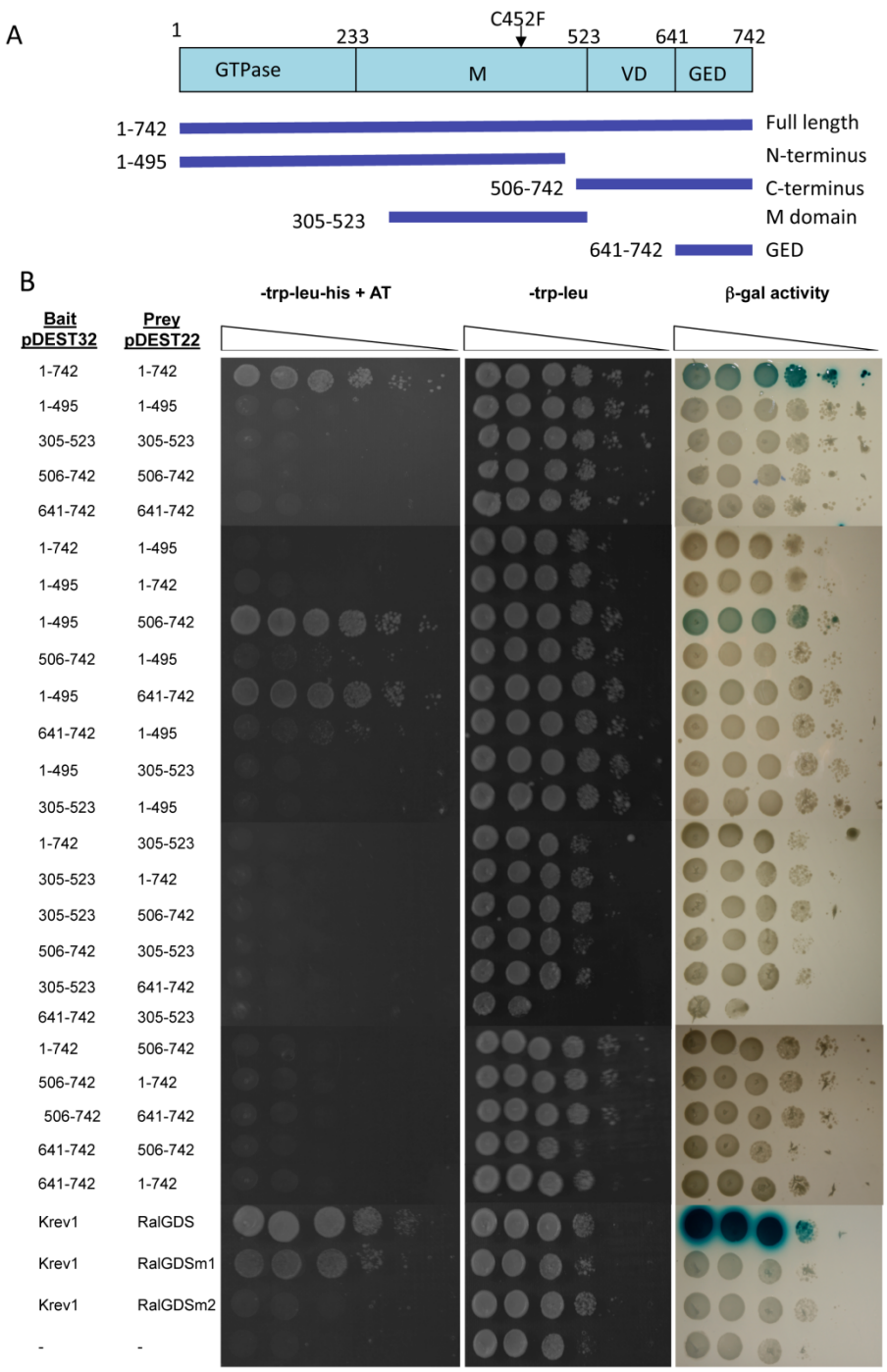

Figure 3.1. Dnm1l domain interactions. (A) The positions of each DNM1L region used in the Y2H assay. (B) All possible interactions as fusion with either GAL4 DNA binding domain in pDEST32 or GAL4 activation domain in pDEST22 of Dnm1l in yeast MaV203 plated in serial 10-fold dilutions from a saturated overnight culture from left to right. Positive interactions were determined by the growth on –trp, -leu, -his + 100mM 3-AT plates (left) and YPD plates containing X-gal (right). Control interactions were Krev1:RalGDS, strong interaction; Krev1:RalGDSm1, weak interaction; Krev1:RalGDSm2, no interaction; and a negative control containing empty plasmid vectors.

The Python mutation was introduced into these plasmids by site-directed mutagenesis. The mutated plasmids were transfected into yeast and assessed in a similar fashion to above. Only the combinations above that gave a detectable interaction were assessed as combinations i.e. 1-742:1-742, 1-495:506-742 and 1-495:641-742. The Python mutation abrogated the N-terminus with C-terminus/GED interactions, but had little affect on interaction between full-length monomers (Fig.3.2A). A liquid β-galactosidase assay, which is more sensitive than the plate β-galactosidase assay, was used to quantify the difference in the strength of interactions. The results indicated that the introduction of the Python mutation completely abrogated the N-terminus:C-terminus and N-terminus:GED interactions with only a minor effect on heterotypic full length monomer interactions (Fig. 3.2B).

A

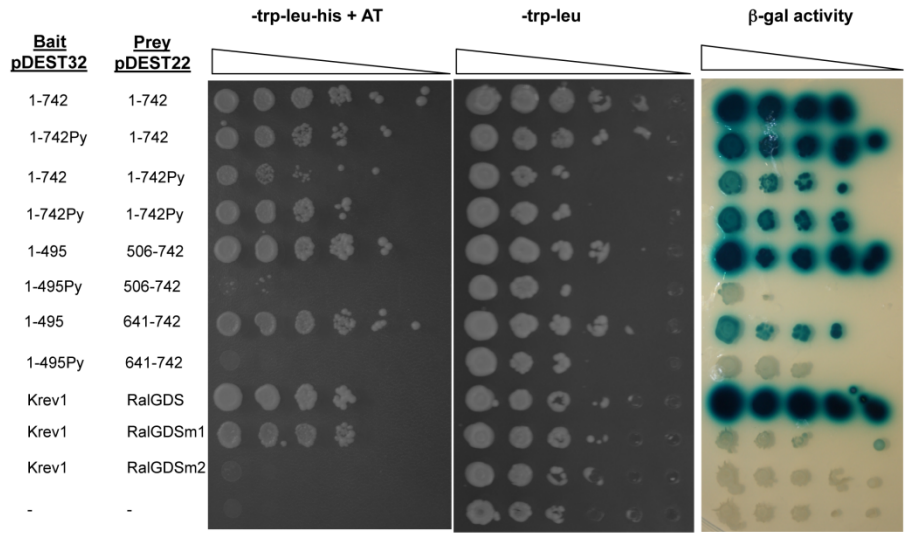

B

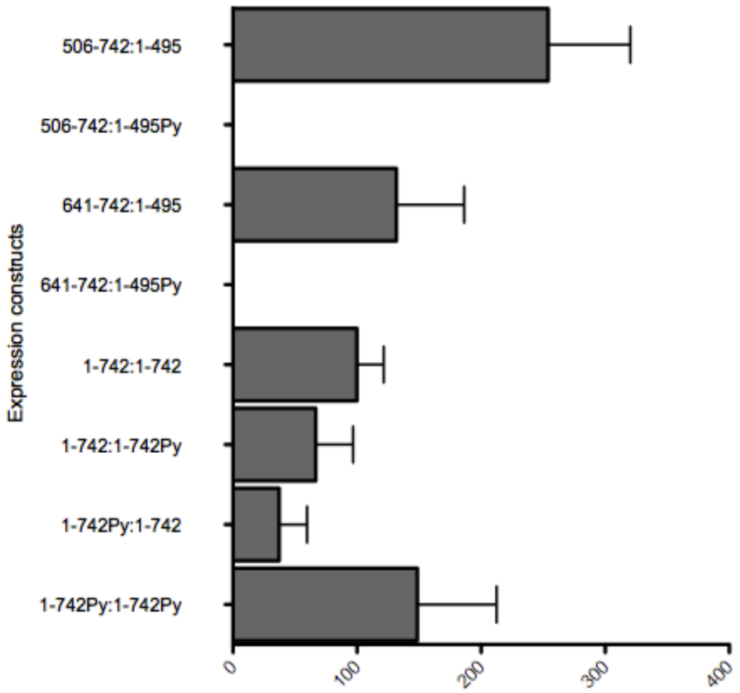

Figure 3.2. Python abrogates some DNM1L domain interactions. (A) A Y2H assay showed that DNM1L interactions between the N-terminus and C-terminus/GED were completely abrogated by Python, whereas effects on full-length interactions were less severe. Control interactions were as in Figure 3.1. (B) A Liquid β-galactosidase assay quantified and confirmed the disruptions of some heterotypic interactions. Full-length interactions were also disrupted, though to a lesser extent (one-way ANOVA, *P*=0.0005, meeting the Bonferroni corrected threshold for significance, 0.05/3 = 0.0167), n=6.

3.1.2 DNM1L protein levels are reduced in Python

Compromising the assembly and activity of DNM1L may also alter protein levels within the cell. For example, the mutant version might be targeted for degradation due to misfolding (Glickman and Ciechanover, 2002). This was examined in Western blots of heart and brain protein extracts from Python heterozygotes and wild type littermate control mice. The amount of protein loaded was normalised by determining the levels of T23, an inner mitochondrial membrane protein and α-tubulin, a structural protein present in the cytosol, neither of which should change between the samples as overall mitochondrial volumes per cell are not significantly altered in Python mice (Ashrafian *et al*., 2010).

A reduction of total DNM1L protein levels of approximately 65% was observed in Python heart samples (Fig. 3.3A). A reduction was also seen in the brain though somewhat less in magnitude (ca. 50% relative to wild type) (Fig 3.3B). The antibody used did not preferentially bind to wild type DNM1L so the DNM1L protein detected would likely include both wild type and Python DNM1L.

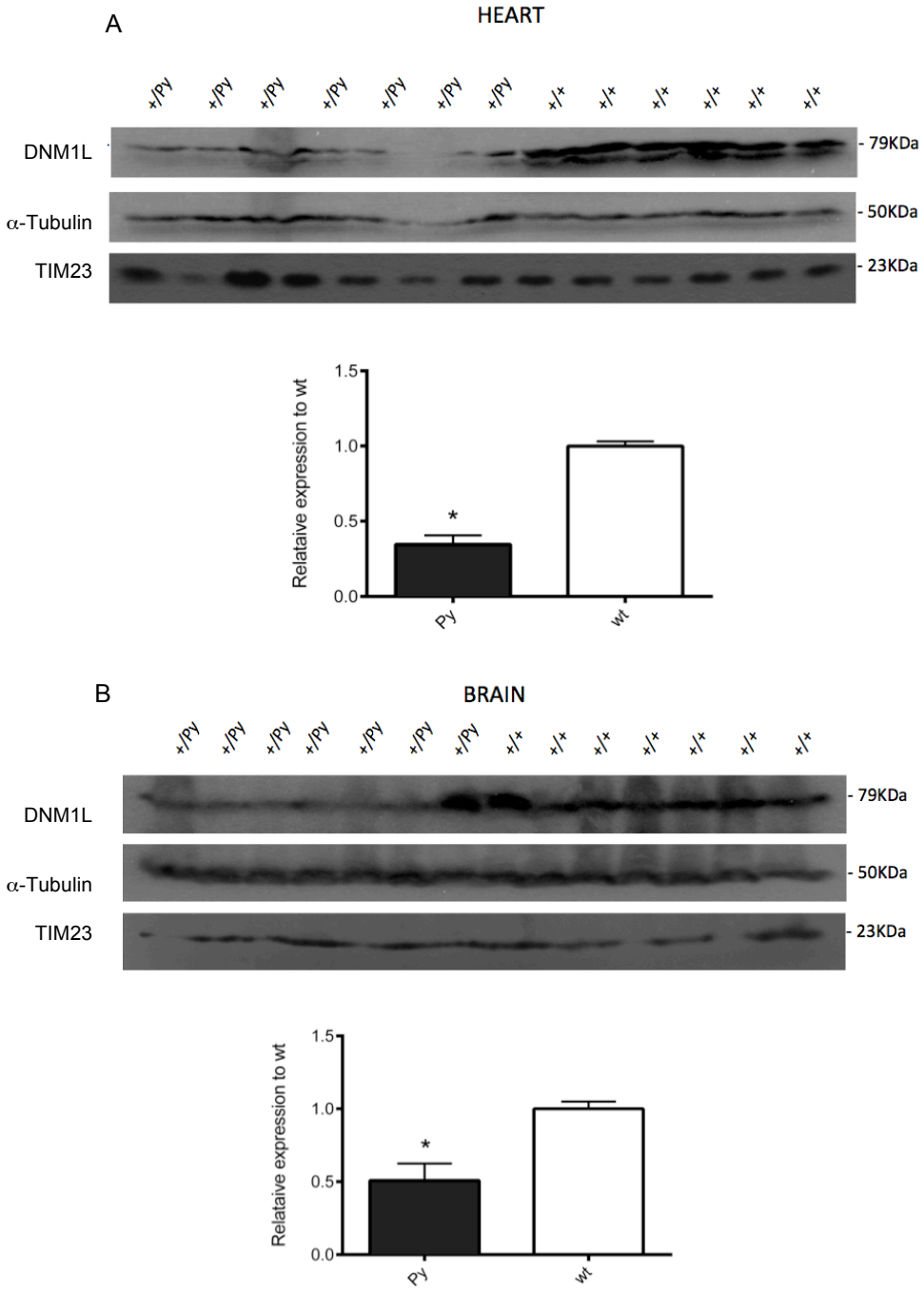

Figure 3.3. Cellular DNM1L levels are reduced in Python mice. Western blot analysis of total protein extracts from heart (A) and brain (B) of seven 13-week-old *+/Py* and six *+/+* male mice on a congenic C57BL/6J background using a Dnm1l-specific antibody. The blots were stripped and reprobed with antibodies to the mitochondrial protein TIM23 and to α-tubulin to confirm loading levels. Densitometry analyses indicate a reduction in DNM1L levels of 65% in the heart (Student's t test, $P<0.0001$) and 50% in the brain (Student's t test, $P=0.0022$) of Python mice.

3.1.3 The Python and wild type alleles are equally expressed

The reduction in DNM1L protein levels in Python heterozygotes seen above could reflect lack of production of the Python protein from the mutated allele though given the reports that *Dnm1l*$^{+/-}$ mice, which contain approximately half the normal levels of DNM1L, appear to thrive similarly to wild type mice (Ishihara *et al*., 2009, Wakabayashi *et al*., 2009), a reduction in DNM1L levels alone of the magnitude seen in Python heterozygotes should not lead to a cardiovascular abnormality. Alternatively, it was possible that the Python protein was leading to some protein degradation (e.g. Python dimers) but that the remaining DNM1L, Python:wild type dimers and wild type only dimers are expressed and Python may be acting in a dominant-negative manner, somehow reducing the activity of Python:wild type heterotypic dimers.

To investigate this further, mRNA from heart and brain was examined for levels of the *Dnm1l*^{Py} mRNA to ascertain if the Python allele was expressed. Quantitative analysis by pyrosequencing is based on the production of light intensity in proportion to the amount of nucleotide detected (Fig. 3.4A). The substitution in Python is a G to a T base (as shown in red in Fig. 3.4A). The following nucleotide in the sequence after the mutated base is also a T. For this reason, in the wild type sample it would be expected that the signal intensity for the G and the following T would be very similar, denoting homozygous G followed by homozygous T. If the Python and wild type alleles were equally expressed in Python heterozygotes, it would be expected that the signal intensity for T would be 150% to that of the wild type signal (GT followed by TT in Python vs. GG followed by TT in wild type). This is because the signal for T represents the heterozygous T as a result of the Python mutation and the adjacent T in the cDNA, which is homozygous. The signal for G will therefore decrease by 50% to that of wild type as half the particular base in that position is present (GT in Python vs. GG in wild type). Total cellular mRNA was isolated from four hearts and six brains of 5-week-old Python and wild type C57BL/6J mice, transcribed into cDNA and subsequently used to determine allelic expression levels by means of pyrosequencing. The result shows that the Python mRNA allele is expressed in equal amounts to the wild type allele in both hearts and brains of Python heterozygotes (Fig 3.4B). Thus it is likely to

be expressed at the protein level in Python heterozygotes and in equal proportions to the wild type protein. This would result in a cellular composition of 25% Python homotypic dimers, 25% wild type homotypic dimers and 50% Python:wild type heterotypic dimers. One possibility is that Python DNM1L dimers might lack any functional activity and are rapidly degraded in the cell while the heterotypic dimers are retained yet have reduced functionality and thus reduce the levels of active DNM1L higher order structures in the cell to a level that enables survival but compromises organ function in certain conditions (such as observed in the heart). The next experiments further investigated this possibility.

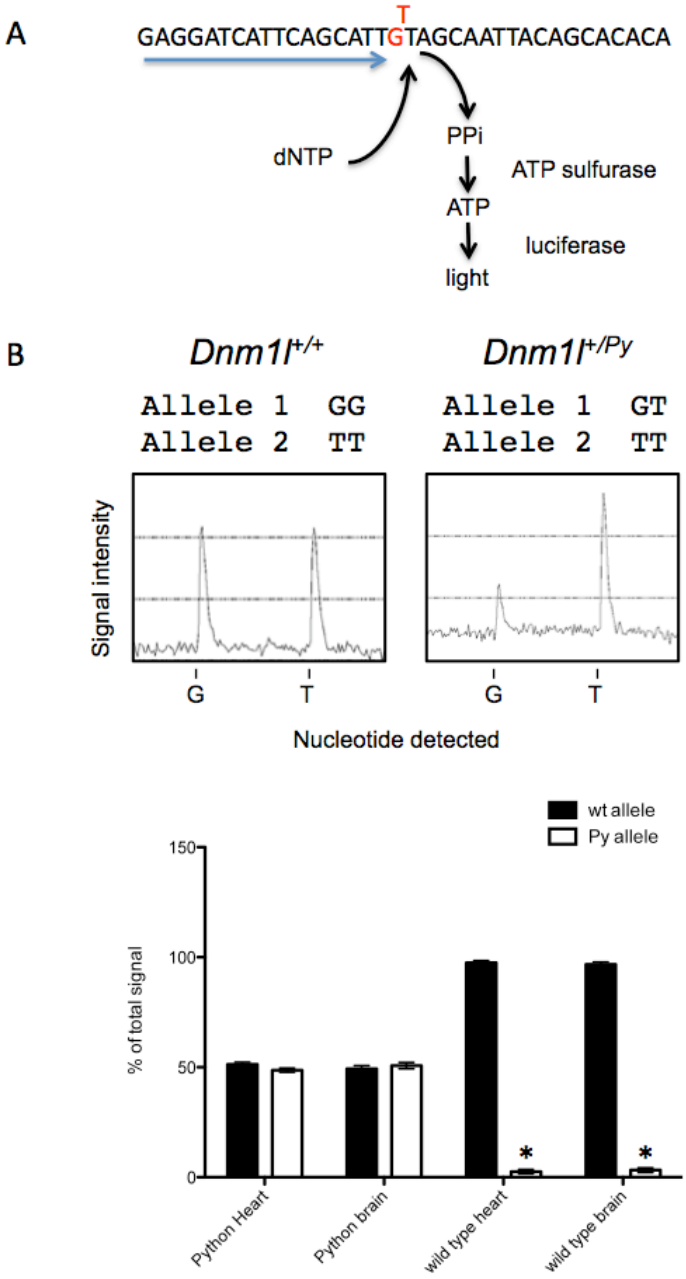

Figure 3.4. The *Dnm1l*^{Py} allele is expressed in heterozygotes. A) The DNA sequence of *Dnm1l* surrounding the mutation site of Python, which is highlighted in red. G is the wild type allele with T being the Python allele. During pyrosequencing analysis, the addition of dNTPs is accompanied with the release of pyrophosphate (PPi), which is then converted to ATP by ATP sulfurase. The ATP is then used to produce light via luciferase activity. B) Pyrosequencing analysis of cDNA transcribed from mRNA of 4 hearts and 6 brains of 5-week-old Python and wild type C57BL/6J male mice reveals the Python and wild type alleles in the Python heterozygotes are equally expressed at the mRNA level. Results shown are typical results that were independently confirmed in 3 different mRNA samples for each genotype.

3.1.4 The DNM1L^{Py} protein has reduced GTPase activity

GTPase activity is an inherent feature of dynamin family proteins and required for dynamin function (Ingerman *et al*., 2005, Ramachandran *et al*., 2007). Alterations to DNM1L that reduce GTPase activity (e.g. the $K_{38}A$ mutation (Pitts *et al*., 1999)) result in mutant proteins that can act in a dominant negative function to affect mitochondrial morphology (Frank *et al*., 2001, Smirnova *et al*., 2001). To test whether GTPase activity was reduced in DNM1L^{Py}, it was produced in bacteria as a his-tag fusion protein (by cloning into the pET101 plasmid (Appendix IV)) (Figure 3.5A), purified and then assayed for GTPase activity. To assess GTPase activity, the P_iColourLock Gold^{TM} system was used. This is a colorimetric assay based on the production of P_i hydrolysed from GTP via the GTPase action of the purified protein. Inorganic phosphate (P_i) is then converted into a P_i-dye complex that is detectable at 635nm. The higher the concentration of P_i detected, the greater the GTPase activity of the protein. The purified Python protein exhibited a 75% reduction in GTPase activity compared to that of the wild type protein (Fig. 3.5B). Therefore, GTPase activity and, as a result, DNM1L function, are reduced in the DNM1L^{Py} protein.

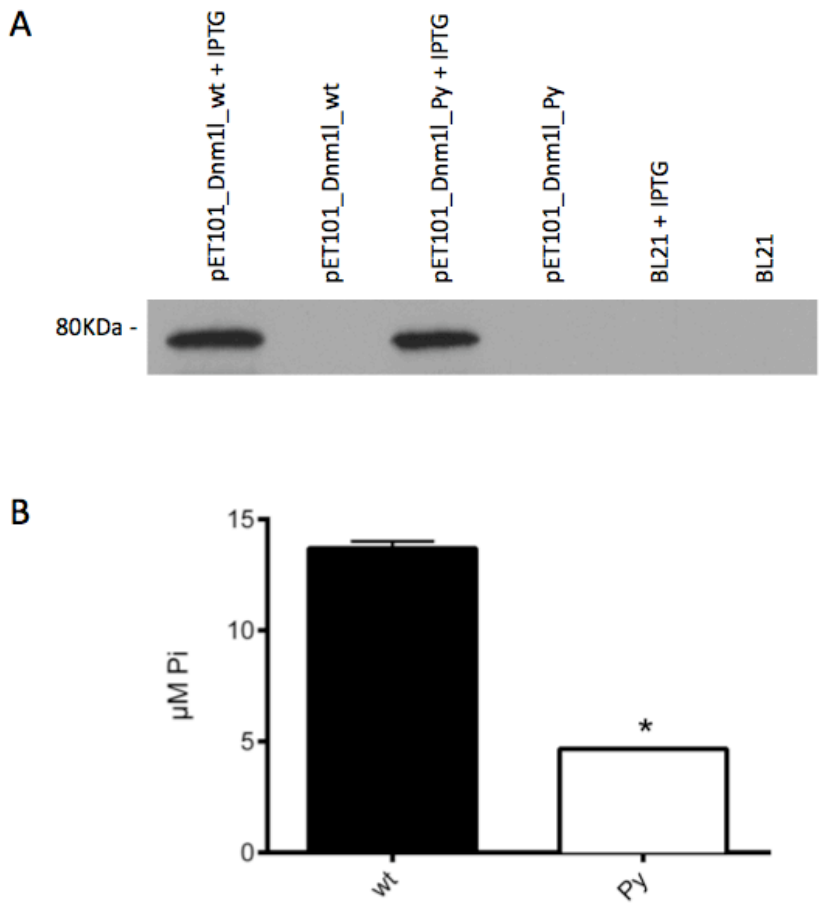

Figure 3.5. GTPase activity of Python DNM1L is reduced. A) Bacterial expression of pET101_Dnm1l fusion proteins for wild type and Python DNM1L. Negative controls included fusion constructs that had not been induced for expression with IPTG and non-transfected BL21 bacterial cells. B) The GTPase activity was measured by the concentration of P_i produced as a result of GTP hydrolysis. Wild type DNM1L displays far greater activity than an equivalent amount of Python DNM1L (Student's t test, *P*>0.0001), n=3.

3.1.5 Python can act in a dominant-negative fashion

If the Python mutation acts in a dominant-negative fashion, then it might be expected that the presence of the mutant protein would have an adverse effect on the activity of wild type protein. One way to ascertain if this is the case is to measure the level of GTPase activity in a sample of purified wild type DNM1L and compare to the same amount of wild type DNM1L renatured with an equal amount of DNM1L^{Py} protein. If the Python mutation is dominant negative, the GTPase activity of purified wild type protein renatured with the same amount of

purified Python protein will reduce the GTPase activity of the dimer when compared with the GTPase activity for the same amount of wild type protein alone. Equal amounts of purified wild type and Python DNM1L were renatured together and assayed for GTPase activity. GTPase activity in wild type:mutant mix is reduced to 75% to that of wild type protein alone (Fig 3.6). This provides molecular evidence that the Python protein can act as a dominant negative, heterodimers having reduced activity compared to wild type homodimers.

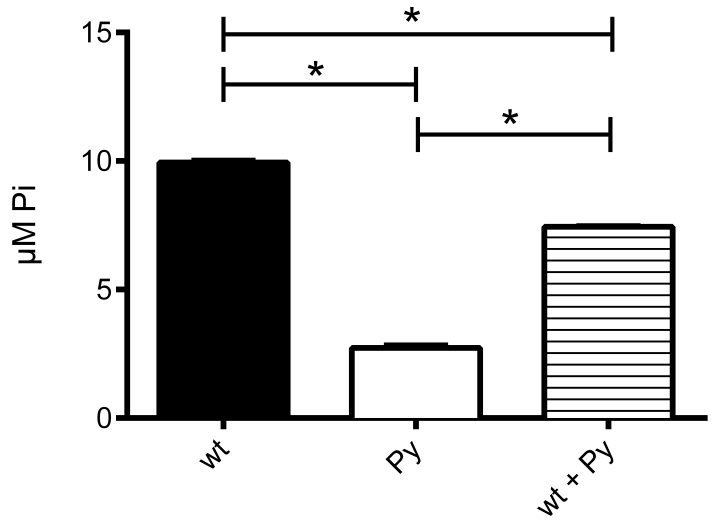

Figure 3.6. Python reduces the GTPase activity of wild type DNM1L. The GTPase activity was measured by the concentration of P_i produced as a result of GTP hydrolysis. 60ng of wild type DNM1L displays far greater activity than 60ng of Python DNM1L. When renaturing 60ng of wild type protein with 60ng of Python protein, the GTPase activity is reduced when compared to wild type alone (one-way ANOVA, P<0.0001), suggesting dominant-negative activity of the mutant protein. n=3.

Manczak *et al* (2012) reported no significant changes in the GTPase activity in the cortex of *Dnm1l*$^{+/-}$ mice when compared to *Dnm1l*$^{+/+}$ mice. A query of Ensembl indicates there are 2468 transcripts related to GTPase activity in the mouse genome. Thus it is not surprising there was no change detected as DNM1L probably only contributes to a very small proportion of overall GTP hydrolysis in any cell. To formally exclude that expression of Python DNM1L does not lower overall GTPase activity in the brain, GTPase activity was measured in whole brain lysates of wild type and Python 5-week-old C57BL/6J mice. Two samples for each genotype were used for analysis. As shown in

Figure 3.7, no significant alteration occurs within the brain lysates of the Python mice compared to the wild type controls. This result, does not, however, exclude the likelihood that DNM1L GTPase activity is reduced in the brain, which still seems likely given the *in vitro* protein expression results above

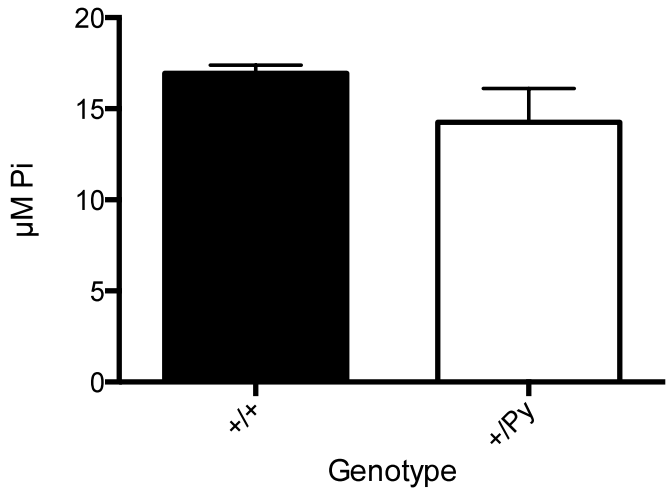

Figure 3.7. Overall GTPase activity within Python brains is not altered. GTPase activity was measured in the brain of samples from 5-week-old male Python and wild type littermate controls. Results shown are duplicate tests of two separate samples for each genotype. n=3.

3.1.6 The *Dnm1l*^{Py} and *Dnm1l*^{A401D} mutations impair DNM1L interactions with UBC9 and MFF.

A number of intermolecular interactions have been reported to influence activity of DNM1L. It is plausible that the Python mutation may impair interactions with such other proteins and therefore subsequent function of DNM1L. Reported interactions important for DNM1L docking on the OMM include ubiquitination through interactions with MARCHV (Karbowski *et al*., 2007), sumoylation, which involves forming a complex with sumo-conjugating enzyme (UBC9) and SUMO1 (Harder *et al*., 2004). FIS1 (Yoon *et al*., 2003) and MFF (Otera *et al*., 2010) have been shown to be important interactions for DNM1L docking on the OMM. An interaction with glycogen synthase kinase-3 beta (GSK3β) was detected using a Y2H system, however the exact function of

this interaction remains unknown (Hong *et al*., 1998). An interaction with Pex19p, which resides on the peroxisomal membrane, may be required for the recruitment of Dnm1 to the peroxisomes in yeast (Vizeacoumar *et al*., 2006), though no mammalian equivalent interaction has been reported.

The full complement of DNM1L-interacting protein is unknown. Although a Y2H screen for DNM1L-interacting proteins has been reported (Harder *et al*., 2004), the published work only refers to 2 proteins – UBC9 and SUMO1 – and not to any other proteins identified in the work. Therefore, to ascertain if there were other unreported interacting proteins, a Y2H screen was performed. *Dnm1l* cDNA was cloned into pAS2-1 (Appendix X) as bait. The resultant fusion protein consists of DNM1L linked to a GAL4 DNA binding domain. As prey, a commercial placental cDNA library cloned into pACT2 (Appendix X) (complexity > 10^6 independent cDNA clones) was used. This expresses cDNAs as fusion proteins with the GAL4 activation domain. The bait and prey vectors were co-expressed in the yeast strain MaV203 and plated on agar -trp -leu -his +10 mM 3AT to select for yeast colonies auxotrophic for histidine. 25 clones were identified and were replica plated onto -trp -leu, -trp -leu –his + 10 mM 3AT and -trp -leu -his + 100 mM 3AT agar plates to confirm if an interaction was present. A β-galactosidase overlay assay of the –trp –leu plates was also used to show the strength of interactions (Fig. 3.8). 4 colonies appeared to be the result of a true interaction. Subsequent DNA isolation and sequencing revealed the only protein interacting with DNM1L identified in this screen was UBC9. Thus, no new interacting proteins were identified. This probably suggests that the screen was sub-optimal as Harder *et al* (2004) reported that UBC9 was only 68% of cDNA interactions identified. Perhaps the Y2H assay used was not sensitive enough and only revealed very strong interactions.

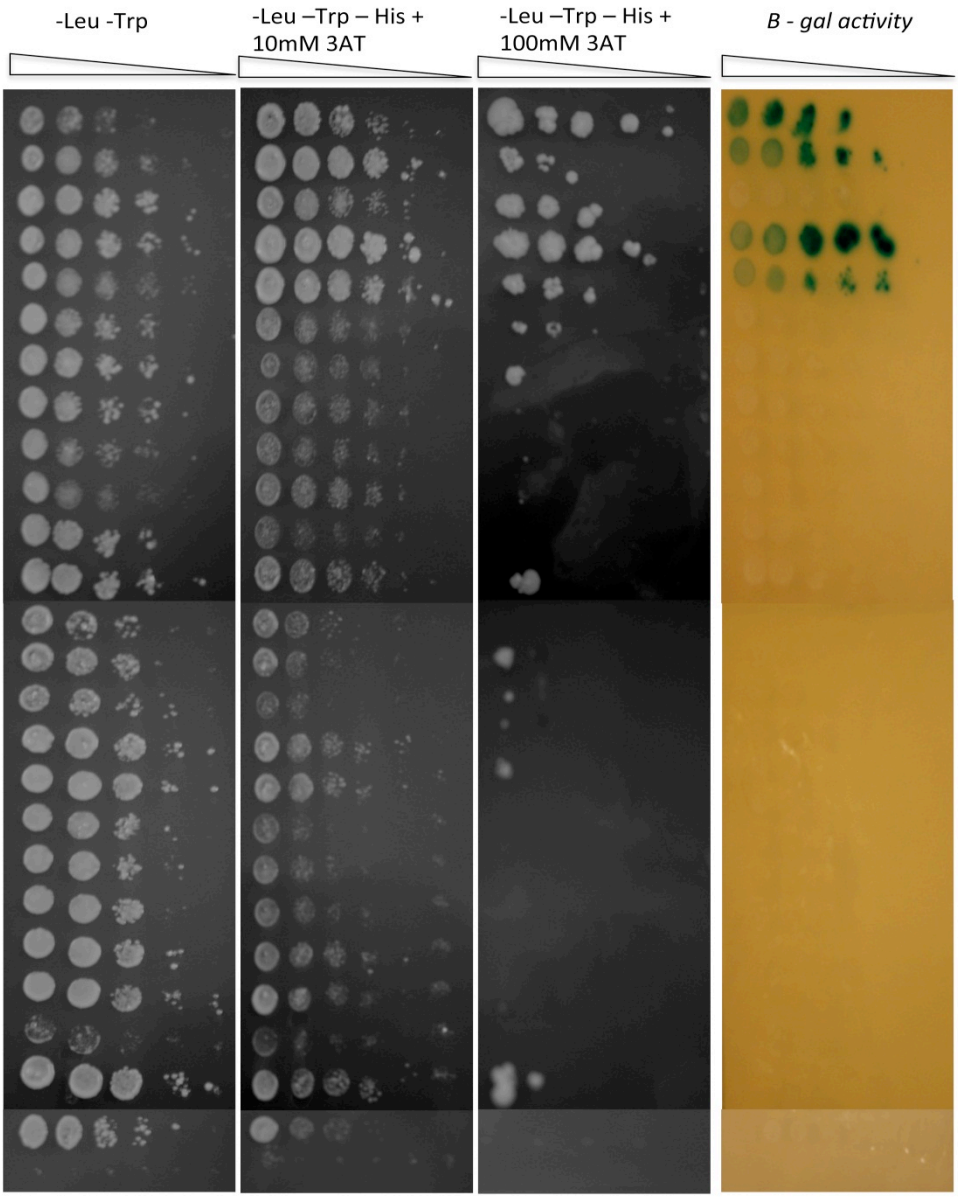

Figure 3.8. Y2H library screen showing positive clones. Clones were picked from a Y2H library screen and replica plated onto the different drop out media plates in 5 10-fold dilutions to identify potential interactions with DNM1L. All 4 positive interactions were identified as UBC9.

The interaction between DNM1L and UBC9 may be important for sumoylation and subsequent translocation to the OMM. M domain mutations such as Python and the $A_{401}D$ (Waterham *et al*., 2007) may impair this interaction, thereby decreasing the amount of DNM1L on the OMM. Impaired interaction with other proteins might also result and reduce DNM1L activity in mutant cells.

To investigate this, *Dnm1l*^{Py} and *Dnm1l*^{A401D} cDNAs in pAS2-1 were generated by site-directed mutagenesis. For the known interacting proteins, cDNA was made from mouse heart mRNA for each and cloned into pACT2. The list of proteins analysed for interaction with DNM1L are shown in Table 3.1.

Table 3.1. List of proteins that were used in interaction experiments with Dnm1l

Protein	**Reference**	**Interaction detected in this study**
UBC9	Harder *et al.* (2004)	Yes
MFF	Otera *et al.* (2010)	Yes
Pex19	Vizaecoumer *et al.* (2003)	No
FIS1	Yoon *et al.* (2003)	No
GSK3B	Hong *et al.* (1998)	No
MARCHV	Nakamura *et al.* (2006)	No

The DNAs were co-transformed into the yeast strain MaV203 and plated on -trp -leu agar plates. Individual colonies were subsequently replica plated in 10-fold dilutions on to plates of dropout medium lacking tryptophan, leucine and histidine supplemented with 50 mM 3AT.

The Dnm1l interactions with UBC9 (Fig. 3.9A) and Mff (Fig. 3.9B) were confirmed in this assay, both of which were abrogated by the introduction of the Python or the $A_{401}D$ mutation. It is possible that DNM1L^{Py} and DNM1L^{A401D} exhibit reduced translocation to the OMM as a consequence of impaired interactions with UBC9. Further to this, should the mutated versions of DNM1l reach the OMM, it is likely they will display reduced stability on the membrane as a result of defective interactions with the docking protein, MFF. The other interactions reported were not identified in this assay (Fig. 3.9C-F), preventing any further examination of the effect of mutations.

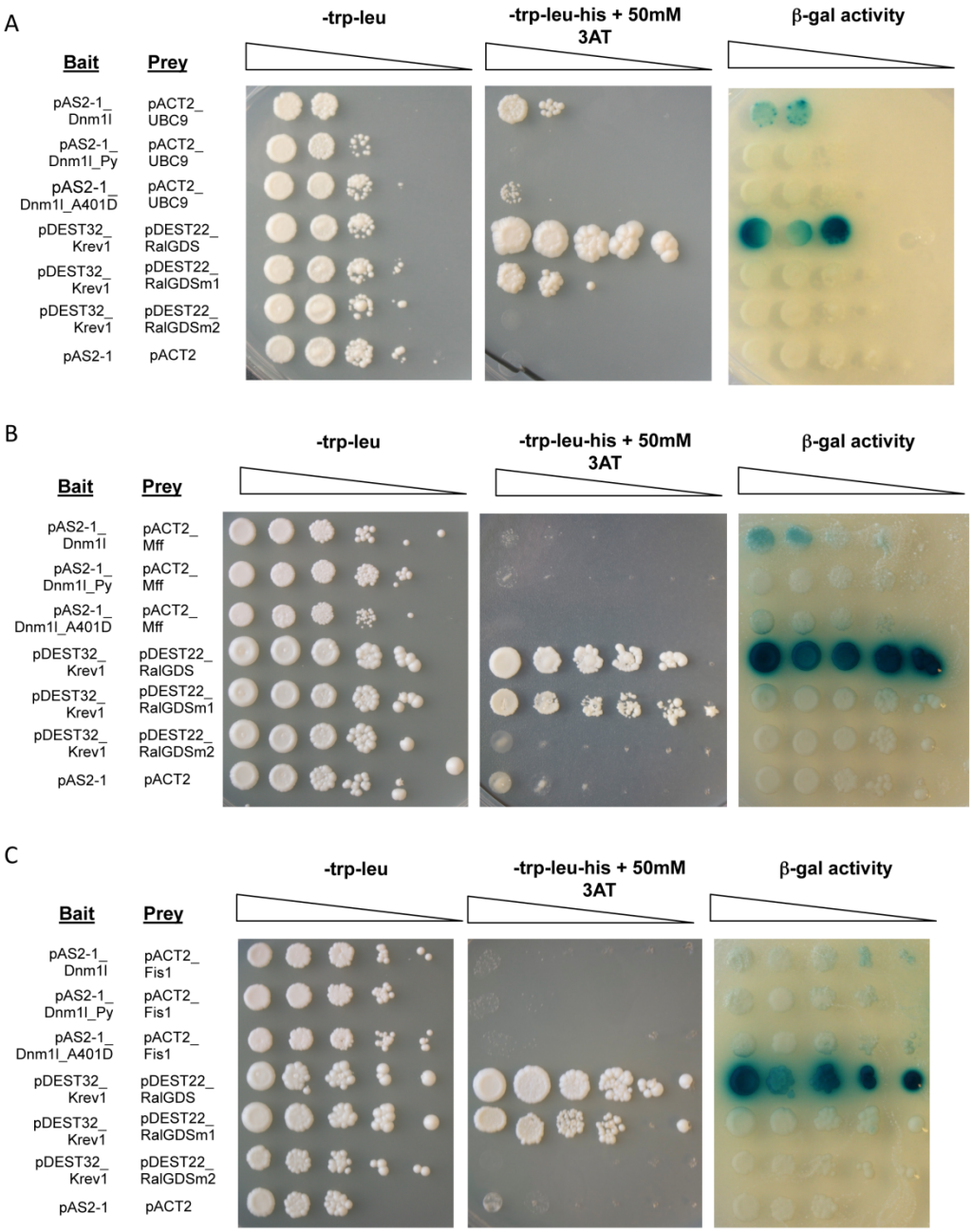
A
-trp-leu
-trp-leu-his + 50mM 3AT
β-gal activity
Bait
Prey
pAS2-1_ Dnm1l
pACT2_ UBC9
pAS2-1_ Dnm1l_Py
pACT2_ UBC9
pAS2-1_ Dnm1l_A401D
pACT2_ UBC9
pDEST32_ Krev1
pDEST22_ RalGDS
pDEST32_ Krev1
pDEST22_ RalGDSm1
pDEST32_ Krev1
pDEST22_ RalGDSm2
pAS2-1
pACT2
B
-trp-leu
-trp-leu-his + 50mM 3AT
β-gal activity
Bait
Prey
pAS2-1_ Dnm1l
pACT2_ Mff
pAS2-1_ Dnm1l_Py
pACT2_ Mff
pAS2-1_ Dnm1l_A401D
pACT2_ Mff
pDEST32_ Krev1
pDEST22_ RalGDS
pDEST32_ Krev1
pDEST22_ RalGDSm1
pDEST32_ Krev1
pDEST22_ RalGDSm2
pAS2-1
pACT2
C
-trp-leu
-trp-leu-his + 50mM 3AT
β-gal activity
Bait
Prey
pAS2-1_ Dnm1l
pACT2_ Fis1
pAS2-1_ Dnm1l_Py
pACT2_ Fis1
pAS2-1_ Dnm1l_A401D
pACT2_ Fis1
pDEST32_ Krev1
pDEST22_ RalGDS
pDEST32_ Krev1
pDEST22_ RalGDSm1
pDEST32_ Krev1
pDEST22_ RalGDSm2
pAS2-1
pACT2

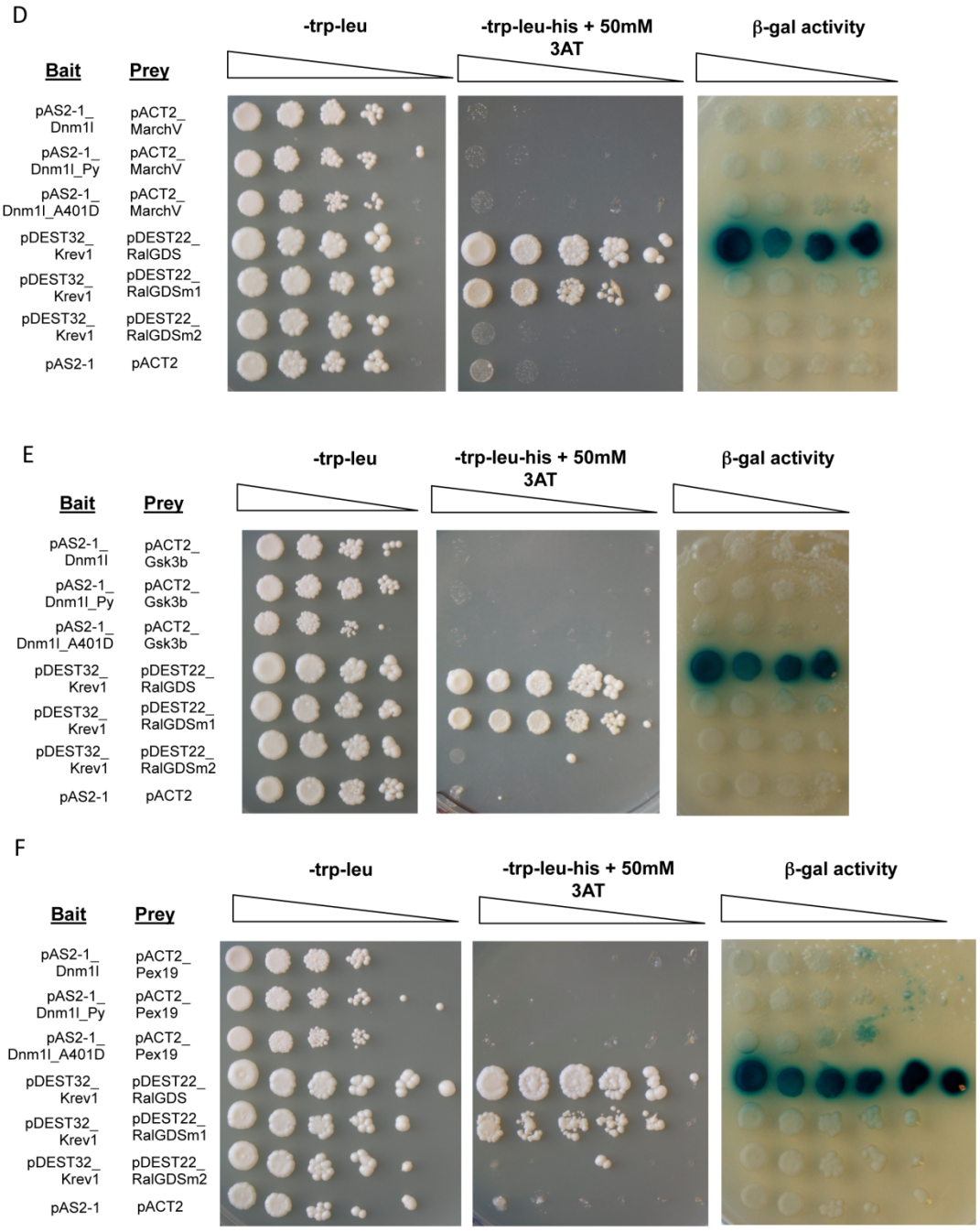

Figure 3.9. Dnm1l interactions with UBC9 and Mff are severely impaired by the introduction of Python or $A_{401}D$ mutations. Y2H interactions of DNM1L with UBC9 (A) or MFF (B) were severely impaired due to the introduction of either mutation. Other reported interactions were not detectable in this system (C-F). Controls for interactions were provided by the known strong interaction between Krev1 and RalGDS, the weak interaction between Krev1 and RalGDSm1, and no interaction between Krev1 and RalGDSm2. Yeast containing empty pAS2-1 and pACT2 vectors was also used as a negative control.

3.1.7 Decreased DNM1L^{Py} stability on the OMM

The translocation of DNM1L from the cytosol to the mitochondrial membrane is a required step in the process of mitochondrial fission (Smirnova *et al*., 1998). Overall cellular levels of DNM1L were reduced when DNM1L^{Py} is present, and an impaired interaction with UBC9 necessary for sumoylation and subsequent translocation to the OMM, had been detected. An interaction with the docking protein, MFF, was also impaired and so the ability of mutant DNM1L to translocate and remain on the OMM may be compromised.

Initially immunocytochemical visualisation of DNM1l in cultured mouse skin fibroblasts from Python and wild type littermates revealed no obvious differences (Fig. 3.10). However, this method would only detect large alterations in subcellular localisation as DNM1L is primarily localised diffuse in the cytoplasm with only a small amount (ca. 3%) associated with the mitochondrial membrane (Smirnova *et al*., 1998).

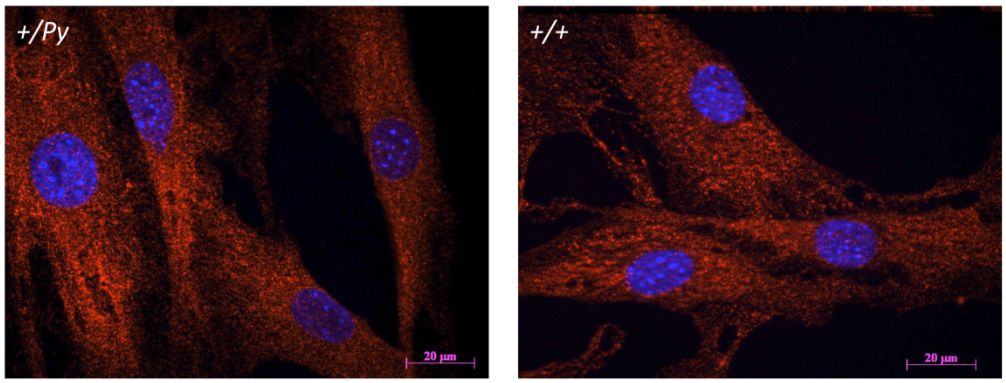

Figure 3.10. DNM1L localisation within the cell. Immunocytochemical staining of DNM1L in mouse skin fibroblasts using an anti-Drp1 antibody was performed to investigate DNM1L localisation as a result of the Python mutation. The resulting diffuse cytoplasmic distribution of DNM1L in *+/Py* and +/+ cultured mouse skin fibroblasts was not a sensitive method to investigate such small changes in DNM1L localisation. Nuclei are stained blue with Hoechst 33258 while antibody bound to DNM1L fluoresces red. Scale bars represent 20µm.

In order to detect a more subtle change in localisation, mitochondria were prepared from 3-month-old Python and wild type hearts and brains, and the DNM1L levels examined by Western blotting of the mitochondrial protein extracts. If there was a change in the amount of DNM1L associated with the mitochondrial membranes, this might be reflected in a change in the amount of protein detected. TIM23 was used to normalise for the general levels of mitochondrial proteins as it had previously been shown mitochondrial volume per cell is not altered (Ashrafian *et al*., 2010). A reduction of over 50% of DNM1L protein is detected on the mitochondria of Python mouse hearts (Fig. 3.11A) and brains (Fig. 3.11B) with respect to wild type controls. This may signify the amount of DNM1L^{Py} reaching the OMM is significantly reduced.

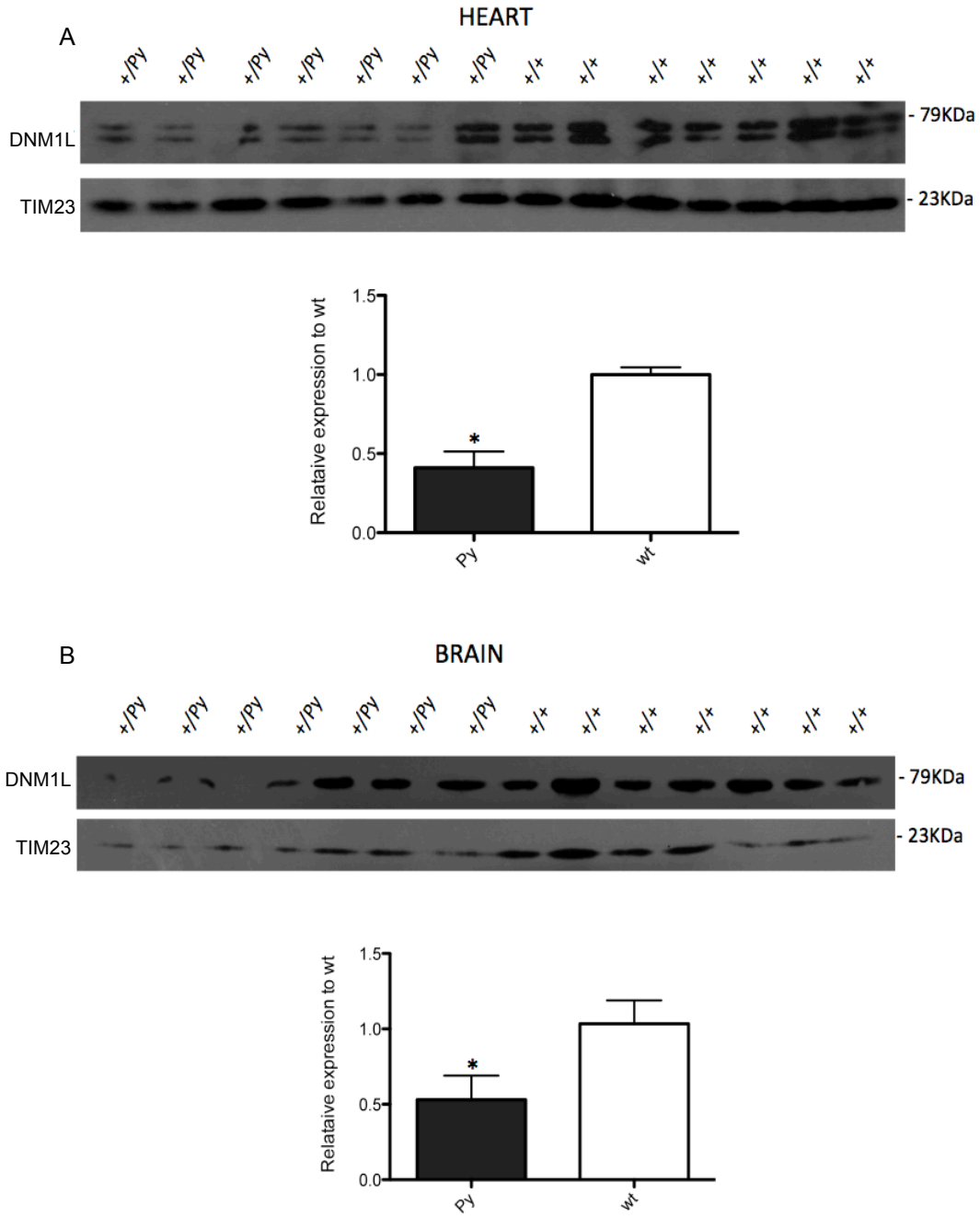

Figure 3.11. A decrease in the level of DNM1L associated with mitochondria of Python mice. Proteins were isolated from the hearts and brains of seven 3-month-old Python and seven 3-month-old wild type female mice on the C57BL/6J background. DNM1L protein levels were detected in the heart (A) and brain (B) by Western blot analysis, which revealed severely reduced levels in Python tissues. Densitometry analyses indicate a reduction of over 50% of mitochondrial protein levels in the heart (Student's t test, *P*=0.002), though a smaller reduction in the brain (Student's t test, *P*=0.0436).

3.2 Discussion

The Python mutation may impair DNM1L activity through one or more of the following mechanisms: altering the physical structure of the monomer; its ability to form dimers, tetramers and high-order structures; its cellular localisation and ability to translocate to the mitochondrial membrane; and GTPase activity. Other mechanisms are also possible.

M domain mutations have been reported to impair intramolecular interactions between the M and the GED domains (Chang *et al*., 2010), an essential interaction in the process of higher-order oligomerisation (Zhu *et al*., 2004). It was therefore plausible that DNM1L^{Py} dysfunction lies in the inability of DNM1L^{Py} to form higher order structures as a result of defective intramolecular interactions. Y2H studies revealed that the Python mutation disrupts interactions between the N-terminus and the C-terminus, as observed in other M domain mutations that have physiological effects (Chang *et al*., 2010). Full-length DNM1L interactions were, in comparison, hardly affected. M domain self-interactions have also been reported, and these interactions are abrogated by certain M domain mutations (Chang *et al*., 2010). Contrary to this, no self-interaction of the M domain was detected in this study. A possible explanation for this is the difference in sensitivity between the Y2H systems used. Chang *et al*. (2010) used the LexA system, compared to the GAL4 system used in this study.

Dr. Narcis Fernandez-Fuentes generated a potential structure for the DNM1L dimer based on homology modelling (Fig. 3.12 and (Ashrafian *et al*., 2010)). This model is supportive of the Y2H findings in that an interaction between the N-terminus and C-terminus/GED domains is not unexpected given the close proximity of α-helices over a significant length of the protein (Fig. 3.12). Also, the location of the Python $C_{452}F$ mutation is within a region that is adjacent to an α-helix from the C-terminus/GED region, so this cysteine could conceivably be involved in stabilizing an interaction between the helices. Thus, the proposed structure and Y2H data support a postulate that the structure of the monomer is altered by the $C_{452}F$ mutation.

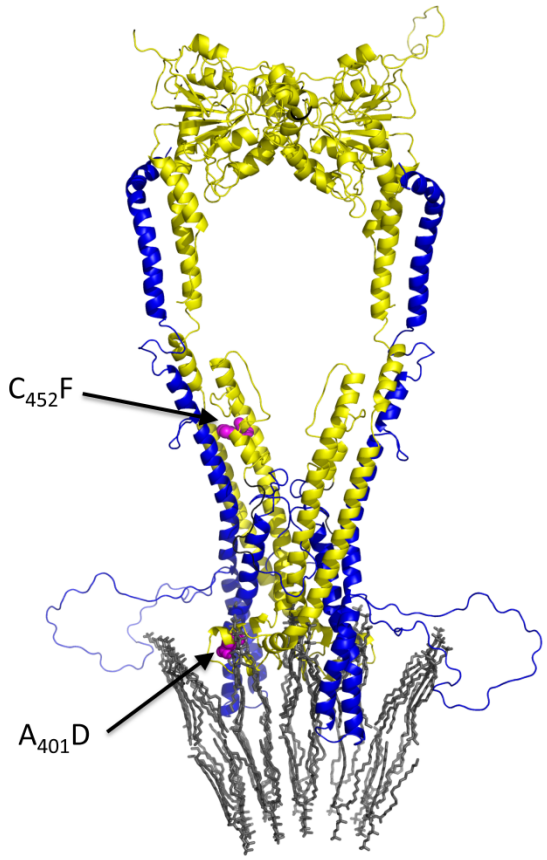

Figure 3.12. Ribbon representation of a homology model of the dimeric form of DNM1L protein in the extended conformation and embedded in a lipid membrane. Homology model highlighting the 1-495 amino acid region in yellow and 506-742 amino acid region in blue. Mutation sites are represented in pink. Generated by Dr. Narcis Fernandez-Fuentes (Ashrafian *et al*., 2010).

Another DNM1L mutation identified in a human patient ($A_{395}D$ in the human protein; the equivalent mouse mutation would be $A_{401}D$) displays a more severe clinical phenotype including the following symptoms: microcephaly, optic atrophy, abnormal brain development, hyperplasia and elevated lactic acid concentrations in the blood and cerebral spinal fluid **(**Waterham *et al*., 2007). This phenotype is in accordance with a global defect in mitochondria, compared to the Python mutation where the heart appears to be the major organ affected. A possible explanation for the differences in severity of the $C_{452}F$ and $A_{401}D$ mutations may lie in the specific location of each mutation within the protein and/or the difference in chemical nature between amino acid substitutions. When amino acid properties are compared, the A→D mutation appears a more divergent substitution than that of C→F. Hydrophobicity,

polarity, charge and bulk are slightly altered in C→F whereas A→D exhibits a more drastic change (Table 3.2).

The $A_{401}D$ mutation has been reported, like Python, to interfere with intramolecular interactions between the M domain and the GED and also showed a clear reduction in the levels of the mitochondrial membrane-bound form (Chang *et al*., 2010). In the homology model, the alanine lies within a region close to an α-helix with which it might interact, and may be involved in stabilizing lipid-binding interactions e.g. when binding to the OMM (Fig. 3.12). Thus, intermolecular and membrane interactions might both be altered to a greater severity by this human DNM1L mutation.

Table 3.2. Chemical properties of the amino acids involved in the $C_{452}F$ and $A_{401}D$ substitutions.

	Python $C_{452}F$		**$A_{401}D$**	
Amino acid substitution	Cysteine	Phenylalanine	Alanine	Aspartic acid
Hydrophobicity	Hydrophobic	Very hydrophobic	Hydrophobic	Hydrophillic
Polarity	Slightly polar	Non-polar	Non-polar	Polar
Charge	Neutral	Neutral	Neutral	Negative (acidic)
Molecular weight (Da)	121	165	89	133

The $A_{401}D$ mutation was idenitified in a human patient whereas the Python mutation was identified in a mouse mutant. It cannot be excluded that the different phenotypes also reflect a potentially different role for the two proteins in human and mouse, though the very high conservation of the protein across species (98% conservation between human and mouse) (Ashrafian *et al*., 2010) suggests this is unlikely. However, it will be necessary in the future to recapitulate the $A_{401}D$ mutation in mice through gene targeting in ES cells to observe whether or not the phenotype mimics the human condition.

DNM1L protein levels in the hearts and brains of Python mice were reduced. It is possible that the reduced protein levels reflect that the Python DNM1L protein is not produced at all. However this is unlikely given that *Dnm1l*$^{+/-}$ mice show no defects, despite only 50% of the Dnm1l protein being present (Ishihara *et al*., 2009, Wakabayashi *et al*., 2009). It raises the

possibility that the Python protein is acting in a dominant negative fashion impairing the function of the wild type protein. As the antibody used for detection does not distinguish between wild type and Python DNM1L proteins, the surrogate marker of the mRNA levels was determined to ascertain if the DNM1L^{Py} protein was likely to be expressed. Pyrosequencing analysis was carried out in collaboration with Dr. Phil Chambers, University of Leeds. In both Python hearts and brains, the Python allele and wild type allele were expressed equally at the mRNA level. It is therefore likely that wild type and Python proteins would be equally expressed in Python heterozygotes. Assuming the dimer is the basic structural unit for higher order oligomerisation (Zhang and Hinshaw, 2001) only 1 in 4 dimers in a cell heterozygous for the Python mutation would be normal as from the data, it is reasonable to conclude that DNM1L^{Py} is able to dimerise with both mutant and wild type DNM1L. Python homodimers may be targeted for degradation as a result of protein misfolding (accounting for the reduced protein levels seen in Python tissues), while wild type:Python heterodimers would be structurally altered and this could alter any combination of GTPase activity, translocation to the OMM, or oligomerisation into higher-order structures. GTPase activity was subsequently shown to be severely reduced in the Python homodimer, exhibiting just 25% activity relative to the wild type homodimer. The wild type:Python heterodimer displayed a GTPase activity less than that of the same amount of the wild type protein alone suggesting that the Python monomer is acting in a dominant negative fashion, and impairing the ability of the dimer to hydrolyse GTP.

DNM1L post-translational modifications have been shown to induce translocation of DNM1L to the OMM. One such modification is that of sumoylation; a process in which an interaction with the E2 ubiquitin ligase (UBC9) is crucial (Okuma *et al*., 1999). Through Y2H assays, Python and the $A_{401}D$ mutant proteins were shown to completely abrogate this interaction. This could compromise translocation of the mutant proteins from the cytosol to the OMM. Interactions with MFF, a docking protein for DNM1L on the OMM (Otera *et al*., 2010) were also found to be severely affected implying that even if Python and $A_{401}D$ mutants could translocate to the OMM, the protein may not have the ability to remain stable on the mitochondrial membrane, a necessity

of mitochondrial fission (Zhang and Hinshaw, 2001). Other DNM1L:protein interactions reported in the literature that were assessed in this study did not reveal an interaction. This could be due to the differences in techniques or systems used. For example, an interaction with FIS1 was identified by co-immunoprecipitation (Yoon *et al*., 2003), a method that allows proteins in interaction complexes to be identified. DNM1L interacts with MFF, which may form a complex with FIS1. Therefore DNM1L would be immunoprecipitated with FIS1, but no direct interaction would necessarily take place, nor be detectable by Y2H, between the two proteins.

The $A_{401}D$ mutation has been reported to decrease the level of DNM1L associated with the OMM (Chang *et al*., 2010). Immunocytochemistry of DNM1L distribution did not reveal any obvious difference in DNM1L localisation between Python and wild type cells. However, given that at any one time only a fraction (3%) of DNM1L is localised to the mitochondria (Smirnova *et al*., 2001), a more sensitive method was required to detect a more subtle change. Examination of DNM1L levels in purified mitochondria suggested a possible reduction in mitochondrial membrane-bound DNM1L in Python cells. The decreased levels associated with the membrane might reflect a failure in ability to translocate from the cytosol, or an instability of the DNM1L complex once on the mitochondrial membrane. This in turn could alter the cellular functions that rely on this.

Chapter 4 : DNM1L^{Py} and organelle morphology

4.1 Results

4.1.1 The Python mutation alters mitochondrial, peroxisomal and ER morphology

The main function known for DNM1L is a role in mitochondrial (Chen and Chan, 2005, Frank *et al*., 2001) and peroxisomal fission (Koch *et al*., 2003), while a single report suggests a role in maintenance of ER morphology (Pitts *et al*., 1999). To identify if the Python mutation impairs DNM1L function in relation to these roles, mitochondria, peroxisomes and ER were examined in Python and wild type cell lines. An impairment of fission would be reflected in elongated mitochondria and peroxisomes.

Initially, mitochondrial morphology was investigated by means of fluorescent imaging in mouse skin fibroblasts (Fig. 4.1A), embryonic stem (ES) cells (Fig. 4.1B) and cardiomyocyte-induced ES cells (Fig. 4.1C). Mitochondrial elongation was evident in all 3 Python cell lines examined, reflecting an impaired function for DNM1L^{Py}. The pathogenic effect of Python appeared to be evident in the heart more than in other tissues given the congestive heart failure (CHF) phenotype so it was necessary to investigate the impact of Python on mitochondrial morphology in intact cardiomyocytes. Due to the nature of mitochondrial rearrangement in adult cardiomyoyctes into a highly organised linear network packed tightly in the cell between the sarcomeres, detecting alterations in morphology would be difficult. Nonetheless, it was still an important question that required answering. Adult cardiomyocytes were cultured from 12-week-old Python and wild type control male mice on the C57BL/6J background. The linear, highly organised arrangement of mitochondria appeared similar in Python and wild type mitochondria (Fig. 4.2).

Peroxisomes in cultured mouse skin fibroblasts were visualised using fluorescent immunocytochemistry and Python fibroblasts had an elongated morphology (Fig. 4.3A), further demonstrating a functional effect of the Python mutation on DNM1L function. ER morphology may also be abnormal in the Python cells. In wild type cells, the ER had a regular web-like pattern. In

contrast, Python cells showed a slightly broken and collapsed ER network (Fig. 4.3B).

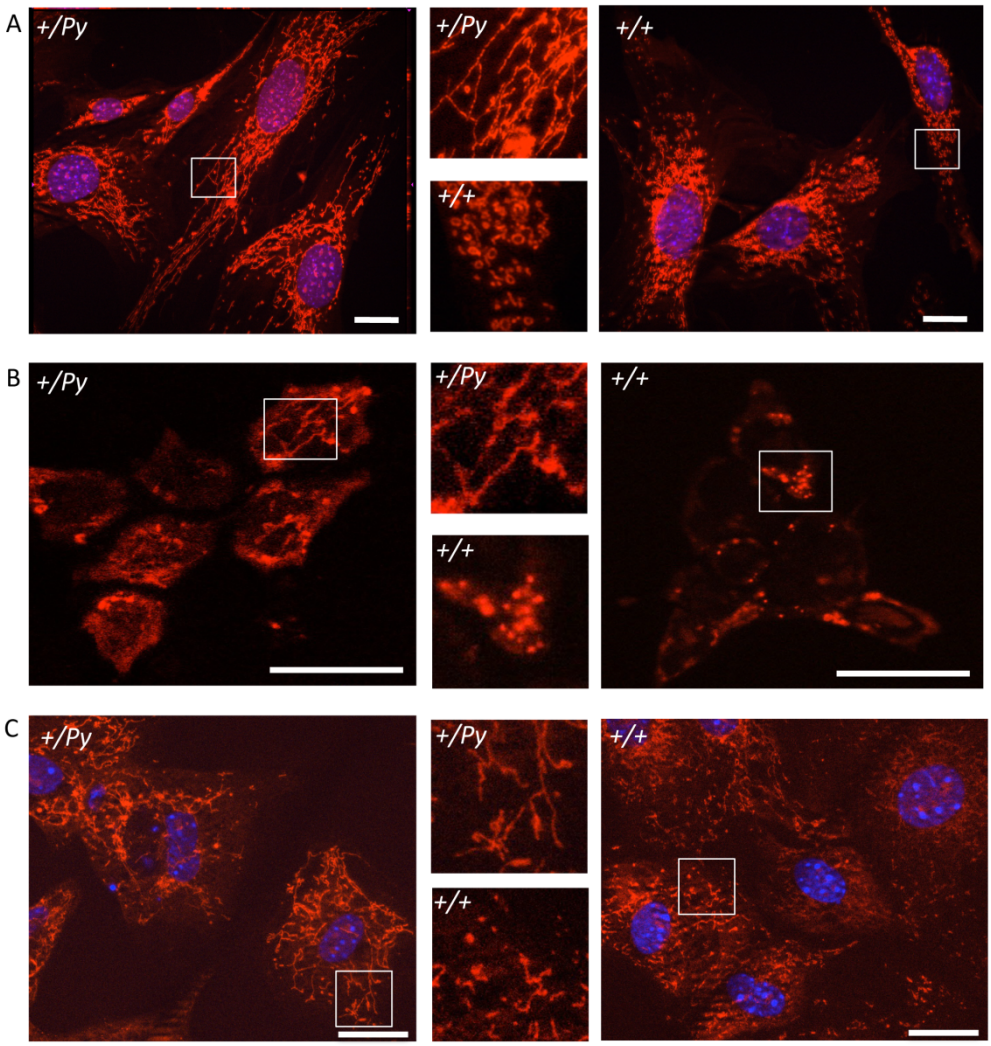

Figure 4.1. **Mitochondrial elongation in cultured Python cell lines**. A comparison of mitochondria, stained with MitoTracker™ Orange, between Python and wild type cell lines: A) mouse skin fibroblasts, B) ES cells and C) cardiomyocyte-induced ES cells. Mitochondrial elongation is evident in all Python cell lines compared to wild type controls. Regions enclosed with white squares are shown magnified in the centre. Nuclei are stained with Hoechst 33258 in A) and C). Scale bars represent 20μm.

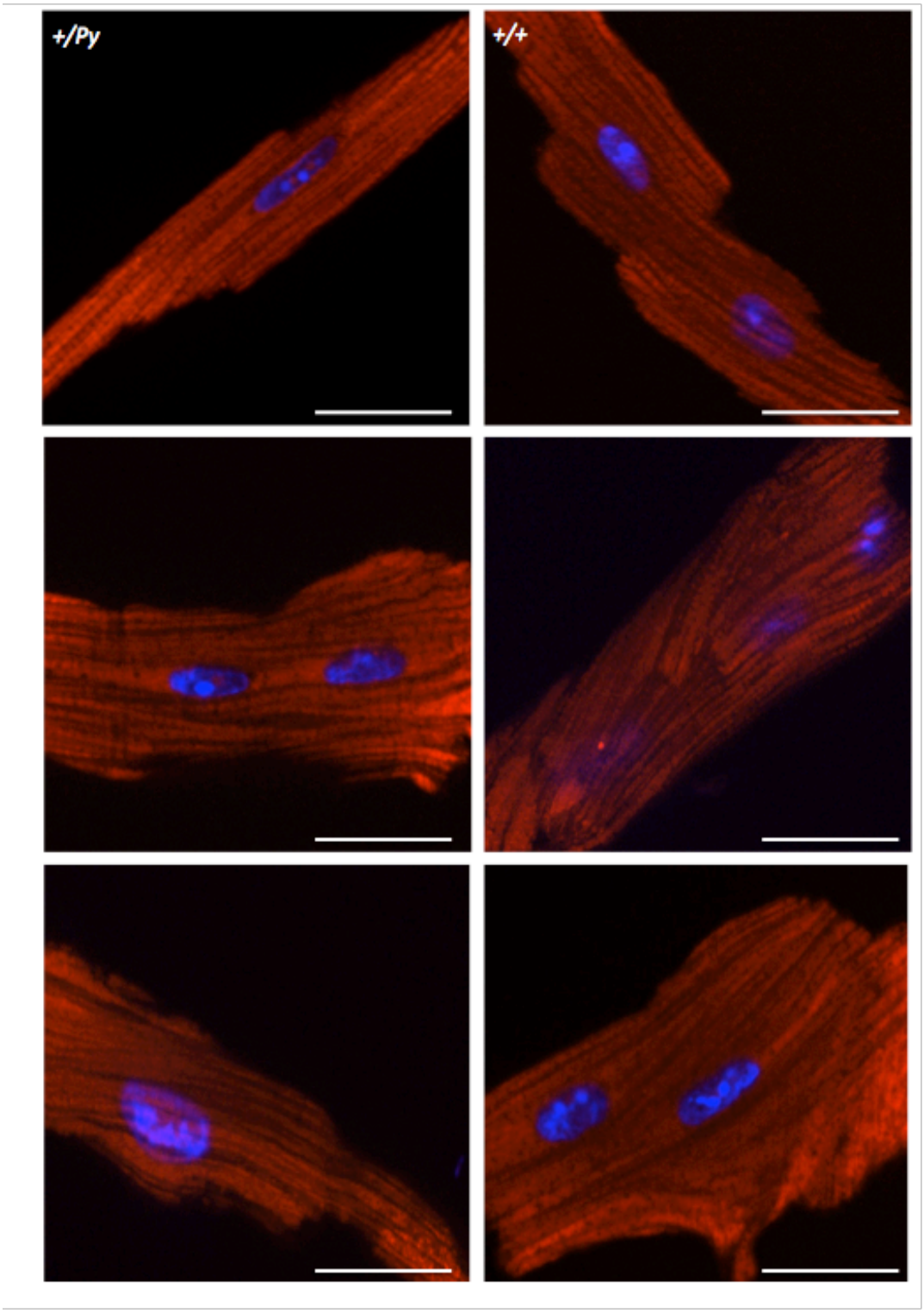

Figure 4.2. Mitochondrial morphology in adult cardiomyocytes. Cardiomyocytes were cultured from 12-week-old Python and wild type males on the C57BL/6J background. Mitochondria are stained with MitoTracker™ Orange. No difference in morphology can be deduced from these images. Nuclei are stained with Hoechst 33258. Scale bars represent 20μm.

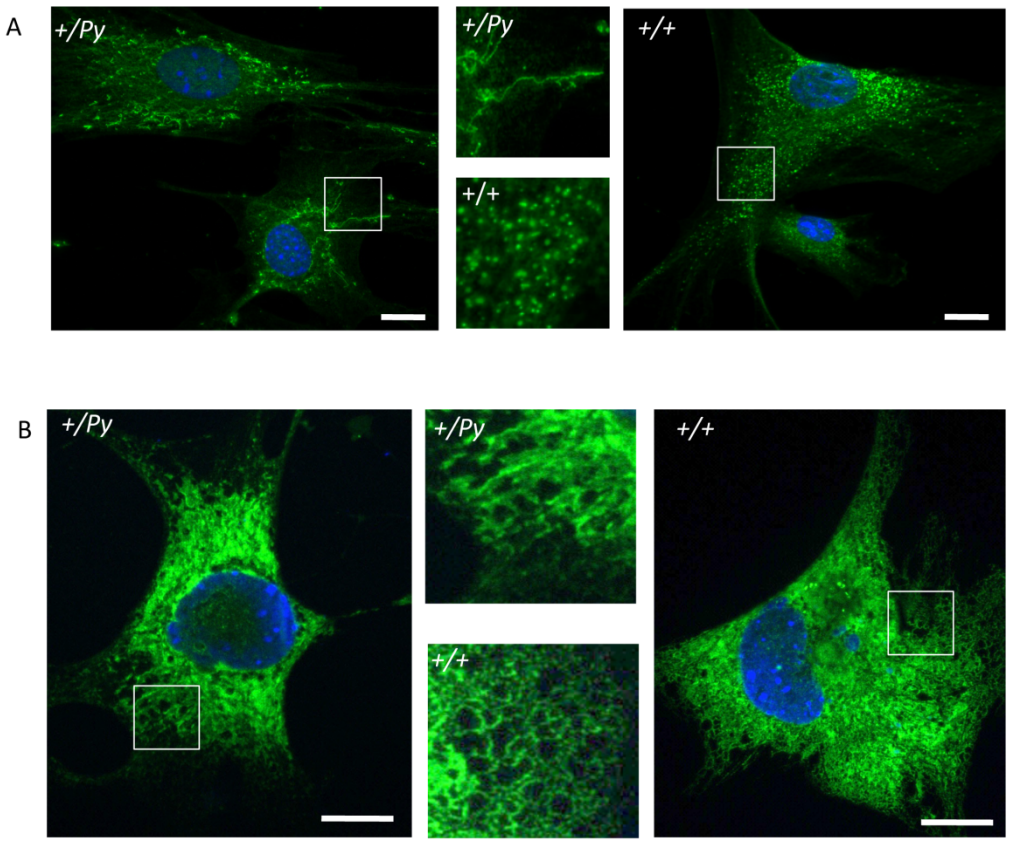

Figure 4.3. Altered peroxisome and ER morphology in cultured Python cells. (A) Peroxisomes visualised by ICC with an anti-catalase antibody and a FITC-labelled secondary IgG antibody in mouse skin fibroblasts, showing an elongated peroxisome phenotype in Python cells. (B) ER structures visualised using the organelle lights ER-GFP assay kit in mouse skin fibroblasts. The ER network in Python cells may show abnormal morphology and a collapsing network. Regions enclosed by the white squares are shown magnified in the centre. Nuclei are stained with Hoechst 33258. Scale bars represent 20μm.

To ascertain if the mitochondrial elongation was due to a dominant effect of the Python mutation, HeLa cells were transfected with constructs expressing wild type or mutant forms of DNM1L and, additionally, GFP (internally via an IRES) from a CMV promoter (Appendix VII). Three expression constructs were transfected into HeLa cells, encoding wild type DNM1L, DNM1L^{Py} and as a positive control, the dominant negative mutant DNM1L^{K38A}. The latter abrogates GTPase activity and consequently mitochondrial fission (Frank *et al*., 2001). An untransfected control was also included (Fig. 4.4A). The expression of GFP acted as a marker for cells that had taken up DNA. Expression of wild type DNM1L revealed no alteration in mitochondrial morphology (Fig. 4.4B), while DNM1L^{Py} expression resulted in elongated mitochondria, similar to the morphology observed in Python fibroblasts (Fig. 4.4C). Expression of DNM1L^{K38A} resulted in an even greater severity of elongated mitochondria (Fig. 4.4D). The result confirms the elongated mitochondrial phenotype observed is due to the Python mutation acting in a dominant fashion, and most likely alters the mitochondrial fission capacity of the cells.

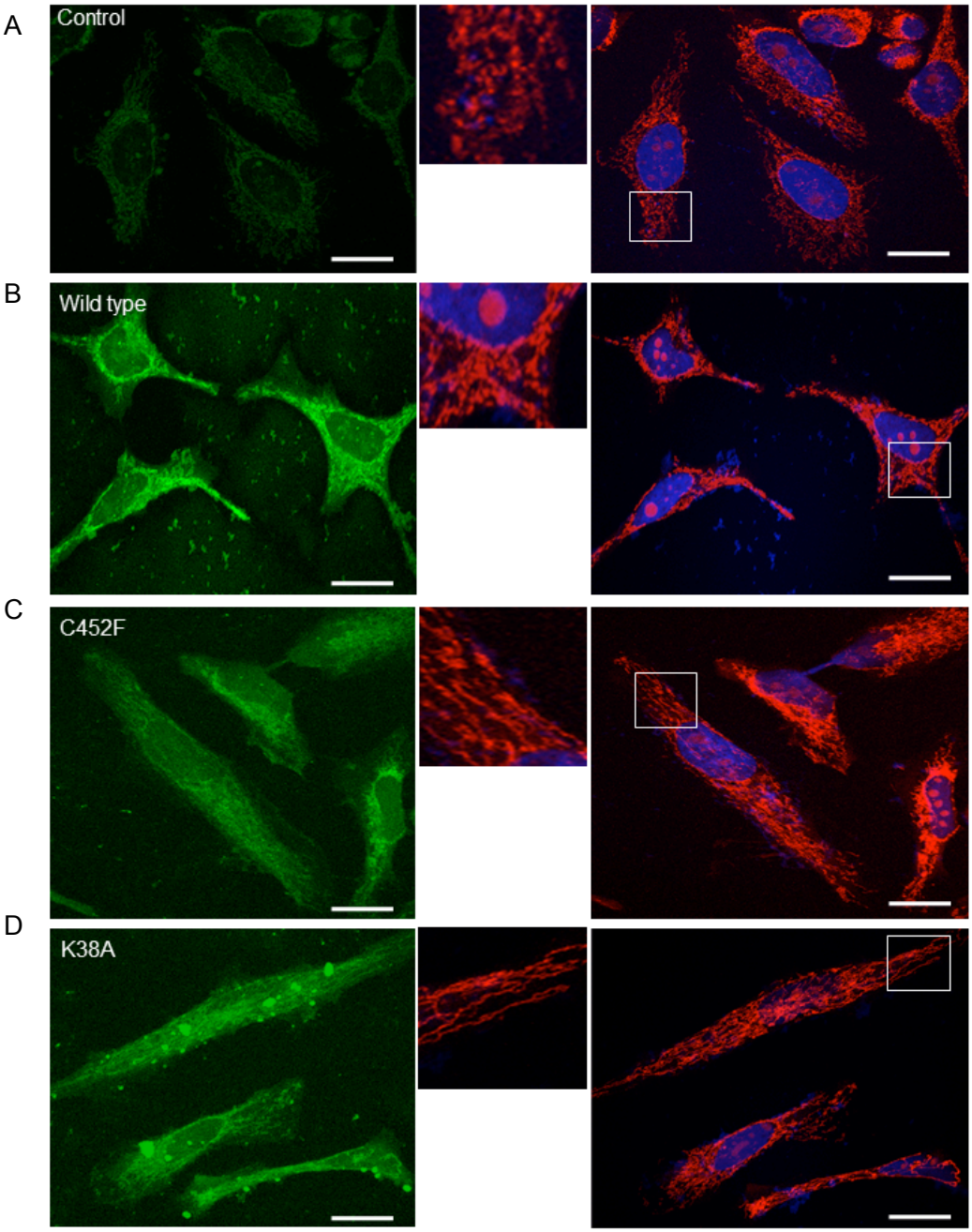

Figure 4.4. Transfection of HeLa cells with DNM1L expression constructs. HeLa cells were transfected with constructs containing (B) wild type *Dnm1l*, (C) *Dnm1l* with the Python mutation and (D) *Dnm1l with* the $K_{38}A$ mutation. An untransfected control was included (A). Mitochondria were stained with MitoTracker™ Orange and nuclei were stained with Hoechst 33258. Wild type expressing cells demonstrated no visible change compared to the control cells while cells expressing *Dnm1l*^{Py} and *Dnm1l*^{K38A} displayed a far more elongated mitochondrial network. Regions enclosed by the white squares are shown magnified. Scale bars represent 20μm.

4.1.2 Highly abnormal mitochondria in fibroblasts homozygous for the Python mutation

Homozygosity for the Python mutation is embryonic lethal at approximately E9.5 (Ashrafian *et al*., 2010). Fibroblasts were cultured from E9.5 embryos, with yolk sacs being used to ascertain the genotype of the embryos. Few homozygous fibroblasts survived from the Python homozygous embryos suggesting there is a cell viability issue associated with homozygosity for the Python mutation. In the few homozygous cells obtained, the nuclei were highly pyknotic and mitochondria were aggregated around the nucleus, whereas wild type and heterozygous fibroblasts displayed an even distribution of mitochondria within the cell (Fig. 4.5). This mitochondrial phenotype may primarily reflect the fact that the cells are dying in culture rather than a change in mitochondrial phenotype *per se*.

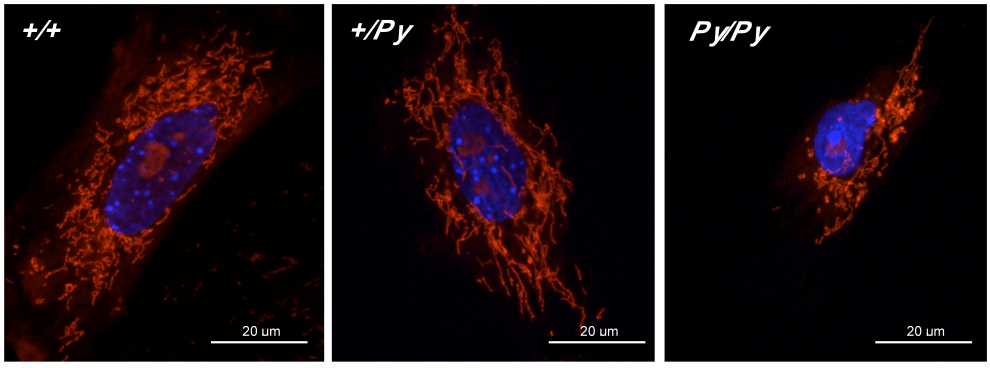

Figure 4.5. Mitochondrial perinuclear aggregation in *Py/Py* fibroblasts. A Comparison of mitochondria in cultured fibroblasts from 9.5-day-old *+/+, +/Py* and *Py/Py* embryos. Mitochondria have been stained with MitoTracker™ Orange and nuclei stained with Hoechst 33258.

4.2 Discussion

As mitochondrial fission is the principle known function of DNM1L (Frank *et al*., 2001), a defect in this protein is likely to alter the proteins capacity to perform this function. The mitochondria were therefore visualised in all cell models available: fibroblasts, ES cells, induced cardiomyocytes and isolated adult cardiomyocytes. Mitochondrial elongation was evident in Python cell lines, implying reduced DNM1L activity. Due to the highly organised arrangement of mitochondria in adult cardiomyocytes, no difference in mitochondrial morphology was detectable, however it cannot be ruled out the likely possibility that mitochondrial morphology is also altered in cardiomyocytes of Python heterozygotes. Transfecting expression vectors containing wild type and Python DNM1L cDNA into HeLa cells confirmed that an elongated mitochondrial phenotype could be caused by the Python mutation. The dominant-negative mutant, *Dnm1l*^{K38A} was also expressed in HeLa cells as a positive control, as this had previously been reported to disrupt GTPase activity and, consequently, mitochondrial fission (Frank *et al*., 2001). In agreement with the literature, this mutant also led to an extended mitochondrial phenotype, more so than those in Python cells. This may be due to the position of the $K_{38}A$ mutation in the GTPase domain, possibly leading to a more severe reduction in GTPase activity and hence, fission. A second function of DNM1L is that of peroxisomal fission (Koch *et al*., 2003) and in accordance with this Python also impairs the ability of DNM1L to divide peroxisomes. DNM1L is also required for mouse embryonic development as demonstrated by the inability of *Dnm1l*$^{-/-}$ embryos to survive to term (Ishihara *et al*., 2009, Wakabayashi *et al*., 2009). Homozygosity for the Python mutation also results in embryonic lethality and mitochondria of the few surviving isolated MEFs from *Py/Py* embryos display a high degree of aggregation around the nucleus. The nuclei themselves were highly pyknotic, possibly representative of dying cells (Ashrafian *et al*., 2010).

The compromised ATP levels in the Python heart are perhaps related to an unknown function of DNM1L, and altered mitochondrial and peroxisomal morphology is an independent readout of the mutation, but not the one relevant to the observed phenotype. One way to investigate the importance of

mitochondrial dynamics in DCM could involve inhibiting fission in another way such as mutating FIS1 and observing the effects *in vivo*. One other aspect to consider is the degree of mitochondrial fission brought about by the Python mutation. Although currently there is no technique to quantify mitochondrial fission, it would be helpful to be able to measure the degree of inhibition of mitochondrial fission in order to deduce whether the degree of altered mitochondrial morphology reflects phenotype severity.

Chapter 5 : The effects of the Python mutation on other aspects of cellular physiology

5.1 Results

Mitochondria are involved in a number of cellular processes key to cell survival. Disruption to mitochondrial morphology may have serious complications if it contributes to such functions. A number of investigations were carried out in order to deduce the molecular pathway from which a disruption in DNM1L protein activity may lead to the compromised energetics that has been observed on the heart (Ashrafian *et al*., 2010). Experiments were performed to investigate the accumulation of mitochondrial DNA (mtDNA) mutations, mitophagy, mitochondrial-ER tethering, Ca^{2+} signalling between the ER and mitochondria and efficiency of oxidative phosphorylation (OXPHOS).

5.1.1 Mitophagy is not altered by DNM1L^{Py}

A possible purpose for mitochondria to continually undergo fusion and fission is that of restoring mitochondrial function. Defective mitochondria may fuse with functional mitochondria and share contents in order to rectify function. Fission may provide a means of segregating abnormal parts of the mitochondria, which are beyond repair, exposing them for mitophagy and the recycling of components (Twig *et al*., 2008, Mouli *et al*., 2009). A reduced ability of mitochondria in Python cells to divide may result in decreased mitophagy, possibly leading to an accumulation of mtDNA mutations. The mitochondrial genome codes for 12 of the 80 subunits that make up the electron transport chain (ETC) complexes and healthy mtDNA, which is critical for efficient OXPHOS. An accumulation of mtDNA mutations would be expected to reduce the efficiency of OXPHOS due to accumulating mutations in proteins that contribute to the function of the ETC, ultimately reducing ATP production.

It has been reported that mutations in the mitochondrial fusion proteins MFN1 and MFN2 result in an accumulation of mtDNA mutations (Chen *et al*., 2010) possibly as a result of the inability of the cell to fuse functional with abnormal mitochondria and repair the DNA. As an initial investigation into

whether DNM1L^{Py} may have a similar effect, primers flanking regions of the mitochondrial genome were used to amplify mtDNA from Python and wild type tissues. The primers chosen were known to flank regions of the genome in which deletions have been detected (Zhang *et al*., 2002). Two primers amplify a 4.6kb region of mtDNA, while two allow amplification of the entire C3H/HeN mtDNA genome (16.5kb) (Appendix VIII). These primers were tested in PCRs using mtDNA isolated from heart, brain and rectus femoris of 5-week-old and 10-week-old Python and littermate control mice on the C3H/HeN background. Deletions of between 0.5kb and 2kb in size were observed in these tissues for both primer sets (Fig. 5.1), though no specific deletions are evident or increased in Python samples. This particular methodology was relatively crude. It can only detect deletions from approximately 100bp up to 2kb in size and only those that are relatively abundant. Therefore, it cannot be ruled out that single nucleotide mutations, larger deletions, or rare mutations of any size in mtDNA do accumulate in Python tissues.

As an accumulation of mtDNA mutations could result from decreased mitophagy unable to remove sufficient dysfunctional mitochondria, another way to assess if this is the case is to visualise the degree of colocalisation between the autophagosome marker LC3 and mitochondria. During autophagic activation, the cytosolic protein, LC3-I is converted through cleavage into LC3-II, which becomes localised to the autophagosome. LC3 was visualised using an anti-LC3 antibody and FITC-labelled secondary antibody. LC3 was broadly diffused across the cytoplasm in both wild type and Python cells (Fig. 5.2). However the punctate foci observed in the wild type cells, that may represent the formation of the autophagosome (Wojtkowiak *et al*., 2012) were not visible in Python cells, possibly suggesting decreased autophagy as a result of the Python mutation. However as the level of colocalisation varied between cells within a genotype it was difficult to ascertain any difference between Python and wild type cells. As a way to overcome such variability, cells were scored for their percentage of colocalisation. This allowed a direct comparison between genotypes. The result in Figure 5.3 represents data taken from 12 Python and 12 wild type cells and shows no difference between the genotypes. Thus, there is no evidence that mitophagy is altered in Python cells.

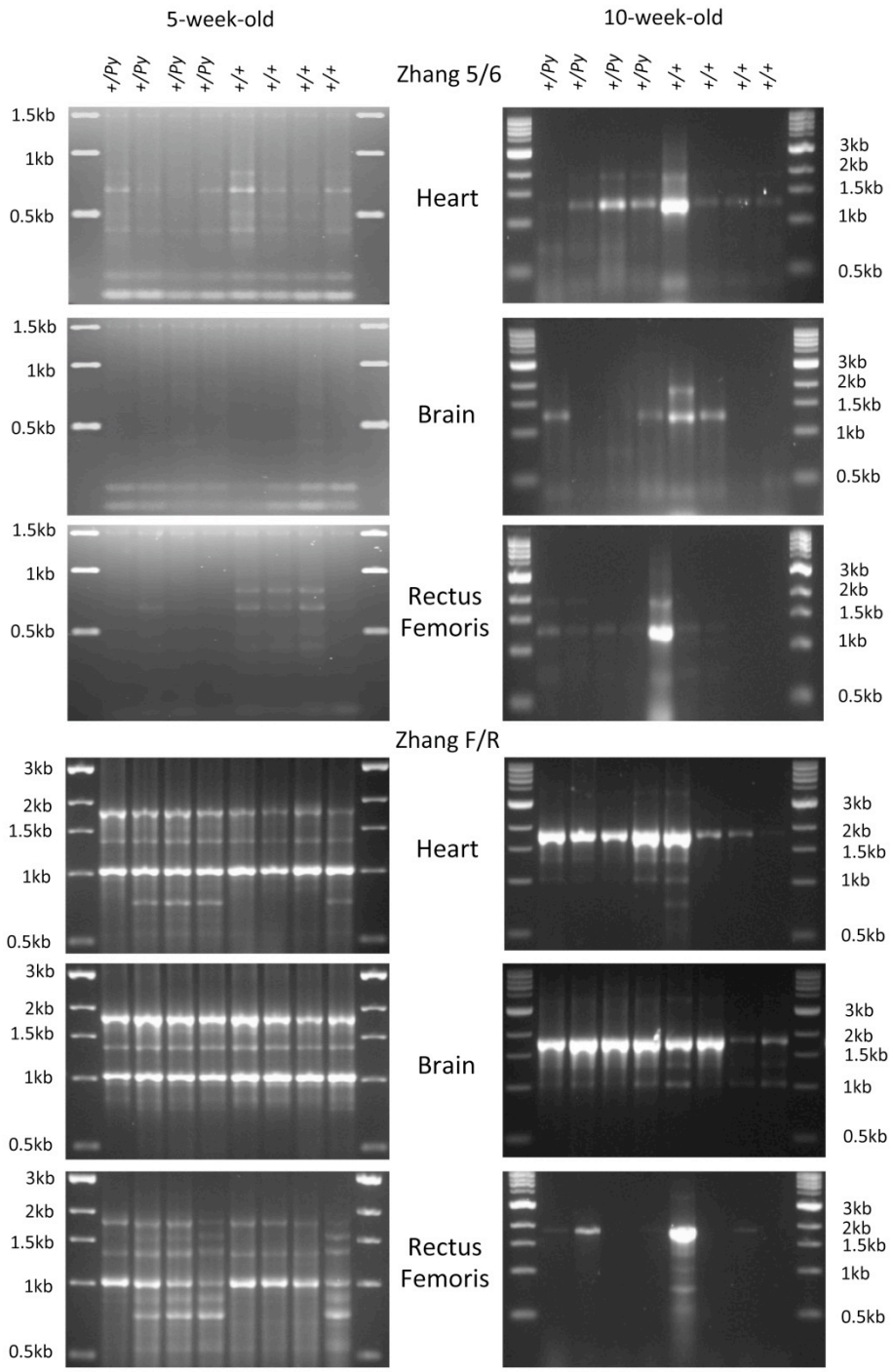

Figure 5.1. Analysis of mtDNA deletions. Primers Zhang 5 and Zhang 6 (Zhang *et al*., 2002) were used to amplify a 4.6kb region of the mouse mtDNA genome, while primers Zhang F and Zhang R were used to amplify the whole C3H/HeN mtDNA genome of 5-week-old and 10-week-old heart, brain and rectus femoris tissues from *+/Py* and *+/+* C3H/HeN mice. A number of mtDNA deletions resulting in PCR fragments from 0.5kb to 2kb occur. However none appear more prevalent or specific to either genotype.

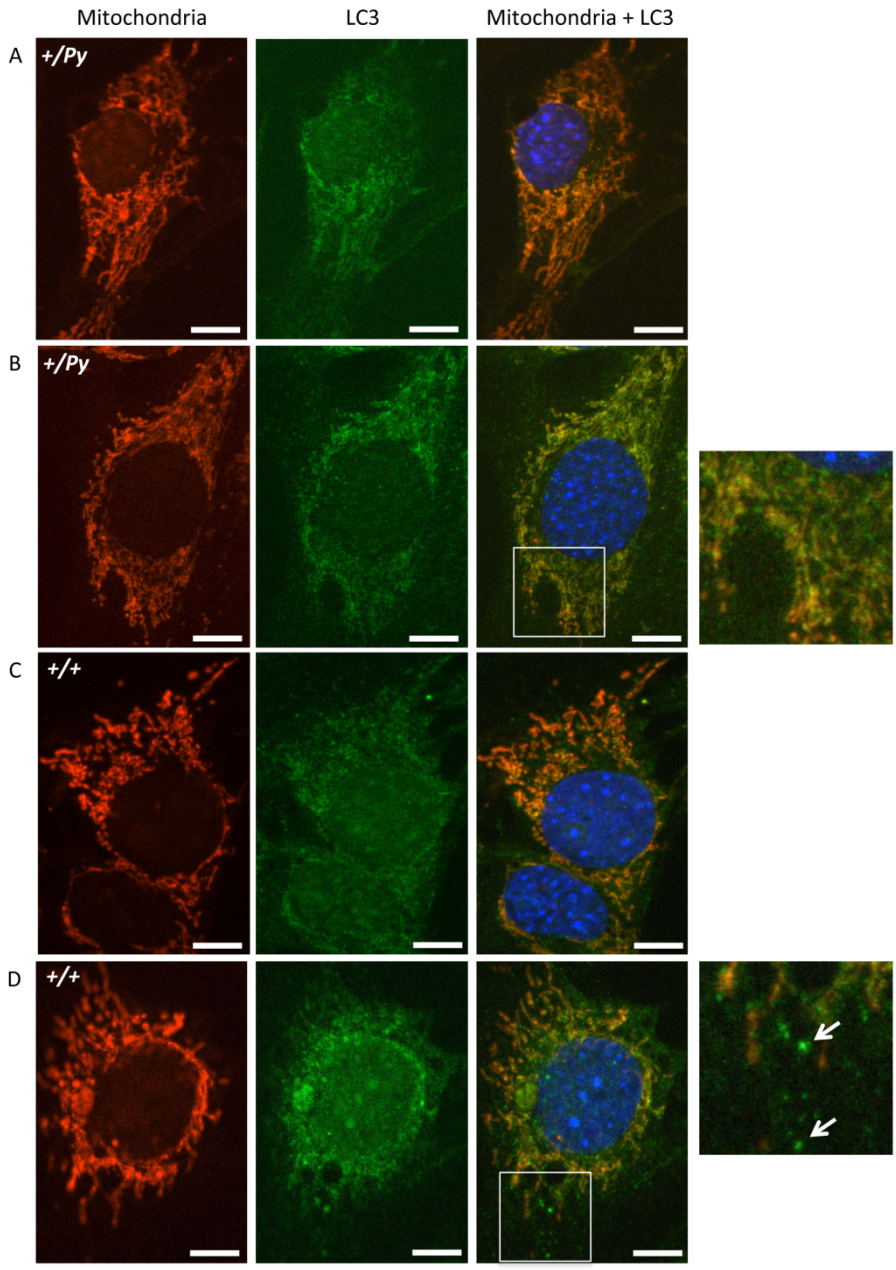

Figure 5.2. LC3-mitochondria colocalisation. Python and wild type fibroblasts were stained with an LC3 antibody and FITC-labelled secondary antibody to visualise LC3 and MitoTracker™ Orange for mitochondria. The level of colocalisation varied within a population of each genotype. Images of cells for high degree of colocalisation are shown in A) and C), whereas images for low colocalisation are shown in B) and D). Note the presence of punctate structures visible in LC3 staining in the wild type cells (examples shown by the white arrows), which are not present in the Python cells. These structures possibly resemble autophagosome formation. Regions enclosed by white squares are shown magnified. Nuclei were stained with Hoechst 33258. Scale bars represent 10μm.

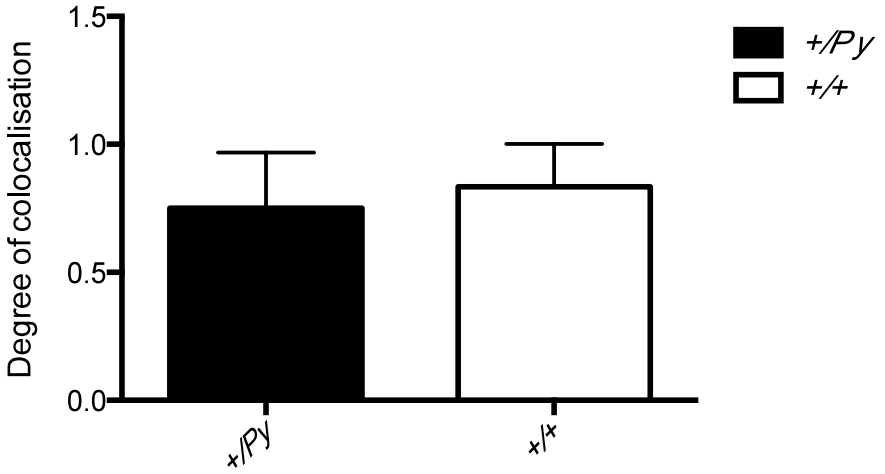

Figure 5.3. **Degree of mitochondria-LC3 colocalisation.** The degree of colocalisation within a given cell was scored on the following scale 0 = low level of colocalisation, 1 = medium level of colocalisation and 2 = high level of colocalisation. The result represents data from 12 cell images for *+/Py* and *+/+* genotypes each and showed no significant difference between them.

Although no difference was found in mtDNA deletions between Python and littermate controls, nor do levels of mitophagy appear to be reduced, it could still be a possibility that autophagy may be increased as a result of ATP depletion in Python hearts. Recent reports claim AMP activated protein kinase (AMPK) is activated by decreased ATP or increased AMP levels. This in turn triggers the formation of the autophagosome through activation of autophagy proteins and finally the cleavage of cytosolic LC3-I into the lipidated form, LC3-II on the autophagosome (Xie and Klionsky, 2007). Activation of AMPK by phosphorylation (P-AMPK) and the subsequent formation of the LC3-II isoform were tested by means of Western blotting proteins isolated from 5- and 13-week-old mouse hearts and brains of the C57BL/6J background. Figure 5.4 shows no evidence of altered levels of LC3-II.

A) 5-week-old Heart

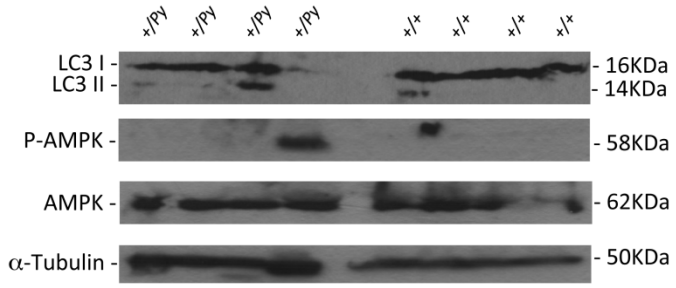

B) 5-week-old Brain

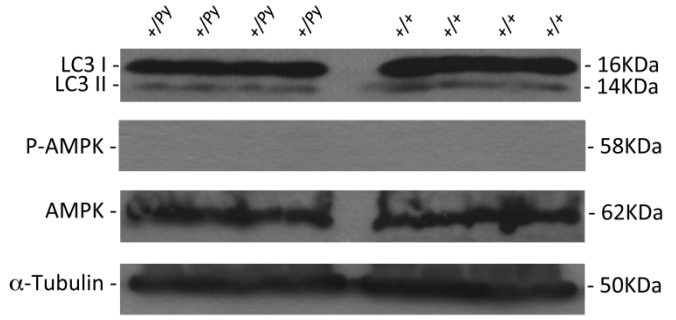

C) 13-week-old Heart

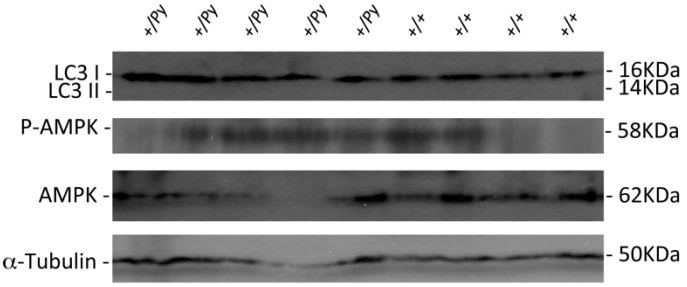

D) 13-week-old Brain

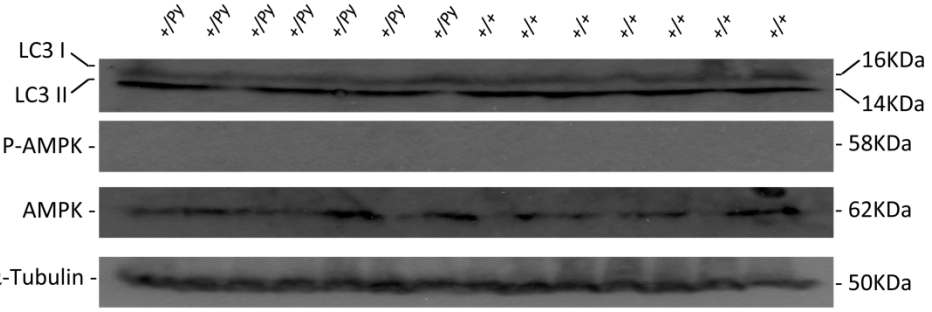

Figure 5.4. Python tissues do not demonstrate evidence of increased mitophagy. Proteins were isolated from the hearts (A & C) and brains (B & D) of Python and wild type C57BL/6J mice at the ages of 5-weeks (A & B) and 13-weeks (C & D). Antibodies to LC3 and P-AMPK were used to detect levels of autophagic activation, while AMPK levels were detected to measure all AMPK isoforms. Protein loading was normalised with α-Tubulin detection.

5.1.2 Reduced ER-Mitochondrial Tethering

Mitochondrial volume is not altered in Python cardiomyocytes and mitochondrial respiratory complex enzymes retain full activity *in vitro*. Yet, ATP depletion is drastic and evident as early as 5 weeks of age (Ashrafian *et al*., 2010). One possibility is that enzyme regulation is altered. Calcium (Ca^{2+}) is a crucial second messenger in cardiomyocytes, key to regulating cardiomyocyte excitation-contraction coupling and OXPHOS (Matsuoka *et al*., 2004). A number of components of the OXPHOS system are Ca^{2+} sensitive, for example dehydrogenases of the citric acid cycle (CAC) and the F_1/F_0 ATP synthase (Balaban, 2009, McCormack and Denton, 1980). The mitochondrial Ca^{2+} concentration is reduced in cardiomyocytes in heart failure (Jones *et al*., 1998, Knollmann *et al*., 2000) and abnormal DNM1L activity has been shown to affect mitochondrial Ca^{2+}. DNM1L overexpression, resulting in fragmentation of mitochondria, leads to reduced mitochondrial Ca^{2+} uptake after histamine-induced ER Ca^{2+} release and a reduction in the propagation of Ca^{2+} 'waves' along the mitochondria while mitochondrial Ca^{2+} overload itself induces mitochondrial fission (Szabadkai *et al*., 2004). Given that the mitochondrial fusion protein MFN2 influences mitochondrial Ca^{2+} uptake via physical tethering of ER, and that DNM1L is localised at sites of mitochondrial-ER tethering (Friedman *et al*., 2011) DNM1L might also perform a tethering function.

Therefore, mitochondrial-ER tethering was investigated. Mitochondrial protein extracts from Python and control hearts and brains were Western blotted and probed with an antibody against the ER integral membrane protein calnexin. If tethering was reduced in Python cells, it might be expected that less ER proteins would be co-purified with the mitochondria. A major reduction (~50%) in the amount of calnexin in Python heart (Fig. 5.5A) and brain (Fig. 5.5B) samples was evident, suggesting a possible decrease in the interaction between the two organelles. TIM23 was detected to normalise for mitochondrial number.

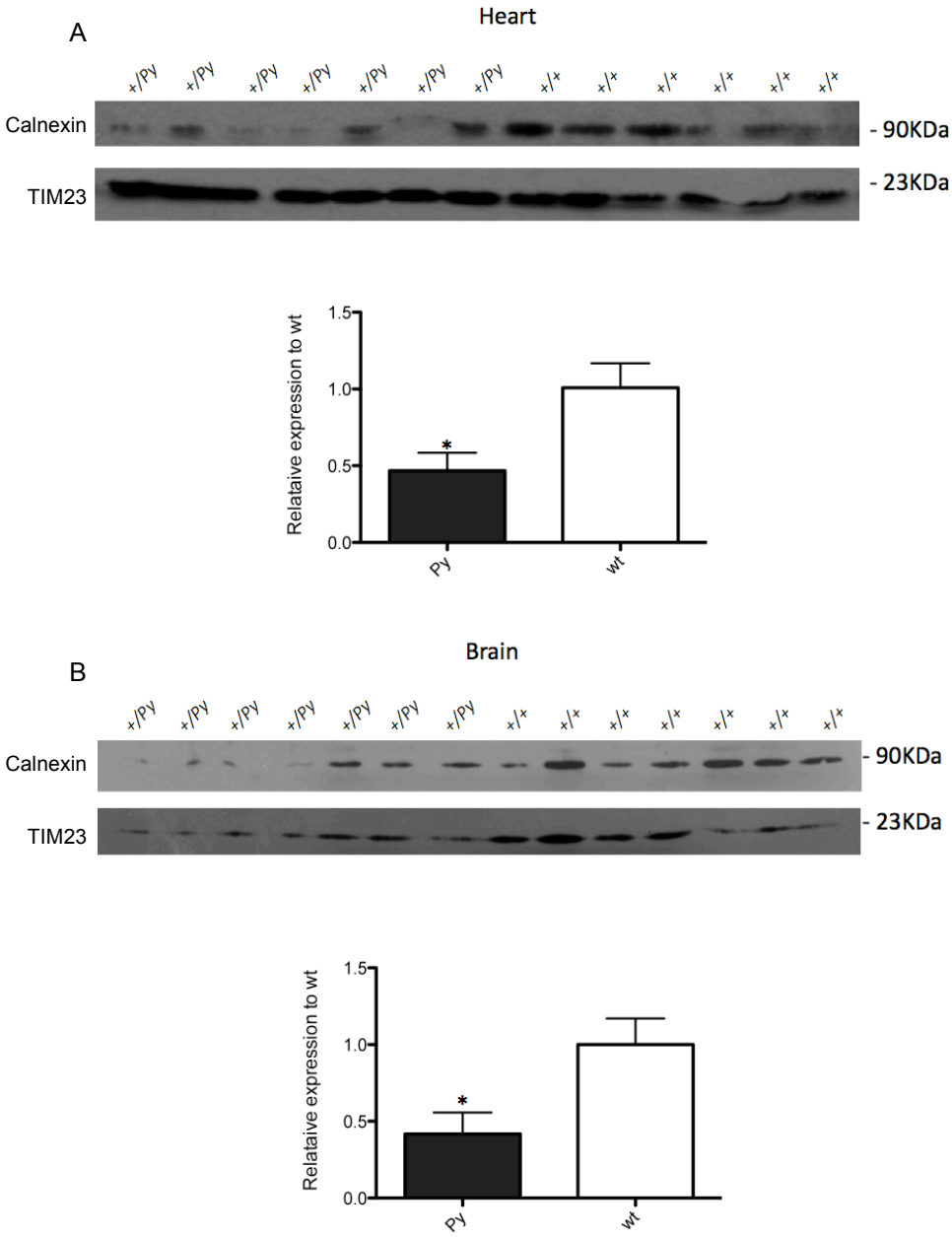

Figure 5.5. Reduced ER protein in mitochondrial preparations from Python tissues. Mitochondrial proteins were extracted from the hearts and brains of seven 3-month-old *+/Py* and seven +/+ female mice on the C57BL/6J background. Calnexin protein levels were detected in the heart (A) and brain (B) by Western blot analysis. As determined by densitometry analyses, over a 50% reduction in the amount of calnexin was present in the mitochondrial preparations from Python mouse hearts (Student's t-test, *P*=0.0176) and brain (Student's t-test, *P*=0.0211) indicating a possible reduction in the interaction between the ER and mitochondria. TIM23 level was used to normalise for mitochondrial protein loading.

Fluorescent imaging was then used to further investigate the effect of Python on tethering. By fluorescently labelling ER and mitochondria in green and red respectively, colocalisation can be visualised by the degree of overlap between the two colours, reflected by yellow labelling. In mouse skin fibroblasts, the ER was labelled using the Organelle Lights™ ER-GFP assay kit and mitochondria using MitoTracker™ Orange. As shown in Figure 5.6, the degree of yellow present in the Python cell is far less than that of wild type supporting the previous data of a decrease in tethering between the two organelles. When examining the image in more detail using the magnified regions, the ER structure appears to be collapsing in Python cells. Whether this is a possible reason for, or a result of, decreased tethering is unknown.

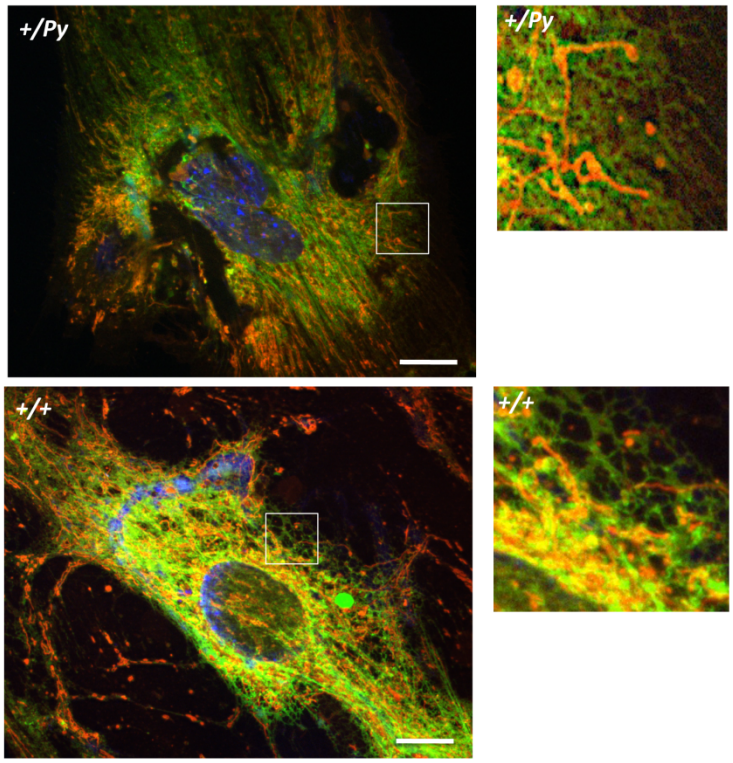

Figure 5.6. Reduced mitochondrial-ER colocalisation in skin fibroblasts. Example of typical labelling of cells. The ER was visualised using the Organelle Lights™ ER-GFP labelling reagent and mitochondria were labelled with MitoTracker™ Orange. Regions enclosed by the white squares are shown magnified. Reduced colocalisation of red and green signals (indicated by yellow) suggests reduced colocalisation between the ER and mitochondria in Python cells. Nuclei are stained with Hoechst 33258. Scale bars represent 20µm.

5.1.3 Calcium signalling is perturbed in Python cells

Mitochondrial-ER tethering allows the mitochondria to remain in close apposition to sites of Ca^{2+} release, facilitating efficient Ca^{2+} uptake by mitochondria. As a reduction in ER-mitochondrial tethering is possible in Python mice, subsequent mitochondrial Ca^{2+} uptake may be less efficient in the Python cells given the lack of juxtaposed sites between the two organelles. Ca^{2+} is a crucial messenger in OXPHOS and if the ability of mitochondria to take up Ca^{2+} is compromised, a drop in ATP production could result, which might be detrimental to the cell. In an initial experiment, the cytosolic Ca^{2+} levels were measured in ES cells using ratiometric measurement of Fura-2 fluorescence. Fura-2 fluoresces at 340nm. Upon Ca^{2+} binding, the fluorescence emission changes to a peak at 380nm. Thus the ratio of fluorescence at 380nm compared to 340nm reflects the amount of Ca^{2+}, which is bound to Fura-2, which is in turn a reflection of the amount of Ca^{2+} in the cytosol. The 340/380 ratio was used to determine the relative level of Ca^{2+} in the cell. ATP was used as an agonist to stimulate Ca^{2+}-release from the ER. As expected, the cytosolic Ca^{2+} concentration rapidly increased in both wild type and Python cells upon stimulation of Ca^{2+}-release from the ER. In wild type cells, the Ca^{2+} concentration quickly returned to the basal level, whereas the cytosolic Ca^{2+} in Python cells remained substantially higher (Fig. 5.7A). A similar result was seen when repeating the experiment in ES cells induced to differentiate to cardiomyocytes (Fig. 5.7B). Note a major difference between the result from ES cells and the induced cardiomyocytes regarding the peak cytosolic Ca^{2+} concentration after ER Ca^{2+} release. The Python induced cardiomyocytes exhibit a far higher peak than wild type cells while in ES cells, the peak cytosolic Ca^{2+} concentrations are similar between wild type and Python. The process of cardiomyocyte differentiation however, appears to be somewhat problematic for the Python ES cells and so data acquired from cardiomyocyte-induced ES cells cannot be interpreted as reliable (see Fig. 5.14). It also became clear that Python cells exhibited a higher baseline cytosolic Ca^{2+} concentration than wild type (Fig. 5.8A) in keeping with the inability of mitochondria to take up Ca^{2+} as efficiently. When intracellular stores are depleted of Ca^{2+}, capacitative Ca^{2+} entry (CCE) is activated triggering Ca^{2+}

influx from the extracellular space. The activity of the CCE was therefore scrutinized by Dr. John Boyle to examine if increased Ca^{2+} in the cytosol is a consequence of increased CCE, but no alteration in CCE activity was evident in Python cells (Fig. 5.8B).

Carbonyl cyanide p-(rifluoromethoxyl)-phenyl-hydrozon (FCCP) is a chemical uncoupler of the ETC and completely dissipates the proton gradient. Oligomycin inhibits OXPHOS by binding to ATP synthase, blocking the proton channel. It would be expected that upon exposure to mitochondrial-deactivating conditions of FCCP + oligomycin, the cytosolic Ca^{2+} concentration would increase as a result of decreased mitochondrial Ca^{2+} uptake. However, if Ca^{2+} uptake was already compromised, the cytosolic Ca^{2+} level may not be expected to increase as much after the mitochondria are inactivated. When the cells were exposed to FCCP and oligomycin to shut down the activity of mitochondria, the Python cells demonstrated a much smaller increase in cytosolic Ca^{2+} concentration compared to wild type cells (Fig. 5.8C). This further supports there being defective mitochondrial Ca^{2+} uptake in Python cells. Compromised mitochondrial Ca^{2+} uptake as a result of the Python mutation would be supported by a lower basal mitochondrial Ca^{2+} concentration, as the mitochondria would be unable to uptake sufficient Ca^{2+} to maintain normal levels. Upon Ca^{2+} release from the ER, the mitochondria in Python cells would be expected to uptake less Ca^{2+} than that of mitochondria in wild type cells, reflected by a smaller increase in the concentration of mitochondrial Ca^{2+}. Measurement of mitochondrial Ca^{2+} concentration was investigated in immortalized embryonic fibroblasts using a mitochondria-targeted aequorin (Appendix XI). Upon Ca^{2+}-binding the prosthetic group of aequorin, coelenterazine – added to the external medium - is converted into light emitting coelenteramide. The amount of light emitted is in proportion to the Ca^{2+} concentration. After agonist-induced ER Ca^{2+}-release, wild type mitochondria are able to take up approximately double the amount of Ca^{2+} compared to mitochondria of Python cells (Fig. 5.7C). This provides further evidence to support the hypothesis of a reduced efficiency of mitochondrial Ca^{2+} uptake as a result of the Python mutation.

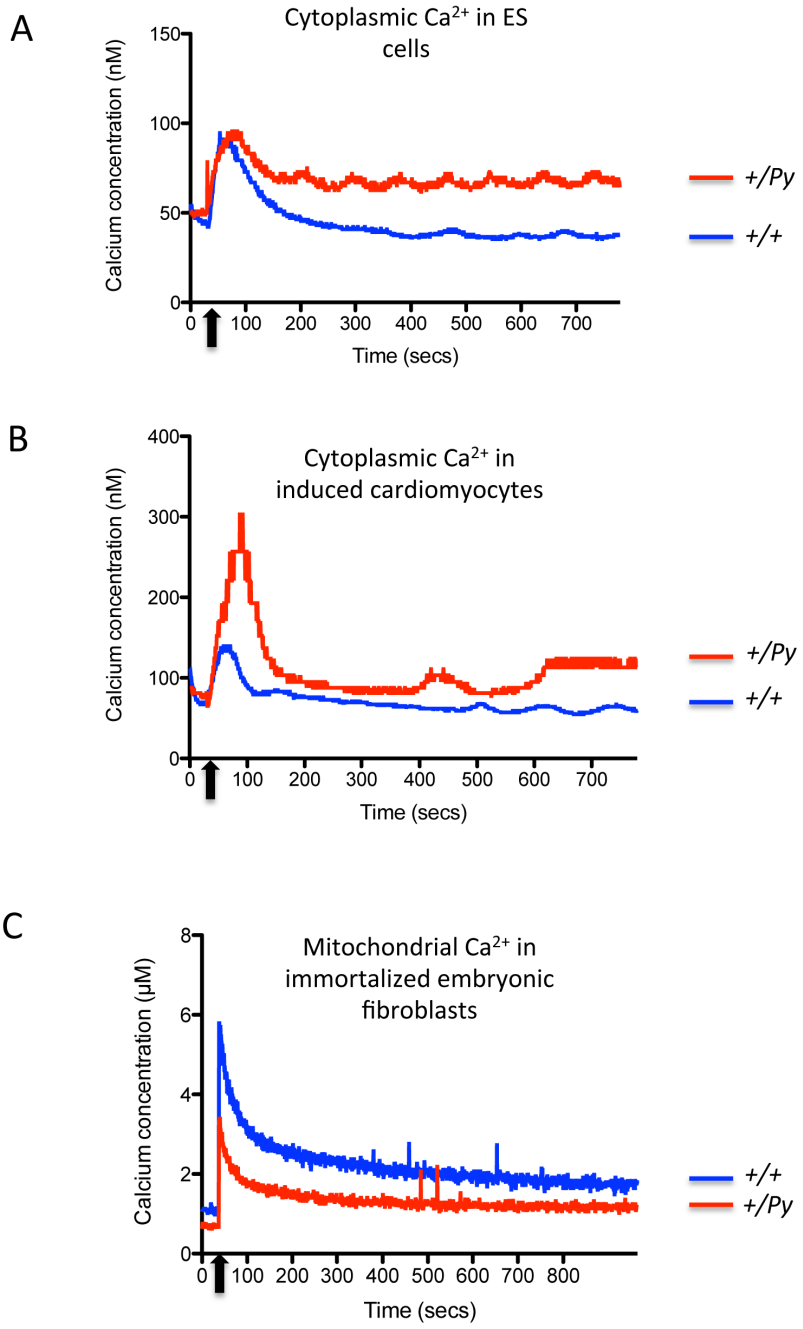

Figure 5.7. Decreased mitochondrial Ca^{2+} uptake in Python cells. The Ca^{2+} concentration was measured in wild type and Python cells. The ER was stimulated to release Ca^{2+} by the addition of ATP at 30s (indicated by the black arrows). Cytosolic Ca^{2+} in (A) Python ES cells and (B) Cardiomyocyte-like cells differentiated from ES cells. (C) Mitochondrial Ca^{2+} was measured using a mitochondria-targeted aequorin.

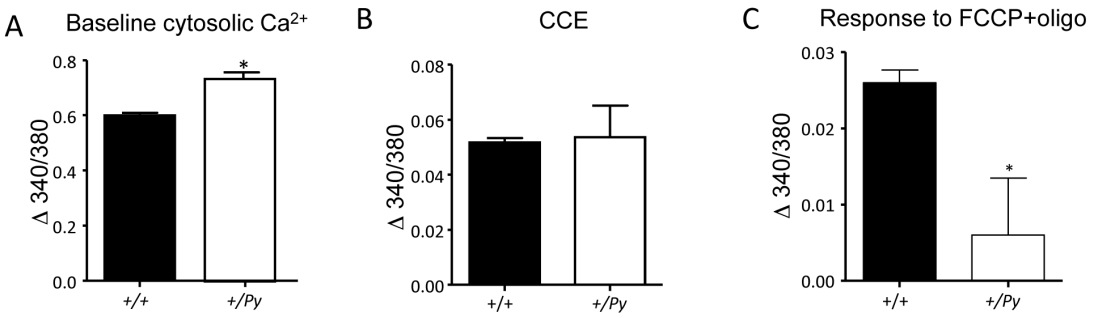

Figure 5.8. Increased cytosolic Ca^{2+} in Python fibroblasts is a result of dysfunctional mitochondria. (A) Baseline cytosolic Ca^{2+} concentration was measured in immortalized fibroblasts using Fura-2. Python cells have higher levels of basal cytosolic Ca^{2+} (Student's t test, *P*=0.0011), n=12 (B) No difference in CCE is evident between wild type and Python immortalized fibroblasts (Student's t test, *P*=0.8598), n=12. (C) When mitochondria are exposed to inactivating conditions: FCCP + oligomycin, wild type cells exhibit an increase in cytosolic Ca^{2+}, whereas Python cells show a much lower response (Student's t test, *P*=0.0177), n=10. Experiments were performed by Dr. John Boyle.

Mitochondrial Ca^{2+} is taken up in order to drive OXPHOS during respiration. During this process, protons are pumped across the ETC into the intermembrane space, producing the mitochondrial membrane potential (MMP). Given that Python mitochondria take up Ca^{2+} less efficiently than wild type mitochondria, the MMP in Python cells may be compromised. To test this theory, the JC-1 dye was loaded into immortalized MEFs and imaged by Dr. John Boyle. JC-1 accumulates in mitochondria in an MMP-dependent manner, accompanied by a shift in fluorescence emission from ~529nm (green), indicating low MMP, to ~590nm (red), signifying a higher MMP. The wild type JC-1 fluorescence ratio is shifted predominantly to the red signal, while the Python cells display predominant green fluorescence (Fig. 5.9A), indicating that mitochondria in Python cells are mostly depolarized. The fluorescence ratio for each genotype was quantified using the ImageJ software. Whole field intensity was measured for red and green fluorescence and subsequent ratios were calculated using the two values (Fig. 5.9B).

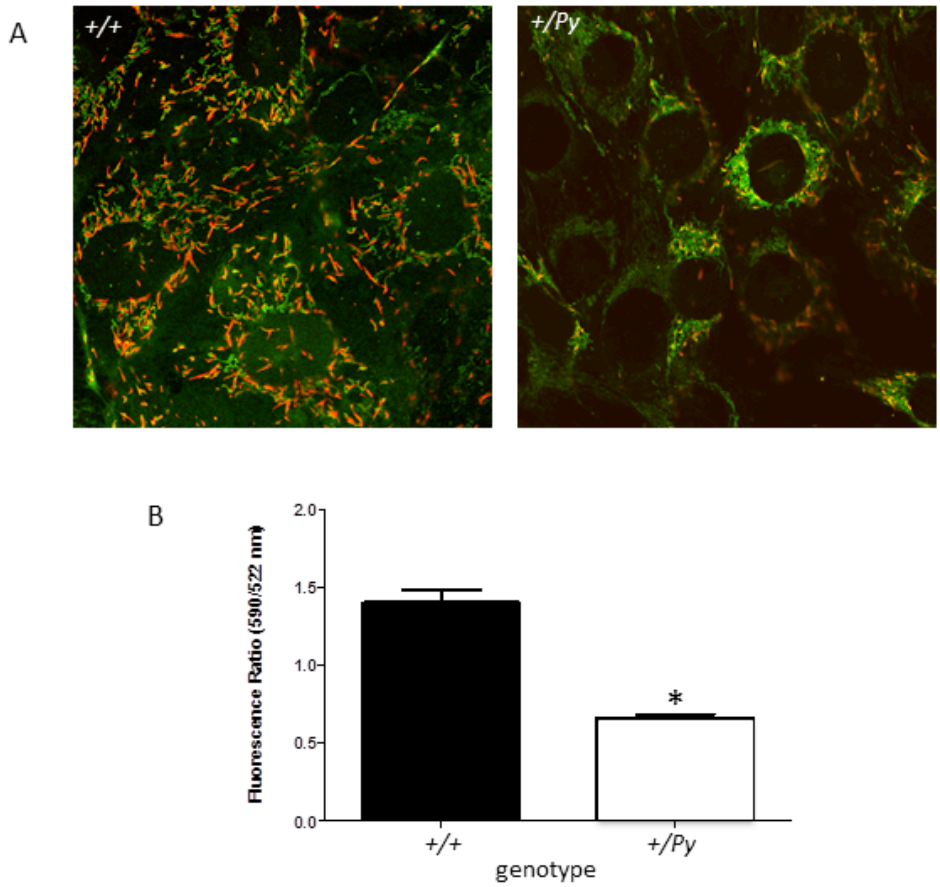

Figure 5.9. Mitochondrial membrane depolarisation in Python cells. (A) Wild type and Python embryonic fibroblasts were loaded with JC-1. At high MMP, JC-1 fluoresces at 590nm (red), and at low MMP, 529nm (green). Imaging reveals an obvious difference between wild type and Python, in which Python cells exhibit a much lower MMP. (B) The fluorescent ratio between 590nm and 522nm was quantified and confirms the much lower MMP in a population of Python cells. Student's t-test, P<0.001, =10. Experiment was performed by Dr. John Boyle.

5.1.4 Age-related decrease in oxidative phosphorylation in Python heart tissue.

OXPHOS is a major process to provide the cell with ATP. Cardiomyocytes rely on this process to generate sufficient energy for contraction. If there was a defect in Ca^{2+} uptake by mitochondria, a number of enzymes involved in OXPHOS may exhibit reduced activity. Gradually, as the MMP is also compromised in Python cells, Ca^{2+} taken up by the mitochondria will also

decline, further reducing the activity of the ETC complexes and subsequently, the MMP, leading to a cascade effect. In order to investigate the activity of OXPHOS, mitochondria were scrutinized in ES cells and immortalized fibroblasts. The cells were placed into a respirometer and exposed to a variety of reagents that inhibit particular enzyme complexes of the ETC and allow analysis of four parameters of OXPHOS: (i) 'Routine' represents the total respiration in cells once the chamber of the respirometer has been sealed and the values are normalised to remove the contribution of non-mitochondrial respiration (such as glycolysis); (ii) Leak is a measure of how tightly coupled OXPHOS is to electron transport and is measured after inhibiting the F_1/F_0 ATP synthase with oligomycin. A higher leak would signify greater uncoupling, hence a greater number of protons passing from the intermembrane space into the matrix via uncoupling proteins rather than ATP synthase. This would therefore produce less ATP from a given proton gradient; (iii) the Electron Transport System (ETS) is the maximum capacity of the OXPHOS system estimated after uncoupling ATP production from proton pumping with proton ionophore FCCP. FCCP permeabilizes the IMM to protons, thus diminishing the proton gradient and thereby uncoupling the ETS from the OXPHOS system; and (iv) Residual O_2 consumption (ROX) shows the O_2 consumption as a result of non-mitochondrial respiration; measured after inhibition of F_1/F_0 ATP synthase with oligomycin, Complex I with rotenone and Complex III with antimycin A. Any continued consumption of O_2 should be the result of non-mitochondrial respiration.

When measuring OXPHOS activity across the ETC in ES cells, no significant difference was observed between wild type and Python cells (Fig. 5.10), (Table 5.1). These are in keeping with a cardiac–specific defect. Comparing the results for ES cells and fibroblasts, there is an increased ROX value in ES cells (Fig. 5.10). This is likely to be because ES cells rely on glycolysis as a primary source of ATP production rather than OXPHOS, therefore the higher ROX value denotes a higher level of non-mitochondrial respiration. Like many cell types, fibroblasts use OXPHOS as the main source of ATP production, and hence demonstrate a lower output for non-mitochondrial respiration.

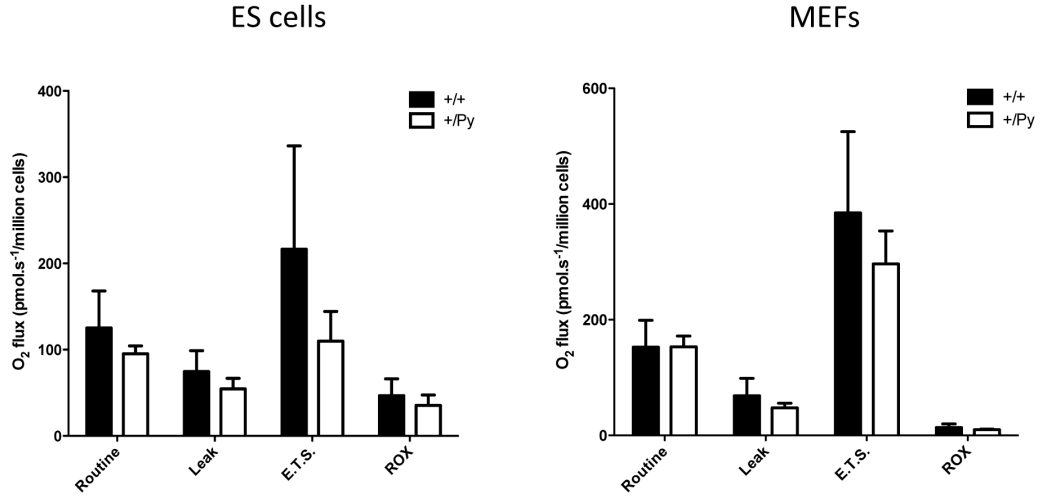

Figure 5.10. OXPHOS efficiency is not compromised in Python ES cells and fibroblasts. Python and wild type ES cells (n=4) and immortalized mouse embryonic fibroblasts (MEFs) (n=6) were exposed to conditions that increase or decrease particular complexes of the ETC. Routine is O_2 consumption due to the general respiration of the cells. Leak is measured after inhibiting ATP F_1/F_0 ATP synthase with oligomycin. ETS represents the maximum capacity of the ETC after the addition of FCCP. ROX is a measure of non-mitochondrial respiration.

Table 5.1. Statistical analyses of OXPHOS between wild type and Python cell lines.

	ES cells	**MEFs**
Routine	*P*=0.52043	*P*=0.9885
Leak	*P*=0.483029	*P*=0.4485
E.T.S	*P*=0.425474	*P*=0.5225
ROX	*P*=0.64314	*P*=0.4834

Student's t tests were used to compare wild type and Python values of O_2 flux for each parameter.

To measure OXPHOS in tissues, the mitochondria must be exposed to different conditions inside the respirometer. The first requirement is to initiate OXPHOS by providing key substrates to the mitochondria for activation of the CAC. These substrates are pyruvate, malate and glutamate. ADP is then added, which is a substrate for ATP synthase. It would be expected that O_2 consumption would increase if ATP synthase were functioning properly.

Succinate is then added to observe the activity of complex II. As this is a complex II substrate, O_2 consumption should, again, increase. FCCP is a chemical uncoupler of OXPHOS from electron transport and is added to the tissue until the OXPHOS system is completely uncoupled to give a measure of the maximum capacity of the OXPHOS system. A complex I inhibitor, rotenone is then added. Complex I activity will then be confirmed if the addition of rotenone decreases respiration. Should no change occur at this point, the general O_2 consumption is therefore a result of OXPHOS without complex I activity. Antimycin A is then added to inhibit complex III activity. Again, a reduction in respiration should accompany this addition if complex III is functioning properly.

When OXPHOS was measured in the hearts of mice on the C57BL/6J background at ages 1, 3, 4 and 5 months, and terminally ill mice that displayed CHF symptoms (~6 months), it became clear that an age-dependent decrease in the efficiency of enzyme activity across the ETC was occurring in hearts of Python mice. Initial signs that the ETC system may be experiencing reduced efficiency becomes evident at 4 months of age (Fig. 5.11), (Table 5.2). By 5 months, a major reduction in the efficiency across all parameters measured (complexes I, II, III and ATP synthase as well as the maximum capacity of the ETC system) is apparent and remains so until the onset of CHF. The addition of rotenone and subsequently antimycin A has a much lower impact on the Python samples from 3 months of age, whereas the wild type samples experience a much greater decrease. This indicates that activities of complexes I and III are reduced in Python mice from 3 months of age. Complex II in Python hearts, however, is able to function comparable to that of the wild type until 5 months of age. At this point the addition of succinate has a majorly reduced effect on O_2 consumption suggesting compromised complex II activity. This is then accompanied by the collapse of activity across all parameters in Python hearts when compared to wild type controls and remains so until the onset of CHF.

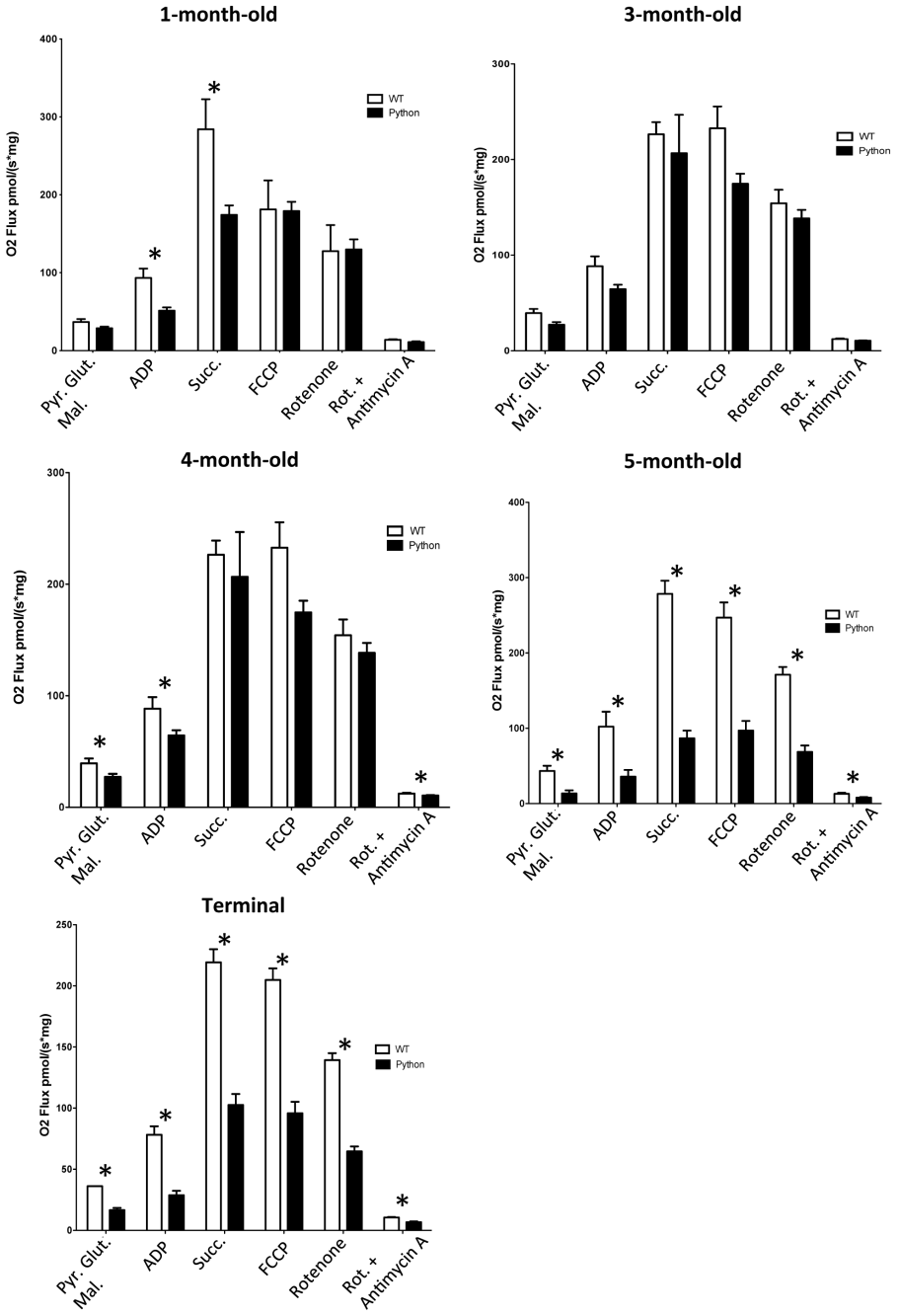

Figure 5.11: **Direct comparison between Python and wild type OXPHOS in the heart.** Mitochondria were analysed from the hearts of Python and wild type C57BL/6J mice through exposure to different conditions. Pyruvate, glutamate and malate are added to initiate respiration. ADP and succinate are substrates of ATP synthase and complex II, respectively and should naturally increase respiration. FCCP uncouples the OXPHOS system, representing the maximum capacity of the ETC. Rotenone and antimycin A are inhibitors of complexes I and III, respectively, leading to a decrease in respiration. Asterisks denote a significant difference.

Table 5.2. Statistical analyses of OXPHOS between wild type and Python heart tissue.

	1 month	3 month	4 month	5 month	Terminal/6 month
Pyr, Glut, Mal.	*P*=0.0582	*P*=0.0725	*P*=0.0030	*P*=0.0039	*P* < 0.0001
ADP	*P*=0.0002	*P*=0.1500	*P*=0.0008	*P*=0.0120	*P* < 0.0001
Succ.	*P*=0.0011	*P*=0.5931	*P*=0.0103	*P* < 0.0001	*P* < 0.0001
FCCP	*P*=0.9466	*P*=0.0867	*P*=0.0094	*P* < 0.0001	*P* < 0.0001
Rot.	*P*=0.9406	*P*=0.4308	*P*=0.0206	*P*< 0.0001	*P* < 0.0001
Rot + AmA	*P*=0.0961	*P*=0.0589	*P*=0.0035	*P*=0.0148	*P* < 0.0001

Student's t tests were used to compare wild type and Python values of O_2 flux for each substrate at each time point. Values highlighted in yellow denote significance. For wt samples, n=8, 6, 24, 6 & 18 for 1-month-, 3-month-, 4-month-, 5-month- and 6-month-old mice, respectively. For Python samples, n=22, 4, 12, 6 & 12 for 1-month-, 3-month-, 4-month-, 5-month-old and terminal mice, respectively.

In Figure 5.12, the data from Figure 5.11 have been displayed differently in order to show the clear age-dependant degeneration of mitochondrial function in the Python heart. Between the ages of 3 and 4 months, a decrease in the general level of respiration is evident in the Python mice, which becomes further reduced by 5 months (Fig. 5.12A). ATP synthase displays a very similar trend with a gradual decrease in activity from 3 months old to the onset of CHF (Fig. 5.12B). Complex II, however, shows no alteration in activity up to 4 months of age, which is then followed by a dramatic reduction at 5 months (Fig. 5.12C). The maximum capacity of the ETC also dramatically reduces at 5 months (Fig. 5.12D), which coincides with the compromised complex II activity. Complex I also exhibits a dramatic reduction at the age of 5 months (Fig. 5.12E). Complex III, gradually declines until the onset of CHF (Fig. 5.12F). In stark contrast, none of the parameters measured show any significant reduction in their activity with age in wild type hearts (Fig. 5.13). Of 42 Python mice in which onset of CHF was measured, a sole Python mouse was able to live far beyond expectation without displaying CHF symptoms. At 239 days of age (approx. 2 months greater than the average age of onset), the Python mouse finally showed signs of CHF. OXPHOS activity was subsequently analysed. Virtually no alteration in O_2 consumption accompanied rotenone addition, implying complex I is severely affected in this animal. However, in

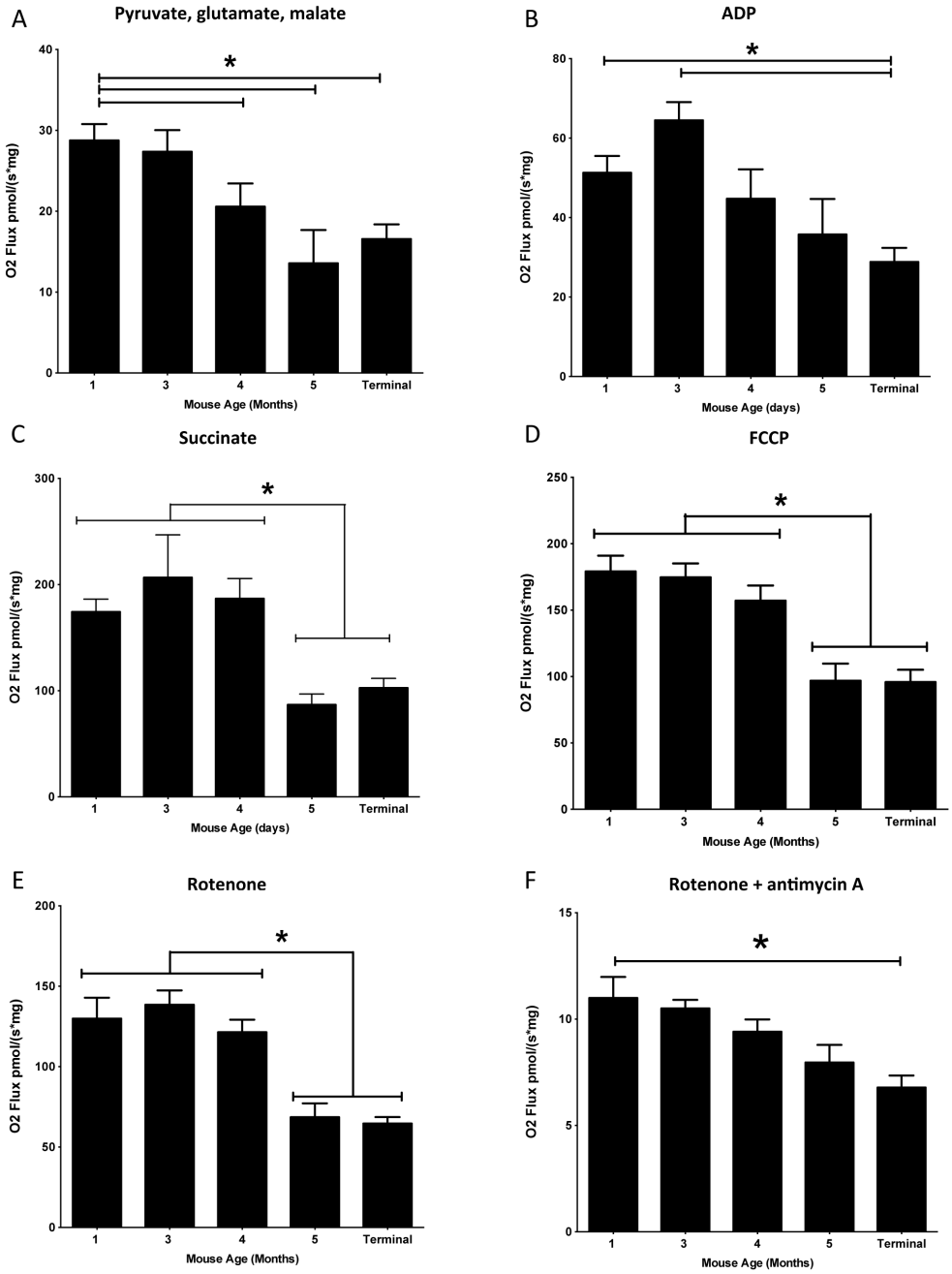

Figure 5.12. **Age-related decrease of OXPHOS efficiency in Python hearts**. (A) General respiration begins to decline at 4 months of age. (B) ATP synthase activity gradually declines from 3 months old until CHF onset. Complexes II (C) and I (E) both show no alteration of OXPHOS activity until 5 months old, when a dramatic reduction becomes evident for both complexes and remains the same until the onset of CHF. (D) The maximum capacity of the ETC also follows a dramatic decline from 5 months. (F) Inhibition with rotenone and antimycin A display a gradual reduction from 3 months old. The asterisks denote a significant difference. Statistical analyses are displayed in Table 5.3.

contrast to the CHF data from all other animals, complexes II and III both gave reasonable respiration, contradicting the age-related decrease in general OXPHOS across all complexes. This is however data provided from one mouse at this time point and therefore its significance cannot be identified at this point.

Table 5.3. Statistical analyses comparing Python OXPHOS values between time points for each substrate added.

Ages compared (months)	Pyr, Mal, Glut	ADP	Succ.	FCCP	Rot.	Rot & AmA
1 vs. 3	*P*>0.05	*P*>0.05	*P*>0.05	*P*>0.05	*P*>0.05	*P*>0.05
1 vs. 4	*P*<0.05	*P*>0.05	*P*>0.05	*P*>0.05	*P*>0.05	*P*>0.05
1 vs. 5	*P*<0.01	*P*>0.05	*P*<0.01	*P*<0.01	*P*<0.05	*P*>0.05
1 vs. Terminal	*P*<0.01	*P*<0.05	*P*<0.001	*P*<0.001	*P*<0.001	*P*<0.01
3 vs. 4	*P*>0.05	*P*>0.05	*P*>0.05	*P*>0.05	*P*>0.05	*P*>0.05
3 vs. 5	*P*>0.05	*P*>0.05	*P*<0.05	*P*<0.05	*P*<0.001	*P*>0.05
3 vs. Terminal	*P*>0.05	*P*<0.05	*P*<0.01	*P*<0.05	*P*<0.05	*P*>0.05
4 vs. 5	*P*>0.05	*P*>0.05	*P*<0.01	*P*<0.01	*P*>0.05	*P*>0.05
4 vs. Terminal	*P*>0.05	*P*>0.05	*P*<0.01	*P*<0.01	*P*<0.01	*P*>0.05
5 vs. Terminal	*P*>0.05	*P*>0.05	*P*>0.05	*P*>0.05	*P*>0.05	*P*>0.05

Newman-Keuls multiple comparisons tests were used to compare Python values of O_2 flux. Values highlighted in yellow denote significance.

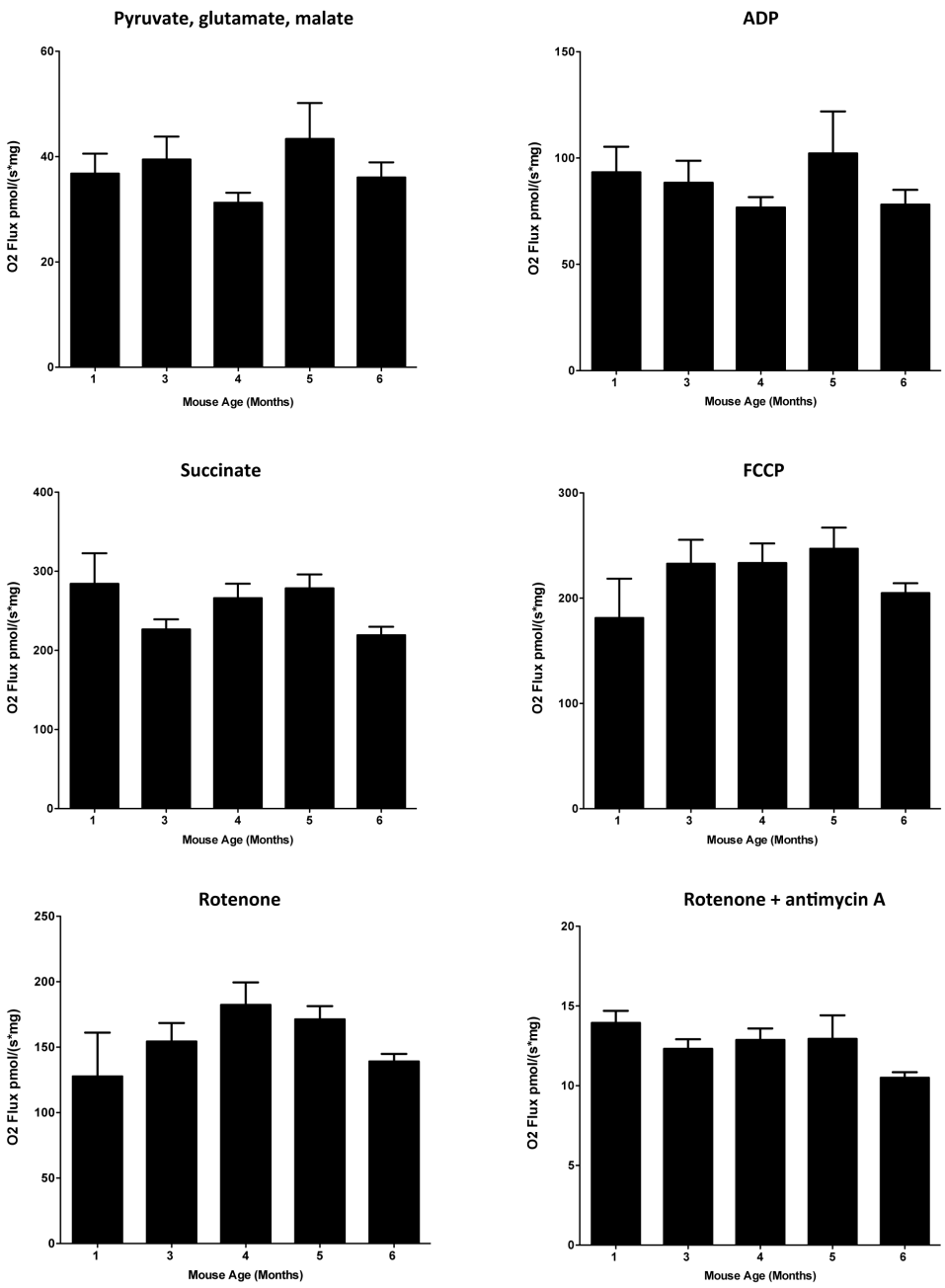

Figure 5.13. OXPHOS activity in wild type hearts. See Figure 5.11 for explanation of each graph. None of the parameters measured showed any reduction with increased age. Newman-Keuls multiple comparisons test showed no significance between values of O_2 flux between time points for each substrate added. *P*>0.05 for all comparisons made.

Taken together the data show that the Python hearts exhibit a severe reduction in OXPHOS at 5 months of age and appear to be able to withstand such an effect before developing CHF symptoms at around 6 months old. This severe reduction in OXPHOS is likely to be initiated by the decreased activity of ATP synthase at 4 months of age, followed by a dramatic reduction in complex I and II activity at 5 months of age, then complex III activity at 6 months. The unique Python mouse that was able to live to 8 months old may have been due to sufficient activity of complexes II and III compared to other Python mice, before complex I activity eventually diminished beyond levels of survival. Such a mouse is rare – only one such animal was observed over 9 years of maintaining the colony where more than 1,000 Python mice had been left to age until they develop CHF symptoms.

5.1.5 Python ES cells fail to differentiate into cardiomyocytes

The ES cells were generated to enable a cardiomyocyte cell culture model to be developed, using established assays to differentiate ES cells along the cardiomyocyte lineage (Burridge *et al*., 2011). Images were taken every 2 days after the onset of stimulation to differentiate until d9 (presence of beating cells) in order to monitor cell confluency and morphology. The wild type cells remained at high confluency throughout the differentiation process, whereas Python cells became more sparse (Fig. 5.14A). Cells were also counted. It became evident that by day 3 of differentiation the amount of cell loss in the Python cell line was double to that of wild type cells, with both cell lines maintaining stable cell numbers from this point onwards (Fig. 5.14B).

In addition to increased cell loss in Python lines, the differentiation process itself appeared to be effected, as no beating cells were present after cardiomyocyte induction (Fig. 5.14C). For the wild type cell line, 11 beating clumps were observed per 10^7 cells. Expression of mRNA for a number of cardiomyocyte markers were also examined to test for extent of cardiomyocyte differentiation (Fig. 5.14D). β-actin (*Actb*) and glyceraldehyde-3-phosphate dehydrogenase (*Gapdh*) are ubiquitously expressed and their equal expression across all samples were used to confirm equal cDNA input levels. POU domain, class 5, transcription factor 1 (*Pou5f1*) is a pluripotent marker

and as expected, expressed at high levels in both ES cell lines. The Python ES cell-differentiated cardiomyocytes also expressed the pluripotent marker, suggesting a problem in differentiating Python ES cells. The three cardiomyocyte markers: GATA binding protein 4 (*Gata4*), myosin light chain 2 (*Myl2*) and β-myosin heavy chain (*Myh7*) were highly expressed in the wild type ES cell-differentiated cardiomyocytes indicating efficient differentiation into cardiomyocytes. In contrast, the Python cardiomyocytes expressed very low levels of these markers. This raises the possibility that Python ES cells undergo problems in cell reprogramming. Based on this inability of Python ES cells to differentiate into cardiomyocytes, the data obtained from experiments in which cardiomyocyte-induced ES cells were used e.g. cytoplasmic Ca^{2+} (Fig. 5.7B) cannot be relaiably interpreted as the control wild type cells are not equivalent to the Python cells.

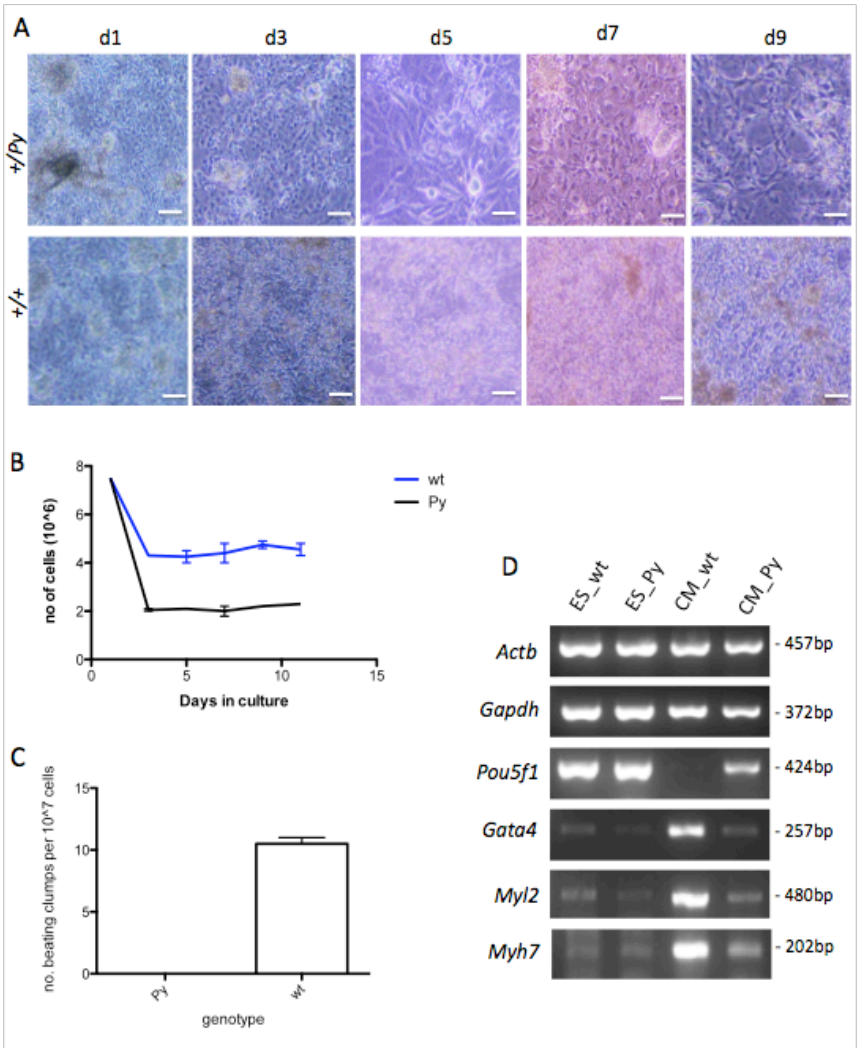

Figure 5.14. Python ES cells fail to differentiate into cardiomyocytes. (A) Images were taken from d1 (the day in which cardiomyocyte-induction started) to d9 at 2 day intervals using Olympus CKX41 microscope and CAMEDIA C-7070 camera. Scale bars represent 100μM. The wild type cells remained confluent throughout the 9 days whereas Python cells became far sparser when driven down the cardiomyocyte lineage. (B) Cell counts of wild type and Python cells as they were being driven down the cardiomyocyte lineage showed an initial decrease in cell number from d1 to d3, however the decrease in the Python cell line was far greater than that of wild type. (C) By d9 beating cell clumps were evident in the wild type cells, 11 clusters on average per 10^7 cells. However no beating clumps were evident in the Python cells. (D) Cardiomyocyte-specific cDNA markers were used to assess the quality of differentiation. *Gata4*, *Myl2* and *Myh7* were shown to be expressed at high levels in wild type induced-cardiomyocytes, but much weaker in the Python cells. *Pou5f1*, a measure of pluripotency indicated the Python cells still retained some of the pluripotent marker, albeit, far less than the ES cells for both wild type and Python lines. *Actb* and *Gapdh* are ubiquitously expressed and were detected across all samples equally, demonstrating equal loading amounts.

5.1.6 ATP levels are reduced in differentiated Python cell lines

Several Python cell lines had been developed for studies – cultured skin fibroblasts, immortalised MEFs and ES cells. ATP levels (measured using a luciferase/luciferin-based assay) were not altered in ES cells (Fig. 5.15A). This is consistent with data showing no alteration in OXPHOS activity for ES cells as ES cells use primarily glycolysis to generate ATP (Cho *et al*., 2006, Prigione *et al*., 2010, Kondoh *et al*., 2007). The Python ES cells begin to show reduced ATP levels as they are differentiated down the cardiomyocyte lineage, first as they form embryoid bodies (Fig. 5.15B) and is maintained in more fully differentiated cardiomyocytes (Fig. 5.15C) though as mentioned above, these differentiated cells are not the equivalent to their wild type counterparts. Surprisingly, Python MEFs also show a reduction in ATP levels (Fig. 5.15D) despite the fact they have normal OXPHOS activity.

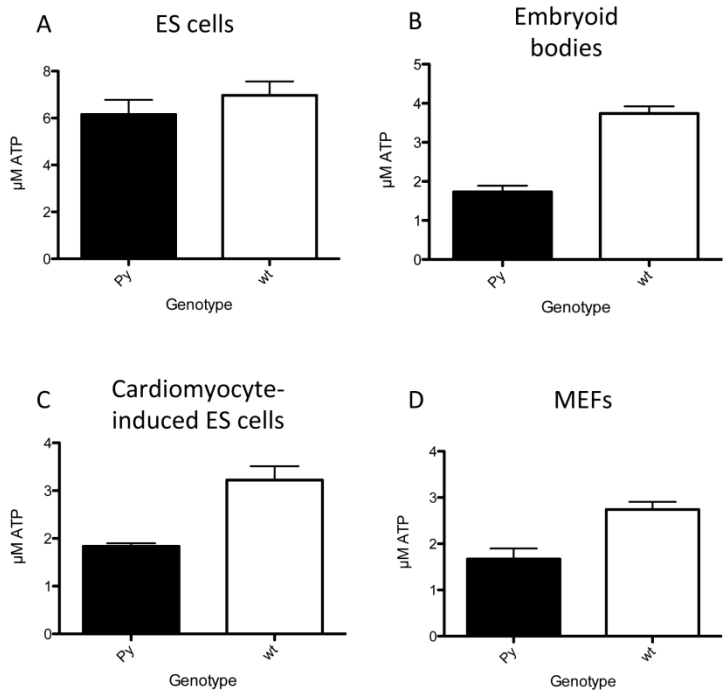

Figure 5.15. ATP levels in cell lines. ATP was measured using a luciferase-based assay. No significant alteration in ATP concentration was evident in ES cells (A) (Student's t test, *P*=0.3572), n=3. However upon ES cell differentiation, a reduction in ATP concentration in Python embryoid bodies became clear (B) (Student's t test, *P*<0.001), n=13 and remained low across cardiomyocyte-induction (C) (Student's t test, *P*=0.012), n=5. Python MEFs were also shown to display a reduced ATP concentration (D) (Student's t test, *P*=0.0025), n=3.

5.1.7 DNM1L protein levels in the heart increase with age

One aspect of the dilated cardiomyopathy (DCM) that occurs in Python mice is that overt symptoms develop at a particular age; an average of 82 days of age on the C3H/HeN background and 168 days on the C57BL/6J background (Appendix XIII). Furthermore, fusion and fission of mitochondria is, apparently, very low in adult cardiomyocytes (Hom and Sheu, 2009), so we wished to examine whether fusion and fission proteins were, indeed, expressed in adult hearts, and whether there was any change over time. Proteins were extracted from the brains and hearts of female and male C57BL/6J mice at the ages of 1 week, 3 weeks, 6 weeks, 3 months, 6 months and 13 months (males only for the last timepoint). The concentrations of extracted proteins were determined and then equal amounts of the three samples at each time point and sex were pooled and used for Western blot analysis. α-Tubulin was used to normalise the protein levels. Strikingly, an increase in DNM1L expression in the heart with age was observed (Fig. 5.16A), particularly that of the 73KDa heart-specific isoform. In contrast there was little, if any, change in brain DNM1L levels (Fig. 5.16B). Other mitochondrial fusion/fission proteins also showed a similar trend. OPA1 is present in 5 isoforms between 80 and 100KDa in size (Akepati *et al*., 2008) and all isoforms are shown to increase with age in the heart, but not in the brain. MFN2 exists in 2 distinct molecular weights. The isoform of approx. 80KDa showed no difference in protein level between tissues or ages while the 50KDa isoform showed a substantial increase with age in the heart, but appears to be barely present in the brain at any age. TIM23, the protein used to reflect mitochondrial abundance in each sample also showed a 2nd isoform that increased in abundance with age. This isoform is seen in the heart and to a lesser extent in the brain from 3 months of age.

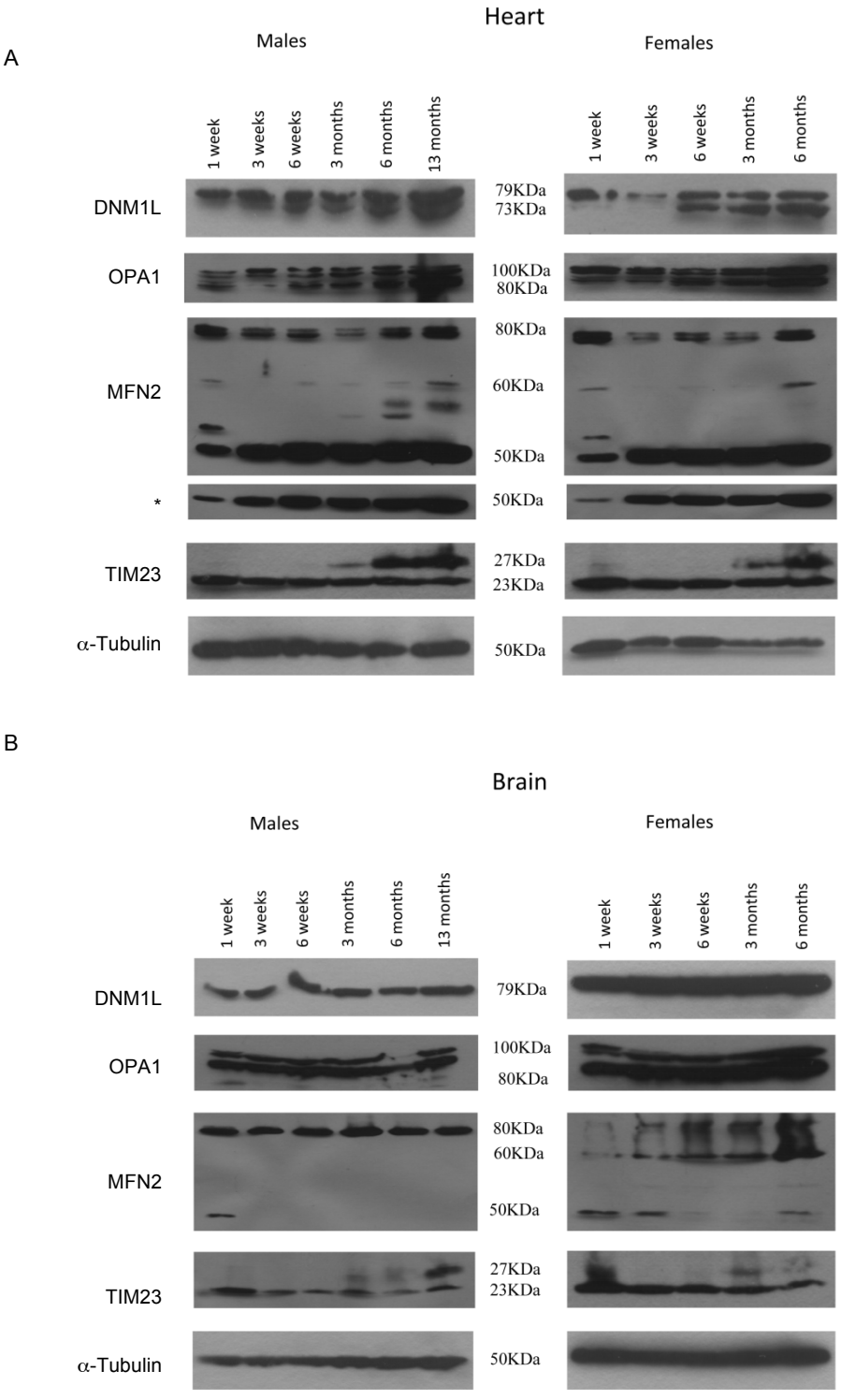

Figure 5.16. **Mitochondrial fusion/fission protein levels increase in the heart with age.** Proteins were isolated from the hearts (A) and brains (B) of male and female C57BL/6J mice at different ages. Western blot analysis of Dnm1l, Opa1 and Mfn2 revealed an age-related increase in expression in the heart. Tim23 and α-Tubulin levels were detected to normalise for mitochondrial and cell number respectively. Asterisk denotes lower exposure for clarity.

5.2 Discussion

Mitochondrial OXPHOS produces ATP, the major source of cellular energy. Cardiomyocytes have high energy demands to cope with the demands of cardiac contraction. For this reason, fatty acid oxidation is the main substrate utilized in OXPHOS in cardiomyocytes and can provide up to 131 ATP molecules per fatty acid, whereas 1 glucose molecule produces only 38 ATP molecules. Python hearts exhibit a severe decline in ATP production that is apparent as early as 5 weeks of age (Ashrafian *et al*., 2010). The questions remain as to (i) why the *Dnm1l*^{Py} mutation mainly affects cardiomyocytes; (ii) why ATP reduction results; (iii) why the onset of DCM takes time to develop postnatally; and (iv) why the onset of DCM develops at different ages in different strain backgrounds. The first may be explained in terms of the severity of the mutation on DNM1L function. If it is proposed that the Python mutation leads to a reduction, but not a complete abrogation, of DNM1L function, then tissues that have high energy demands for ATP and use OXPHOS as the primary ATP generation pathway, such as the heart, are more likely to be affected. Also, the heart may not be the only organ affected but possibly a reduction in the functional capacity of other organs does not have as deleterious effect on the organism as a reduction in cardiac output or is perhaps more difficult to detect phenotypically.

Regarding the age at which overt DCM symptoms first appear, this might reflect a changing role of DNM1L over time in the heart that does not occur in other tissues. In the C3H/HeN background, the change is more precipitate than in the C57BL/6J background. As an initial investigation of this possibility, the expression of DNM1L was examined in mice of various ages. Surprisingly, DNM1L expression levels were shown to increase in the heart with age, whereas little change was observed in the brain. In particular, a 73KDa isoform present in the heart increases more drastically than the 79KDa isoform. The significance of this change is unknown, as indeed, is the nature of the difference between the two heart isoforms. OPA1 isoforms and the 50KDa isoform of MFN2 also showed a similar trend. The general increase in fusion and fission proteins specific to the heart may go some way in providing the answer as to why Python mice develop an age-related defect in OXPHOS in

the heart, when the mutation is present in all tissues. For instance as the mouse ages, cardiomyocyte size increases, requiring an increase in the production of ATP to maintain sufficient contraction. By 6 months of age, ATP production cannot match energy demands. This cell size/ATP requirement increase also requires an increase in mitochondrial volume and, *ipso facto*, all the proteins that participate in mitochondrial dynamics. However, this cannot explain all of the increase in DNM1L levels as even when normalised to the mitochondrial protein TIM23, there was still a massive increase with age in levels of DNM1L and other fusion/fission proteins.

Interestingly the OXPHOS system has also been shown to exhibit an age-related decrease in efficiency in the Python heart. By 5 months of age on the C57BL/6J background, all complexes of the ETC display reduced activity, the most notable being that of complexes I and II. The mouse is still viable at this point. By 6 months of age, mice on this background radically develop CHF and die within 48 hours. The reduced efficiency of OXPHOS at this point is reflected in an ATP output below a threshold required for the survival of cardiomyocytes. Cardiomyocytes are high-energy demanding cells; other cells at this time point may remain healthy as they may be able to tolerate lower levels of ATP production due to lower energy demands. One Python mouse was able to live far longer than expected, to 239 days. Analysis of the ETC revealed that complex I activity was very diminished, although other aspects of the ETC remained functional. This may explain why that particular mouse was able to live so long. If all complexes, but complex I are functioning sufficiently, then ATP production may remain above the threshold required for cardiomyocyte function for longer. Progressive decline in complex I activity eventually hindered ATP production leading to CHF and the same symptoms as other Python mice.

One possibility how OXPHOS efficiency gradually declines over age in Python mice may lie in a capability of DNM1L to function in tethering between the ER and mitochondria. Ca^{2+} is a key regulator of enzyme complexes that participate in the CAC and ETC. Therefore mitochondrial Ca^{2+} uptake is a vital process in cell survival. Physical tethering between the ER and mitochondria allows the mitochondria to be within close proximity to Ca^{2+} when released from the ER. The highly organised linear arrangement of mitochondria in

cardiomyocytes may allow for a shorter distance between the two organelles, facilitating more efficient Ca^{2+} uptake by the mitochondria and a more regular rate of ATP production for these constantly contracting cells. Upon ER-Ca^{2+} release, cytoplasmic Ca^{2+} concentration increases but rapidly returns to basal levels in wild type cells, though remains high in Python cells. Cytoplasmic Ca^{2+} levels were measured in ES cells and cardiomyocyte-induced ES cells. A notable difference between the two cell types was the peak cytoplasmic Ca^{2+} concentration after release from the ER. In ES cells, this peak was equal between wild type and Python cells whereas Python cardiomyocyte-induced ES cells exhibited a far higher peak compared to their wild type counterparts. As ES cells don't rely primarily on OXPHOS, but use the glycolytic pathway to generate ATP, there is less need for large Ca^{2+} stores and regular ER-mediated Ca^{2+} release. Cardiomyocytes, however, rely heavily on OXPHOS. When Ca^{2+} is released from the ER, if mitochondria are unable to take it up efficiently, it is possible that the ER will take back more Ca^{2+} through the sarcoplasmic/endoplasmic reticulum Ca^{2+}-ATPase (SERCA). This would gradually increase the concentration of Ca^{2+} in the sarcoplasmic reticulum (SR) lumen, thereby resulting in a larger Ca^{2+} release upon stimulation. After the initial increase in cytoplasmic Ca^{2+} as a result of release from the ER, cytoplasmic Ca^{2+} will normally drop due to mitochondrial Ca^{2+} uptake via the mitochondrial Ca^{2+} uniporter (MCU) and ER Ca^{2+} uptake via the SERCA. A reduction in mitochondrial Ca^{2+} uptake along with lower ATP levels to activate the SERCA may contribute to a prolonged cytosolic Ca^{2+} concentration. Dysfunction in mitochondrial Ca^{2+} uptake in Python cells was confirmed when measuring mitochondrial Ca^{2+} levels upon agonist–induced ER Ca^{2+} release. This is likely to be a result of decreased tethering and hence, the increased distance between the two organelles (Friedman *et al*., 2011).

Ca^{2+} is taken up via the MCU, a transmembrane protein located in the IMM. Activity of the MCU is maintained by the MMP (Hansford and Zorov, 1998). The MMP is also responsible for the activity of ATP synthase. The protons in the intermembrane space pass through the ATP synthase, providing energy to catalyse the conversion of ADP + P_i into ATP. Upon MMP dissipation, ATP production is impaired, as is mitochondrial Ca^{2+} uptake. The MCU was recently shown to modulate contraction in neonatal cardiomyocytes

(Drago *et al*., 2012). Inhibition of MCU activity is likely to affect the efficiency of the ETC as a result of inefficient Ca^{2+} uptake. As a consequence, protons will not be pumped into the intermembrane space, therefore leading to a reduced MMP. This will initially reduce ATP production, but mitochondrial Ca^{2+} uptake will also be further impeded by reduced MCU activity. This will lead to a progressive decline in ETC activity and ATP production along with continued dissipation of the MMP.

mtDNA deletions and membrane dissipation have been linked to a reduced respiratory output (Parone *et al*., 2006, Legros *et al*., 2002, Twig *et al*., 2008). It is possible that fusion and fission are important processes in the maintenance and restoration of functional mitochondria, allowing the cell to cope with mutations in mtDNA (Mouli *et al*., 2009). For example, fusion would allow mixing of contents and thus, functional mtDNA and membrane potential to be shared with functionally challenged mitochondria. Fission may allow segregation of defective mitochondrial units e.g. one which is depolarized and beyond restoration; this is then targeted for mitophagy to recycle metabolites and synthesize new macromolecules (Mouli *et al*., 2009, Twig *et al*., 2008). Reduced mitochondrial fission or fusion may therefore lead to the accumulation of either damaged mtDNA and or dysfunctional mitochondria in the cell. However, no obvious increase in mutant mtDNA forms was detected in Python heart, brain and rectus femoris samples suggesting this is not the reason for the respiratory dysfunction. The method used in this study would only detect mtDNA deletions upto 2kb in size and was relatively crude in nature. In comparison, a better way to detect mtDNA mutations would be that of a 'random-mutation capture assay', as used by Chen *et al* (2010). In this method deep sequencing methodology was used to detect base pair mutations and small deletions.

Further experiments were carried out to detect alterations in the level of autophagy. ATP levels are monitored by the energy sensor AMPK (Cardenas *et al*., 2010, Green and Wang, 2010). Sufficient ATP levels maintain the inactivation of AMPK, while insufficient ATP results in the phosphorylation of this sensor protein, forming P-AMPK. P-AMPK then activates the autophagic pathway by stimulating fusion between autophagosomes and lysosomes, breaking down metabolites engulfed by the autophagosome and providing

nutrients such as acetyl coA for the CAC and subsequent mitochondrial OXPHOS to re-establish sufficient ATP levels. Because ATP depletion is present in the Python heart, an increase in autophagy was predicted. However, protein detections of P-AMPK showed no alteration between Python and wild type hearts and brains at 5 weeks and 13 weeks of age. Upon completion of the autophagosome, LC3-I is converted to LC3-II by cleavage and lipidation and becomes localised to the autophagosome membrane (Kabeya *et al*., 2000). The conversion of LC3-I to LC3-II was also investigated by means of Western blotting, but again, no alteration was evident in Python mice. However, distinct punctate structures visualised by immunocytochemical staining of LC3 were present in wild type cells, but not Python cells and may suggest a decrease in autophagy in Python cells. Further experiments may be required to detect more subtle changes in autophagy and deduce the impact of Python on autophagy. As ATP depletion coincides with CHF onset in Python mice, it may be necessary to examine levels of autophagy in terminally ill mice.

Inhibition of DNM1L activity has recently been shown to disrupt cell reprogramming of somatic cells into induced pluripotent stem cells (iPSCs) (Vazquez-Martin *et al*., 2012). A crucial difference between somatic cells and iPSCs is their mechanism of energy metabolism. While somatic cells rely mainly on mitochondrial OXPHOS, pluripotent stem cells use glycolysis. In the study of Vazques-Martin *et al* (2012), the mitochondrial division inhibitor mdivi-1 (Cassidy-Stone *et al*., 2008) was used to inhibit DNM1L activity in human fibroblasts. Mitochondrial elongation was a notable effect due to decreased fission. Another consequence of inhibiting DNM1L was decreased mitophagy. This is possibly due to the inability of mitochondria to divide and so unable to expose small fragments of damaged mitochondria for elimination (Cassidy-Stone *et al*., 2008). Reprogramming was shown to be less efficient when DNM1L was inhibited. It was postulated that DNM1L-mediated mitophagy promotes the degradation of mitochondria during reprogramming of somatic cells, possibly leading to a reduction in mitochondrial number, and size, driving a more efficient conversion of ATP production back to glycolysis (Vazquez-Martin *et al*., 2012). Furthermore, DNM1L inhibition of successfully reprogrammed iPSCs induced differentiation, implying a role for DNM1L in maintaining pluripotency.

In the current study, ES cells were one of the models used to investigate the effect of Python. Although DNM1L activity in ES cells derived from Python heterozygotes was clearly reduced as seen by an enlarged mitochondrial network, the cells appeared morphologically similar to wild type ES cells (Appendix XIV) and exhibited similar growth rates (Appendix XV). Nor were ATP levels compromised. The phenotype of the Python heterozygote appears to be primarily manifested in the heart and so ES cells were differentiated down a cardiomyocyte-specific lineage. It became clear that the Python ES cells did not differentiate properly and retained some pluripotency as indicated by the presence of *Pou5f1* mRNA (a marker of pluripotency). Contrary to the findings of Vasquez-Martin *et al* (2012) reduced DNM1L activity in Python cells appears to prevent proper differentiation, whereas DNM1L inhibition with mdivi-1 appears to promote differentiation. Differences between species, differences between ES cells and iPSCs, or differences between the level of DNM1L activity inhibition may account for this variability. Alternatively the effect of the Python mutation and mdivi-1 action may produce alterations in two distinctly different processes. However it seems that energy metabolism might play a central role in reprogramming in general, whether back to a pluripotent state or to drive differentiation down a specific lineage. Similarly ATP levels were shown to be reduced when differentiating ES cells down the cardiomyocyte lineage. It may be this reduction in energy metabolism due to DNM1L^{Py} that becomes problematic for reprogramming of any cell. An irreconcilable difference is that Python ES cells did not differentiate *in vitro* normally, yet *in vivo* mice are viable and appear relatively normal at birth, implying differentiation is not adversely affected to any significant degree.

Chapter 6 : Introduction of the Python mutation into R6/2 mice does not ameliorate progressive development of Huntington's disease.

6.1 Introduction

Huntington's disease (HD) is a progressive neurodegenerative disorder. The mutation responsible for this disease is a CAG/polyglutamine (polyQ) repeat expansion in the *HTT* gene. Unaffected individuals possess 6 – 35 polyQ repeats while 36 – 39 repeats demonstrates HD with incomplete penetrance, and over 40 repeats results in HD with complete penetrance (Rubinsztein *et al*., 1996). These polyQ HTT proteins aggregate in the nuclei and cytosol in the cortex and striatum (DiFiglia *et al*., 1997, Gutekunst *et al*., 1999, Maat-Schieman *et al*., 1999) accompanied with striatal neurodegeneration and general atrophy of the brain (Vonsattel and DiFiglia, 1998). Age of onset for HD symptoms range from childhood to old age with increased severity being linked to a larger number of repeats. Symptoms for adult onset HD include psychiatric disturbances, impairment of motor coordination, cognitive decline and weight loss. Juvenile HD (onset before 21 years of age) is the result of more than 65 polyQ repeats. Patients with juvenile HD exhibit additional symptoms such as rigidity, tremors and seizures.

The most extensively characterised mouse model of HD is the transgenic R6/2 line (Mangiarini *et al*., 1996). The transgene consists of ~1kb of 5' untralnslated region sequences, exon 1 of the *HTT* gene carrying 144 polyQ repeats, plus the first 262bp of intron 1. By 6 weeks of age, R6/2 mice display symptoms of HD, including impaired motor coordination and balance as revealed through a rotarod test (Bett *et al*., 2006, Hockly *et al*., 2006). Grip strength is also weaker then that of wild type controls by 12 weeks of age (Bett *et al*., 2006, Hockly *et al*., 2006). Weight gain rate also slows from a similar time point, with the reduction in males being more prominent (Bett *et al*., 2006, Hockly *et al*., 2006, Hockly *et al*., 2003). Symptoms progressively worsen with age and by 15 weeks are so severe that animals rarely survive past this point (Woodman *et al*., 2007). The R6/2 model of HD resembles that of human HD

in many aspects though there are some difference (e.g. earlier age of onset) (Lione *et al*., 1999).

Deducing the molecular mechanisms involved in HD pathogenesis will help to develop therapeutic targets. Recent reports demonstrate increased DNM1L activity in HD. DNM1L is stimulated to translocate to the OMM via an increase in the direct interaction between HTT and DNM1L (Song *et al*., 2011). Also, as a result of increased ER Ca^{2+} efflux, DNM1L-dephophorylation by calcineurin is also increased leading to increased translocation to the OMM. The result is increased mitochondrial fragmentation (Costa *et al*., 2010, Song *et al*., 2011). Expression of the dominant-negative mutation, DNM1L^{K38A} can restore normal mitochondrial morphology in lymphocytes (Costa *et al*., 2010).

If altered mitochondrial morphology is pathogenic, correcting mitochondrial morphology might ameliorate HD (Costa *et al*., 2010, Song *et al*., 2011). Since Python alters DNM1L activity and mitochondrial morphology, a correction in DNM1L activity and mitochondrial morphology would be restored by combining the R6/2 transgene (increased DNM1L activity and increased fission) and the Python mutation (decreased DNM1L activity and decreased fission). This theory can be tested in mice.

Transgenic R6/2$^{0/T}$ male mice (provided by Professor Gillian Bates) were mated with *Dnm1l*$^{+/Py}$ female mice on the C57BL/6J background. Offspring were of 4 genotypes: (i) R6/2$^{0/0}$ *Dnm1l*$^{+/+}$, which are wild type mice; (ii) R6/2$^{0/0}$ *Dnm1l*$^{+/Py}$, which represent positive for the Python mutation; (iii) R6/2$^{0/T}$ *Dnm1l*$^{+/+}$, which are positive for the R6/2 transgene; and (iv) R6/2$^{0/T}$ *Dnm1l*$^{+/Py}$ (hereafter referred to as R6/2 x Python mice), which contain both the Python mutation and the R6/2 transgene. If animals containing both mutations were to improve or ameliorate the symptoms of the disease, this would be noticed via observations and analyses such as weight gain, grip strength, limb clasping, and brain weights. Mitochondrial morphology was also investigated to see if this corrected and correlated with any improvement in symptoms.

6.2 Results

6.2.1 Introduction of the Python mutation into R6/2 mice corrects the mitochondrial morphology defect.

It has previously been shown that the altered mitochondrial morphology phenotype can be observed in non-neuronal cells in HD patients such as fibroblasts and lymphoblasts (Costa *et al*., 2010, Song *et al*., 2011). Fibroblasts were cultured from mouse tails for each genotype at two age points: 5 weeks and 15 weeks. Figures 6.1A and 6.2A clearly show a reduction in mitochondrial fragmentation in R6/2 x Python mice compared to R6/2 mice. To quantify this, the length of 50 mitochondria were measured for each genotype using ImageJ and this revealed that not only is fragmentation reduced, but also their phenotypic length is restored to one very similar to that of wild type mitochondria (Figs. 6.1B, 6.2B).

Neurodegeneration is a hallmark of HD. Therefore it was also necessary to investigate mitochondrial morphology in neurons. As only 50% of R6/2 males successfully produce offspring (Mangiarini *et al*., 1996), maintenance of the colony proved difficult. For this reason mitochondrial morphology was initially investigated in neurons of Python and wild type mice only, while R6/2 and R6/2 x Python mice were being bred. A striking difference is observed. Wild type neurons possess mainly circular mitochondria, equally distributed along the axons. The purpose of such circular formations is unknown. In contrast, the mitochondria in Python neurons are far more elongated and don't form circular structures at all (Fig. 6.3). Mitochondria have been shown to be able to translocate along axons (Banks *et al*., 1969), and in Python neurons many mitochondria are aggregated around the nucleus, possibly because these are too large to travel along axons (Fig. 6.3). Due to time constraints, it was not possible to analyse mitochondrial morphology in the striatal neurons of R6/2 and R6/2 x Python mice. Therefore, the extent to which the mitochondrial morphology phenotype is corrected in R6/2 neurons by introduction of Python is not known, though the observed correction in fibroblasts is suggestive that a similar correction could be seen in neurons.

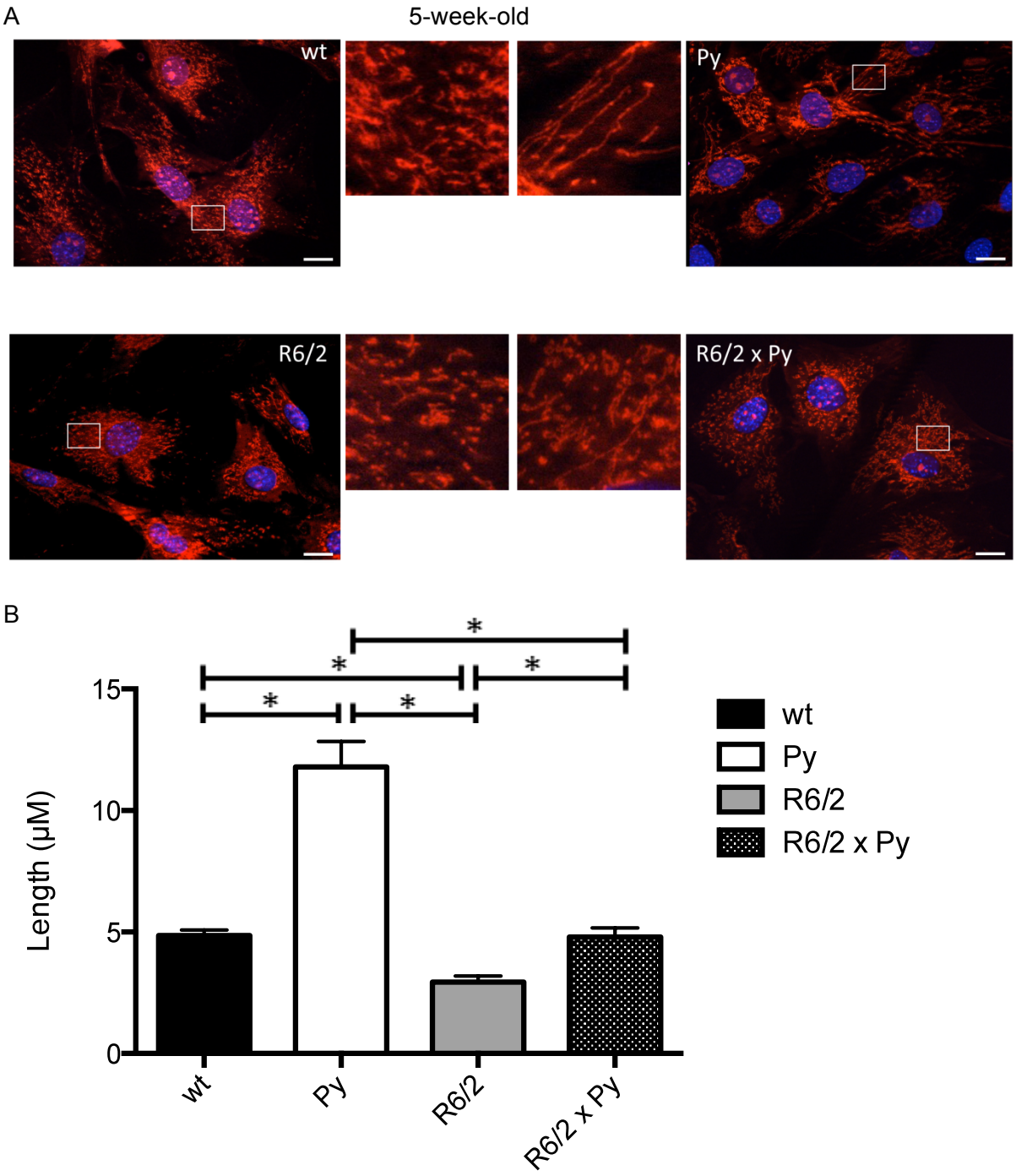

Figure 6.1. Mitochondrial morphology in 5-week-old R6/2 mice is restored by the introduction of the Python mutation. (A) Fibroblasts were cultured from the tail biopsies of 5-week-old wild type, R6/2, Python and R6/2 x Python mice. Mitochondria were stained with MitoTracker™ Orange and nuclei were stained with Hoechst 33258. Regions enclosed by white squares are shown magnified. Scale bars represent 20µm. (B) Count of n = 50 mitochondria for lengths and were measured using ImageJ. Mitochondrial morphology in R6/2 cells was restored by the addition of the Python mutation. Statistical analyses are displayed in Table 6.1.

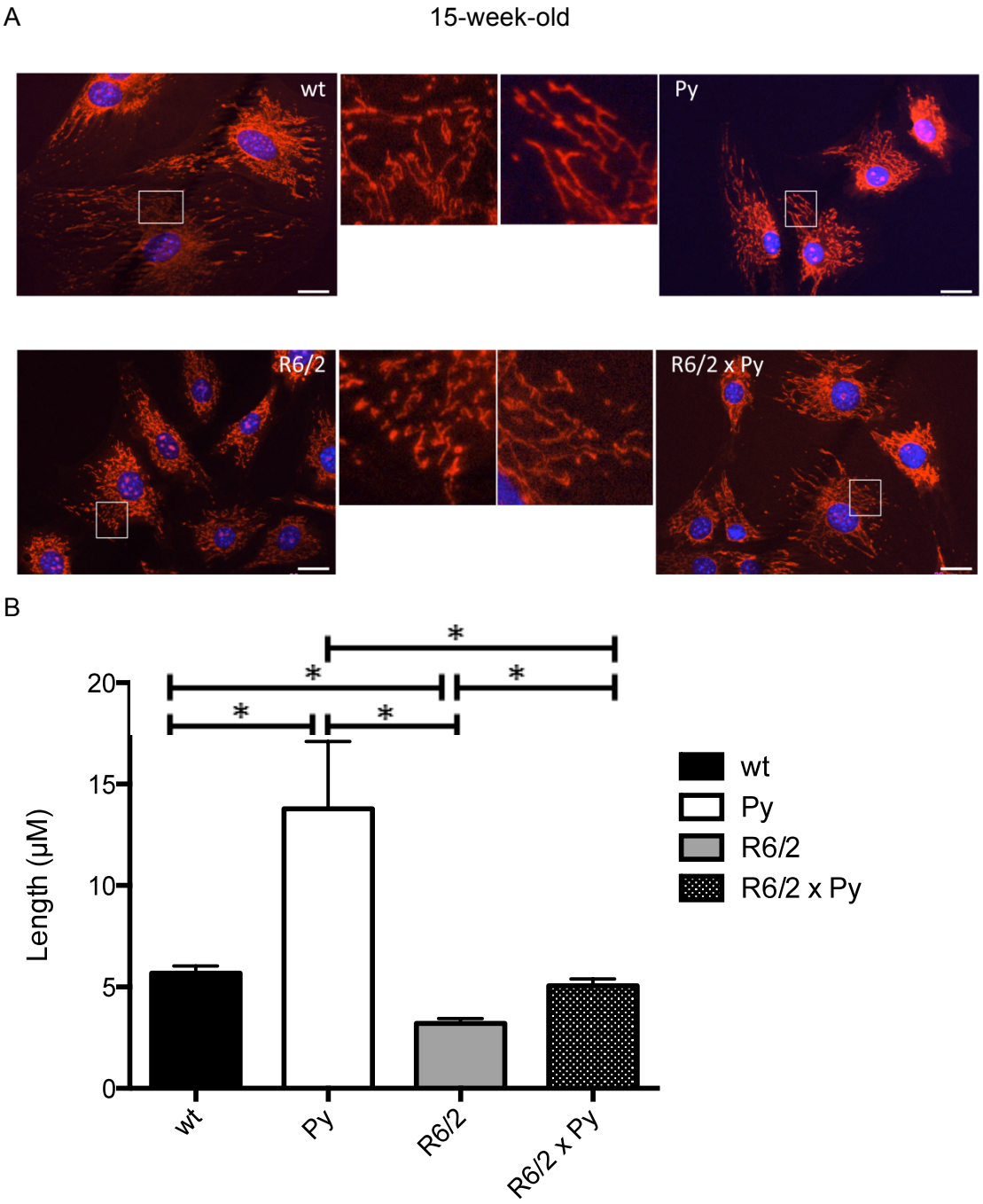

Figure 6.2. Mitochondrial morphology in 15-week-old R6/2 mice is restored by the introduction of the Python mutation. (A) Fibroblasts were cultured from the tail biopsies of 15-week-old wild type, R6/2, Python and R6/2 x Python mice. Mitochondria were stained with MitoTracker™ Orange and nuclei were stained with Hoechst 33258. Regions enclosed by white squares are shown magnified. Scale bars represent 20µm. (B) Count of n = 50 mitochondria for lengths and were measured using ImageJ. Mitochondrial morphology in R6/2 cells was restored by the addition of the Python mutation. Statistical analyses are displayed in Table 6.1.

Table 6.1. Statistical analyses for mitochondrial length.

	5-week-old	15-week-old
wt : Py	*P*<0.0001	*P*=0.0169
wt : R6/2	*P*<0.0001	*P*<0.0001
wt : R6/2 x Py	*P*=0.8875	*P*=0.2051
Py : R6/2	*P*<0.0001	*P*=0.0019
Py : R6/2 x Py	*P*<0.0001	*P*=0.0103
R6/2 : R6/2 x Py	*P*<0.0001	*P*<0.0001

Student's t tests were used to compare mitochondrial lengths of each genotype in the above combinations. Values highlighted in yellow denote significance.

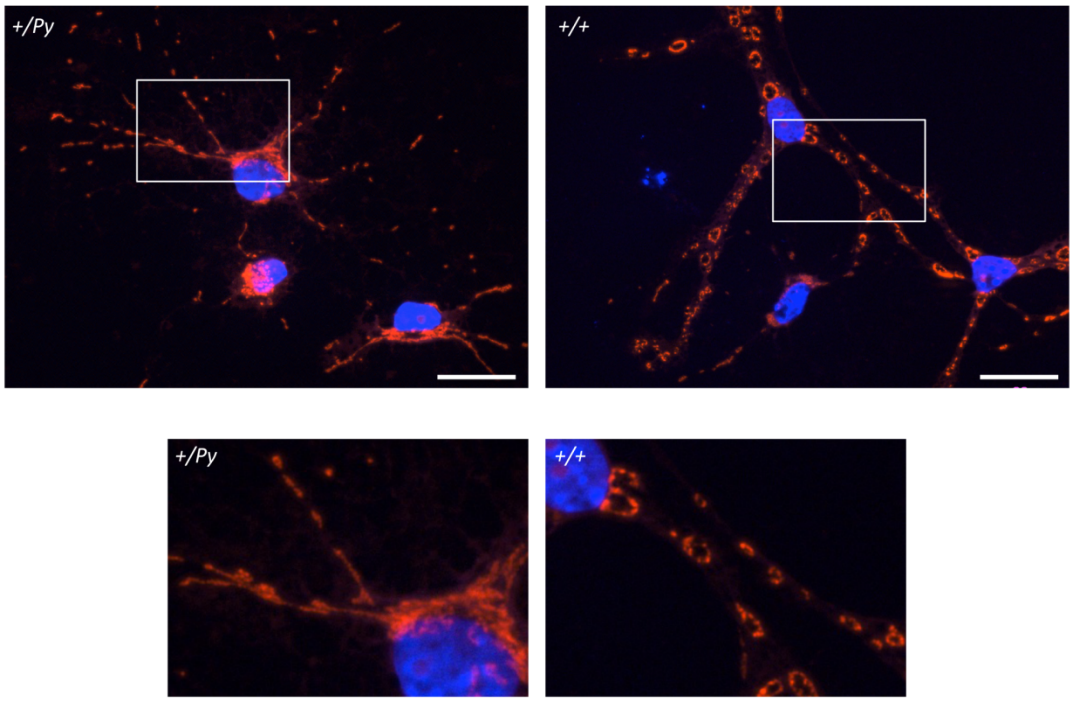

Figure 6.3. Mitochondrial elongation and nuclear aggregation in Python neurons. Neurons were cultured from 2-day-old Python and wild type neonates. Mitochondria were stained with MitoTracker™ Orange and nuclei were stained with Hoechst 33258. Regions enclosed with white squares are shown magnified. Scale bars represent 20μm.

6.2.2 Introduction of the Python mutation does not alter HD symptoms.

Severe declines in body weight and grip strength are initial signs of HD onset, accompanied with atrophy, in particular, of the brain. Body weights and grip strength were monitored until the onset of severe HD symptoms at

approximately 15 weeks. If the Python mutation was to improve the health of R6/2 mice, then HD symptoms would appear later on, or be less severe. In a cohort of over 70 mice of both sexes, R6/2 x Python mice were observed to exhibit the same severity and progression of symptoms to those of R6/2 mice.

Body weights of R6/2 and R6/2 x Python mice showed a progressive decline from the age of 11 weeks, whereas wild type and Python mice continued to gain weight. This was evident in both males and females (Fig. 6.4). At the age of 15 weeks the weight decline in both R6/2 and R6/2 x Python mice resulted in a weight reminiscent of 5-week-old mice. Python mice actually show lower weight gain from the age of 8-9 weeks onwards, in comparison to wild type mice, revealing another phenotype in Python mice.

Forelimb grip strength measurements revealed a natural decline of grip strength with age for all mice. However from the age of 12-weeks-old, R6/2 and R6/2 x Python mice displayed significantly greater declines in grip strength in comparison to wild type controls but there was no difference between R6/2 and R6/2 x Python mice (Fig. 6.5).

Brain weights were measured at 15 weeks of age for all mice. Atrophy of the brain in R6/2 mice was evident as reflected in decreased weight (Fig. 6.6), consistent with previous reports (Cepeda-Prado *et al*., 2012). No improvement is observed in mice possessing the R6/2 transgene and the Python mutation (Fig. 6.6). Interestingly in male mice, combining the 2 mutations reduces the brain weight even further (Fig. 6.6B), (Table 6.2). However this is not replicated in female mice (Fig. 6.6A), (Table 6.2). If the Python mutation alone reduced brain weight, this might explain that in combination with the R6/2 transgene, the severity of brain atrophy would increase, but the reduction seen between wild type and Python mice is not significant in females (Fig. 6.6A) nor males (Fig. 6.6B) (Table 6.2).

It was also noted that during the experiment, upon handling of mice by the tip of the tail, hind limb clasping was evident in the R6/2 and R6/2 x Python mice from 7 weeks of age. Clasping progressively worsened for both genotypes with a more rapid clasping response to handling and progression to 4-limb clasping.

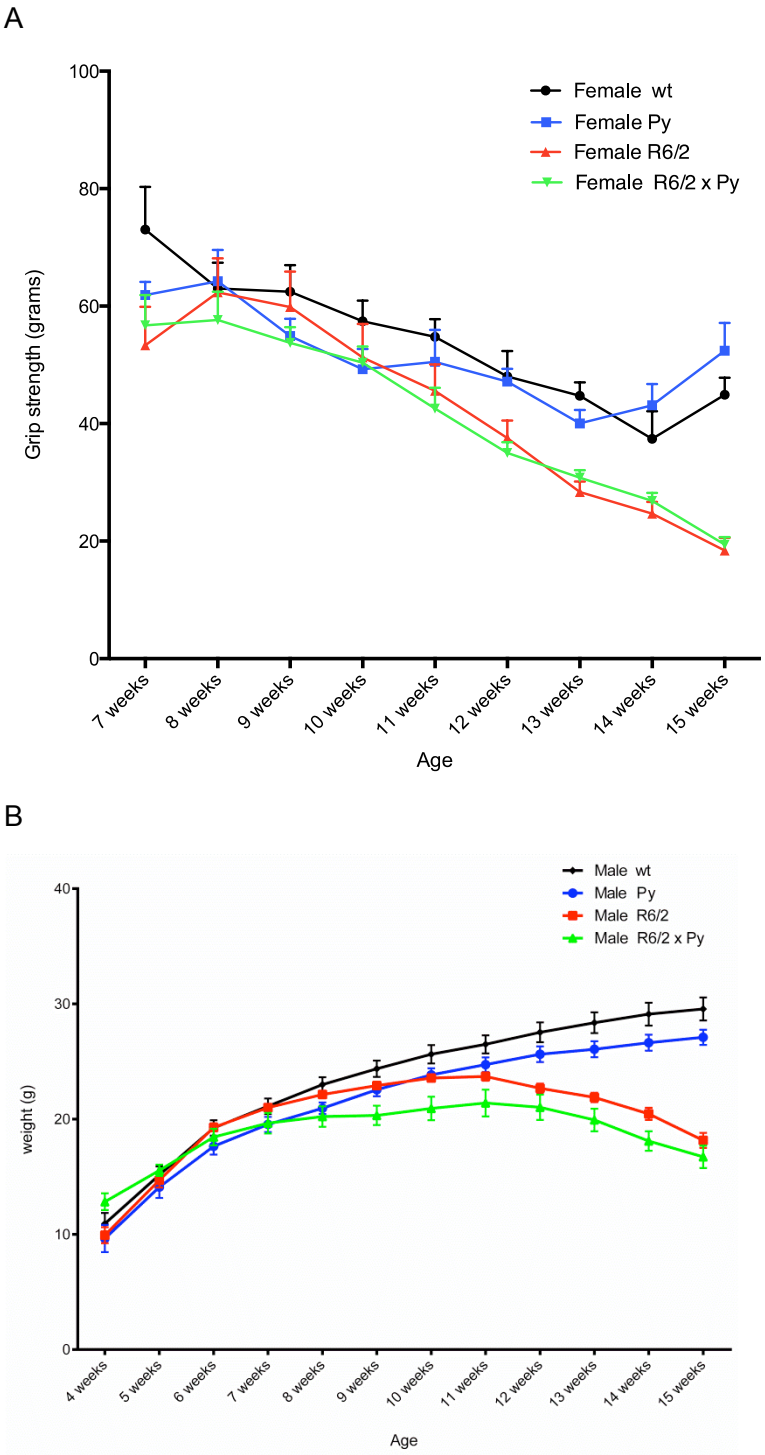

Figure 6.4. **A progressive decrease in body weight for R6/2 mice is not rescued by the presence of Python.** Mice were weighed twice a week from 3-weeks-old until the onset of HD symptoms. From 11 weeks, body weight begins to decline for both R6/2 and R6/2 x Python female (A) and male (B) mice.

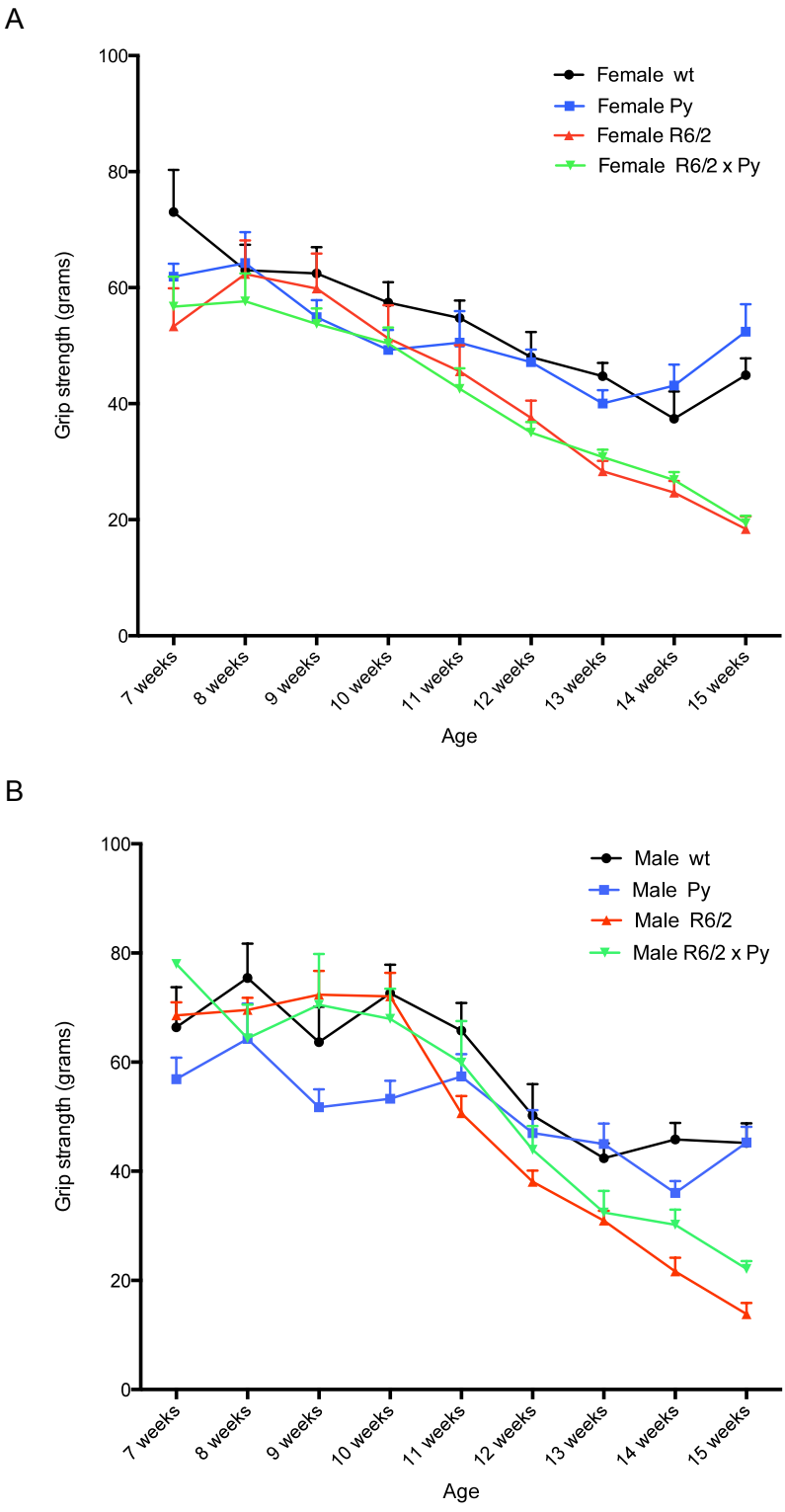

Figure 6.5. Decline in grip strength in R6/2 mice is not improved by the presence of Python. Grip strength was measured from the age of 7-weeks until culling of mice at 15 weeks of age.

A

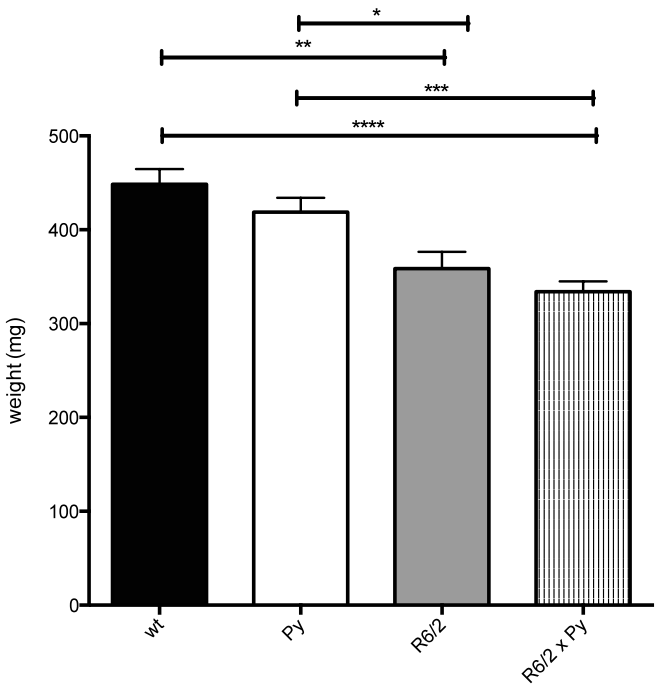

B

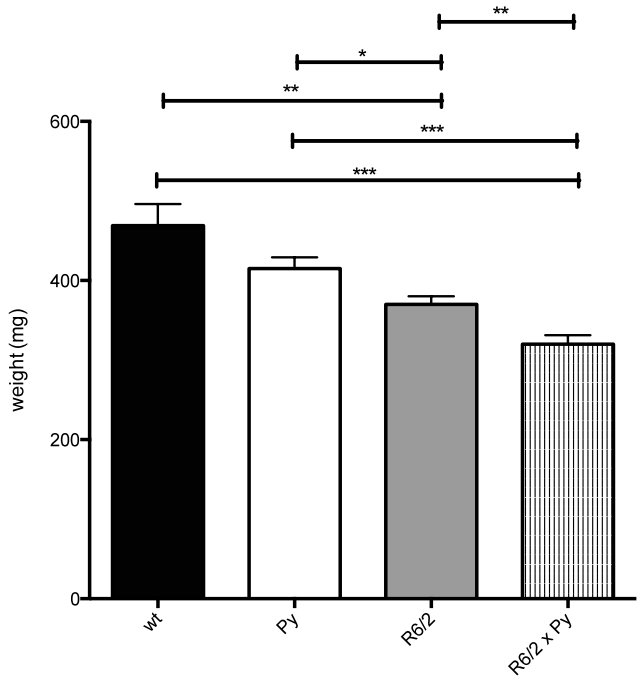

Figure 6.6. Brain weights severely reduced in the presence of the R6/2 transgene. Whole brains were extracted from mice at 15 weeks of age for all genotypes. A reduction in weight is apparent when either the Python mutation or more so, the R6/2 transgene is present. When both mutations are present the brain weight is reduced even further in males (B), though not significantly in females (A). Asterisks denote level of significance.

Table 6.2. Statistical analyses for brain weights.

	Female	Male
wt : Py	*P*=0.2009	*P*=0.1119
wt : R6/2	*P*=0.0028	*P*=0.0026
wt : R6/2 x Py	*P*<0.0001	*P*=0.0101
Py : R6/2	*P*=0.0228	*P*=0.0172
Py : R6/2 x Py	*P*=0.0003	*P*=0.0003
R6/2 : R6/2 x Py	*P*=0.2365	*P*=0.0070

Student's t tests were used to compare brain weights of each genotype in the above combinations. Values highlighted in yellow denote significance.

6.2.3 HTT aggregation remains in R6/2 x Python cortex

Mutant HTT (mHTT) protein is expressed throughout the brain of HD patients (Aronin *et al*., 1995), but neuronal degeneration is localised to the striatal and cortical regions. Aggregation of mHTT was shown to develop selectively in the cortex and striata of HD symptomatic patients and proposed as a possible reason for neuronal cell death (DiFiglia *et al*., 1997). Nuclear aggregates have also been reported in R6/2 transgenic mice (Davies *et al*., 1997). These aggregates are insoluble and therefore detectable by Western blot in the insoluble fraction of an SDS polyacrylamide gel. Examination of the level of mHTT protein aggregation was detected by Western blot of cortical protein extracts (Fig. 6.7). The antibody used, mEM48, preferentially binds to mHTT. Aggregation of the mutant protein was shown to remain in R6/2 x Python mice as much as in R6/2 mice. This may help to explain why an improvement in HD symptoms was not seen when combining the Python mutation with the R6/2 transgene.

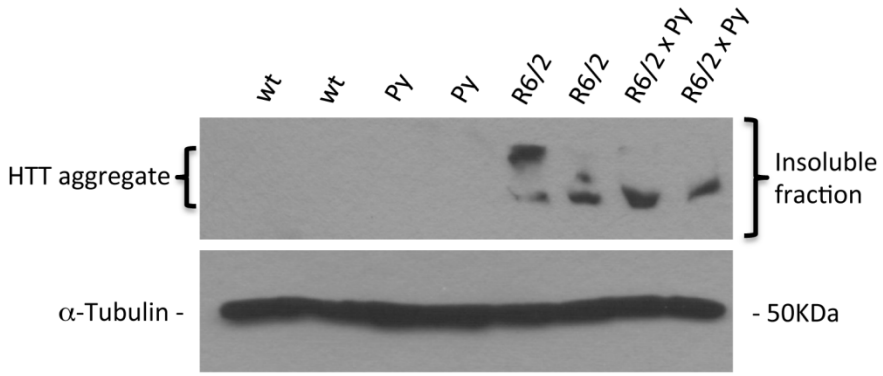

Figure 6.7. HTT aggregation in the cortex of R6/2 and R6/2 x Python mice. Proteins were extracted from the cortex of 15-week-old mice. Mutant HTT protein was detected with the mEM48 antibody. HTT aggregates were present in the insoluble fraction of the SDS PAGE gel in samples from R6/2 and R6/2 x Python mice. α-Tubulin levels were detected to normalise for cell number.

6.2.4 ATP levels are reduced in R6/2 and R6/2 x Python striata

There is evidence to suggest that impaired energy metabolism via mitochondrial dysfunction may also be responsible for the disease phenotype (Beal, 2005). Impaired mitochondrial ATP production has been detected in striatal neurons from HD patients (Tabrizi *et al*., 1999), and brain tissue of the transgenic R6/2 mouse (Smith *et al*., 2006). However it is unknown whether a reduction in ATP production is a cause of, or a consequence of, neuronal cell death. Preserved mitochondrial OXPHOS activity early in HD when neuronal cell loss is already present provides an argument for the latter (Powers *et al*., 2007, Guidetti *et al*., 2001).

We therefore wished to examine ATP levels in the R6/2 x Python mouse to see if the Python mutation was able to restore ATP production. Whole brain and striatal lysate was measured for ATP levels by a luciferase assay. No difference was observed in whole brain lysate between all 4 strains of mice (Fig. 6.8A), however when selectively measuring ATP levels in striatal lysate, there is a clear reduction exhibited by R6/2 mice compared to wild type or Python mice. The reduction of R6/2 striatal ATP concentration is not improved by the presence of the Python mutation (Fig. 6.8B).

A

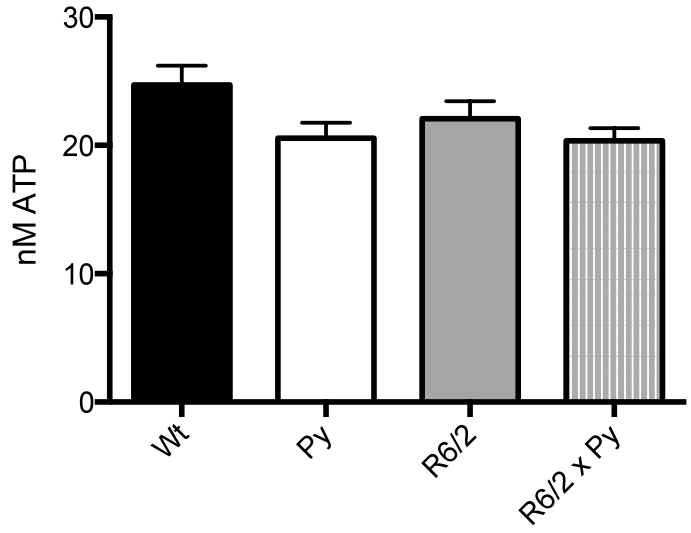

B

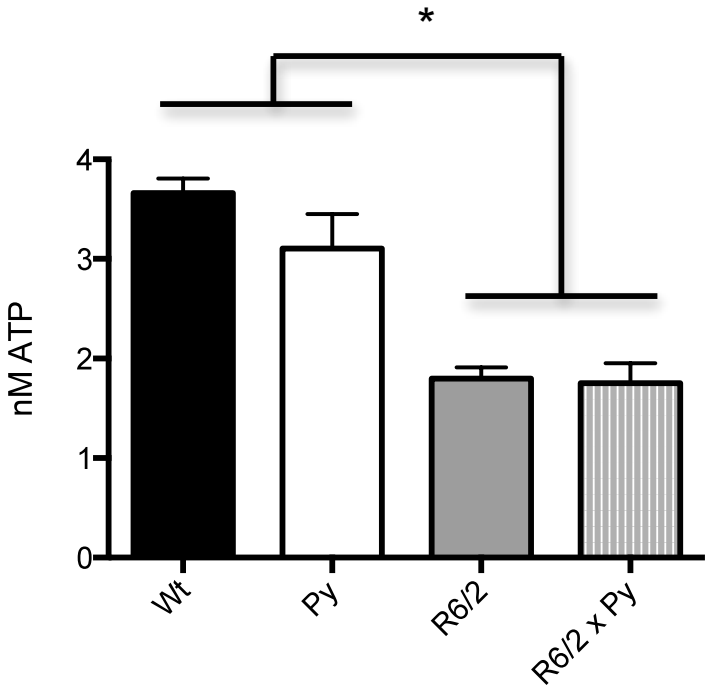

Figure 6.8. ATP is reduced in the striata of R6/2 and R6/2 x Python mice. Whole brains (A) and striata (B) were lysed and subsequently measured for ATP levels via a luciferase assay. No difference was found between whole brains of wild type, Python, R6/2 and R6/2 x Python mice (A) (One-way ANOVA, $P>0.05$ for all comparisons). However R6/2 and R6/2 x Python striata exhibited lower ATP levels when compared to wild type and Python striata (B) (One-way ANOVA, $P<0.01$ when comparing wt or Py with R6/2 or R6/2 x Py). n=3 for (A) and (B). The results represent ATP levels in 1.75µg of whole brain proteins and 160ng of striatal proteins.

6.2.5 The R6/2 transgene does not increase DNM1L levels in Python mice.

It may be that Python does not alter the presumptive increased DNM1L activity caused by the R6/2 transgene. There was no direct readout possible for DNM1L activity in mice. However, cellular DNM1L levels could be measured by Western blot analysis. Proteins were extracted from the heart, brain and rectus femoris and Western blotted to detect levels of DNM1L protein expression. Mice that contain the Python mutation (Py and R6/2 x Py) exhibit lower total DNM1L protein levels when compared to wild type or R6/2 mice (Fig. 6.7) suggesting that introduction of the Python mutation was resulting in lower DNM1L levels in double mutant mice compared to R6/2 mice. By extension, DNM1L activity might be reduced in the R6/2 x Python mice compared to R6/2 alone given the reduced DNM1L levels. Regardless, introduction of *Dnm1l*^{Py} was not able to correct for the adverse effects of the R6/2 transgene.

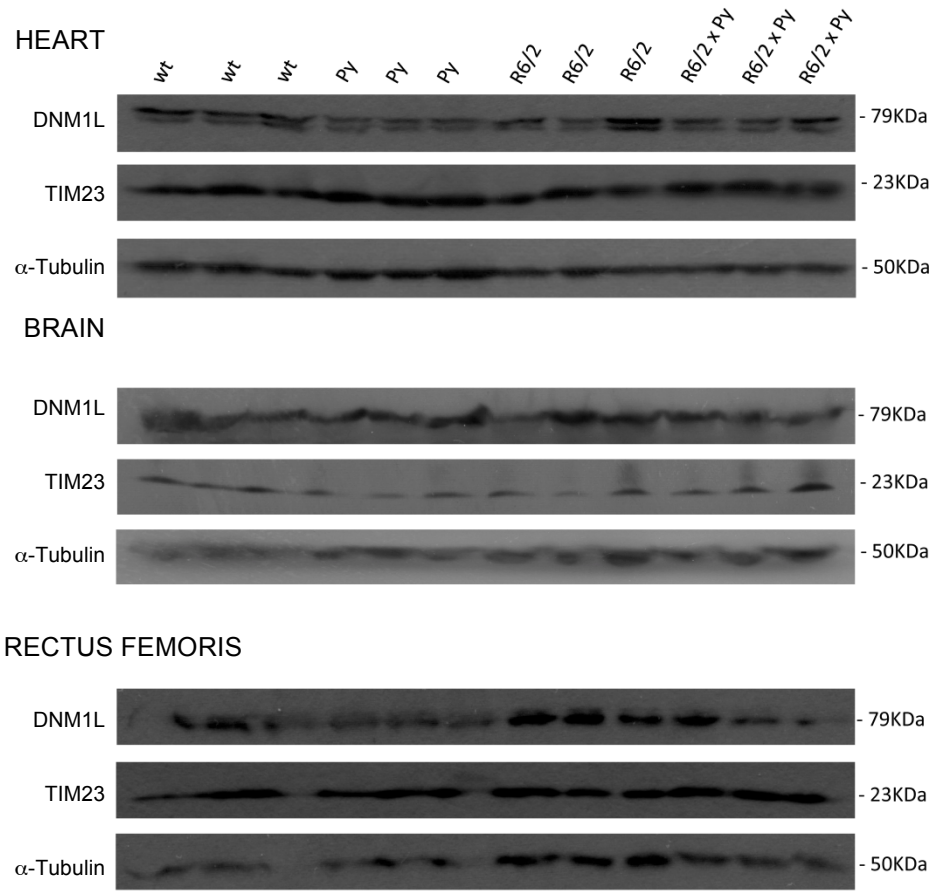

Figure 6.9. Lower cellular Dnm1l levels in R6/2 x Python. DNM1L protein levels were detected in proteins extracted from the heart, brain and rectus femoris of 15-week-old Python x R6/2 mice. α-Tubulin and TIM23 were detected to normalise for cell number and mitochondrial number, respectively.

6.3 Discussion

HD is characterized by striatal neuron degeneration (Vonsattel and DiFiglia, 1998). The mutation responsible for this disorder is a polyQ repeat expansion of exon 1 of the *HTT* gene. The greater the number of repeats, the more severe the phenotype (Duyao *et al*., 1993). The R6/2 mouse model of HD, which expresses exon 1 containing 144 polyQ repeats of the human *HTT* gene, has been a useful model due to the rapid onset of HD symptoms (Mangiarini *et al*., 1996).

Recently, abnormalities in mitochondrial morphology and DNM1L activity have been implicated in HD. An increased interaction between mutant HTT and DNM1L induces translocation to the OMM and GTPase activation, leading to increased fragmentation of the mitochondria (Song *et al*., 2011). Dephosphorylation of DNM1L by the increased activity of calcineurin also increases the translocation and activity of DNM1L (Costa *et al*., 2010). By restoring mitochondrial morphology, through expression of the dominant-negative version DNM1L^{K38A} has been reported to reverse defects within the cell such as mitochondrial anterograde and retrograde movement and neuronal apoptosis (Song *et al*., 2011). It is therefore possible that overexpression of a mutant DNM1L displaying decreased GTPase activity may ameliorate HD symptoms be correcting the defect of hyperactive DNM1L activity.

To test this hypothesis, R6/2 mice were crossed with Python mice to produce offspring containing both mutations. Mitochondrial morphology was shown to be restored to that of wild type length in fibroblasts, though the extent to which the Python mutation corrects mitochondrial morphology in neuron remains unknown. Progressive HD symptoms such as decreased body weight, decreased grip strength, clasping and decreased brain weight revealed the presence of HD symptoms were unchanged. Data provided in the literature for R6/2 body weights is somewhat variable. Although weight gain has been observed to be reduced in R6/2 mice from 8 weeks of age, the animals did not always lose weight (Bett *et al*., 2006, Hockly *et al*., 2006). In another study, weight loss becomes apparent by 10 weeks old in the R6/2 males, but not until 12 weeks in females, with the loss in males being far more dramatic (Hockly *et*

al., 2003). The current study presents data displaying a drop in body weight from 12 weeks in males and 13 weeks in females in accordance with a more prominent loss in males.

Grip strength studies also display some variation. In one study, grip strength increases with age for both wild type and R6/2 animals, but with a significantly lower increase in R6/2 mice after 10 weeks of age (Bett *et al*., 2006). In a separate study, grip strength shows a progressive decline with age for all mice, with R6/2 mice displaying significantly greater decline from 9 weeks of age (Hockly *et al*., 2006). In agreement with the latter, grip strength was shown to decline with age for all mice, wild type included, in the current study. Those possessing the R6/2 transgene exhibited a greater decrease by 13 weeks of age.

PolyQ aggregates have been reported to accumulate in the nuclei of the cortex and striatum of HD individuals (DiFiglia *et al*., 1997, Gutekunst *et al*., 1999, Maat-Schieman *et al*., 1999) and in R6/2 mice as early as 4 weeks of age (Davies *et al*., 1997, Li *et al*., 1999b). HTT aggregation was confirmed in the R6/2 mouse cortex, which showed no improvement when the Python mutation was also present. However mHTT aggregation was not detectable in the striata of R6/2 or R6/2 x Python mice during this study. It has been suggested that aggregation of the mutant protein occurs initially in the cortex. As striatal aggregates are detected more rarely, their formation may lead to sudden neuronal death in the striata, making detection more difficult (Gutekunst *et al*., 1999). It would also be necessary to investigate the distribution of this aggregation by immunohistochemistry of brain sections in mice containing the R6/2 transgene and the Python mutation to see if it was altered at all.

Impaired ATP production has been shown to be present in the striatal neurons of HD patients (Tabrizi *et al*., 1999) and has also been replicated in the brain of the R6/2 mouse (Smith *et al*., 2006), though this impairment is likely to be a result of neuronal cell death given that striatal demise is detected earlier than mitochondrial dysfunction (Powers *et al*., 2007, Guidetti *et al*., 2001). Contrary to the study of Smith *et al* (2006), in the current study, ATP levels showed no alteration between whole brains of wild type and R6/2 mice.

However measuring ATP levels of the striatal regions revealed a significant reduction, which was not improved by the introduction of the Python mutation.
It's clear that reducing mitochondrial fission in the R6/2 mouse has not improved behavioural symptoms or the molecular biological consequences of progressive HD. Despite these results, ameliorating HD symptoms by expression of a mutant form of DNM1L should not be excluded as a potential useful amelioration factor; it may require a fine balance in the expression levels of DNM1L^{Py} to have a positive effect on the improvement of HD symptoms.

Chapter 7 : General discussion

A mutation named Python was generated in mice by means of a large-scale ENU mutagenesis screen. The mutation is located in exon 11 of the *Dnm1l* gene. Although the protein is ubiquitously expressed, an apparent heart-specific energy-deficient phenotype is the result in mice heterozygous for the mutation. The phenotype manifests itself in an age-dependent manner from around 5 weeks of age, eventually triggering the onset of congestive heart failure (CHF). Homozygous Python mice, however, die during embryogenesis. Investigations of the *Dnm1l*^{Py} mutation were intended to ascertain (i) how the mutation leads to an alteration in the normal activity of the DNM1L protein; (ii) how this altered activity affects the normal cellular function(s) of this protein and, ultimately (iii) how the altered cellular functions lead to heart failure.

7.1 How the Python mutation alters DNM1L activity

DNM1L is involved in the process of mitochondrial fission. Reduced DNM1L protein levels were observed in the hearts and brains of Python heterozygotes, however the Python allele was shown to be expressed in equal amounts to the wild type allele at the mRNA level in both tissues and therefore likely to be expressed in equal amounts at the protein level. The mutation completely abrogates the interaction between the M and GED domains within the DNM1L monomer. Due to misfolding of the protein, DNM1L may be targeted for degradation, leading to a decrease in DNM1L levels in the cell. Defective intramolecular interactions are also likely to effect interactions with other proteins, one of which - UBC9 - is an important substrate for sumoylation and subsequent translocation to the outer mitochondrial membrane (OMM). These findings, together with decreased DNM1L protein levels, suggest that translocation to the OMM could be impaired. Interactions with the docking protein, MFF were also shown to be completely abrogated, and so if the Python protein is able to translocate via other post-translational modifications, the ability of the fission protein to remain stable on the OMM is likely to be reduced.

DNM1L self-assembly relies on contact between DNM1L assembly units on the OMM to form a polymer around the membrane. As a result of decreased stability on the OMM, the Python mutation is likely to impair the ability of Dnm1l to form higher-order structures. This in turn can lead to various defects. Assembly into higher order structures is required for maximal GTPase activity (Muhlberg *et al*., 1997, Smirnova *et al*., 1998). Consequently GTPase activity exhibited by the Python protein would be further reduced.

The Python mutation probably acts in a dominant negative fashion. It was shown that the mutant protein could still interact with the wild type protein, thereby forming dimers. However, the GTPase activity of wild type DNM1L was reduced by the presence of DNM1L^{Py}. This dominant negative activity explains why the heterozygous phenotype is less severe than the homozygous phenotype, and why the homozygous phenotype is generally similar to the homozygous DNM1L-null phenotype (Ishihara *et al*., 2009, Wakabayashi *et al*., 2009). One difference between homozygous phenotypes of *Dnm1l*$^{Py/Py}$ and *Dnm1l*$^{-/-}$ mutations was noticeable though; failure of *Dnm1l*$^{Py/Py}$ embryo fibroblasts to proliferate compared to normal proliferation of *Dnm1l*$^{-/-}$ fibroblasts (Ishihara *et al*., 2009, Wakabayashi *et al*., 2009). This difference may be the consequence of novel molecular functions of the protein encoded by *Dnm1l*^{Py}.

Reduced stability on the OMM and reduced GTPase activity naturally leads to a reduction in mitochondrial fission, thereby resulting in mitochondrial elongation. This was confirmed in mutant fibroblasts and ES cells, and also in HeLa cells transfected with a construct containing the mutated version of *Dnm1l* cDNA. Peroxisomal and ER morphology also appear to be abnormal as a result of the Python mutation.

7.2. How the Python mutation might result in energy dysregulation.

The ability of DNM1L to remain stable on the OMM might be critical for the process of tethering between mitochondria and the ER, given that DNM1L has been shown to interact with the ER at sites of mitochondrial fission (Friedman *et al*, 2010). The reduced amount of DNM1L on mitochondria in Python fibroblasts suggests a possible reduction in the tethering capability of

mitochondria and the ER though further work would be necessary to confirm this e.g. detailed imaging of mitochondrial-ER contact points in cells. If tethering were reduced, mitochondria might be unable to remain in close proximity to the ER. When Ca^{2+} is then released from the ER, the increased distance between the mitochondria and the ER is likely to cause reduced mitochondrial Ca^{2+} uptake. A reduced mitochondrial Ca^{2+} uptake was shown to be the case in ES cells. Independently, collaborators confirmed a similar phenotype in immortalized Python fibroblasts (Dr. Houman Ashrafian and Dr. Tom Cahill, University of Oxford; Dr. John Boyle, University of Leeds, unpublished data). As a result, key enzymes of mitochondrial respiration, which are regulated by Ca^{2+}, display a progressive decline in activity over time. Fewer protons would be pumped into the intermembrane space, reducing the mitochondrial membrane potential (MMP). The MMP is directly used in ATP production and also mitochondrial Ca^{2+} uptake.

ATP was shown to be reduced in the heart, but not brain or liver in the heterozygous Python mouse. In the C57BL/6J strain, there was an age-related reduction in oxidative phosphorylation (OXPHOS) activity in Python mice. This corresponded to an age-related increased protein expression of Dnm1l in the heart, which wasn't observed in the brain. This may signify a function for Dnm1l that is either specific to the heart or greatly increases in importance in the heart with age. Eventually, the effect of the Python mutation leads to a reduction in ATP production beyond survival capabilities, while other cells are able to maintain viability. In addition, because the MMP becomes compromised as a result of defective mitochondrial Ca^{2+} uptake, this not only directly reduces ATP production, but also reduces further mitochondrial Ca^{2+} uptake via the mitochondrial Ca^{2+} uniporter (MCU), which is dependent on MMP (Hansford and Zorov, 1998). This will lead to a gradual reduction in mitochondrial Ca^{2+} uptake and a subsequent progressive reduction in the efficiency of enzyme activity across the electron transport chain (ETC), leading to a progressive decline in ATP production. It may be that during this gradual decline, as long as ATP production stays above a threshold, heart function is sufficient for survival. However, when ATP production drops below a threshold, which may be higher in cardiomyocytes given their high energy requirements, ATP production begins to fail and the mouse develops CHF.

Mitophagy was investigated as alterations in mitochondrial morphology can alter mitophagy and subsequently lead to energy dysregulation (Chen *et al*., 2009, Gomes *et al*., 2011). One purpose of mitochondrial fission might be to segregate parts of the mitochondria that are beyond repair, exposing them for mitophagy and recycling of the components. If this process is hindered then mitochondria containing mutated mtDNA and depolarized membranes may accumulate within a cell, causing mitochondrial dysfunction. No evidence was found in this study to suggest that mitophagy is altered nor were specific mtDNA deletions identified in Python tissues, though for the latter the method used was relatively insensitive. Further investigations may be required to clarify the effect of Python on mitophagy, such as experiments to identify single base pair mutations or small deletions in the mtDNA genome, and analysis of autophagic markers in terminal mice.

7.3 How dilation might result from energy dysregulation

Cardiac hypertrophy is a normal physiological process that enables the heart to increase in size after birth. Myocyte enhancer factor-2 (MEF2) is an important protein in this process (Lin *et al*., 1997, Kolodziejczyk *et al*., 1999), while transcription factor GATA-4 is important in myocardial differentiation. Pathological consequences occur when hypertrophy increases beyond control and as a result cardiac function is diminished. Dilation of the heart results from cardiomyocyte hypertrophy where cardiomyocyte length increases far more than cardiomyocyte width (Fig. 7.1). This is in contrast to hypertrophic cardiomyopathy, where the increase in cardiomyocyte width is greater than cardiomyocyte length (Fig. 7.1). It has been proposed that hypertrophic stimuli result from energy dysregulation and subsequent higher cytosolic Ca^{2+} concentrations.

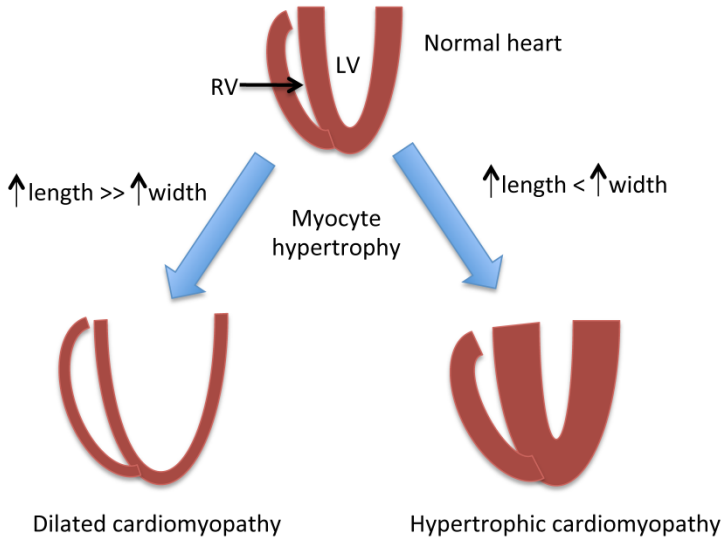

Figure 7.1. The effect of myocyte hypertrophy. In dilated cardiomyopathy, myocytes exhibit hypertrophy with the increase in length being much larger than the increase in myocyte width, resulting in thinner walls. In contrast hypertrophic cardiomyopathy results from myocyte hypertrophy when the increase in width is larger than the increase in length, leading to much thicker walls. LV: left ventricle, RV: right ventricle.

Python cells were shown to exhibit higher cytoplasmic Ca^{2+} concentrations. This is a likely result from two main defects: (i) reduced mitochondrial Ca^{2+} uptake as a result of possible decreased tethering between the ER and mitochondria and (ii) reduced sarcoplasmic/endoplasmic reticulum ATPase (SERCA) activity. Normally, during diastole, the sarcoplasmic reticulum (SR) in cardiomyoyctes will take up Ca^{2+} from the cytosol via the SERCA. This process requires ATP and given that ATP production is impaired as a result of the Python mutation, Ca^{2+} re-uptake by the SR will also be reduced, again leading to an increased cytosolic Ca^{2+} concentration. As both of these defects will progressively become more severe, the cytosolic Ca^{2+} concentration is likely to continue to increase.

Calcineurin becomes activated by cytosolic Ca^{2+} when bound to the Ca^{2+} adapter protein, calmodulin. Upon activation, calcineurin dephosphorylates Nuclear Factor of activated T cells (NFAT), leading to translocation to the nucleus (Clipstone and Crabtree, 1992, Okamura *et al.*, 2000). NFAT is only capable of weak binding to DNA directly, and is, therefore, prone to binding to other nuclear transcription factors such as MEF2 and

GATA4 in order to strengthen DNA binding capability (Hogan *et al*., 2003) Activated calcineurin also mediates MEF2 activation. Calcineurin activation is therefore regarded as a hypertrophic regulator. The increased cytosolic Ca^{2+} concentration in Python cells may increase calcineurin activity and lead to the overexpression of prohypertrophic proteins such as NFAT, MEF2 and GATA4, leading to uncontrolled hypertrophy of the heart. In Python this hypertrophy increases myocyte length far more than width leading to dilation. As the cytosolic Ca^{2+} concentration increases with age, expression of prohypertrophic proteins might also increase. In the Python mouse, this pathway might lead to myocardial dilation, the severity of which increases over time until the heart exhibits severe dysfunction and is no longer capable of sufficient contractile function. Summary of the possible pathway from Python to dilated cardiomyopathy is displayed in Figure 7.2.

Further investigations are required to deduce what downstream signals are altered by increased cytosolic Ca^{2+} concentration in Python cells, but a starting point would be to examine the activity of calcineurin,

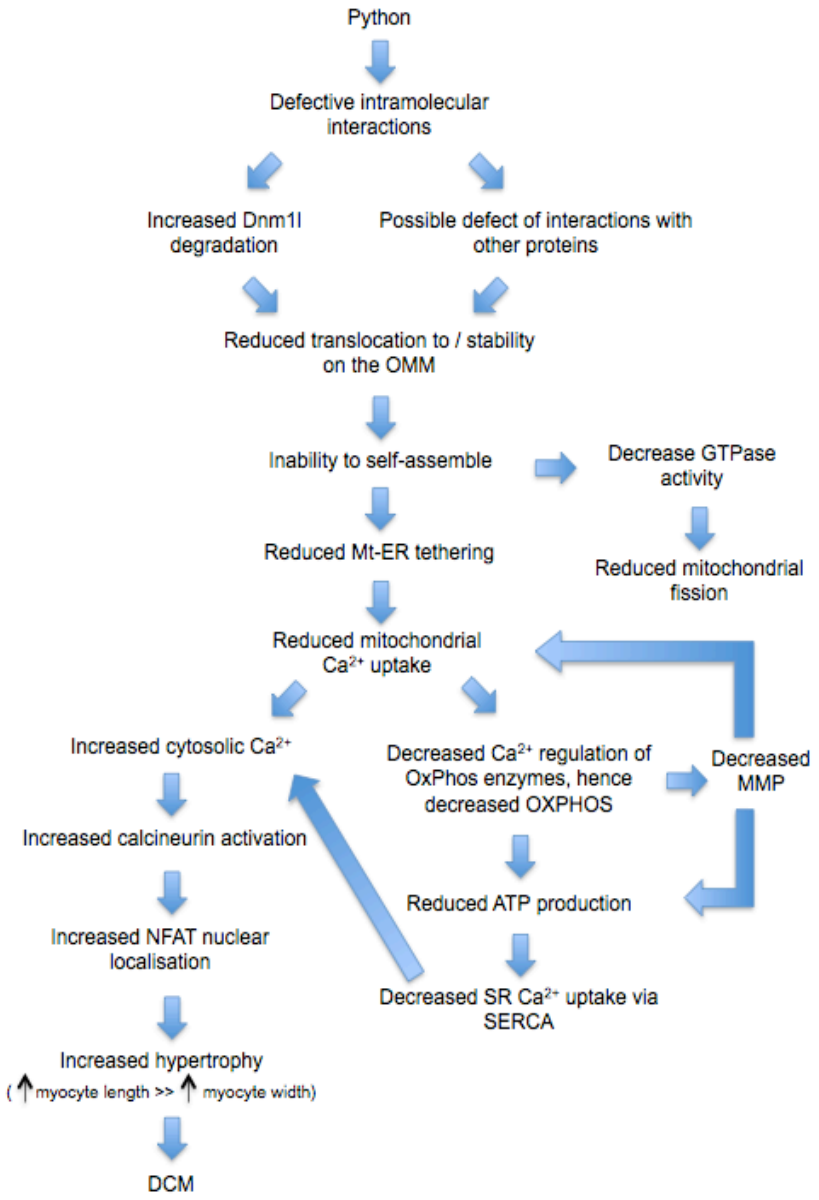

Figure 7.2. Summary of a possible pathway in which the Python mutation leads to DCM. The Python mutation impairs intramolecular interactions possibly leading to increased DNM1L degradation and abrogation of interactions with UBC9 and MFF. This leads to reduced translocation/stability on the OMM, decreasing oligomerisation, GTPase activity and mitochondrial fission. ER-mitochondrial tethering is also impaired leading to defective mitochondrial Ca^{2+} uptake and reduced OXPHOS enzyme efficiency, hence reduced ATP production. The MMP will also be reduced as a consequence of decreased proton pumping by OXPHOS enzymes, which progressively reduces the mitochondrial Ca^{2+} uptake leading to a gradual decline in the efficiency of OXPHOS. This may lead to a gradual increase in cytosolic Ca^{2+}, triggering prohypertrophic protein expression via calcineurin-NFAT activation, ultimately resulting in DCM.

7.4 DNM1L^{Py} does not appear to ameliorate the symptoms of Huntington's disease in R6/2 mice

A sideline of the studies on the Python mice was that it might be a model by which to investigate a recent theory for the basis of Huntington's disease (HD). Mitochondrial morphology in fibroblasts and lymphocytes of HD patients has been shown to exhibit excessive mitochondrial fragmentation. Increased DNM1L activity was also found. Mutant HTT is able to bind directly to DNM1L and stimulate its translocation to the OMM and subsequent GTPase activity (Song *et al*., 2011). In addition, calcineurin activation was also increased, which further triggers DNM1L for translocation via dephosphorylation (Costa *et al*., 2010). In vitro, neuronal cell death can be prevented by the correction of the mitochondrial morphology (Song *et al*., 2011). As a result of these studies, it has been postulated that reducing activity of DNM1L in HD patients might improve symptoms.

To test this theory *in vivo*, the R6/2 mouse model was used. This is an extensively characterized model of HD that expresses exon 1 of the human *HTT* gene containing 144 polyQ repeats (Mangiarini *et al*., 1996). R6/2 male mice were mated with Python female mice to create offspring harboring both the R6/2 transgene and the Python mutation. DNM1L activity was reduced and mitochondrial morphology restored in fibroblasts, however symptoms of HD remained as severe in the R6/2 x Python mice as in the R6/2 mice. This may imply that mitochondrial morphology is not a cause of HD or that the fusion/fission balance was not restored to the appropriate degree. Furthermore, fibroblasts were used to examine mitochondrial morphology defects and it will be necessary to examine mitochondrial morphology in striatal neurons of R6/2 x Python mice as striatal degeneration is a hallmark of HD.

7.5 Future studies on the Python model of DCM

The work reported in this thesis has provided insight into DNM1L^{Py} protein biology and how this leads to energy dysregulation in the heart. Future experiments regarding Python as a model of DCM will endeavor to unravel the molecular mechanisms by which energy dysregulation leads to dilation of the myocardium. Deducing the molecular pathway by which DNM1L participates in Ca^{2+} regulation might identify novel targets for therapy of DCM and similar cardiac disorders.

It has also been demonstrated that the age of onset of CHF is dependent on strain background (Ashrafian *et al*., 2010). This indicates that there are other genetic factors that influence the age of onset of CHF in the Python model. Identifying such factors (by QTL analysis) would provide further insights into the development of CHF.

References

AKEPATI, V. R., MULLER, E. C., OTTO, A., STRAUSS, H. M., PORTWICH, M. & ALEXANDER, C. 2008. Characterization of OPA1 isoforms isolated from mouse tissues. *J Neurochem,* 106**,** 372-83.

ALAVI, M. V., BETTE, S., SCHIMPF, S., SCHUETTAUF, F., SCHRAERMEYER, U., WEHRL, H. F., RUTTIGER, L., BECK, S. C., TONAGEL, F., PICHLER, B. J., KNIPPER, M., PETERS, T., LAUFS, J. & WISSINGER, B. 2007. A splice site mutation in the murine Opa1 gene features pathology of autosomal dominant optic atrophy. *Brain,* 130**,** 1029-42.

ALAVI, M. V., FUHRMANN, N., NGUYEN, H. P., YU-WAI-MAN, P., HEIDUSCHKA, P., CHINNERY, P. F. & WISSINGER, B. 2009. Subtle neurological and metabolic abnormalities in an Opa1 mouse model of autosomal dominant optic atrophy. *Exp Neurol,* 220**,** 404-9.

ANDERSSON, S. G. & KURLAND, C. G. 1999. Origins of mitochondria and hydrogenosomes. *Curr Opin Microbiol,* 2**,** 535-41.

ARBER, S. & CARONI, P. 1996. Specificity of single LIM motifs in targeting and LIM/LIM interactions in situ. *Genes Dev,* 10**,** 289-300.

ARBER, S., HALDER, G. & CARONI, P. 1994. Muscle LIM protein, a novel essential regulator of myogenesis, promotes myogenic differentiation. *Cell,* 79**,** 221-31.

ARBER, S., HUNTER, J. J., ROSS, J., JR., HONGO, M., SANSIG, G., BORG, J., PERRIARD, J. C., CHIEN, K. R. & CARONI, P. 1997. MLP-deficient mice exhibit a disruption of cardiac cytoarchitectural organization, dilated cardiomyopathy, and heart failure. *Cell,* 88**,** 393-403.

ARBUSTINI, E., PILOTTO, A., REPETTO, A., GRASSO, M., NEGRI, A., DIEGOLI, M., CAMPANA, C., SCELSI, L., BALDINI, E., GAVAZZI, A. & TAVAZZI, L. 2002. Autosomal dominant dilated cardiomyopathy with atrioventricular block: a lamin A/C defect-related disease. *J Am Coll Cardiol,* 39**,** 981-90.

ARONIN, N., CHASE, K., YOUNG, C., SAPP, E., SCHWARZ, C., MATTA, N., KORNREICH, R., LANDWEHRMEYER, B., BIRD, E., BEAL, M. F. & *ET AL*. 1995. CAG expansion affects the expression of mutant Huntingtin in the Huntington's disease brain. *Neuron,* 15**,** 1193-201.

ASHRAFIAN, H., DOCHERTY, L., LEO, V., TOWLSON, C., NEILAN, M., STEEPLES, V., LYGATE, C. A., HOUGH, T., TOWNSEND, S., WILLIAMS, D., WELLS, S., NORRIS, D., GLYN-JONES, S., LAND, J., BARBARIC, I., LALANNE, Z., DENNY, P., SZUMSKA, D., BHATTACHARYA, S., GRIFFIN, J. L., HARGREAVES, I., FERNANDEZ-FUENTES, N., CHEESEMAN, M., WATKINS, H. & DEAR, T. N. 2010. A mutation in the mitochondrial fission gene Dnm1l leads to cardiomyopathy. *PLoS Genet,* 6**,** e1001000.

ASHRAFIAN, H., REDWOOD, C., BLAIR, E. & WATKINS, H. 2003. Hypertrophic cardiomyopathy:a paradigm for myocardial energy depletion. *Trends Genet,* 19**,** 263-8.

BALABAN, R. S. 2009. The role of Ca(2+) signaling in the coordination of mitochondrial ATP production with cardiac work. *Biochim Biophys Acta,* 1787**,** 1334-41.

BALOYANNIS, S. J. 2006. Mitochondrial alterations in Alzheimer's disease. *J Alzheimers Dis,* 9**,** 119-26.

BANKS, P., MANGNALL, D. & MAYOR, D. 1969. The re-distribution of cytochrome oxidase, noradrenaline and adenosine triphosphate in adrenergic nerves constricted at two points. *J Physiol,* 200**,** 745-62.

BARIS, O., DELETTRE, C., AMATI-BONNEAU, P., SURGET, M. O., CHARLIN, J. F., CATIER, A., DERIEUX, L., GUYOMARD, J. L., DOLLFUS, H., JONVEAUX, P., AYUSO, C., MAUMENEE, I., LORENZ, B., MOHAMMED, S., TOURMEN, Y., BONNEAU, D., MALTHIERY, Y., HAMEL, C. & REYNIER, P. 2003. Fourteen novel OPA1 mutations in autosomal dominant optic atrophy including two de novo mutations in sporadic optic atrophy. *Hum Mutat,* 21**,** 656.

BEAL, M. F. 1992. Does impairment of energy metabolism result in excitotoxic neuronal death in neurodegenerative illnesses? *Ann Neurol,* 31**,** 119-30.

BEAL, M. F. 2005. Mitochondria take center stage in aging and neurodegeneration. *Ann Neurol,* 58**,** 495-505.

BECANE, H. M., BONNE, G., VARNOUS, S., MUCHIR, A., ORTEGA, V., HAMMOUDA, E. H., URTIZBEREA, J. A., LAVERGNE, T., FARDEAU, M., EYMARD, B., WEBER, S., SCHWARTZ, K. & DUBOC, D. 2000. High incidence of sudden death with conduction system and myocardial disease due to laminutes A and C gene mutation. *Pacing Clin Electrophysiol,* 23**,** 1661-6.

BENARD, G., FAUSTIN, B., PASSERIEUX, E., GALINIER, A., ROCHER, C., BELLANCE, N., DELAGE, J. P., CASTEILLA, L., LETELLIER, T. & ROSSIGNOL, R. 2006. Physiological diversity of mitochondrial oxidative phosphorylation. *Am J Physiol Cell Physiol,* 291**,** C1172-82.

BETT, J. S., GOELLNER, G. M., WOODMAN, B., PRATT, G., RECHSTEINER, M. & BATES, G. P. 2006. Proteasome impairment does not contribute to pathogenesis in R6/2 Huntington's disease mice: exclusion of proteasome activator REGgamma as a therapeutic target. *Hum Mol Genet,* 15**,** 33-44.

BEZPROZVANNY, I. & HAYDEN, M. R. 2004. Deranged neuronal calcium signaling and Huntington disease. *Biochem Biophys Res Commun,* 322**,** 1310-7.

BIENENGRAEBER, M., OLSON, T. M., SELIVANOV, V. A., KATHMANN, E. C., O'COCHLAIN, F., GAO, F., KARGER, A. B., BALLEW, J. D., HODGSON, D. M., ZINGMAN, L. V., PANG, Y. P., ALEKSEEV, A. E. & TERZIC, A. 2004. ABCC9 mutations identified in human dilated cardiomyopathy disrupt catalytic KATP channel gating. *Nat Genet,* 36**,** 382-7.

BIONE, S., D'ADAMO, P., MAESTRINI, E., GEDEON, A. K., BOLHUIS, P. A. & TONIOLO, D. 1996. A novel X-linked gene, G4.5. is responsible for Barth syndrome. *Nat Genet,* 12**,** 385-9.

BLATCH, G. L. & LASSLE, M. 1999. The tetratricopeptide repeat: a structural motif mediating protein-protein interactions. *Bioessays,* 21**,** 932-9.

BOSSY, B., PETRILLI, A., KLINGLMAYR, E., CHEN, J., LUTZ-MEINDL, U., KNOTT, A. B., MASLIAH, E., SCHWARZENBACHER, R. & BOSSY-WETZEL, E. 2010. S-Nitrosylation of DRP1 does not affect enzymatic activity and is not specific to Alzheimer's disease. *J Alzheimers Dis,* 20 Suppl 2**,** S513-26.

BRAZ, J. C., GREGORY, K., PATHAK, A., ZHAO, W., SAHIN, B., KLEVITSKY, R., KIMBALL, T. F., LORENZ, J. N., NAIRN, A. C., LIGGETT, S. B., BODI, I., WANG, S., SCHWARTZ, A., LAKATTA, E. G., DEPAOLI-ROACH, A. A., ROBBINS, J., HEWETT, T. E., BIBB, J. A., WESTFALL, M. V., KRANIAS, E. G. & MOLKENTIN, J. D. 2004. PKC-alpha regulates cardiac contractility and propensity toward heart failure. *Nat Med,* 10**,** 248-54.

BRENNAN, W. A., JR., BIRD, E. D. & APRILLE, J. R. 1985. Regional mitochondrial respiratory activity in Huntington's disease brain. *J Neurochem,* 44**,** 1948-50.

BRIDGES, L. R. 1986. The association of cardiac muscle necrosis and inflammation with the degenerative and persistent myopathy of MDX mice. *J Neurol Sci,* 72**,** 147-57.

BRODSKY, G. L., MUNTONI, F., MIOCIC, S., SINAGRA, G., SEWRY, C. & MESTRONI, L. 2000. Lamin A/C gene mutation associated with dilated cardiomyopathy with variable skeletal muscle involvement. *Circulation,* 101**,** 473-6.

BROOKES, P. S., YOON, Y., ROBOTHAM, J. L., ANDERS, M. W. & SHEU, S. S. 2004. Calcium, ATP, and ROS: a mitochondrial love-hate triangle. *Am J Physiol Cell Physiol,* 287**,** C817-33.

BROWNE, S. E., BOWLING, A. C., MACGARVEY, U., BAIK, M. J., BERGER, S. C., MUQIT, M. M., BIRD, E. D. & BEAL, M. F. 1997. Oxidative damage and metabolic dysfunction in Huntington's disease: selective vulnerability of the basal ganglia. *Ann Neurol,* 41**,** 646-53.

BURRIDGE, P. W., THOMPSON, S., MILLROD, M. A., WEINBERG, S., YUAN, X., PETERS, A., MAHAIRAKI, V., KOLIATSOS, V. E., TUNG, L. & ZAMBIDIS, E. T. 2011. A universal system for highly efficient cardiac differentiation of human induced pluripotent stem cells that eliminates interline variability. *PLoS One,* 6**,** e18293.

CARDENAS, C., MILLER, R. A., SMITH, I., BUI, T., MOLGO, J., MULLER, M., VAIS, H., CHEUNG, K. H., YANG, J., PARKER, I., THOMPSON, C. B., BIRNBAUM, M. J., HALLOWS, K. R. & FOSKETT, J. K. 2010. Essential regulation of cell bioenergetics by constitutive InsP3 receptor Ca2+ transfer to mitochondria. *Cell,* 142**,** 270-83.

CARNIEL, E., TAYLOR, M. R., SINAGRA, G., DI LENARDA, A., KU, L., FAIN, P. R., BOUCEK, M. M., CAVANAUGH, J., MIOCIC, S., SLAVOV, D., GRAW, S. L., FEIGER, J., ZHU, X. Z., DAO, D., FERGUSON, D. A., BRISTOW, M. R. & MESTRONI, L. 2005. Alpha-myosin heavy chain: a sarcomeric gene

associated with dilated and hypertrophic phenotypes of cardiomyopathy. *Circulation,* 112**,** 54-9.

CASSIDY-STONE, A., CHIPUK, J. E., INGERMAN, E., SONG, C., YOO, C., KUWANA, T., KURTH, M. J., SHAW, J. T., HINSHAW, J. E., GREEN, D. R. & NUNNARI, J. 2008. Chemical inhibition of the mitochondrial division dynamin reveals its role in Bax/Bak-dependent mitochondrial outer membrane permeabilization. *Dev Cell,* 14**,** 193-204.

CEPEDA-PRADO, E., POPP, S., KHAN, U., STEFANOV, D., RODRIGUEZ, J., MENALLED, L. B., DOW-EDWARDS, D., SMALL, S. A. & MORENO, H. 2012. R6/2 Huntington's disease mice develop early and progressive abnormal brain metabolism and seizures. *J Neurosci,* 32**,** 6456-67.

CEREGHETTI, G. M., STANGHERLIN, A., MARTINS DE BRITO, O., CHANG, C. R., BLACKSTONE, C., BERNARDI, P. & SCORRANO, L. 2008. Dephosphorylation by calcineurin regulates translocation of Drp1 to mitochondria. *Proc Natl Acad Sci U S A,* 105**,** 15803-8.

CHANG, C. R. & BLACKSTONE, C. 2007. Cyclic AMP-dependent protein kinase phosphorylation of Drp1 regulates its GTPase activity and mitochondrial morphology. *J Biol Chem,* 282**,** 21583-7.

CHANG, C. R. & BLACKSTONE, C. 2010. Dynamic regulation of mitochondrial fission through modification of the dynamin-related protein Drp1. *Ann N Y Acad Sci,* 1201**,** 34-9.

CHANG, C. R., MANLANDRO, C. M., ARNOULT, D., STADLER, J., POSEY, A. E., HILL, R. B. & BLACKSTONE, C. 2010. A lethal de novo mutation in the middle domain of the dynamin-related GTPase Drp1 impairs higher order assembly and mitochondrial division. *J Biol Chem,* 285**,** 32494-503.

CHEN, H. & CHAN, D. C. 2005. Emerging functions of mammalian mitochondrial fusion and fission. *Hum Mol Genet,* 14 Spec No. 2**,** R283-9.

CHEN, H. & CHAN, D. C. 2009. Mitochondrial dynamics--fusion, fission, movement, and mitophagy--in neurodegenerative diseases. *Hum Mol Genet,* 18**,** R169-76.

CHEN, H., CHOMYN, A. & CHAN, D. C. 2005. Disruption of fusion results in mitochondrial heterogeneity and dysfunction. *J Biol Chem,* 280**,** 26185-92.

CHEN, H., DETMER, S. A., EWALD, A. J., GRIFFIN, E. E., FRASER, S. E. & CHAN, D. C. 2003. Mitofusins Mfn1 and Mfn2 coordinately regulate mitochondrial fusion and are essential for embryonic development. *J Cell Biol,* 160**,** 189-200.

CHEN, H., VERMULST, M., WANG, Y. E., CHOMYN, A., PROLLA, T. A., MCCAFFERY, J. M. & CHAN, D. C. 2010. Mitochondrial fusion is required for mtDNA stability in skeletal muscle and tolerance of mtDNA mutations. *Cell,* 141**,** 280-9.

CHEN, L., GONG, Q., STICE, J. P. & KNOWLTON, A. A. 2009. Mitochondrial OPA1, apoptosis, and heart failure. *Cardiovasc Res,* 84**,** 91-9.

CHEN-IZU, Y., WARD, C. W., STARK, W., JR., BANYASZ, T., SUMANDEA, M. P., BALKE, C. W., IZU, L. T. & WEHRENS, X. H. 2007. Phosphorylation of RyR2 and shortening of RyR2 cluster spacing in spontaneously hypertensive rat with heart failure. *Am J Physiol Heart Circ Physiol,* 293**,** H2409-17.

CHIDSEY, C. A., WEINBACH, E. C., POOL, P. E. & MORROW, A. G. 1966. Biochemical studies of energy production in the failing human heart. *J Clin Invest,* 45**,** 40-50.

CHO, D. H., NAKAMURA, T., FANG, J., CIEPLAK, P., GODZIK, A., GU, Z. & LIPTON, S. A. 2009. S-nitrosylation of Drp1 mediates beta-amyloid-related mitochondrial fission and neuronal injury. *Science,* 324**,** 102-5.

CHO, Y. M., KWON, S., PAK, Y. K., SEOL, H. W., CHOI, Y. M., PARK DO, J., PARK, K. S. & LEE, H. K. 2006. Dynamic changes in mitochondrial biogenesis and antioxidant enzymes during the spontaneous differentiation of human embryonic stem cells. *Biochem Biophys Res Commun,* 348**,** 1472-8.

CLIPSTONE, N. A. & CRABTREE, G. R. 1992. Identification of calcineurin as a key signalling enzyme in T-lymphocyte activation. *Nature,* 357**,** 695-7.

COHEN, J., EFFAT, H., GOODWIN, J. F., OAKLEY, C. M. & STEINER, R. E. 1964. Hypertrophic Obstructive Cardiomyopathy. *Br Heart J,* 26**,** 16-32.

CORDES, S. P. 2005. N-ethyl-N-nitrosourea mutagenesis: boarding the mouse mutant express. *Microbiol Mol Biol Rev,* 69**,** 426-39.

COSTA, V., GIACOMELLO, M., HUDEC, R., LOPREIATO, R., ERMAK, G., LIM, D., MALORNI, W., DAVIES, K. J., CARAFOLI, E. & SCORRANO, L. 2010. Mitochondrial fission and cristae disruption increase the response of cell models of Huntington's disease to apoptotic stimuli. *EMBO Mol Med,* 2**,** 490-503.

CRIBBS, J. T. & STRACK, S. 2007. Reversible phosphorylation of Drp1 by cyclic AMP-dependent protein kinase and calcineurin regulates mitochondrial fission and cell death. *EMBO Rep,* 8**,** 939-44.

D'ADAMO, P., FASSONE, L., GEDEON, A., JANSSEN, E. A., BIONE, S., BOLHUIS, P. A., BARTH, P. G., WILSON, M., HAAN, E., ORSTAVIK, K. H., PATTON, M. A., GREEN, A. J., ZAMMARCHI, E., DONATI, M. A. & TONIOLO, D. 1997. The X-linked gene G4.5 is responsible for different infantile dilated cardiomyopathies. *Am J Hum Genet,* 61**,** 862-7.

DAEHMLOW, S., ERDMANN, J., KNUEPPEL, T., GILLE, C., FROEMMEL, C., HUMMEL, M., HETZER, R. & REGITZ-ZAGROSEK, V. 2002. Novel mutations in sarcomeric protein genes in dilated cardiomyopathy. *Biochem Biophys Res Commun,* 298**,** 116-20.

DAGDA, R. K., CHERRA, S. J., 3RD, KULICH, S. M., TANDON, A., PARK, D. & CHU, C. T. 2009. Loss of PINK1 function promotes mitophagy

through effects on oxidative stress and mitochondrial fission. *J Biol Chem,* 284**,** 13843-55.

DALLA VOLTA, S. 1989. Arrhythmogenic cardiomyopathy of the right ventricle: thoughts on aetiology. *Eur Heart J,* 10 Suppl D**,** 2-6.

DAMIANO, M., GALVAN, L., DEGLON, N. & BROUILLET, E. 2010. Mitochondria in Huntington's disease. *Biochim Biophys Acta,* 1802**,** 52-61.

DAVIES, S. W., TURMAINE, M., COZENS, B. A., DIFIGLIA, M., SHARP, A. H., ROSS, C. A., SCHERZINGER, E., WANKER, E. E., MANGIARINI, L. & BATES, G. P. 1997. Formation of neuronal intranuclear inclusions underlies the neurological dysfunction in mice transgenic for the HD mutation. *Cell,* 90**,** 537-48.

DAVIES, V. J., HOLLINS, A. J., PIECHOTA, M. J., YIP, W., DAVIES, J. R., WHITE, K. E., NICOLS, P. P., BOULTON, M. E. & VOTRUBA, M. 2007. Opa1 deficiency in a mouse model of autosomal dominant optic atrophy impairs mitochondrial morphology, optic nerve structure and visual function. *Hum Mol Genet,* 16**,** 1307-18.

DE BRITO, O. M. & SCORRANO, L. 2008. Mitofusin 2 tethers endoplasmic reticulum to mitochondria. *Nature,* 456**,** 605-10.

DE MEYER, G. R., DE KEULENAER, G. W. & MARTINET, W. 2010. Role of autophagy in heart failure associated with aging. *Heart Fail Rev,* 15**,** 423-30.

DELETTRE, C., LENAERS, G., GRIFFOIN, J. M., GIGAREL, N., LORENZO, C., BELENGUER, P., PELLOQUIN, L., GROSGEORGE, J., TURC-CAREL, C., PERRET, E., ASTARIE-DEQUEKER, C., LASQUELLEC, L., ARNAUD, B., DUCOMMUN, B., KAPLAN, J. & HAMEL, C. P. 2000. Nuclear gene OPA1, encoding a mitochondrial dynamin-related protein, is mutated in dominant optic atrophy. *Nat Genet,* 26**,** 207-10.

DETMER, S. A., VANDE VELDE, C., CLEVELAND, D. W. & CHAN, D. C. 2008. Hindlimb gait defects due to motor axon loss and reduced distal muscles in a transgenic mouse model of Charcot-Marie-Tooth type 2A. *Hum Mol Genet,* 17**,** 367-75.

DIFIGLIA, M., SAPP, E., CHASE, K. O., DAVIES, S. W., BATES, G. P., VONSATTEL, J. P. & ARONIN, N. 1997. Aggregation of huntingtin in neuronal intranuclear inclusions and dystrophic neurites in brain. *Science,* 277**,** 1990-3.

DODART, J. C. & MAY, P. 2005. Overview on rodent models of Alzheimer's disease. *Curr Protoc Neurosci,* Chapter 9**,** Unit 9 22.

DRAGO, I., DE STEFANI, D., RIZZUTO, R. & POZZAN, T. 2012. Mitochondrial Ca2+ uptake contributes to buffering cytoplasmic Ca2+ peaks in cardiomyocytes. *Proc Natl Acad Sci U S A,* 109**,** 12986-91.

DUNN, J. F. & RADDA, G. K. 1991. Total ion content of skeletal and cardiac muscle in the mdx mouse dystrophy: Ca2+ is elevated at all ages. *J Neurol Sci,* 103**,** 226-31.

DUYAO, M., AMBROSE, C., MYERS, R., NOVELLETTO, A., PERSICHETTI, F., FRONTALI, M., FOLSTEIN, S., ROSS, C., FRANZ, M., ABBOTT, M. & *ET*

AL. 1993. Trinucleotide repeat length instability and age of onset in Huntington's disease. *Nat Genet,* 4**,** 387-92.

ELMORE, S. P., QIAN, T., GRISSOM, S. F. & LEMASTERS, J. J. 2001. The mitochondrial permeability transition initiates autophagy in rat hepatocytes. *FASEB J,* 15**,** 2286-7.

ESKES, R., ANTONSSON, B., OSEN-SAND, A., MONTESSUIT, S., RICHTER, C., SADOUL, R., MAZZEI, G., NICHOLS, A. & MARTINOU, J. C. 1998. Bax-induced cytochrome C release from mitochondria is independent of the permeability transition pore but highly dependent on Mg2+ ions. *J Cell Biol,* 143**,** 217-24.

ESPOSITO, L. A., MELOV, S., PANOV, A., COTTRELL, B. A. & WALLACE, D. C. 1999. Mitochondrial disease in mouse results in increased oxidative stress. *Proc Natl Acad Sci U S A,* 96**,** 4820-5.

FAELBER, K., POSOR, Y., GAO, S., HELD, M., ROSKE, Y., SCHULZE, D., HAUCKE, V., NOE, F. & DAUMKE, O. 2011. Crystal structure of nucleotide-free dynamin. *Nature,* 477**,** 556-60.

FATKIN, D., MACRAE, C., SASAKI, T., WOLFF, M. R., PORCU, M., FRENNEAUX, M., ATHERTON, J., VIDAILLET, H. J., JR., SPUDICH, S., DE GIROLAMI, U., SEIDMAN, J. G., SEIDMAN, C., MUNTONI, F., MUEHLE, G., JOHNSON, W. & MCDONOUGH, B. 1999. Missense mutations in the rod domain of the lamin A/C gene as causes of dilated cardiomyopathy and conduction-system disease. *N Engl J Med,* 341**,** 1715-24.

FENG, B., SCHWARZ, H. & JESUTHASAN, S. 2002. Furrow-specific endocytosis during cytokinesis of zebrafish blastomeres. *Exp Cell Res,* 279**,** 14-20.

FORD, M. G., JENNI, S. & NUNNARI, J. 2011. The crystal structure of dynamin. *Nature,* 477**,** 561-6.

FRANK, S., GAUME, B., BERGMANN-LEITNER, E. S., LEITNER, W. W., ROBERT, E. G., CATEZ, F., SMITH, C. L. & YOULE, R. J. 2001. The role of dynamin-related protein 1, a mediator of mitochondrial fission, in apoptosis. *Dev Cell,* 1**,** 515-25.

FRIEDMAN, J. R., LACKNER, L. L., WEST, M., DIBENEDETTO, J. R., NUNNARI, J. & VOELTZ, G. K. 2011. ER tubules mark sites of mitochondrial division. *Science,* 334**,** 358-62.

FUKUSHIMA, N. H., BRISCH, E., KEEGAN, B. R., BLEAZARD, W. & SHAW, J. M. 2001. The GTPase effector domain sequence of the Dnm1p GTPase regulates self-assembly and controls a rate-limiting step in mitochondrial fission. *Mol Biol Cell,* 12**,** 2756-66.

GERULL, B., GRAMLICH, M., ATHERTON, J., MCNABB, M., TROMBITAS, K., SASSE-KLAASSEN, S., SEIDMAN, J. G., SEIDMAN, C., GRANZIER, H., LABEIT, S., FRENNEAUX, M. & THIERFELDER, L. 2002. Mutations of TTN, encoding the giant muscle filament titin, cause familial dilated cardiomyopathy. *Nat Genet,* 30**,** 201-4.

GIACOMELLO, M., HUDEC, R. & LOPREIATO, R. 2011. Huntington's disease, calcium, and mitochondria. *Biofactors,* 37**,** 206-18.

GISPERT, S., RICCIARDI, F., KURZ, A., AZIZOV, M., HOEPKEN, H. H., BECKER, D., VOOS, W., LEUNER, K., MULLER, W. E., KUDIN, A. P., KUNZ, W. S., ZIMMERMANN, A., ROEPER, J., WENZEL, D., JENDRACH, M., GARCIA-ARENCIBIA, M., FERNANDEZ-RUIZ, J., HUBER, L., ROHRER, H., BARRERA, M., REICHERT, A. S., RUB, U., CHEN, A., NUSSBAUM, R. L. & AUBURGER, G. 2009. Parkinson phenotype in aged PINK1-deficient mice is accompanied by progressive mitochondrial dysfunction in absence of neurodegeneration. *PLoS One,* 4**,** e5777.

GLICKMAN, M. H. & CIECHANOVER, A. 2002. The ubiquitin-proteasome proteolytic pathway: destruction for the sake of construction. *Physiol Rev,* 82**,** 373-428.

GOLD, E. S., UNDERHILL, D. M., MORRISSETTE, N. S., GUO, J., MCNIVEN, M. A. & ADEREM, A. 1999. Dynamin 2 is required for phagocytosis in macrophages. *J Exp Med,* 190**,** 1849-56.

GOMES, L. C., DI BENEDETTO, G. & SCORRANO, L. 2011. During autophagy mitochondria elongate, are spared from degradation and sustain cell viability. *Nat Cell Biol,* 13**,** 589-98.

GREEN, D. R. & WANG, R. 2010. Calcium and energy: making the cake and eating it too? *Cell,* 142**,** 200-2.

GRIFFIN, E. E., GRAUMANN, J. & CHAN, D. C. 2005. The WD40 protein Caf4p is a component of the mitochondrial fission machinery and recruits Dnm1p to mitochondria. *J Cell Biol,* 170**,** 237-48.

GUAN, K., FARH, L., MARSHALL, T. K. & DESCHENES, R. J. 1993. Normal mitochondrial structure and genome maintenance in yeast requires the dynamin-like product of the MGM1 gene. *Curr Genet,* 24**,** 141-8.

GUIDETTI, P., CHARLES, V., CHEN, E. Y., REDDY, P. H., KORDOWER, J. H., WHETSELL, W. O., JR., SCHWARCZ, R. & TAGLE, D. A. 2001. Early degenerative changes in transgenic mice expressing mutant huntingtin involve dendritic abnormalities but no impairment of mitochondrial energy production. *Exp Neurol,* 169**,** 340-50.

GUO, X., CHEN, K. H., GUO, Y., LIAO, H., TANG, J. & XIAO, R. P. 2007a. Mitofusin 2 triggers vascular smooth muscle cell apoptosis via mitochondrial death pathway. *Circ Res,* 101**,** 1113-22.

GUO, Y. H., CHEN, K., GAO, W., LI, Q., CHEN, L., WANG, G. S. & TANG, J. 2007b. Overexpression of Mitofusin 2 inhibited oxidized low-density lipoprotein induced vascular smooth muscle cell proliferation and reduced atherosclerotic lesion formation in rabbit. *Biochem Biophys Res Commun,* 363**,** 411-7.

GUTEKUNST, C. A., LI, S. H., YI, H., MULROY, J. S., KUEMMERLE, S., JONES, R., RYE, D., FERRANTE, R. J., HERSCH, S. M. & LI, X. J. 1999. Nuclear and neuropil aggregates in Huntington's disease: relationship to neuropathology. *J Neurosci,* 19**,** 2522-34.

HAGHIGHI, K., KOLOKATHIS, F., PATER, L., LYNCH, R. A., ASAHI, M., GRAMOLINI, A. O., FAN, G. C., TSIAPRAS, D., HAHN, H. S., ADAMOPOULOS, S., LIGGETT, S. B., DORN, G. W., 2ND, MACLENNAN, D. H., KREMASTINOS, D. T. & KRANIAS, E. G. 2003. Human

phospholamban null results in lethal dilated cardiomyopathy revealing a critical difference between mouse and human. *J Clin Invest,* 111**,** 869-76.

HAN, X. J., LU, Y. F., LI, S. A., KAITSUKA, T., SATO, Y., TOMIZAWA, K., NAIRN, A. C., TAKEI, K., MATSUI, H. & MATSUSHITA, M. 2008. CaM kinase I alpha-induced phosphorylation of Drp1 regulates mitochondrial morphology. *J Cell Biol,* 182**,** 573-85.

HANSFORD, R. G. & ZOROV, D. 1998. Role of mitochondrial calcium transport in the control of substrate oxidation. *Mol Cell Biochem,* 184**,** 359-69.

HANSON, E. L., JAKOBS, P. M., KEEGAN, H., COATES, K., BOUSMAN, S., DIENEL, N. H., LITT, M. & HERSHBERGER, R. E. 2002. Cardiac troponin T lysine 210 deletion in a family with dilated cardiomyopathy. *J Card Fail,* 8**,** 28-32.

HARDER, Z., ZUNINO, R. & MCBRIDE, H. 2004. Sumo1 conjugates mitochondrial substrates and participates in mitochondrial fission. *Curr Biol,* 14**,** 340-5.

HARDIE, D. G. 2007. AMP-activated/SNF1 protein kinases: conserved guardians of cellular energy. *Nat Rev Mol Cell Biol,* 8**,** 774-85.

HAYASHI, T., SHIMOMURA, H., TERASAKI, F., TOKO, H., OKABE, M., DEGUCHI, H., HIROTA, Y., KITAURA, Y. & KAWAMURA, K. 1998. Collagen subtypes and matrix metalloproteinase in idiopathic restrictive cardiomyopathy. *Int J Cardiol,* 64**,** 109-16.

HEINEKE, J. & MOLKENTIN, J. D. 2006. Regulation of cardiac hypertrophy by intracellular signalling pathways. *Nat Rev Mol Cell Biol,* 7**,** 589-600.

HENLEY, J. R., KRUEGER, E. W., OSWALD, B. J. & MCNIVEN, M. A. 1998. Dynamin-mediated internalization of caveolae. *J Cell Biol,* 141**,** 85-99.

HENZE, K. & MARTIN, W. 2003. Evolutionary biology: essence of mitochondria. *Nature,* 426**,** 127-8.

HERMANN, G. J., THATCHER, J. W., MILLS, J. P., HALES, K. G., FULLER, M. T., NUNNARI, J. & SHAW, J. M. 1998. Mitochondrial fusion in yeast requires the transmembrane GTPase Fzo1p. *J Cell Biol,* 143**,** 359-73.

HERSHBERGER, R. E., HANSON, E. L., JAKOBS, P. M., KEEGAN, H., COATES, K., BOUSMAN, S. & LITT, M. 2002. A novel lamin A/C mutation in a family with dilated cardiomyopathy, prominent conduction system disease, and need for permanent pacemaker implantation. *Am Heart J,* 144**,** 1081-6.

HOCKLY, E., TSE, J., BARKER, A. L., MOOLMAN, D. L., BEUNARD, J. L., REVINGTON, A. P., HOLT, K., SUNSHINE, S., MOFFITT, H., SATHASIVAM, K., WOODMAN, B., WANKER, E. E., LOWDEN, P. A. & BATES, G. P. 2006. Evaluation of the benzothiazole aggregation inhibitors riluzole and PGL-135 as therapeutics for Huntington's disease. *Neurobiol Dis,* 21**,** 228-36.

HOCKLY, E., WOODMAN, B., MAHAL, A., LEWIS, C. M. & BATES, G. 2003. Standardization and statistical approaches to therapeutic trials in the R6/2 mouse. *Brain Res Bull,* 61**,** 469-79.

HOFFMANN, H. P. & AVERS, C. J. 1973. Mitochondrion of yeast: ultrastructural evidence for one giant, branched organelle per cell. *Science,* 181**,** 749-51.

HOGAN, P. G., CHEN, L., NARDONE, J. & RAO, A. 2003. Transcriptional regulation by calcium, calcineurin, and NFAT. *Genes Dev,* 17**,** 2205-32.

HOM, J. & SHEU, S. S. 2009. Morphological dynamics of mitochondria--a special emphasis on cardiac muscle cells. *J Mol Cell Cardiol,* 46**,** 811-20.

HONG, Y. R., CHEN, C. H., CHENG, D. S., HOWNG, S. L. & CHOW, C. C. 1998. Human dynamin-like protein interacts with the glycogen synthase kinase 3beta. *Biochem Biophys Res Commun,* 249**,** 697-703.

HUTTEMANN, M., KLEWER, S., LEE, I., PECINOVA, A., PECINA, P., LIU, J., LEE, M., DOAN, J. W., LARSON, D., SLACK, E., MAGHSOODI, B., ERICKSON, R. P. & GROSSMAN, L. I. 2012. Mice deleted for heart-type cytochrome c oxidase subunit 7a1 develop dilated cardiomyopathy. *Mitochondrion,* 12**,** 294-304.

IDE, T., TSUTSUI, H., KINUGAWA, S., UTSUMI, H., KANG, D., HATTORI, N., UCHIDA, K., ARIMURA, K., EGASHIRA, K. & TAKESHITA, A. 1999. Mitochondrial electron transport complex I is a potential source of oxygen free radicals in the failing myocardium. *Circ Res,* 85**,** 357-63.

IMOTO, M., TACHIBANA, I. & URRUTIA, R. 1998. Identification and functional characterization of a novel human protein highly related to the yeast dynamin-like GTPase Vps1p. *J Cell Sci,* 111 (Pt 10)**,** 1341-9.

INGERMAN, E., PERKINS, E. M., MARINO, M., MEARS, J. A., MCCAFFERY, J. M., HINSHAW, J. E. & NUNNARI, J. 2005. Dnm1 forms spirals that are structurally tailored to fit mitochondria. *J Cell Biol,* 170**,** 1021-7.

ISHIHARA, N., FUJITA, Y., OKA, T. & MIHARA, K. 2006. Regulation of mitochondrial morphology through proteolytic cleavage of OPA1. *EMBO J,* 25**,** 2966-77.

ISHIHARA, N., NOMURA, M., JOFUKU, A., KATO, H., SUZUKI, S. O., MASUDA, K., OTERA, H., NAKANISHI, Y., NONAKA, I., GOTO, Y., TAGUCHI, N., MORINAGA, H., MAEDA, M., TAKAYANAGI, R., YOKOTA, S. & MIHARA, K. 2009. Mitochondrial fission factor Drp1 is essential for embryonic development and synapse formation in mice. *Nat Cell Biol,* 11**,** 958-66.

ITOH-SATOH, M., HAYASHI, T., NISHI, H., KOGA, Y., ARIMURA, T., KOYANAGI, T., TAKAHASHI, M., HOHDA, S., UEDA, K., NOUCHI, T., HIROE, M., MARUMO, F., IMAIZUMI, T., YASUNAMI, M. & KIMURA, A. 2002. Titin mutations as the molecular basis for dilated cardiomyopathy. *Biochem Biophys Res Commun,* 291**,** 385-93.

JAKOBS, P. M., HANSON, E. L., CRISPELL, K. A., TOY, W., KEEGAN, H., SCHILLING, K., ICENOGLE, T. B., LITT, M. & HERSHBERGER, R. E. 2001. Novel lamin A/C mutations in two families with dilated cardiomyopathy and conduction system disease. *J Card Fail,* 7**,** 249-56.

JIANG, M. T., LOKUTA, A. J., FARRELL, E. F., WOLFF, M. R., HAWORTH, R. A. & VALDIVIA, H. H. 2002. Abnormal Ca2+ release, but normal ryanodine receptors, in canine and human heart failure. *Circ Res,* 91**,** 1015-22.

JONES, B. A. & FANGMAN, W. L. 1992. Mitochondrial DNA maintenance in yeast requires a protein containing a region related to the GTP-binding domain of dynamin. *Genes Dev,* 6**,** 380-9.

JONES, L. R., SUZUKI, Y. J., WANG, W., KOBAYASHI, Y. M., RAMESH, V., FRANZINI-ARMSTRONG, C., CLEEMANN, L. & MORAD, M. 1998. Regulation of Ca2+ signaling in transgenic mouse cardiac myocytes overexpressing calsequestrin. *J Clin Invest,* 101**,** 1385-93.

JORDENS, E. Z., PALMIERI, L., HUIZING, M., VAN DEN HEUVEL, L. P., SENGERS, R. C., DORNER, A., RUITENBEEK, W., TRIJBELS, F. J., VALSSON, J., SIGFUSSON, G., PALMIERI, F. & SMEITINK, J. A. 2002. Adenine nucleotide translocator 1 deficiency associated with Sengers syndrome. *Ann Neurol,* 52**,** 95-9.

KABEYA, Y., MIZUSHIMA, N., UENO, T., YAMAMOTO, A., KIRISAKO, T., NODA, T., KOMINAMI, E., OHSUMI, Y. & YOSHIMORI, T. 2000. LC3, a mammalian homologue of yeast Apg8p, is localized in autophagosome membranes after processing. *EMBO J,* 19**,** 5720-8.

KAMIMOTO, T., NAGAI, Y., ONOGI, H., MURO, Y., WAKABAYASHI, T. & HAGIWARA, M. 1998. Dymple, a novel dynamin-like high molecular weight GTPase lacking a proline-rich carboxyl-terminal domain in mammalian cells. *J Biol Chem,* 273**,** 1044-51.

KAMISAGO, M., SHARMA, S. D., DEPALMA, S. R., SOLOMON, S., SHARMA, P., MCDONOUGH, B., SMOOT, L., MULLEN, M. P., WOOLF, P. K., WIGLE, E. D., SEIDMAN, J. G. & SEIDMAN, C. E. 2000. Mutations in sarcomere protein genes as a cause of dilated cardiomyopathy. *N Engl J Med,* 343**,** 1688-96.

KARBOWSKI, M., LEE, Y. J., GAUME, B., JEONG, S. Y., FRANK, S., NECHUSHTAN, A., SANTEL, A., FULLER, M., SMITH, C. L. & YOULE, R. J. 2002. Spatial and temporal association of Bax with mitochondrial fission sites, Drp1, and Mfn2 during apoptosis. *J Cell Biol,* 159**,** 931-8.

KARBOWSKI, M., NEUTZNER, A. & YOULE, R. J. 2007. The mitochondrial E3 ubiquitin ligase MARCH5 is required for Drp1 dependent mitochondrial division. *J Cell Biol,* 178**,** 71-84.

KERR, J. F., WYLLIE, A. H. & CURRIE, A. R. 1972. Apoptosis: a basic biological phenomenon with wide-ranging implications in tissue kinetics. *Br J Cancer,* 26**,** 239-57.

KLUCK, R. M., BOSSY-WETZEL, E., GREEN, D. R. & NEWMEYER, D. D. 1997. The release of cytochrome c from mitochondria: a primary site for Bcl-2 regulation of apoptosis. *Science,* 275**,** 1132-6.

KNOLL, R., HOSHIJIMA, M., HOFFMAN, H. M., PERSON, V., LORENZEN-SCHMIDT, I., BANG, M. L., HAYASHI, T., SHIGA, N., YASUKAWA, H., SCHAPER, W., MCKENNA, W., YOKOYAMA, M., SCHORK, N. J., OMENS, J. H., MCCULLOCH, A. D., KIMURA, A., GREGORIO, C. C., POLLER, W., SCHAPER, J., SCHULTHEISS, H. P. & CHIEN, K. R. 2002. The cardiac mechanical stretch sensor machinery involves a Z disc complex that is defective in a subset of human dilated cardiomyopathy. *Cell,* 111**,** 943-55.

KNOLLMANN, B. C., KNOLLMANN-RITSCHEL, B. E., WEISSMAN, N. J., JONES, L. R. & MORAD, M. 2000. Remodelling of ionic currents in hypertrophied and failing hearts of transgenic mice overexpressing calsequestrin. *J Physiol,* 525 Pt 2**,** 483-98.

KNOLLMANN, B. C. & RODEN, D. M. 2008. A genetic framework for improving arrhythmia therapy. *Nature,* 451**,** 929-36.

KO, H. S., KIM, S. W., SRIRAM, S. R., DAWSON, V. L. & DAWSON, T. M. 2006. Identification of far upstream element-binding protein-1 as an authentic Parkin substrate. *J Biol Chem,* 281**,** 16193-6.

KO, H. S., VON COELLN, R., SRIRAM, S. R., KIM, S. W., CHUNG, K. K., PLETNIKOVA, O., TRONCOSO, J., JOHNSON, B., SAFFARY, R., GOH, E. L., SONG, H., PARK, B. J., KIM, M. J., KIM, S., DAWSON, V. L. & DAWSON, T. M. 2005. Accumulation of the authentic parkin substrate aminoacyl-tRNA synthetase cofactor, p38/JTV-1, leads to catecholaminergic cell death. *J Neurosci,* 25**,** 7968-78.

KOCH, A., THIEMANN, M., GRABENBAUER, M., YOON, Y., MCNIVEN, M. A. & SCHRADER, M. 2003. Dynamin-like protein 1 is involved in peroxisomal fission. *J Biol Chem,* 278**,** 8597-605.

KOCHS, G. & HALLER, O. 1999a. GTP-bound human MxA protein interacts with the nucleocapsids of Thogoto virus (Orthomyxoviridae). *J Biol Chem,* 274**,** 4370-6.

KOCHS, G. & HALLER, O. 1999b. Interferon-induced human MxA GTPase blocks nuclear import of Thogoto virus nucleocapsids. *Proc Natl Acad Sci U S A,* 96**,** 2082-6.

KOLODZIEJCZYK, S. M., WANG, L., BALAZSI, K., DEREPENTIGNY, Y., KOTHARY, R. & MEGENEY, L. A. 1999. MEF2 is upregulated during cardiac hypertrophy and is required for normal post-natal growth of the myocardium. *Curr Biol,* 9**,** 1203-6.

KONDOH, H., LLEONART, M. E., NAKASHIMA, Y., YOKODE, M., TANAKA, M., BERNARD, D., GIL, J. & BEACH, D. 2007. A high glycolytic flux supports the proliferative potential of murine embryonic stem cells. *Antioxid Redox Signal,* 9**,** 293-9.

KOSHIBA, T., DETMER, S. A., KAISER, J. T., CHEN, H., MCCAFFERY, J. M. & CHAN, D. C. 2004. Structural basis of mitochondrial tethering by mitofusin complexes. *Science,* 305**,** 858-62.

LABROUSSE, A. M., ZAPPATERRA, M. D., RUBE, D. A. & VAN DER BLIEK, A. M. 1999. C. elegans dynamin-related protein DRP-1 controls severing of the mitochondrial outer membrane. *Mol Cell,* 4**,** 815-26.

LARSSON, N. G., WANG, J., WILHELMSSON, H., OLDFORS, A., RUSTIN, P., LEWANDOSKI, M., BARSH, G. S. & CLAYTON, D. A. 1998. Mitochondrial transcription factor A is necessary for mtDNA maintenance and embryogenesis in mice. *Nat Genet,* 18**,** 231-6.

LEBOVITZ, R. M., ZHANG, H., VOGEL, H., CARTWRIGHT, J., JR., DIONNE, L., LU, N., HUANG, S. & MATZUK, M. M. 1996. Neurodegeneration, myocardial injury, and perinatal death in mitochondrial superoxide dismutase-deficient mice. *Proc Natl Acad Sci U S A,* 93**,** 9782-7.

LEE, S., JEONG, S. Y., LIM, W. C., KIM, S., PARK, Y. Y., SUN, X., YOULE, R. J. & CHO, H. 2007. Mitochondrial fission and fusion mediators, hFis1 and OPA1, modulate cellular senescence. *J Biol Chem,* 282**,** 22977-83.

LEGROS, F., LOMBES, A., FRACHON, P. & ROJO, M. 2002. Mitochondrial fusion in human cells is efficient, requires the inner membrane potential, and is mediated by mitofusins. *Mol Biol Cell,* 13**,** 4343-54.

LI, D., CZERNUSZEWICZ, G. Z., GONZALEZ, O., TAPSCOTT, T., KARIBE, A., DURAND, J. B., BRUGADA, R., HILL, R., GREGORITCH, J. M., ANDERSON, J. L., QUINONES, M., BACHINSKI, L. L. & ROBERTS, R. 2001. Novel cardiac troponin T mutation as a cause of familial dilated cardiomyopathy. *Circulation,* 104**,** 2188-93.

LI, D., TAPSCOFT, T., GONZALEZ, O., BURCH, P. E., QUINONES, M. A., ZOGHBI, W. A., HILL, R., BACHINSKI, L. L., MANN, D. L. & ROBERTS, R. 1999a. Desmin mutation responsible for idiopathic dilated cardiomyopathy. *Circulation,* 100**,** 461-4.

LI, H., LI, S. H., CHENG, A. L., MANGIARINI, L., BATES, G. P. & LI, X. J. 1999b. Ultrastructural localization and progressive formation of neuropil aggregates in Huntington's disease transgenic mice. *Hum Mol Genet,* 8**,** 1227-36.

LI, Y., HUANG, T. T., CARLSON, E. J., MELOV, S., URSELL, P. C., OLSON, J. L., NOBLE, L. J., YOSHIMURA, M. P., BERGER, C., CHAN, P. H., WALLACE, D. C. & EPSTEIN, C. J. 1995. Dilated cardiomyopathy and neonatal lethality in mutant mice lacking manganese superoxide dismutase. *Nat Genet,* 11**,** 376-81.

LIMAS, C. J., OLIVARI, M. T., GOLDENBERG, I. F., LEVINE, T. B., BENDITT, D. G. & SIMON, A. 1987. Calcium uptake by cardiac sarcoplasmic reticulum in human dilated cardiomyopathy. *Cardiovasc Res,* 21**,** 601-5.

LIN, Q., SCHWARZ, J., BUCANA, C. & OLSON, E. N. 1997. Control of mouse cardiac morphogenesis and myogenesis by transcription factor MEF2C. *Science,* 276**,** 1404-7.

LIONE, L. A., CARTER, R. J., HUNT, M. J., BATES, G. P., MORTON, A. J. & DUNNETT, S. B. 1999. Selective discrimination learning impairments in mice expressing the human Huntington's disease mutation. *J Neurosci,* 19**,** 10428-37.

LOW, H. H. & LOWE, J. 2006. A bacterial dynamin-like protein. *Nature,* 444**,** 766-9.

LOW, H. H., SACHSE, C., AMOS, L. A. & LOWE, J. 2009. Structure of a bacterial dynamin-like protein lipid tube provides a mechanism for assembly and membrane curving. *Cell,* 139**,** 1342-52.

LUKOWITZ, W., MAYER, U. & JURGENS, G. 1996. Cytokinesis in the Arabidopsis embryo involves the syntaxin-related KNOLLE gene product. *Cell,* 84**,** 61-71.

LUSTBADER, J. W., CIRILLI, M., LIN, C., XU, H. W., TAKUMA, K., WANG, N., CASPERSEN, C., CHEN, X., POLLAK, S., CHANEY, M., TRINCHESE, F., LIU, S., GUNN-MOORE, F., LUE, L. F., WALKER, D. G., KUPPUSAMY, P., ZEWIER, Z. L., ARANCIO, O., STERN, D., YAN, S. S. & WU, H. 2004. ABAD directly links Abeta to mitochondrial toxicity in Alzheimer's disease. *Science,* 304**,** 448-52.

MAAT-SCHIEMAN, M. L., DORSMAN, J. C., SMOOR, M. A., SIESLING, S., VAN DUINEN, S. G., VERSCHUUREN, J. J., DEN DUNNEN, J. T., VAN OMMEN, G. J. & ROOS, R. A. 1999. Distribution of inclusions in neuronal nuclei and dystrophic neurites in Huntington disease brain. *J Neuropathol Exp Neurol,* 58**,** 129-37.

MAI, S., KLINKENBERG, M., AUBURGER, G., BEREITER-HAHN, J. & JENDRACH, M. 2010. Decreased expression of Drp1 and Fis1 mediates mitochondrial elongation in senescent cells and enhances resistance to oxidative stress through PINK1. *J Cell Sci,* 123**,** 917-26.

MANCZAK, M., ANEKONDA, T. S., HENSON, E., PARK, B. S., QUINN, J. & REDDY, P. H. 2006. Mitochondria are a direct site of A beta accumulation in Alzheimer's disease neurons: implications for free radical generation and oxidative damage in disease progression. *Hum Mol Genet,* 15**,** 1437-49.

MANGIARINI, L., SATHASIVAM, K., SELLER, M., COZENS, B., HARPER, A., HETHERINGTON, C., LAWTON, M., TROTTIER, Y., LEHRACH, H., DAVIES, S. W. & BATES, G. P. 1996. Exon 1 of the HD gene with an expanded CAG repeat is sufficient to cause a progressive neurological phenotype in transgenic mice. *Cell,* 87**,** 493-506.

MARIAN, A. J. 2000. Pathogenesis of diverse clinical and pathological phenotypes in hypertrophic cardiomyopathy. *Lancet,* 355**,** 58-60.

MARTINOU, I., DESAGHER, S., ESKES, R., ANTONSSON, B., ANDRE, E., FAKAN, S. & MARTINOU, J. C. 1999. The release of cytochrome c from mitochondria during apoptosis of NGF-deprived sympathetic neurons is a reversible event. *J Cell Biol,* 144**,** 883-9.

MARX, S. O., REIKEN, S., HISAMATSU, Y., JAYARAMAN, T., BURKHOFF, D., ROSEMBLIT, N. & MARKS, A. R. 2000. PKA phosphorylation dissociates FKBP12.6 from the calcium release channel (ryanodine receptor): defective regulation in failing hearts. *Cell,* 101**,** 365-76.

MATSUOKA, S., SARAI, N., JO, H. & NOMA, A. 2004. Simulation of ATP metabolism in cardiac excitation-contraction coupling. *Prog Biophys Mol Biol,* 85**,** 279-99.

MCCORMACK, J. G. & DENTON, R. M. 1980. Role of calcium ions in the regulation of intramitochondrial metabolism. Properties of the Ca2+-sensitive dehydrogenases within intact uncoupled mitochondria from the white and brown adipose tissue of the rat. *Biochem J,* 190**,** 95-105.

MEIER, P., FINCH, A. & EVAN, G. 2000. Apoptosis in development. *Nature,* 407**,** 796-801.

MIYABAYASHI, S., HANAMIZU, H., NAKAMURA, R., ENDO, H. & TADA, K. 1992. Defects of mitochondrial respiratory enzymes in cloned cells from MELAS fibroblasts. *J Inherit Metab Dis,* 15**,** 797-802.

MOHAPATRA, B., JIMENEZ, S., LIN, J. H., BOWLES, K. R., COVELER, K. J., MARX, J. G., CHRISCO, M. A., MURPHY, R. T., LURIE, P. R., SCHWARTZ, R. J., ELLIOTT, P. M., VATTA, M., MCKENNA, W., TOWBIN, J. A. & BOWLES, N. E. 2003. Mutations in the muscle LIM protein and alpha-actinin-2 genes in dilated cardiomyopathy and endocardial fibroelastosis. *Mol Genet Metab,* 80**,** 207-15.

MONTESSUIT, S., SOMASEKHARAN, S. P., TERRONES, O., LUCKEN-ARDJOMANDE, S., HERZIG, S., SCHWARZENBACHER, R., MANSTEIN, D. J., BOSSY-WETZEL, E., BASANEZ, G., MEDA, P. & MARTINOU, J. C. 2010. Membrane remodeling induced by the dynamin-related protein Drp1 stimulates Bax oligomerization. *Cell,* 142**,** 889-901.

MOULI, P. K., TWIG, G. & SHIRIHAI, O. S. 2009. Frequency and selectivity of mitochondrial fusion are key to its quality maintenance function. *Biophys J,* 96**,** 3509-18.

MUHLBERG, A. B., WARNOCK, D. E. & SCHMID, S. L. 1997. Domain structure and intramolecular regulation of dynamin GTPase. *EMBO J,* 16**,** 6676-83.

MUNTONI, F., CAU, M., GANAU, A., CONGIU, R., ARVEDI, G., MATEDDU, A., MARROSU, M. G., CIANCHETTI, C., REALDI, G., CAO, A. & *ET AL*. 1993. Brief report: deletion of the dystrophin muscle-promoter region associated with X-linked dilated cardiomyopathy. *N Engl J Med,* 329**,** 921-5.

MURPHY, R. T., MOGENSEN, J., SHAW, A., KUBO, T., HUGHES, S. & MCKENNA, W. J. 2004. Novel mutation in cardiac troponin I in recessive idiopathic dilated cardiomyopathy. *Lancet,* 363**,** 371-2.

NAKADA, K., INOUE, K. & HAYASHI, J. 2001. Interaction theory of mammalian mitochondria. *Biochem Biophys Res Commun,* 288**,** 743-6.

NAKAMURA, N., KIMURA, Y., TOKUDA, M., HONDA, S. & HIROSE, S. 2006. MARCH-V is a novel mitofusin 2- and Drp1-binding protein able to change mitochondrial morphology. *EMBO Rep,* 7**,** 1019-22.

NAKATOGAWA, H., SUZUKI, K., KAMADA, Y. & OHSUMI, Y. 2009. Dynamics and diversity in autophagy mechanisms: lessons from yeast. *Nat Rev Mol Cell Biol,* 10**,** 458-67.

NARULA, N., ZARAGOZA, M. V., SENGUPTA, P. P., LI, P., HAIDER, N., VERJANS, J., WAYMIRE, K., VANNAN, M. & WALLACE, D. C. 2011.

Adenine nucleotide translocase 1 deficiency results in dilated cardiomyopathy with defects in myocardial mechanics, histopathological alterations, and activation of apoptosis. *JACC Cardiovasc Imaging,* 4**,** 1-10.

NUNNARI, J., MARSHALL, W. F., STRAIGHT, A., MURRAY, A., SEDAT, J. W. & WALTER, P. 1997. Mitochondrial transmission during mating in Saccharomyces cerevisiae is determined by mitochondrial fusion and fission and the intramitochondrial segregation of mitochondrial DNA. *Mol Biol Cell,* 8**,** 1233-42.

OH, P., MCINTOSH, D. P. & SCHNITZER, J. E. 1998. Dynamin at the neck of caveolae mediates their budding to form transport vesicles by GTP-driven fission from the plasma membrane of endothelium. *J Cell Biol,* 141**,** 101-14.

OKAMURA, H., ARAMBURU, J., GARCIA-RODRIGUEZ, C., VIOLA, J. P., RAGHAVAN, A., TAHILIANI, M., ZHANG, X., QIN, J., HOGAN, P. G. & RAO, A. 2000. Concerted dephosphorylation of the transcription factor NFAT1 induces a conformational switch that regulates transcriptional activity. *Mol Cell,* 6**,** 539-50.

OKUMA, T., HONDA, R., ICHIKAWA, G., TSUMAGARI, N. & YASUDA, H. 1999. In vitro SUMO-1 modification requires two enzymatic steps, E1 and E2. *Biochem Biophys Res Commun,* 254**,** 693-8.

OLICHON, A., BARICAULT, L., GAS, N., GUILLOU, E., VALETTE, A., BELENGUER, P. & LENAERS, G. 2003. Loss of OPA1 perturbates the mitochondrial inner membrane structure and integrity, leading to cytochrome c release and apoptosis. *J Biol Chem,* 278**,** 7743-6.

OLSON, T. M., ILLENBERGER, S., KISHIMOTO, N. Y., HUTTELMAIER, S., KEATING, M. T. & JOCKUSCH, B. M. 2002. Metavinculin mutations alter actin interaction in dilated cardiomyopathy. *Circulation,* 105**,** 431-7.

OLSON, T. M., KISHIMOTO, N. Y., WHITBY, F. G. & MICHELS, V. V. 2001. Mutations that alter the surface charge of alpha-tropomyosin are associated with dilated cardiomyopathy. *J Mol Cell Cardiol,* 33**,** 723-32.

OLSON, T. M., MICHELS, V. V., THIBODEAU, S. N., TAI, Y. S. & KEATING, M. T. 1998. Actin mutations in dilated cardiomyopathy, a heritable form of heart failure. *Science,* 280**,** 750-2.

ONG, S. B., SUBRAYAN, S., LIM, S. Y., YELLON, D. M., DAVIDSON, S. M. & HAUSENLOY, D. J. 2010. Inhibiting mitochondrial fission protects the heart against ischemia/reperfusion injury. *Circulation,* 121**,** 2012-22.

OTERA, H., WANG, C., CLELAND, M. M., SETOGUCHI, K., YOKOTA, S., YOULE, R. J. & MIHARA, K. 2010. Mff is an essential factor for mitochondrial recruitment of Drp1 during mitochondrial fission in mammalian cells. *J Cell Biol,* 191**,** 1141-58.

OTSUGA, D., KEEGAN, B. R., BRISCH, E., THATCHER, J. W., HERMANN, G. J., BLEAZARD, W. & SHAW, J. M. 1998. The dynamin-related GTPase,

Dnm1p, controls mitochondrial morphology in yeast. *J Cell Biol,* 143**,** 333-49.

PALACINO, J. J., SAGI, D., GOLDBERG, M. S., KRAUSS, S., MOTZ, C., WACKER, M., KLOSE, J. & SHEN, J. 2004. Mitochondrial dysfunction and oxidative damage in parkin-deficient mice. *J Biol Chem,* 279**,** 18614-22.

PALMIERI, L., ALBERIO, S., PISANO, I., LODI, T., MEZNARIC-PETRUSA, M., ZIDAR, J., SANTORO, A., SCARCIA, P., FONTANESI, F., LAMANTEA, E., FERRERO, I. & ZEVIANI, M. 2005. Complete loss-of-function of the heart/muscle-specific adenine nucleotide translocator is associated with mitochondrial myopathy and cardiomyopathy. *Hum Mol Genet,* 14**,** 3079-88.

PARONE, P. A., JAMES, D. I., DA CRUZ, S., MATTENBERGER, Y., DONZE, O., BARJA, F. & MARTINOU, J. C. 2006. Inhibiting the mitochondrial fission machinery does not prevent Bax/Bak-dependent apoptosis. *Mol Cell Biol,* 26**,** 7397-408.

PERRY, T. L., HANSEN, S. & KLOSTER, M. 1973. Huntington's chorea. Deficiency of gamma-aminobutyric acid in brain. *N Engl J Med,* 288**,** 337-42.

PESCH, U. E., FRIES, J. E., BETTE, S., KALBACHER, H., WISSINGER, B., ALEXANDER, C. & KOHLER, K. 2004. OPA1, the disease gene for autosomal dominant optic atrophy, is specifically expressed in ganglion cells and intrinsic neurons of the retina. *Invest Ophthalmol Vis Sci,* 45**,** 4217-25.

PESCH, U. E., LEO-KOTTLER, B., MAYER, S., JURKLIES, B., KELLNER, U., APFELSTEDT-SYLLA, E., ZRENNER, E., ALEXANDER, C. & WISSINGER, B. 2001. OPA1 mutations in patients with autosomal dominant optic atrophy and evidence for semi-dominant inheritance. *Hum Mol Genet,* 10**,** 1359-68.

PITTS, K. R., YOON, Y., KRUEGER, E. W. & MCNIVEN, M. A. 1999. The dynamin-like protein DLP1 is essential for normal distribution and morphology of the endoplasmic reticulum and mitochondria in mammalian cells. *Mol Biol Cell,* 10**,** 4403-17.

POOLE, A. C., THOMAS, R. E., ANDREWS, L. A., MCBRIDE, H. M., WHITWORTH, A. J. & PALLANCK, L. J. 2008. The PINK1/Parkin pathway regulates mitochondrial morphology. *Proc Natl Acad Sci U S A,* 105**,** 1638-43.

POWERS, W. J., VIDEEN, T. O., MARKHAM, J., MCGEE-MINNICH, L., ANTENOR-DORSEY, J. V., HERSHEY, T. & PERLMUTTER, J. S. 2007. Selective defect of in vivo glycolysis in early Huntington's disease striatum. *Proc Natl Acad Sci U S A,* 104**,** 2945-9.

PRAEFCKE, G. J. & MCMAHON, H. T. 2004. The dynamin superfamily: universal membrane tubulation and fission molecules? *Nat Rev Mol Cell Biol,* 5**,** 133-47.

PRIGIONE, A., FAULER, B., LURZ, R., LEHRACH, H. & ADJAYE, J. 2010. The senescence-related mitochondrial/oxidative stress pathway is

repressed in human induced pluripotent stem cells. *Stem Cells,* 28**,** 721-33.

RAMACHANDRAN, R., SURKA, M., CHAPPIE, J. S., FOWLER, D. M., FOSS, T. R., SONG, B. D. & SCHMID, S. L. 2007. The dynamin middle domain is critical for tetramerization and higher-order self-assembly. *EMBO J,* 26**,** 559-66.

RAPAPORT, D., BRUNNER, M., NEUPERT, W. & WESTERMANN, B. 1998. Fzo1p is a mitochondrial outer membrane protein essential for the biogenesis of functional mitochondria in Saccharomyces cerevisiae. *J Biol Chem,* 273**,** 20150-5.

RICHARDSON, P., MCKENNA, W., BRISTOW, M., MAISCH, B., MAUTNER, B., O'CONNELL, J., OLSEN, E., THIENE, G., GOODWIN, J., GYARFAS, I., MARTIN, I. & NORDET, P. 1996. Report of the 1995 World Health Organization/International Society and Federation of Cardiology Task Force on the Definition and Classification of cardiomyopathies. *Circulation,* 93**,** 841-2.

RIZZUTO, R., DUCHEN, M. R. & POZZAN, T. 2004. Flirting in little space: the ER/mitochondria Ca2+ liaison. *Sci STKE,* 2004**,** re1.

ROJO, M., LEGROS, F., CHATEAU, D. & LOMBES, A. 2002. Membrane topology and mitochondrial targeting of mitofusins, ubiquitous mammalian homologs of the transmembrane GTPase Fzo. *J Cell Sci,* 115**,** 1663-74.

ROSSE, T., OLIVIER, R., MONNEY, L., RAGER, M., CONUS, S., FELLAY, I., JANSEN, B. & BORNER, C. 1998. Bcl-2 prolongs cell survival after Bax-induced release of cytochrome c. *Nature,* 391**,** 496-9.

RUBINSZTEIN, D. C., LEGGO, J., COLES, R., ALMQVIST, E., BIANCALANA, V., CASSIMAN, J. J., CHOTAI, K., CONNARTY, M., CRAUFORD, D., CURTIS, A., CURTIS, D., DAVIDSON, M. J., DIFFER, A. M., DODE, C., DODGE, A., FRONTALI, M., RANEN, N. G., STINE, O. C., SHERR, M., ABBOTT, M. H., FRANZ, M. L., GRAHAM, C. A., HARPER, P. S., HEDREEN, J. C., HAYDEN, M. R. & *ET AL*. 1996. Phenotypic characterization of individuals with 30-40 CAG repeats in the Huntington disease (HD) gene reveals HD cases with 36 repeats and apparently normal elderly individuals with 36-39 repeats. *Am J Hum Genet,* 59**,** 16-22.

SANTEL, A. & FULLER, M. T. 2001. Control of mitochondrial morphology by a human mitofusin. *J Cell Sci,* 114**,** 867-74.

SARMA, S., LI, N., VAN OORT, R. J., REYNOLDS, C., SKAPURA, D. G. & WEHRENS, X. H. 2010. Genetic inhibition of PKA phosphorylation of RyR2 prevents dystrophic cardiomyopathy. *Proc Natl Acad Sci U S A,* 107**,** 13165-70.

SAWA, A., WIEGAND, G. W., COOPER, J., MARGOLIS, R. L., SHARP, A. H., LAWLER, J. F., JR., GREENAMYRE, J. T., SNYDER, S. H. & ROSS, C. A. 1999. Increased apoptosis of Huntington disease lymphoblasts associated with repeat length-dependent mitochondrial depolarization. *Nat Med,* 5**,** 1194-8.

SCHIFF, M., OGIER DE BAULNY, H. & LOMBES, A. 2011. Neonatal cardiomyopathies and metabolic crises due to oxidative phosphorylation defects. *Semin Fetal Neonatal Med,* 16**,** 216-21.

SCHMITT, J. P., KAMISAGO, M., ASAHI, M., LI, G. H., AHMAD, F., MENDE, U., KRANIAS, E. G., MACLENNAN, D. H., SEIDMAN, J. G. & SEIDMAN, C. E. 2003. Dilated cardiomyopathy and heart failure caused by a mutation in phospholamban. *Science,* 299**,** 1410-3.

SEBILLON, P., BOUCHIER, C., BIDOT, L. D., BONNE, G., AHAMED, K., CHARRON, P., DROUIN-GARRAUD, V., MILLAIRE, A., DESRUMEAUX, G., BENAICHE, A., CHARNIOT, J. C., SCHWARTZ, K., VILLARD, E. & KOMAJDA, M. 2003. Expanding the phenotype of LMNA mutations in dilated cardiomyopathy and functional consequences of these mutations. *J Med Genet,* 40**,** 560-7.

SHEPARD, K. A. & YAFFE, M. P. 1999. The yeast dynamin-like protein, Mgm1p, functions on the mitochondrial outer membrane to mediate mitochondrial inheritance. *J Cell Biol,* 144**,** 711-20.

SHIMIZU, S. & TSUJIMOTO, Y. 2000. Proapoptotic BH3-only Bcl-2 family members induce cytochrome c release, but not mitochondrial membrane potential loss, and do not directly modulate voltage-dependent anion channel activity. *Proc Natl Acad Sci U S A,* 97**,** 577-82.

SHIN, H. W., TAKATSU, H., MUKAI, H., MUNEKATA, E., MURAKAMI, K. & NAKAYAMA, K. 1999. Intermolecular and interdomain interactions of a dynamin-related GTP-binding protein, Dnm1p/Vps1p-like protein. *J Biol Chem,* 274**,** 2780-5.

SHIRENDEB, U. P., CALKINS, M. J., MANCZAK, M., ANEKONDA, V., DUFOUR, B., MCBRIDE, J. L., MAO, P. & REDDY, P. H. 2012. Mutant huntingtin's interaction with mitochondrial protein Drp1 impairs mitochondrial biogenesis and causes defective axonal transport and synaptic degeneration in Huntington's disease. *Hum Mol Genet,* 21**,** 406-20.

SHOU, W., AGHDASI, B., ARMSTRONG, D. L., GUO, Q., BAO, S., CHARNG, M. J., MATHEWS, L. M., SCHNEIDER, M. D., HAMILTON, S. L. & MATZUK, M. M. 1998. Cardiac defects and altered ryanodine receptor function in mice lacking FKBP12. *Nature,* 391**,** 489-92.

SMIRNOVA, E., GRIPARIC, L., SHURLAND, D. L. & VAN DER BLIEK, A. M. 2001. Dynamin-related protein Drp1 is required for mitochondrial division in mammalian cells. *Mol Biol Cell,* 12**,** 2245-56.

SMIRNOVA, E., SHURLAND, D. L., RYAZANTSEV, S. N. & VAN DER BLIEK, A. M. 1998. A human dynamin-related protein controls the distribution of mitochondria. *J Cell Biol,* 143**,** 351-8.

SMITH, K. M., MATSON, S., MATSON, W. R., CORMIER, K., DEL SIGNORE, S. J., HAGERTY, S. W., STACK, E. C., RYU, H. & FERRANTE, R. J. 2006. Dose ranging and efficacy study of high-dose coenzyme Q10 formulations in Huntington's disease mice. *Biochim Biophys Acta,* 1762**,** 616-26.

SONG, W., CHEN, J., PETRILLI, A., LIOT, G., KLINGLMAYR, E., ZHOU, Y., POQUIZ, P., TJONG, J., POULADI, M. A., HAYDEN, M. R., MASLIAH, E.,

ELLISMAN, M., ROUILLER, I., SCHWARZENBACHER, R., BOSSY, B., PERKINS, G. & BOSSY-WETZEL, E. 2011. Mutant huntingtin binds the mitochondrial fission GTPase dynamin-related protein-1 and increases its enzymatic activity. *Nat Med,* 17**,** 377-82.

SOUVERIJN, J. H., HUISMAN, L. A., ROSING, J. & KEMP, A., JR. 1973. Comparison of ADP and ATP as substrates for the adenine nucleotide translocator in rat-liver mitochondria. *Biochim Biophys Acta,* 305**,** 185-98.

STAUB, O. & ROTIN, D. 2006. Role of ubiquitylation in cellular membrane transport. *Physiol Rev,* 86**,** 669-707.

SUEN, D. F., NORRIS, K. L. & YOULE, R. J. 2008. Mitochondrial dynamics and apoptosis. *Genes Dev,* 22**,** 1577-90.

SUZUKI, M., JEONG, S. Y., KARBOWSKI, M., YOULE, R. J. & TJANDRA, N. 2003. The solution structure of human mitochondria fission protein Fis1 reveals a novel TPR-like helix bundle. *J Mol Biol,* 334**,** 445-58.

SWEITZER, S. M. & HINSHAW, J. E. 1998. Dynamin undergoes a GTP-dependent conformational change causing vesiculation. *Cell,* 93**,** 1021-9.

SZABADKAI, G., SIMONI, A. M., CHAMI, M., WIECKOWSKI, M. R., YOULE, R. J. & RIZZUTO, R. 2004. Drp-1-dependent division of the mitochondrial network blocks intraorganellar Ca2+ waves and protects against Ca2+-mediated apoptosis. *Mol Cell,* 16**,** 59-68.

SZALAI, G., KRISHNAMURTHY, R. & HAJNOCZKY, G. 1999. Apoptosis driven by IP(3)-linked mitochondrial calcium signals. *EMBO J,* 18**,** 6349-61.

SZANDA, G., HALASZ, E. & SPAT, A. 2010. Protein kinases reduce mitochondrial Ca2+ uptake through an action on the outer mitochondrial membrane. *Cell Calcium,* 48**,** 168-75.

TABRIZI, S. J., CLEETER, M. W., XUEREB, J., TAANMAN, J. W., COOPER, J. M. & SCHAPIRA, A. H. 1999. Biochemical abnormalities and excitotoxicity in Huntington's disease brain. *Ann Neurol,* 45**,** 25-32.

TAGUCHI, N., ISHIHARA, N., JOFUKU, A., OKA, T. & MIHARA, K. 2007. Mitotic phosphorylation of dynamin-related GTPase Drp1 participates in mitochondrial fission. *J Biol Chem,* 282**,** 11521-9.

TAKIMOTO, E. & KASS, D. A. 2007. Role of oxidative stress in cardiac hypertrophy and remodeling. *Hypertension,* 49**,** 241-8.

TAYLOR, M. R., FAIN, P. R., SINAGRA, G., ROBINSON, M. L., ROBERTSON, A. D., CARNIEL, E., DI LENARDA, A., BOHLMEYER, T. J., FERGUSON, D. A., BRODSKY, G. L., BOUCEK, M. M., LASCOR, J., MOSS, A. C., LI, W. L., STETLER, G. L., MUNTONI, F., BRISTOW, M. R. & MESTRONI, L. 2003. Natural history of dilated cardiomyopathy due to lamin A/C gene mutations. *J Am Coll Cardiol,* 41**,** 771-80.

THIENE, G., NAVA, A., CORRADO, D., ROSSI, L. & PENNELLI, N. 1988. Right ventricular cardiomyopathy and sudden death in young people. *N Engl J Med,* 318**,** 129-33.

THISELTON, D. L., ALEXANDER, C., MORRIS, A., BROOKS, S., ROSENBERG, T., EIBERG, H., KJER, B., KJER, P., BHATTACHARYA, S. S. & VOTRUBA,

M. 2001. A frameshift mutation in exon 28 of the OPA1 gene explains the high prevalence of dominant optic atrophy in the Danish population: evidence for a founder effect. *Hum Genet,* 109**,** 498-502.

THISELTON, D. L., ALEXANDER, C., TAANMAN, J. W., BROOKS, S., ROSENBERG, T., EIBERG, H., ANDREASSON, S., VAN REGEMORTER, N., MUNIER, F. L., MOORE, A. T., BHATTACHARYA, S. S. & VOTRUBA, M. 2002. A comprehensive survey of mutations in the OPA1 gene in patients with autosomal dominant optic atrophy. *Invest Ophthalmol Vis Sci,* 43**,** 1715-24.

THOMPSON, H. M., SKOP, A. R., EUTENEUER, U., MEYER, B. J. & MCNIVEN, M. A. 2002. The large GTPase dynamin associates with the spindle midzone and is required for cytokinesis. *Curr Biol,* 12**,** 2111-7.

TIAN, Q. & BARGER, P. M. 2006. Deranged energy substrate metabolism in the failing heart. *Curr Hypertens Rep,* 8**,** 465-71.

TIEU, Q. & NUNNARI, J. 2000. Mdv1p is a WD repeat protein that interacts with the dynamin-related GTPase, Dnm1p, to trigger mitochondrial division. *J Cell Biol,* 151**,** 353-66.

TOWBIN, J. A., HEJTMANCIK, J. F., BRINK, P., GELB, B., ZHU, X. M., CHAMBERLAIN, J. S., MCCABE, E. R. & SWIFT, M. 1993. X-linked dilated cardiomyopathy. Molecular genetic evidence of linkage to the Duchenne muscular dystrophy (dystrophin) gene at the Xp21 locus. *Circulation,* 87**,** 1854-65.

TSUBATA, S., BOWLES, K. R., VATTA, M., ZINTZ, C., TITUS, J., MUHONEN, L., BOWLES, N. E. & TOWBIN, J. A. 2000. Mutations in the human delta-sarcoglycan gene in familial and sporadic dilated cardiomyopathy. *J Clin Invest,* 106**,** 655-62.

TWIG, G., ELORZA, A., MOLINA, A. J., MOHAMED, H., WIKSTROM, J. D., WALZER, G., STILES, L., HAIGH, S. E., KATZ, S., LAS, G., ALROY, J., WU, M., PY, B. F., YUAN, J., DEENEY, J. T., CORKEY, B. E. & SHIRIHAI, O. S. 2008. Fission and selective fusion govern mitochondrial segregation and elimination by autophagy. *EMBO J,* 27**,** 433-46.

VATTA, M., MOHAPATRA, B., JIMENEZ, S., SANCHEZ, X., FAULKNER, G., PERLES, Z., SINAGRA, G., LIN, J. H., VU, T. M., ZHOU, Q., BOWLES, K. R., DI LENARDA, A., SCHIMMENTI, L., FOX, M., CHRISCO, M. A., MURPHY, R. T., MCKENNA, W., ELLIOTT, P., BOWLES, N. E., CHEN, J., VALLE, G. & TOWBIN, J. A. 2003. Mutations in Cypher/ZASP in patients with dilated cardiomyopathy and left ventricular non-compaction. *J Am Coll Cardiol,* 42**,** 2014-27.

VAZQUEZ-MARTIN, A., CUFI, S., COROMINAS-FAJA, B., OLIVERAS-FERRAROS, C., VELLON, L. & MENENDEZ, J. A. 2012. Mitochondrial fusion by pharmacological manipulation impedes somatic cell reprogramming to pluripotency: new insight into the role of mitophagy in cell stemness. *Aging (Albany NY),* 4**,** 393-401.

VIZEACOUMAR, F. J., VREDEN, W. N., FAGARASANU, M., EITZEN, G. A., AITCHISON, J. D. & RACHUBINSKI, R. A. 2006. The dynamin-like

protein Vps1p of the yeast Saccharomyces cerevisiae associates with peroxisomes in a Pex19p-dependent manner. *J Biol Chem,* 281**,** 12817-23.

VONSATTEL, J. P. & DIFIGLIA, M. 1998. Huntington disease. *J Neuropathol Exp Neurol,* 57**,** 369-84.

WAKABAYASHI, J., ZHANG, Z., WAKABAYASHI, N., TAMURA, Y., FUKAYA, M., KENSLER, T. W., IIJIMA, M. & SESAKI, H. 2009. The dynamin-related GTPase Drp1 is required for embryonic and brain development in mice. *J Cell Biol,* 186**,** 805-16.

WALLACE, D. C. 1999. Mitochondrial diseases in man and mouse. *Science,* 283**,** 1482-8.

WANG, H., SONG, P., DU, L., TIAN, W., YUE, W., LIU, M., LI, D., WANG, B., ZHU, Y., CAO, C., ZHOU, J. & CHEN, Q. 2011. Parkin ubiquitinates Drp1 for proteasome-dependent degradation: implication of dysregulated mitochondrial dynamics in Parkinson disease. *J Biol Chem,* 286**,** 11649-58.

WANG, J., WILHELMSSON, H., GRAFF, C., LI, H., OLDFORS, A., RUSTIN, P., BRUNING, J. C., KAHN, C. R., CLAYTON, D. A., BARSH, G. S., THOREN, P. & LARSSON, N. G. 1999. Dilated cardiomyopathy and atrioventricular conduction blocks induced by heart-specific inactivation of mitochondrial DNA gene expression. *Nat Genet,* 21**,** 133-7.

WANG, X., SU, B., FUJIOKA, H. & ZHU, X. 2008. Dynamin-like protein 1 reduction underlies mitochondrial morphology and distribution abnormalities in fibroblasts from sporadic Alzheimer's disease patients. *Am J Pathol,* 173**,** 470-82.

WANG, X., SU, B., ZHENG, L., PERRY, G., SMITH, M. A. & ZHU, X. 2009. The role of abnormal mitochondrial dynamics in the pathogenesis of Alzheimer's disease. *J Neurochem,* 109 Suppl 1**,** 153-9.

WATERHAM, H. R., KOSTER, J., VAN ROERMUND, C. W., MOOYER, P. A., WANDERS, R. J. & LEONARD, J. V. 2007. A lethal defect of mitochondrial and peroxisomal fission. *N Engl J Med,* 356**,** 1736-41.

WESTERMANN, B. 2010. Mitochondrial fusion and fission in cell life and death. *Nat Rev Mol Cell Biol,* 11**,** 872-84.

WHITE, K. E., DAVIES, V. J., HOGAN, V. E., PIECHOTA, M. J., NICHOLS, P. P., TURNBULL, D. M. & VOTRUBA, M. 2009. OPA1 deficiency associated with increased autophagy in retinal ganglion cells in a murine model of dominant optic atrophy. *Invest Ophthalmol Vis Sci,* 50**,** 2567-71.

WOJTKOWIAK, J. W., ROTHBERG, J. M., KUMAR, V., SCHRAMM, K. J., HALLER, E., PROEMSEY, J. B., LLOYD, M. C., SLOANE, B. F. & GILLIES, R. J. 2012. Chronic Autophagy Is a Cellular Adaptation to Tumor Acidic pH Microenvironments. *Cancer Res,* 72**,** 3938-47.

WOODMAN, B., BUTLER, R., LANDLES, C., LUPTON, M. K., TSE, J., HOCKLY, E., MOFFITT, H., SATHASIVAM, K. & BATES, G. P. 2007. The Hdh(Q150/Q150) knock-in mouse model of HD and the R6/2 exon

1 model develop comparable and widespread molecular phenotypes. *Brain Res Bull,* 72**,** 83-97.

XIE, Z. & KLIONSKY, D. J. 2007. Autophagosome formation: core machinery and adaptations. *Nat Cell Biol,* 9**,** 1102-9.

YANG, J., LIU, X., BHALLA, K., KIM, C. N., IBRADO, A. M., CAI, J., PENG, T. I., JONES, D. P. & WANG, X. 1997. Prevention of apoptosis by Bcl-2: release of cytochrome c from mitochondria blocked. *Science,* 275**,** 1129-32.

YANG, Y., OUYANG, Y., YANG, L., BEAL, M. F., MCQUIBBAN, A., VOGEL, H. & LU, B. 2008. Pink1 regulates mitochondrial dynamics through interaction with the fission/fusion machinery. *Proc Natl Acad Sci U S A,* 105**,** 7070-5.

YANG, Z. & KLIONSKY, D. J. 2010. Eaten alive: a history of macroautophagy. *Nat Cell Biol,* 12**,** 814-22.

YOON, Y., KRUEGER, E. W., OSWALD, B. J. & MCNIVEN, M. A. 2003. The mitochondrial protein hFis1 regulates mitochondrial fission in mammalian cells through an interaction with the dynamin-like protein DLP1. *Mol Cell Biol,* 23**,** 5409-20.

ZHANG, P. & HINSHAW, J. E. 2001. Three-dimensional reconstruction of dynamin in the constricted state. *Nat Cell Biol,* 3**,** 922-6.

ZHANG, R., KHOO, M. S., WU, Y., YANG, Y., GRUETER, C. E., NI, G., PRICE, E. E., JR., THIEL, W., GUATIMOSIM, S., SONG, L. S., MADU, E. C., SHAH, A. N., VISHNIVETSKAYA, T. A., ATKINSON, J. B., GUREVICH, V. V., SALAMA, G., LEDERER, W. J., COLBRAN, R. J. & ANDERSON, M. E. 2005. Calmodulin kinase II inhibition protects against structural heart disease. *Nat Med,* 11**,** 409-17.

ZHANG, X., HAN, D., DING, D., DAI, P., YANG, W., JIANG, S. & SALVI, R. J. 2002. Cochlear mitochondrial DNA3867bp deletion in aged mice. *Chin Med J (Engl),* 115**,** 1390-3.

ZHANG, Y. & CHAN, D. C. 2007. Structural basis for recruitment of mitochondrial fission complexes by Fis1. *Proc Natl Acad Sci U S A,* 104**,** 18526-30.

ZHAO, J., LIU, T., JIN, S., WANG, X., QU, M., UHLEN, P., TOMILIN, N., SHUPLIAKOV, O., LENDAHL, U. & NISTER, M. 2011. Human MIEF1 recruits Drp1 to mitochondrial outer membranes and promotes mitochondrial fusion rather than fission. *EMBO J,* 30**,** 2762-78.

ZHU, P. P., PATTERSON, A., STADLER, J., SEEBURG, D. P., SHENG, M. & BLACKSTONE, C. 2004. Intra- and intermolecular domain interactions of the C-terminal GTPase effector domain of the multimeric dynamin-like GTPase Drp1. *J Biol Chem,* 279**,** 35967-74.

ZUCHNER, S., MERSIYANOVA, I. V., MUGLIA, M., BISSAR-TADMOURI, N., ROCHELLE, J., DADALI, E. L., ZAPPIA, M., NELIS, E., PATITUCCI, A., SENDEREK, J., PARMAN, Y., EVGRAFOV, O., JONGHE, P. D., TAKAHASHI, Y., TSUJI, S., PERICAK-VANCE, M. A., QUATTRONE, A., BATTALOGLU, E., POLYAKOV, A. V., TIMMERMAN, V., SCHRODER, J. M. & VANCE, J. M. 2004. Mutations in the mitochondrial GTPase

mitofusin 2 cause Charcot-Marie-Tooth neuropathy type 2A. *Nat Genet,* 36**,** 449-51.

Appendices

Appendix I. Amino acid reference sequence for DNM1L

The reference sequence was obtained from UniProtAccessionNumberQ8K1M6.

MEALIPVINKLQDVFNTVGADIIQLPQIVVVGTQSSGKSSVLESLVGRDLLPR
GTGVVTRRPLILQLVHVSPEDKRKTTGEENGKFQSWRVEAEEWGKFLHTKNKL
YTDFDEIRQEIENETERISGNNKGVSPEPIHLKVFSPNVVNLTLVDLPGMTKV
PVGDQPKDIELQIRELILRFISNPNSIILAVTAANTDMATSEALKISREVDPD
GRRTLAVITKLDLMDAGTDAMDVLMGRVIPVKLGIIGVVNRSQLDINNKKSVT
DSIRDEYAFLQKKYPSLANRNGTKYLARTLNRLLMHHIRDCLPELKTRINVLA
AQYQSLLNSYGEPVDDKSATLLQLITKFATEYCNTIEGTAKYIETSELCGGAR
ICYIFHETFGRTLESVDPLGGLNTIDILTAIRNATGPRPALFVPEVSFELLVK
RQIKRLEEPSLRCVELVHEEMQRIIQHCSNYSTQELLRFPKLHDAIVEVVTCL
LRKRLPVTNEMVHNLAVAIELAYINTKHPDFADACGLMNNNIEEQRRNRLARE
LPSAGSRDKSSKVPSALAPASQEPPPAASAEADGKLIQDNRRETKNVPSAGGG
IGDGGQEPTTGNWRGMLKTSKAEELLAEEKSKPIPIMPASPQKGHAVNLLDVP
VPVARKLSAREQRDCEVIERLIKSYFLIVRKNIQDSVPKAVMHFLVNHVKDTL
QSELVGQLYKSSLLDDLLTESEDMAQRRKEAADMLKALQGASQIIAEIRETHL
W

The highlighted amino acids represent the mutations under analysis in this study. The alanine converted to aspartic acid is at position 401, while the cysteine is converted to phenylalanine at position 452 in Python.

Appendix II. Primers for Python genotyping.

Primers were designed to mutate the cytosine (C) base indicated in yellow to an adenine (A) base (also shown in yellow of the primer sequence), thereby creating a restriction site for XapI (G^AATTG), but only when the guanine (G) highlighted in red is mutated to a thymidine (T), as in Python. The resulting fragments after cleavage will be 129bp and 16bp. The wild type *Dnm1l* however will not cleave and remain a single band at 145bp. Therefore Python heterozygotes will show all possible fragments.

Primers:

PLF	5'-d(GCAGAGGATCATTCAGAATT) 3'
PLR	5'-d(TGGCATTTCAAATCAGTGTCA) 3'

XapI restriction site:

5' R^AATTY 3', where R represents an A or a G and Y represents a C or a T.

Dnm1l exon 11 and intron 12. Primer regions are underlined:

GGCCCCCGTCCTGCTTTATTTGTGCCTGAAGTTTCATTTGAGTTACTGGTCAA
ACGTCAGATTAAGCGTCTAGAAGAGCCCAGCCTACGGTGTGTGGAGCTGGTCC
ATGAGGAGATGCAGAGGATCATTCAGCATTGTAGCAATTACAGCACACAGGTA
TTGTGAATGACAGGGCTCACCAGAAAGTCCTCATAGAATGGGAGGAAATGAGC
TAAAAGTAACATCATTAGCTTCCTTACCTGACACTGATTTGAAATGCCATTCT
TAAATGTAAGATCCAAATCTAATTCAGTACTTTAGTGATTGTTTCATTTCCAG
TTAGACAGACTAACATTTTTAACTTCTTTATTACATTCAG

Appendix III. Python genotyping result.

The restriction product was loaded onto a 4% gel to separate the DNA bands. Samples 1-5 are of unknown genotype. These are digested with the XapI restriction enzyme along with 3 controls in parallel, analysed on the same gel. The first control is the DNA from a known Python heterozygote (*+/Py*), producing DNA fragments at 145bp and 129bp. The second control is the DNA of a known wild type (+/+) mouse, which produces one fragment at 145bp. The third control is a no template control (NTC), therefore should not contain any DNA fragments. The example below can assign samples 3 and 5 as *+/Py* and 1,2 and 4 as +/+. The 16bp band expected in Python samples is too small to be visualized on agarose gels.

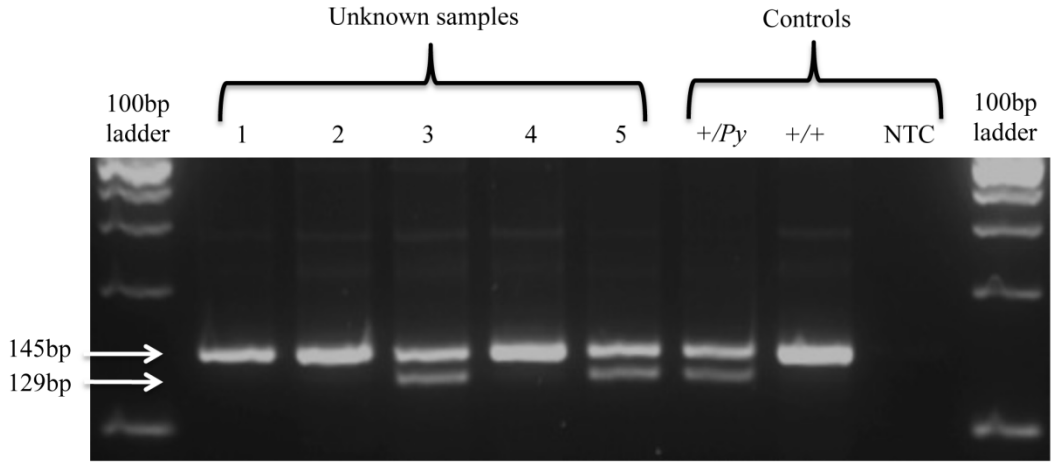

Appendix IV. pET101

Wild type *Dnm1l* and *Dnm1l*^{Py} were cloned into the pET101 vector creating 2 separate constructs. The vector contains a his-tag at the C-terminus of *Dnm1l*, allowing purification of the expressed fusion proteins. Purified wild type and Python Dnm1l were used to measure GTPase activity and investigate the dominant-negative effect of the Python monomer. The Python mutation, present at amino acid position 452 is shown indicated on the vector below. The vector contains ampicillin (β-lactamase) and tetracycline (Taylor *et al*.) resistance genes for selection in bacteria and a pBR322 origin to initiate DNA replication.

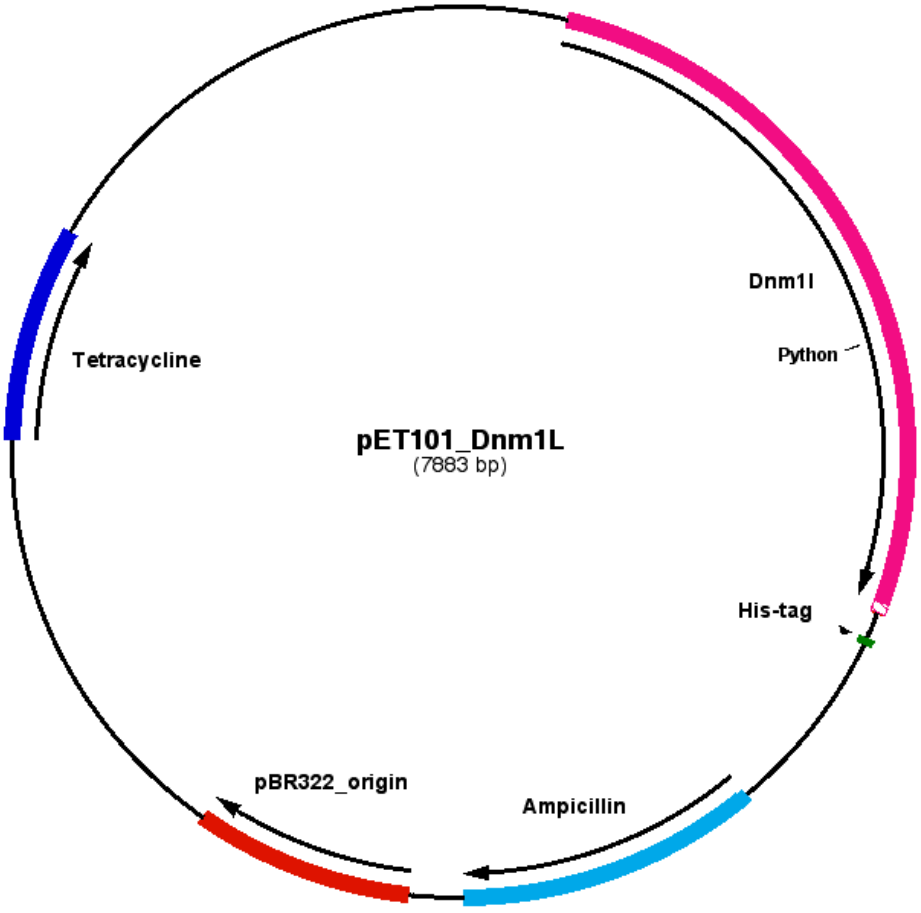

Appendix V. primers for pyrosequencing

A 286bp fragment containing *Dnm1l* exon 11 was amplified by PCR using the primers: Dnm1l_11F and Dnm1l_11R Biotin. The reverse primer contains a biotin tag to allow for purification of the fragment. The PSQ_Py primer is designed in complement to the *Dnm1l* sequence prior to the site of the Python mutation. Pyrosequencing analysis then begins by quantification of allelic expression at the mutation site. Red indicates exon 11 of Dnm1l, blue indicates the primer sequences and green represents the mutation site. Sequences flanking exon 11 are intron boundaries.

TGAAAACAAGAATAAATGTCTTAGCTGCTCAGTATCAGTCTCTTCTAAATAGC
TATGGTGAACCGGTGGATGATAAAAGTGCTACTTTACTCCAGCTTATTACCAA
ATTTGCCACAGAGTATTGTAACACGATTGAAGGAACCGCAAAGTACATTGAAA
CTTCTGAGCTATGCGGTGGTGCTAGGATTTGTTATATTTTCCATGAGACTTTC
GGGCGAACCTTAGAATCTGTGGACCCACTAGGTGGCCTTAACACTATTGACAT
CCTGACTGCCATCAGAAATGCTACTGGCCCCCGTCCTGCTTTATTTGTGCCTG
AAGTTTCATTTGAGTTACTGGTCAAACGTCAGATTAAGCGTCTAGAAGAGCCC
AGCCTACGGTGTGTGGAGCTGGTCCATGAGGAGATGCAGAGGATCATTCAGCA
TTGTAGCAATTACAGCACACAGGAATTGTTACGGTTCCCTAAACTTCACGATG
CCATAGTTGAAGTAGTGACCTGTCTTCTTCGTAAAAGGTTGCCCGTGACAAAT
GAAATGGTGCATAACTTAGTGGCAATTGAGCTAGCGTATATCAACACAAAACA
CCCCGACTTTGCTGATGCCTGTGGGCTAATGAACAATAATATAGAGGAACAAA
GAAGAAACAGGCTAGCAAGAGAGCTGCCTTCAGCTGGATCACGGGACAAGGTC
CCATCTGCAGGTGGTGGGATTGGAGACGGTGGTCAGGAACCAACAAC

PCR product 286bp

Primers:

Dnm1l_11F	5'-d(CCCACTAGGTGGCCTTAACACTAT)3'
Dnm1l_11R Biotin	5'-d(BIOTIN-GGGCAACCTTTTACGAAGAAGAC)3'
PSQ_Py	5'-d(GAGGATCATTCAGCATT)3'

Exon 11

Mutation: wild type: G
Mutant: T

Appendix VI. Primers for mouse cDNA cardiomyocyte markers

Primers were used to verify DNA loading amounts (*Actb* and *Gapdh*), pluripotency (*Pou5f1*) and cardiomyocyte differentiation (*Gata4*, *Myl7* and *Myh7*). Primers were published by Yuasa *et al*., (2005).

Gene	Sense primer (5' → 3')	Antisense primer (5' → 3')	Expected product size (bp)
Actb	TTCTTTGCAGCTCCTTCGTTGCCG	TGGATGGCTACGTACATGGCTGGG	457
Gapdh	TTCAACGGCACAGTCAAGG	CATGGACTGTGGTCATGAG	372
Pou5f1	CTCGAACCACATCCTTCTCT	GGCGTTCTCTTTGGAAAGGTGTTC	424
Gata4	CTGTCATCTCACTATGGGCA	CCAAGTCCGAGCAGGAATTT	257
Myl7	GCCAAGAAGCGGATAGAAGG	CTGTGGTTCAGGGCTCAGTC	480
Myh7	GCCAACACCAACCTGTCCAAGTTC	TGCAAAGGCTCCAGGTCTGAGGGC	202

Appendix VII. pLd11 construct

3 pLd11 constructs containing wild type *Dnm1l*, *Dnm1l*^{Py} and *Dnm1l*^{K38A} separately were used in the HeLa cell transfection. The construct also expresses GFP via an IRES from a CMV promoter, in order to identify transfected cells through visualization under the green excitation fluorescence filter of the microscope. The vector contains neomycin phophotransferase II, which allows for selection in bacteria against neomycin and also G418 in eukayotes. Dnm1l expression is under the control of a cytomegalovirus (CMV) promoter.

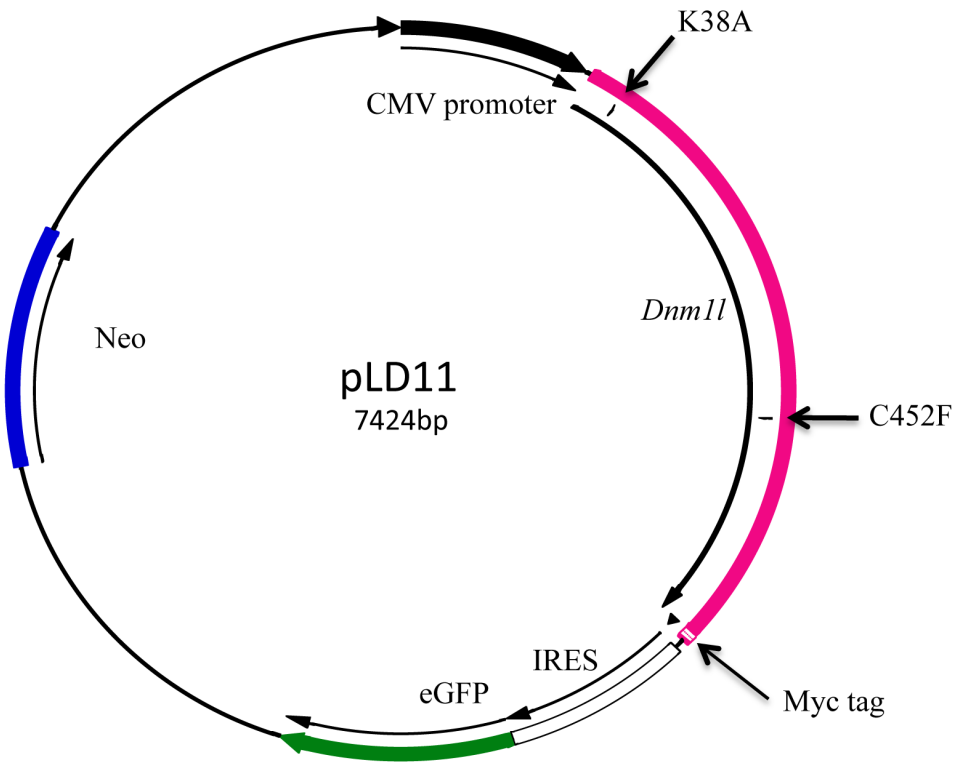

Appendix VIII. The mouse mtDNA C3H/HEH genome

The mtDNA genome is 16351bp. Zhang F and Zhang R primers are used to amplify the whole genome. Zhang 5 and Zhang 6 are used to amplify a 4.6kb region of the genome (Zhang *et al*., 2002). The genes are colour coded in the schematic and denote the respiratory enzyme sub-units they encode (see key). Also, tRNA genes are shown in cyan and rRNA genes are represented in green.

Primers:

Zhang F	5'-d(GAGGTGATGTTTTTGGTAAACAGG)3'
Zhang R	5'-d(GGTTCGTTTGTTCAACGATTAAAGTCCTACGTG)3'
Zhang 5	5'-d(ACCAACAGCTACCATTACATT)3'
Zhang 6	5'-d(TGATTGGGTTTAGGTCTG)3'

Key:

Enzyme	Colour	Subunits
NADH dehydrogenase (Complex I)	Red	ND1 – ND6
Cytochrome BC1 (Complex III)	Black	CYTB
Cytochrome C oxidase (Complex IV)	Blue	COX1 – COX3
ATP synthase	Pink	ATP6, ATP8

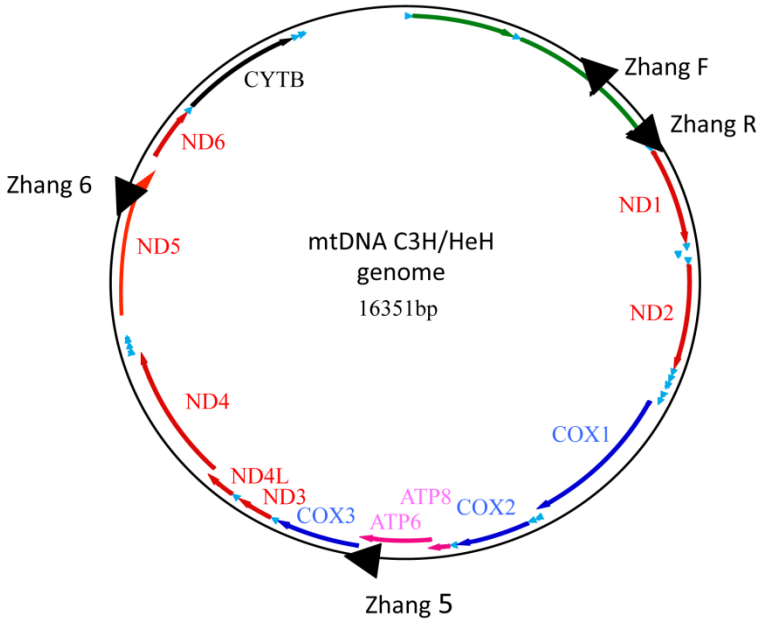

Appendix IX. pDEST32 & pDEST22 vectors

The ProQuest™ Gateway destination vectors used in a Yeast-2-Hybrid experiment were pDEST32, containing the GAL4 DNA binding domain and pDEST22, containing the GAL4 activation domain. Sequences encoding desired proteins or protein regions were cloned into the region between *att*R1 and *att*R2, replacing the fragment in the vectors. Within this fragment *ccd*B gene, which becomes lethal to the cell if expressed. Therefore cells will not survive if this part of the plasmid is not replaced with the desired gene. The pDEST32 contains the *LEU2* gene, which allows for yeast selection in medium lacking leucine and the aminoglycosidase N(3')-acetyl transferase I for gentamycin resistance (Gm^r) in bacteria. Whereas pDEST22 contains the *TRP1* gene, allowing for yeast selection in medium lacking tryptophan and bacterial selection the ampicillin resistance gene (Ap^r), β-lactamase. Transcription is under the control of the alcohol dehydrogenase promoter (pADH) and termination sequence (TerADH). Both plasmids contain 3 origins of replication: ARS4/Cen6 for replication in yeast, pUC origin (ori) for bacterial replication and the F1 intergenic region for replication in bacteriophage. pDEST32 also possesses the CYH2 gene, conferring sensitivity to cycloheximide. pDEST 22 contains a nuclear localization sequence in order to tag the fusion protein for import into the nucleus and subsequent transcription.

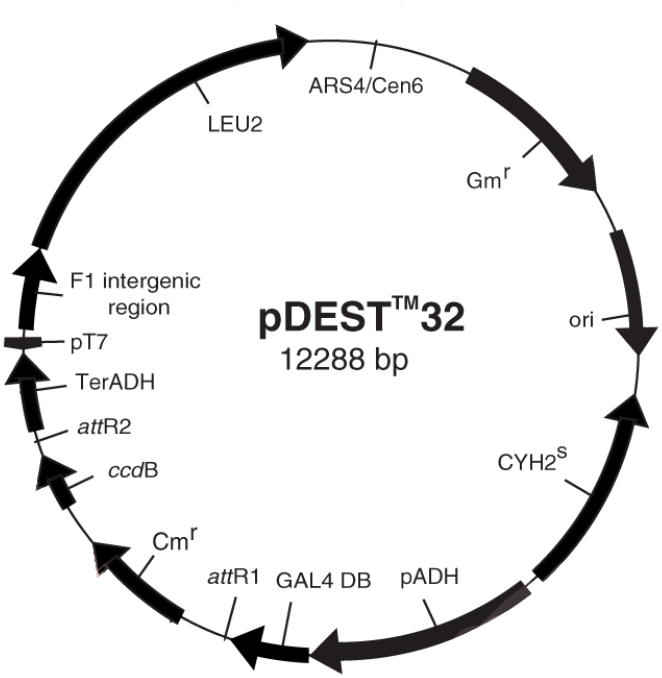
ARS4/Cen6
LEU2
Gm^r
F1 intergenic region
pT7
TerADH
attR2
ccdB
Cm^r
attR1
GAL4 DB
pADH
CYH2^s
ori
pDEST™32
12288 bp

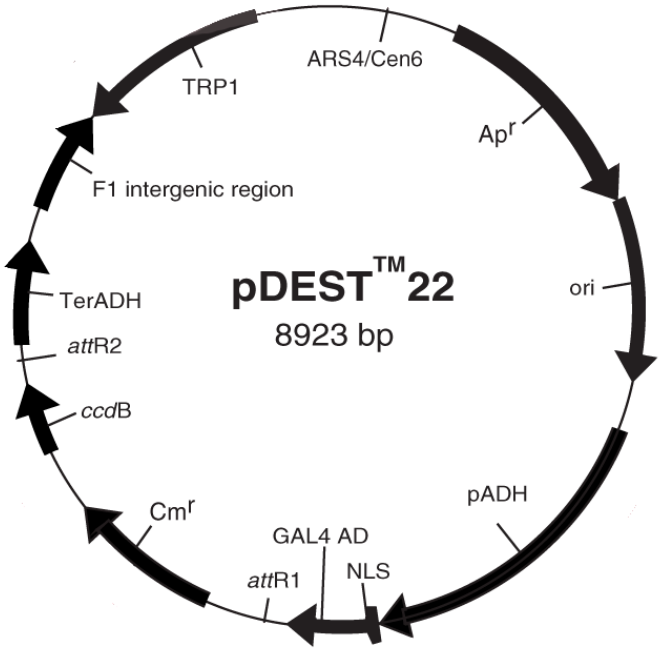
ARS4/Cen6
TRP1
Ap^r
F1 intergenic region
TerADH
attR2
ccdB
Cm^r
attR1
GAL4 AD
NLS
pADH
ori
pDEST™22
8923 bp

Appendix X. pAS2-1 and pACT2 vectors

Matchmaker Gal4 Yeast-Two-Hybrid vectors were used to detect a number of reported interactions with DNM1L. pAS2-1 contains the GAL4 DNA binding domai, while pACT2 contains the GAL4 activation domain. Selection in yeast is achieved by the *TRP1* gene in pAS2-1 and *LEU2* in pACT2. Both vectors contain the β-lactamase gene conferring resistance to ampicillin in bacteria. Transcription is under the control of the alcohol dehydrogenase promoter (P_{ADH1}) and termination sequence (T_{ADH1}). pAS2-1 contains 3 origins of replication: 2 micron (2μ) ori for replication in yeast, Col E1 ori for bacterial replication and the F1 intergenic region (f1 ori) for replication in bacteriophage. pACT2 lacks that of f1 ori. pAS2-1 also contains the *CYH2* gene conferring sensitivity to cycloheximide.

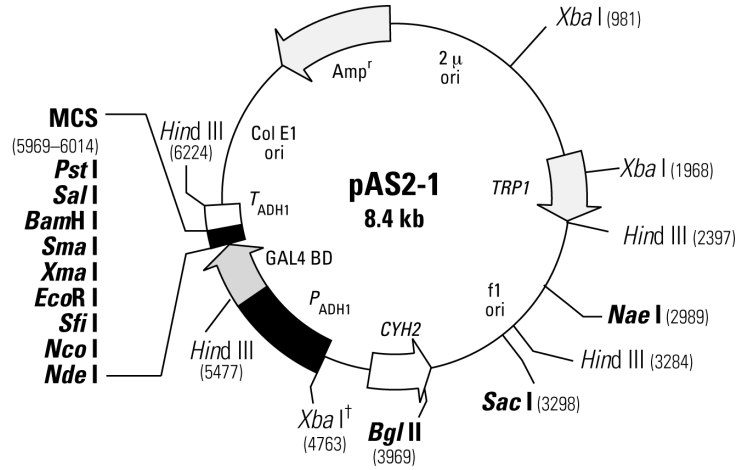

Appendix XI. Mitochondrial aequorin vector

Prof Rosario Rizzuto of University of Farrara supplied the mitochondrial aequorin vector. The parent vector is pcDNA3.1. The aequorin sequence has been fused to a human Cox VIII sequence to produce a mitochondria-targeted vector. The vector also contains an HA tag and is Ampicillin resistant (β-lactamase gene) and neomycin / kanamycin resistant (neomycin phophotransferase II gene) in bacteria. neomycin phophotransferase II also confers resistance to G418 in eukaryotes.

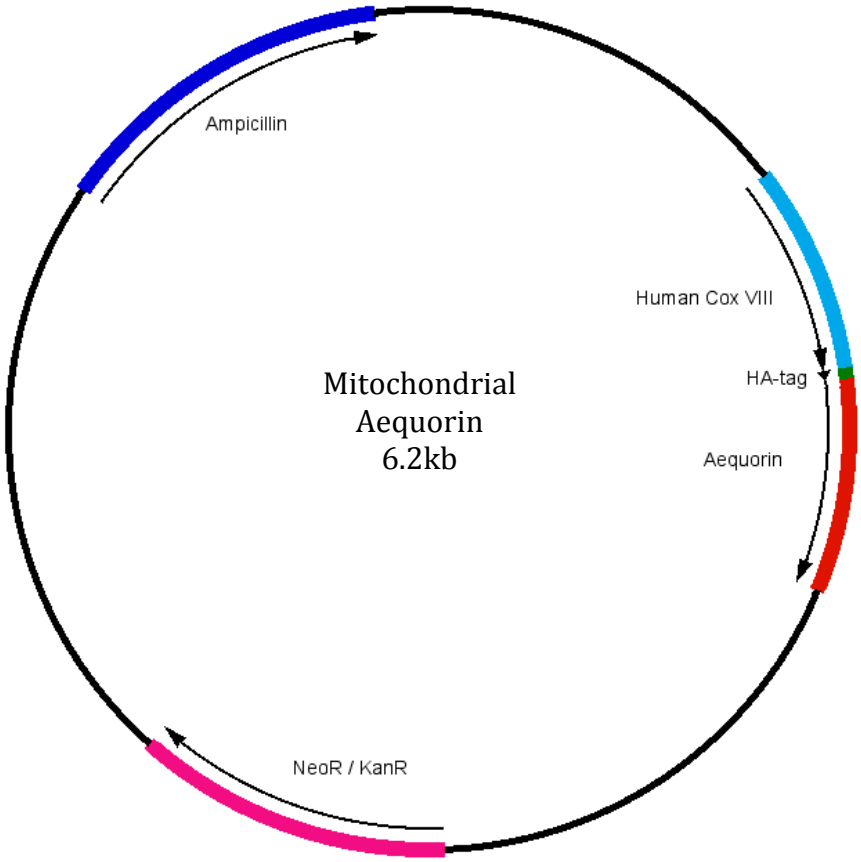

Appendix XII. R6/2 genotyping

Primers were designed by the Jackson laboratories (Bar Harbor, ME) in order to genotype the presence of the R6/2 transgene. The PCR identifies animals, which are positive for the transgene with a 170bp fragment. The wild type animals will not possess this size fragment. Analysis of DNA bands was carried out on a 3% agarose gel. DNA from a known R6/2 mouse and a known wild type mouse were used as controls along with a NTC. The example below can assign samples 3 and 5 as *0/T* and 1,2 and 4 as +/+.

Primers:

R6/2F	5'-d(CGCAGGCTAGGGCTGTCAATCATGCT)3'
R6/2BR1	5'-d(TGGAAGGACTTGAGGGACTC)3'

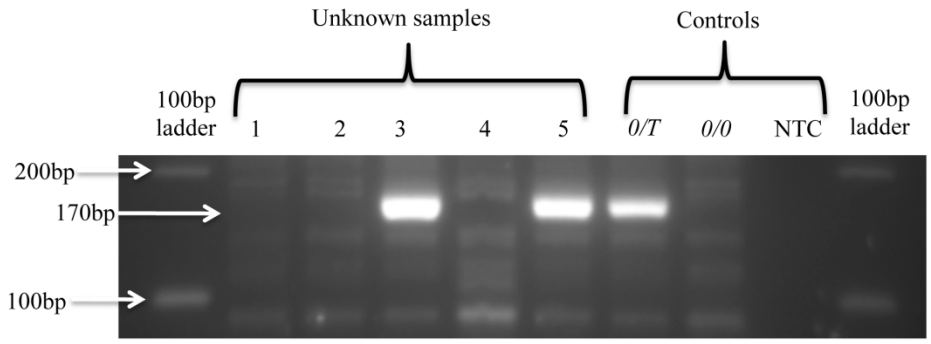

Appendix XIII. Strain specific onset of CHF.

The onset of overt CHF symptoms in the Python C3H mice occurs on average at 82 days in males and 85 days in females. On the C57BL/6J background, mice develop CHF after 168 days on average for males and 166 on average for females. The F1 generation represents the offspring from the initial backcross of C3H mice to C57BL/6J mice, therefore would be expected to develop CHF symptoms at an age between the 2 genetic background. On average females of the F1 generation develop CHF at 119 days, while males develop it at 108 days.

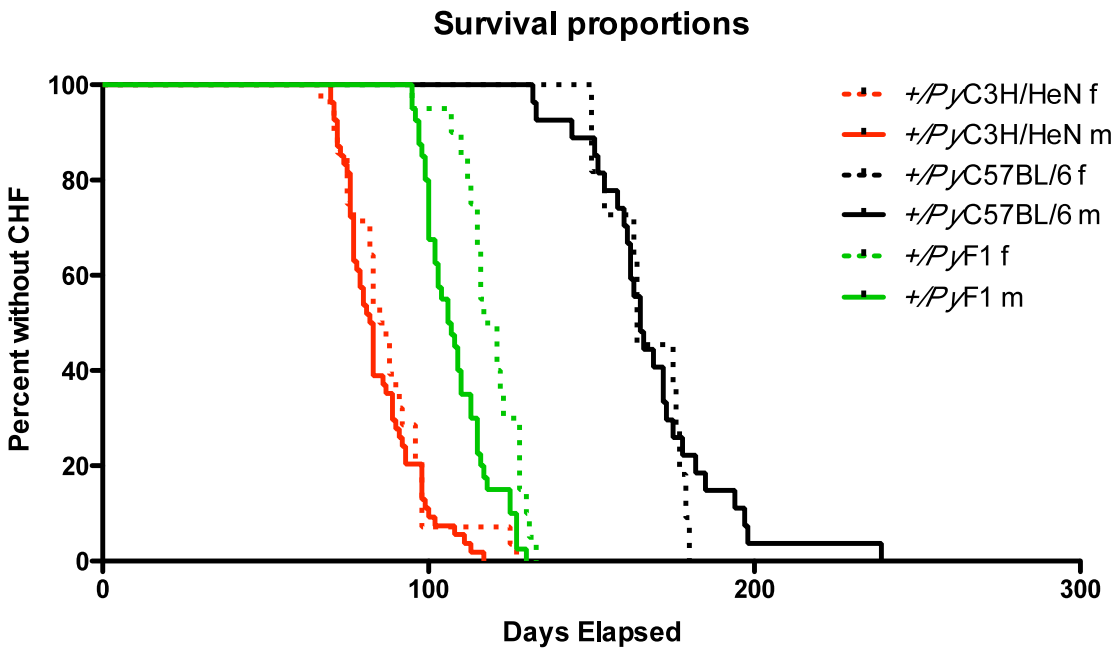

Appendix XIV. Subcloning to derive ES cell models

ES cells were initially isolated from Python and wild type C57BL/6J mice: Py_4 and wt_1. As these clones contained heterogeneous populations, subcloning was used to derive homogenous populations and provide an ES cell model. Python subclones: Py_D9 and Py_D8 and wild type subclones: wt_B10 and wt_B5 were chosen to use as cell models based on their homogeneity and morphology.

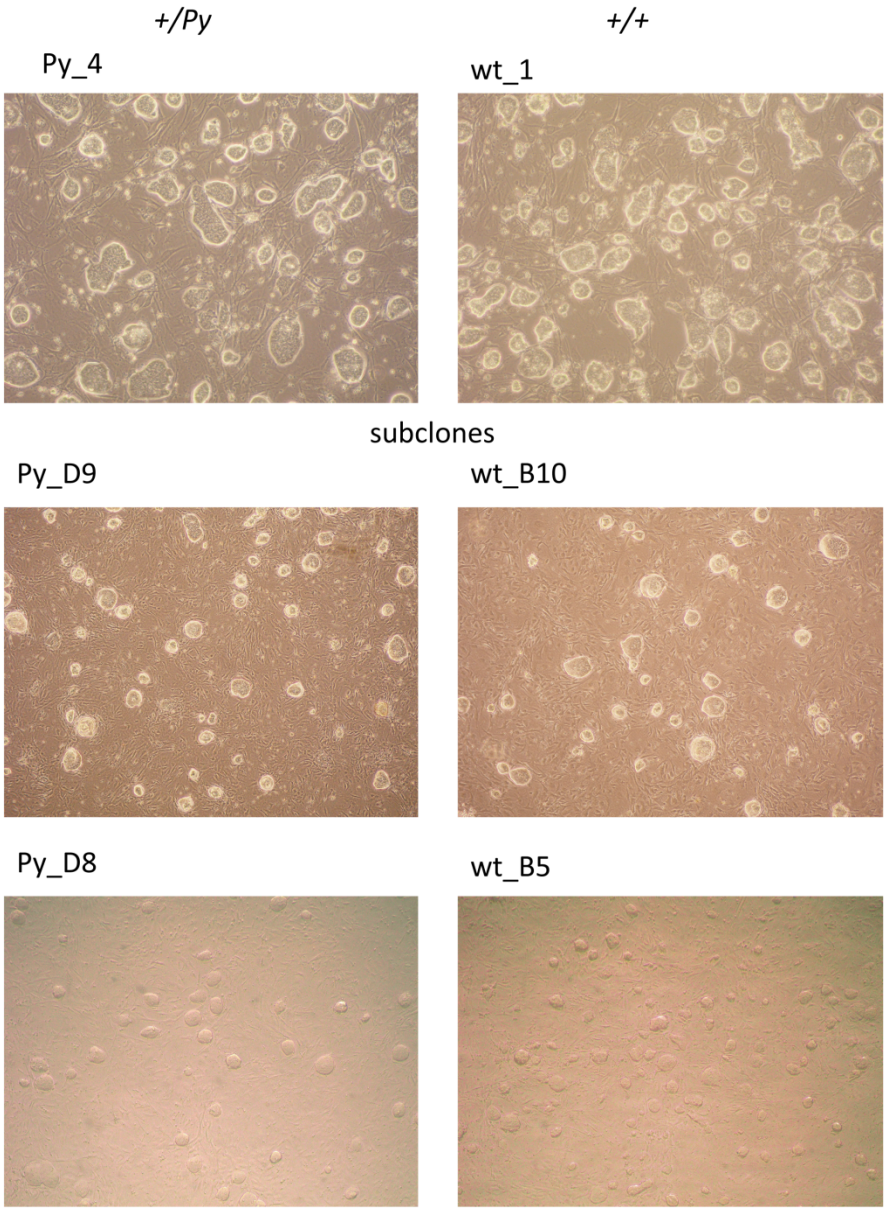

Appendix XV. Growth rates of *+/Py* and +/+ ES cell lines

Growth rates were investigated for Python and wild type ES cell lines to establish if the Python mutation had any impact on this. The experiment revealed the growth rates for both genotypes were very similar.

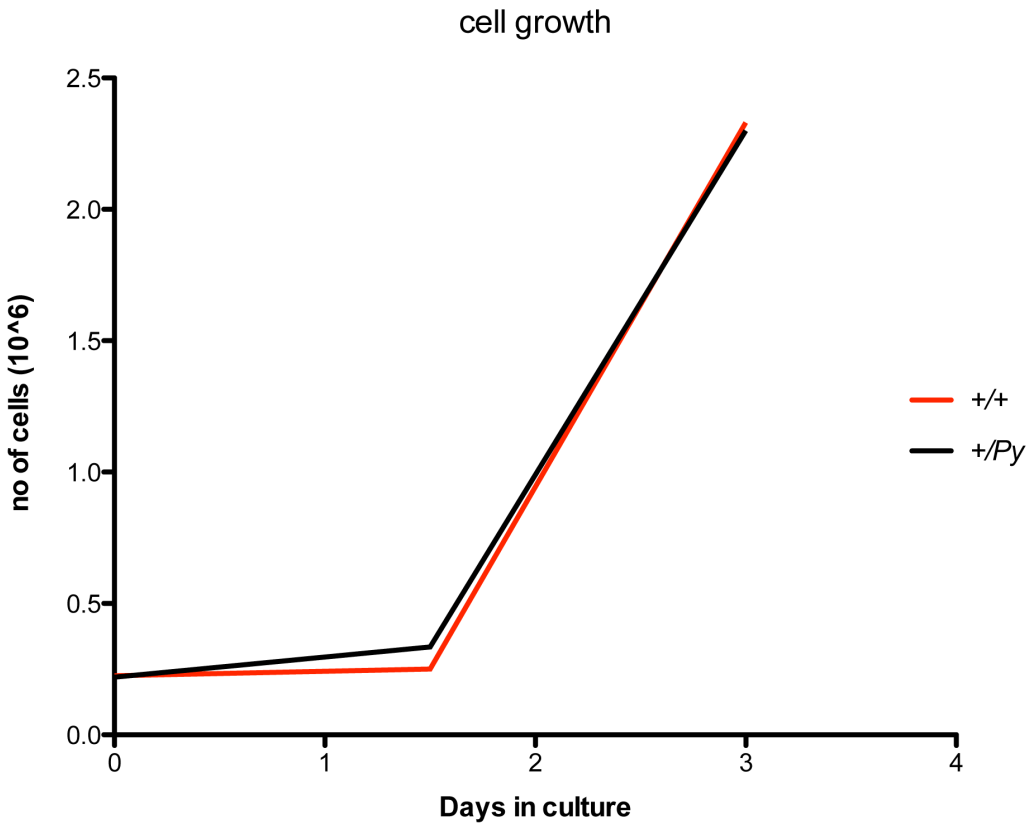

Appendix XVI. Publication

ASHRAFIAN, H., DOCHERTY, L., LEO, V., TOWLSON, C., NEILAN, M., STEEPLES, V., LYGATE, C. A., HOUGH, T., TOWNSEND, S., WILLIAMS, D., WELLS, S., NORRIS, D., GLYN-JONES, S., LAND, J., BARBARIC, I., LALANNE, Z., DENNY, P., SZUMSKA, D., BHATTACHARYA, S., GRIFFIN, J. L., HARGREAVES, I., FERNANDEZ-FUENTES, N., CHEESEMAN, M., WATKINS, H. & DEAR, T. N. A mutation in the mitochondrial fission gene Dnm1l leads to cardiomyopathy. *PLoS Genet,* 6, e1001000.

OPEN ACCESS Freely available online

PLoS GENETICS

A Mutation in the Mitochondrial Fission Gene *Dnm1l* Leads to Cardiomyopathy

Houman Ashrafian[1], Louise Docherty[2], Vincenzo Leo[3], Christopher Towlson[2], Monica Neilan[2], Violetta Steeples[1], Craig A. Lygate[1], Tertius Hough[3], Stuart Townsend[3], Debbie Williams[4], Sara Wells[4], Dominic Norris[4], Sarah Glyn-Jones[5], John Land[6], Ivana Barbaric[7], Zuzanne Lalanne[4], Paul Denny[4], Dorota Szumska[1], Shoumo Bhattacharya[1], Julian L. Griffin[5], Iain Hargreaves[6], Narcis Fernandez-Fuentes[3], Michael Cheeseman[4], Hugh Watkins[1], T. Neil Dear[2,3,4]*

1 Department of Cardiovascular Medicine and Wellcome Trust Centre for Human Genetics, University of Oxford, Oxford, United Kingdom, **2** Mammalian Genetics of Disease Unit, School of Medicine, University of Sheffield, Sheffield, United Kingdom, **3** Leeds Institute of Molecular Medicine, Wellcome Trust Brenner Building, St. James's University Hospital, Leeds, United Kingdom, **4** Mary Lyon Centre and Mammalian Genetics Unit, Medical Research Council, Harwell, United Kingdom, **5** Department of Biochemistry, University of Cambridge, Cambridge, United Kingdom, **6** Neurometabolic Unit, National Hospital, London, United Kingdom, **7** Department of Biomedical Science, University of Sheffield, Sheffield, United Kingdom

Abstract

Mutations in a number of genes have been linked to inherited dilated cardiomyopathy (DCM). However, such mutations account for only a small proportion of the clinical cases emphasising the need for alternative discovery approaches to uncovering novel pathogenic mutations in hitherto unidentified pathways. Accordingly, as part of a large-scale *N*-ethyl-*N*-nitrosourea mutagenesis screen, we identified a mouse mutant, Python, which develops DCM. We demonstrate that the Python phenotype is attributable to a dominant fully penetrant mutation in the dynamin-1-like (*Dnm1l*) gene, which has been shown to be critical for mitochondrial fission. The C452F mutation is in a highly conserved region of the M domain of Dnm1l that alters protein interactions in a yeast two-hybrid system, suggesting that the mutation might alter intramolecular interactions within the Dnm1l monomer. Heterozygous Python fibroblasts exhibit abnormal mitochondria and peroxisomes. Homozygosity for the mutation results in the death of embryos midway though gestation. Heterozygous Python hearts show reduced levels of mitochondria enzyme complexes and suffer from cardiac ATP depletion. The resulting energy deficiency may contribute to cardiomyopathy. This is the first demonstration that a defect in a gene involved in mitochondrial remodelling can result in cardiomyopathy, showing that the function of this gene is needed for the maintenance of normal cellular function in a relatively tissue-specific manner. This disease model attests to the importance of mitochondrial remodelling in the heart; similar defects might underlie human heart muscle disease.

Citation: Ashrafian H, Docherty L, Leo V, Towlson C, Neilan M, et al. (2010) A Mutation in the Mitochondrial Fission Gene *Dnm1l* Leads to Cardiomyopathy. PLoS Genet 6(6): e1001000. doi:10.1371/journal.pgen.1001000

Editor: Marshall S. Horwitz, University of Washington, United States of America

Received September 24, 2009; **Accepted** May 25, 2010; **Published** June 24, 2010

Funding: HW and TND acknowledge support from the British Heart Foundation (including project grant PG/06/070/21110 to TND), and HW and HA acknowledge support from the Wellcome Trust (including a Clinical Training Fellowship to HA). The funders had no role in study design, data collection and analysis, decision to publish or preparation of the manuscript.

Competing Interests: The authors have declared that no competing interests exist.

* E-mail: t.n.dear@leeds.ac.uk

Introduction

Idiopathic dilated cardiomyopathy (DCM) is characterised by unexplained left ventricular (LV) cavity enlargement with LV systolic impairment [1]. DCM is an important cause of congestive heart failure (CHF) with a prevalence of 36 cases per 100,000 in the United States [2]. Although the molecular pathways responsible for DCM remain largely unknown, it is estimated that between 20–50% of DCM cases are familial in nature, the large majority being inherited as an autosomal dominant trait [3]. Accordingly, the study of single gene disorders that remodel the heart to cause DCM may provide a valuable opportunity to identify critical molecules involved in disease pathways [4].

Over the past decade, DCM-causing mutations have been identified in genes encoding sarcomeric, cytoskeletal, nuclear envelope, intermediary filament, sarcoplasmic reticulum and desmosomal proteins. These findings have implicated pathogenic mechanisms whereby structural integrity, contractile force dynamics, and calcium regulation within the cardiomyocyte are perturbed. Yet such mutations only account for a minority of DCM cases [5] and many of the genes underlying DCM remain to be elucidated. A number of gene knockouts in the mouse produce features of DCM, but these phenotypes are usually recessive and so do not model the human disease. One approach that has been applied successfully to the characterisation of new disease alleles is the use of *N*-ethyl-*N*-nitrosourea (ENU) mutagenesis [6]. Treatment of mice with ENU results in a high frequency of predominantly single point mutations in the mouse germline that recapitulate the spectrum of mutations observed in many human genetic diseases. Screening of offspring reveals phenotypic variants, and the identification of the mutations underlying the abnormal phenotype can reveal new genetic regulators and novel pathways associated with disease pathogenesis. Such an approach is 'hypothesis neutral', making no prior assumptions about the

Author Summary

Heart disease is very common. Some cases of heart disease are strongly influenced by lifestyle and diet, whereas others have a strong genetic component. A certain form of heart failure, known as dilated cardiomyopathy (DCM) quite often runs in families suggesting that a defective gene or genes underlie this disease. We describe a new mouse mutant called "Python" which suffers from a heart disease similar to DCM. We were able to pinpoint the defective gene responsible for the disease. This gene is normally involved in the division of mitochondria, the "power plants" of the cell that generate one of the main energy supplies for the cell. This is a unique model that implicates a new gene and mechanism of disease for further investigation.

nature of the genes or pathways involved. Using this approach we describe a novel mouse model of DCM in which a mutation in the Dynamin-1-like gene (*Dnm1l*) leads to autosomal dominant DCM and congestive heart failure.

Results

Python mice develop biventricular DCM

The Python mouse was identified on the basis of rapid size increase, piloerection, and shallow rapid breathing in a visual screen of adult G_1 offspring of ENU-mutagenized BALB/cAnNCrl males crossed with C3H/HeH females (Figure 1A). The phenotype was inherited in an autosomal dominant fashion with complete penetrance in both sexes. The median age of onset of overt symptoms of CHF on a C3H/HeN genetic background was 91 days for females and 83 days for males. A similar phenotype with much later onset occurred on a C57BL/6J background (median age of onset = 164 days for females, 171 days for males; Figure 1B) suggesting that strain-specific genetic modifiers influence disease onset.

The hearts of Python mice were grossly dilated by the time of overt CHF (Figure 1C). The Python hearts exhibited both biatrial and biventricular thinning and dilatation consistent with DCM (Figure 1D). The visible increase in size of Python mice was the result of substantial ascites and subcutaneous oedema (Figure 1E) accompanied on occasion by pleural effusion. In the heart, myocyte hypertrophy and interstitial fibrosis (Figure 1F) was evident. Morphometric analysis of MSB-stained sections revealed that collagenous tissue increased by almost 7-fold in hearts of terminal Python mice (Figure 1G). Prominent cardiac calcification was also evident (Figure 1H). Python mice developed CHF under specified pathogen-free (SPF) conditions, where infectious agents capable of causing myocarditis were absent. There was no microscopic evidence of myocarditis, coronary artery disease or amyloidosis, nor was there hypertrophy of pulmonary blood vessels that would indicate pulmonary hypertension. MRI analysis of embryonic hearts did not reveal any obvious anatomical abnormalities (data not shown). TUNEL staining did not reveal accelerated apoptosis in late-stage Python hearts (data not shown). We did observe hepatic congestion at the time of overt CHF, preceded by increases in the plasma levels of liver enzymes aspartate aminotransferase and alanine aminotransferase (data not shown), possibly reflecting congestive cardiac hepatopathy secondary to heart failure.

Cardiac function was analysed in male Python mice on the C3H/HeN background aged 71–78 days, i.e. approximately 2 weeks before overt clinical signs of CHF become evident. The results are summarised in Table 1. Heart rates in these conscious mice did not significantly differ between Python mice and controls, and there were no differences in any measurement of ECG interval duration (data not shown). However, LV catheterisation revealed that pressure generation was severely impaired in Python mice, with LV end-systolic pressure 22 mmHg lower than in littermate controls, and contractility 40% lower, as measured by dP/dt_{max}. This reduction was not due to differences in loading conditions since dP/dt_{max} remained impaired after normalisation to instantaneous pressure. Furthermore, the Python mice had significantly elevated end-diastolic pressure commensurate with impaired contractile function. Under conditions of maximal b-adrenergic stimulation with dobutamine, Python mice had a reduced contractile reserve and a severely impaired maximum contractility. Consistent with these findings, aortic blood pressures were significantly reduced. Relaxation was also impaired in Python mice with dP/dt_{min} 46% lower than controls, and significant prolongation of the isovolumetric constant of relaxation (Tau), which is less sensitive to loading conditions. These changes occurred in the absence of LV hypertrophy or dilatation at this time point and were confirmed at post-mortem by no differences in LV or RV weights. Although at this stage lung weights were normal, indicating the absence of significant pulmonary congestion, later, at the time of appearance of overt CHF (approximately 2 weeks later) gross ascites and pulmonary congestion become rapidly manifest, consistent with the precipitous deterioration in LV function. No thrombi were observed in the atria, nor, indeed, in any heart chamber (data not shown). Finally, haematocrits were normal in all mice (data not shown), ruling out a low red blood cell count as a mechanism for LV dysfunction.

Positional cloning of the Python mutation

The Python mutation was generated on a BALB/cAnN genetic background, and the original mouse exhibiting the CHF phenotype was a BALB/cAnNCrl x C3H/HeH F_1 hybrid male. This individual was backcrossed to C3H/HeH and offspring exhibiting the CHF phenotype were examined with a panel of 53 polymorphic SNP markers spanning the entire genome at regular intervals. A strong linkage signal was observed on chromosome 16 at marker D8Mit213 (LOD score of 3.3 for a recombination fraction = 0.1). Subsequent fine mapping by backcrossing to C3H/HeH, C3H/HeN and, finally, to C57BL/6J mice narrowed the critical region containing the mutation to 787 Kb (Figure 2A). Three genes are located within this region - *Pkp2*, *Fdg4* and *Dnm1l*. Sequencing of all exons and exon-intron boundaries identified only a single mutation in Python mice; a G/C to T/A transversion in exon 11 of the *Dnm1l* gene (the official gene name as specified by the International Committee on Standardized Genetic Nomenclature for Mice but often referred to in the literature as *Drp1* or *Dlp1*) (Figure 2B). Based on the known ENU-induced mutation rate for this strain and ENU dose (1 mutation per 1.8 Mb) [7], the probability of there being an additional intronic or intergenic mutation anywhere in this region is extremely low ($P = 0.00001$) [8]. There was complete concordance between animals suffering from CHF and the Python mutation. We retrospectively regenotyped 145 DNA samples isolated from C3H and C57BL/6J Python mice that had suffered from CHF and all contained the mutation while it was absent in 189 samples from non-affected littermate control mice. None of the wild types strain examined (BALB/cAnNCrl, C3H/HeN, C3H/HeH, C57BL/6J, DBA/2J, CBA/J, 101/H, 129/S5) contained the mutation. Although *PKP2* dominant mutations have been associated with arrhythmogenic right ventricular cardiomyopathy in humans [9] an intronic or intergenic mutation is unlikely to account for the Python

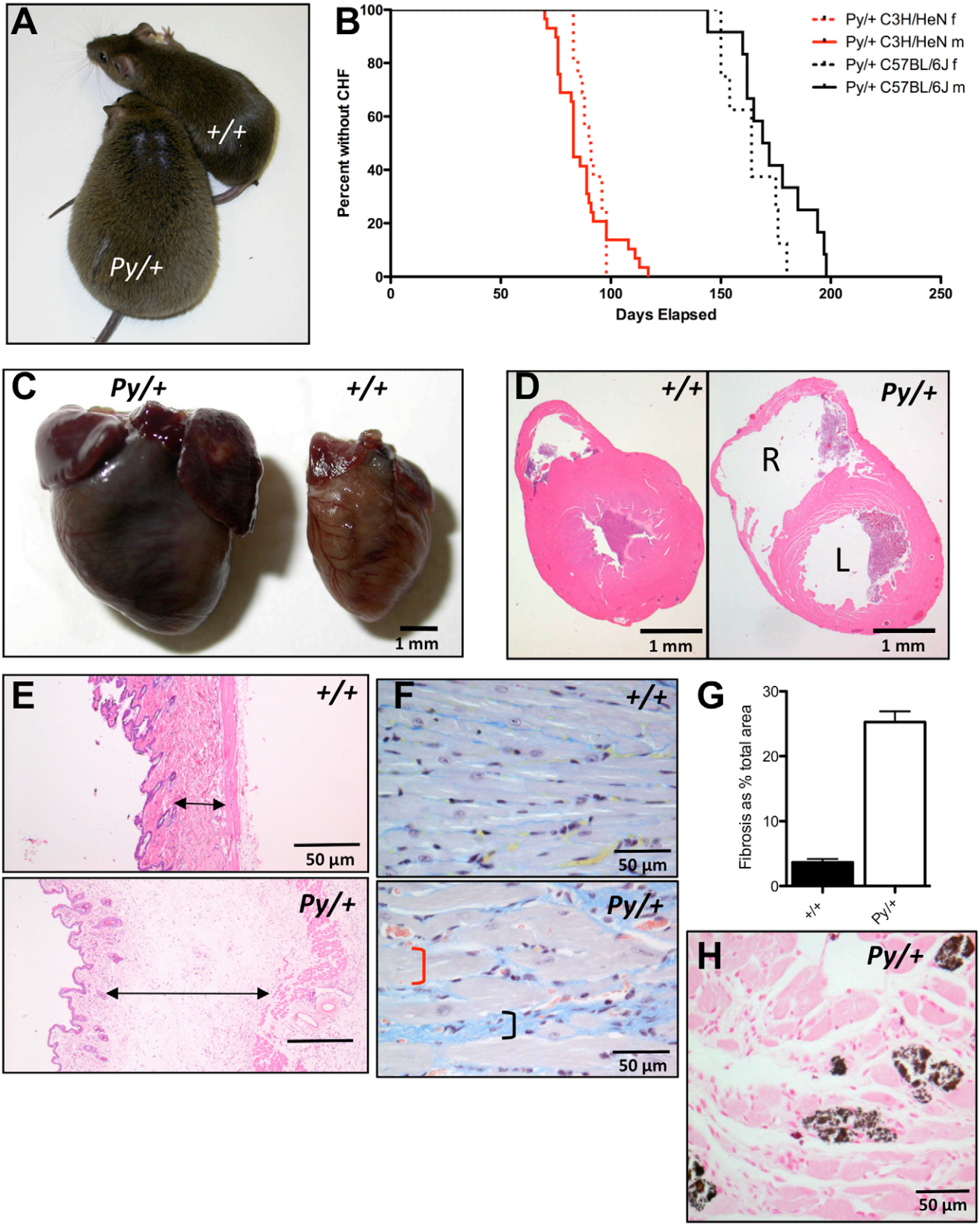

Figure 1. The Python mutation leads to dilated cardiomyopathy. (A) A 13-week-old Python mouse compared to a littermate control. (B) Kaplan-Meier analysis of onset of overt CHF in Python mice on the C3H/HeN and C57BL/6J genetic backgrounds compared to wild type littermate controls. (C) Photo of the excised hearts from a 13-week-old Python and wild type mouse. Note the grossly enlarged ventricles and atria. (D) H&E section through a wild type and Python heart showing showing clinical signs of CHF. Note the distended ventricles; R = right, L = left. (E) Oedematous

dermal connective tissue evident in a H&E-stained section from a Python mouse showing clinical signs of CHF compared to a littermate control. (F) MSB staining of heart sections of Python mice showing clinical signs of CHF. Note enlarged cardiomyocytes (indicated by red bracket) and increased collagen deposition (indicated by black bracket). (G) Morphometric analysis of MSB-stained section demonstrating the level of increase in collagen deposition. Data shown is % of image area (mean ± SEM) that is taken up by collagen deposition from 3 *Py/+* showing overt signs of CHF and 3 *+/+* age-matched males. Five images were taken per sample. (H) Evidence of cardiac calcification in a Von Kossa-stained section of a Python heart.
doi:10.1371/journal.pgen.1001000.g001

phenotype as all human *PKP2* mutations found to date occur in the coding region or splice sites which are not mutated in Python mice, the homozygous phenotype for the null *Pkp2* mutation is very different from the Python homozygote [10] and *Pkp2* mRNA level is not altered in Python hearts as judged by microarray analysis (data not shown) suggesting no disease-causing non-coding regulatory changes. These facts, coupled with the observation that ENU-induced mutations resulting in detectable phenotypes occur almost exclusively in the coding exons or exon-intron boundaries of genes [11], strongly suggested that this base change was the Python mutation.

The Python mutation results in the replacement of the cysteine by a phenylalanine at position 452 in the predicted Dnm1l protein (amino acid numbering according to EBI reference protein Accession No. Q8K1M6) (Figure 2C). This cysteine is located within the middle (M) domain of the protein and is fully conserved in all Dnm1l orthologues, and even the yeast dynamin homologue DNM1 (Figure 2D). The degree of evolutionary conservation of the Dnm1l protein is very high. For example, overall homology between human and mouse Dnm1l is 98%, and between zebrafish and mouse is 89%. The M domain conservation is even higher with 96% sequence conservation between mouse and zebrafish over the 291 amino acids of this domain. The cysteine residue is also conserved in the M domain of the mouse homologues of Dnm1, Dnm2 and Dnm3 (Figure 2E) despite overall homology with these domains being less than 40% (Table S1) suggesting that this cysteine plays an important role in M domain function.

The Python mutation impairs intramolecular interaction of Dnm1l

There is no available crystal structure of any mammalian dynamin proteins but a crystal structure has been described for a bacterial dynamin-like protein. In this structure the M domain forms an elongated alpha-helical domain where the tip of the M domain helices interact with a similar region of the 'mate' in the dynamin homodimer [12]. Accordingly, a model of mouse Dnm1l was constructed on the basis of comparative sequence homology to the bacterial dynamin-like protein BDLP for which there is a crystal structure [12] and an electron cryomicroscopy reconstruction of BDLP assembled around a lipid tube [13]. A predicted structure could be created for most of the protein, apart from one region where there is no homology in BDLP (indicated by an 'a' in Figure 3A). The predicted structure of the dimeric asymmetric repeating unit in the extended confirmation (i.e. after lipid binding) is shown in Figure 3A.

There are six mutations, all dominant or semi-dominant, that have been reported in the M of domain of DNM1L or its yeast homologue DNM1–three in yeast [14], and one each in a human

Table 1. Cardiovascular parameters in 11-week-old male mice.[1]

	Littermate controls (n = 6)	Python (n = 6)	*P* value
Organ weights			
Body weight (g)	34.0±2.8	32.5±2.1	0.31
LV weight (mg)	94±6	90±6	0.30
RV weight (mg)	28±4	27±3	0.72
Lung weight (mg)	138±5	141±16	0.65
Echocardiography			
End-diastolic area (cm^2)	0.123±0.015	0.132±0.009	0.22
End-systolic area (cm^2)	0.069±0.017	0.082±0.014	0.19
Ejection fraction (%)	44±8	38±9	0.24
Wall thickness (mm)	0.82±0.03	0.80±0.03	0.19
Heart rate (bpm)	460±52	461±59	0.98
Haemodynamics			
LV systolic pressure (mmHg)	97±8	75±3	0.00007
LV end-diastolic pressure (mmHg)	3.8±1.1	17.7±9.2	0.004
dP/dt_{max}(mmHg/s)	8531±1084	5140±1135	0.0004
dP/dt_{max}/instantaneous pressure (s^{-1})	149±8	107±23	0.002
dP/dt_{min}(mmHg/s)	−8449±1381	−4564±1308	0.001
Tau (ms)	8.5±1.5	16.6±6.8	0.017
Mean arterial pressure (mmHg)	75±9	60±6	0.006
Central venous pressure (mmHg)	1.8±2.0	1.6±0.8	0.83
Dobutamine dP/dt_{max}(mmHg/s)	13003±1832	6344±1424	0.00004

[1]Mice were on a C3H/HeN genetic background. All data is mean ± SD with comparisons made by Student's *t*-test.
doi:10.1371/journal.pgen.1001000.t001

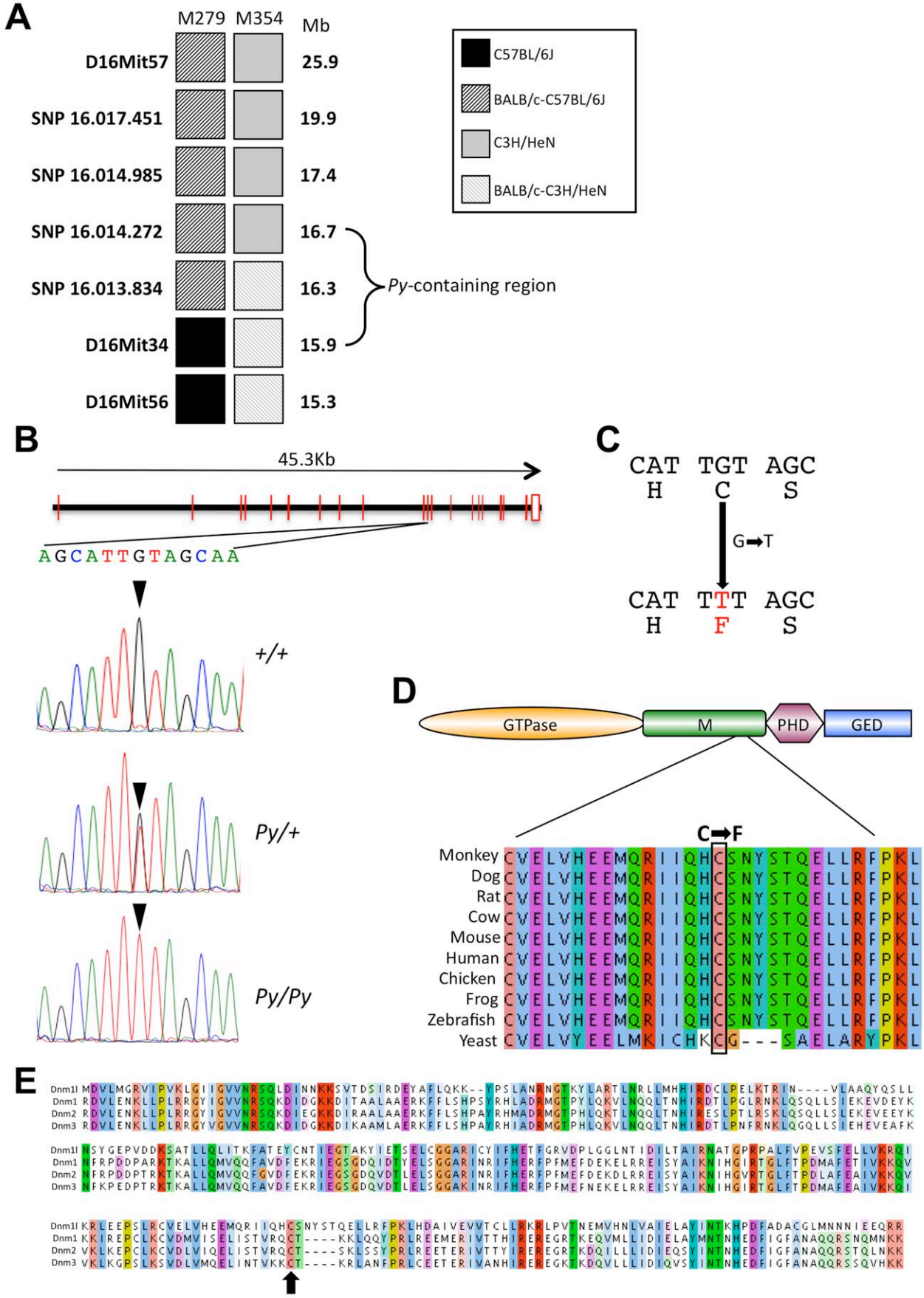
A
M279
M354
Mb
D16Mit57
25.9
SNP 16.017.451
19.9
SNP 16.014.985
17.4
SNP 16.014.272
16.7
SNP 16.013.834
16.3
D16Mit34
15.9
D16Mit56
15.3
Py-containing region
C57BL/6J
BALB/c-C57BL/6J
C3H/HeN
BALB/c-C3H/HeN
B
45.3Kb
AGCATTGTAGCAA
+/+
Py/+
Py/Py
C
CAT TGT AGC
H C S
G→T
CAT TTT AGC
H F S
D
GTPase
M
PHD
GED
C→F
Monkey CVELVHEEMQRIIQHCSNYSTQELLRFPKL
Dog CVELVHEEMQRIIQHCSNYSTQELLRFPKL
Rat CVELVHEEMQRIIQHCSNYSTQELLRFPKL
Cow CVELVHEEMQRIIQHCSNYSTQELLRFPKL
Mouse CVELVHEEMQRIIQHCSNYSTQELLRFPKL
Human CVELVHEEMQRIIQHCSNYSTQELLRFPKL
Chicken CVELVHEEMQRIIQHCSNYSTQELLRFPKL
Frog CVELVHEEMQRIIQHCSNYSTQELLRFPKL
Zebrafish CVELVHEEMQRIIQHCSNYSTQELLRFPKL
Yeast CVELVYEELMKICHKCG---SAELARYPKL
E
Dnm1l MDVLMGRVIPVKLGIIGVVNRSQLDINNKKSVTDSIRDEYAFLQKK--TPSLANRNGTKYLARTLNRLLMHHIRDCLPELKTRIN----VLAAQYQSLL
Dnm1 RDVLENKLLPLRRGYIGVVNRSQKDIDGKKDITAALAAERKFFLSHPSYRHLADRMGTPYLQKVLNQQLTNHIRDTLPGLRNKLQSQLLSIEKEVDEYK
Dnm2 RDVLENKLLPLRRGYIGVVNRSQKDIEGKKDIRAALAAERKFFLSHPAYRHMADRMGTPHLQKTLNQQLTNHIRESLPTLRSKLQSQLLSLEKEVEEYK
Dnm3 RDVLENKLLPLRRGYVGVVNRSQKDIDGKKDIKAAMLAERKFFLSHPAYRHIADRMGTPHLQKVLNQQLTNHIRDTLPNFRNKLQGQLLSIEHEVEAFK
Dnm1l NSYGEPVDDKSATLLQLITKFATEYCNTIEGTAKYIETSELCGGARICYIFHETFGRVDPLGGLNTIDILTAIRNATGPRPALFVPEVSFELLVKRQI
Dnm1 NFRPDDPARKTKALLQMVQQFAVDFEKRIEGSGDQIDTYELSGGARINRIFHERFPFMEFDEKELRREISYAIKNIHGIRTGLFTPDMAFETIVKKQV
Dnm2 NFRPDDPTRKTKALLQMVQQFGVDFEKRIEGSGDQVDTLELSGGARINRIFHERFPFMEFDEKDLRREISYAIKNIHGVRTGLFTPDLAFEAIVKKQV
Dnm3 NFKPEDPTRKTKALLQMVQQFAVDFEKRIEGSGDQVDTLELSGGAKINRIFHERFPFMEFNEKELRREISYAIKNIHGIRTGLFTPDMAFEAIVKKQI
Dnm1l KRLEEPSLRCVELVHEEMQRIIQHCSNYSTQELLRFPKLHDAIVEVVTCLLRKKLPVTNEMVHNLVAIELAYINTKHPDFADACGLMNNNIEEQRR
Dnm1 KKIREPCLKCVDMVISELISTVRQCT----KKLQQYPRLREEMERIVTTHIRERGRTKEQVMLLIDIELAYMNTNHEDFIGFANAQQRSNQMNKK
Dnm2 VKLKEPCLKCVDLVIQELISTVRQCT----SKLSSYPRLREETERIVTTYIRERGRTKDQILLLIDIEQSYINTNHEDFIGFANAQQRSTQLNKK
Dnm3 VKLKGPSLKSVDLVMQELINTVKKCT----KRLANFPRLCEETERIVANHIRERGKTKDQVLLLIDIQVSYINTNHEDFIGFANAQQRSSQVHKK

Figure 2. Genetic linkage analysis and positional cloning of the *Py* mutation. (A) Genotypes of two informative recombinants exhibiting the Python phenotype. The mutation was localized to a 787 Kb interval (indicated by the bracketed region). (B) Sequence of part of the 11th exon of the *Dnm1l* gene reveals a G–T substitution in the Python allele. The reading frame of part of exon 11 is shown with the amino acid substitution that results. (C) ClustalW2 alignment of part of domain M of vertebrate Dnm1l orthologues and the yeast Dnm1 homologue. Note that the cysteine residue is conserved in all species examined. Amino acid colours represent similarity groupings. (D) Alignment of the entire domain M of the mouse dynamins Dnm1l, Dnm1, Dnm2 and Dnm3. Identical or functionally very similar amino acids are shown grouped together by colour on the basis of size, charge and hydropathy. The arrow indicates the position of the cysteine altered by the Python mutation.
doi:10.1371/journal.pgen.1001000.g002

patient [15], a CHO cell line [16], and Python (Figure S1). These were mapped on to the predicted structure (Figure 3A). The Python mutation is located in an alpha-helix that is not predicted to affect interaction between Dnm1l monomers. However, it is located close to several other helical regions of the domain M. Furthermore, a helix-wheel projection of the region around the Python mutation-containing region predicts that one face of the predicted helix contains principally hydrophobic residues (Figure 3B). Taken together, these findings are suggestive of this face being involved in an intramolecular interaction within the Dnm1l monomer.

To test this further, we used the yeast two-hybrid assay based on GAL4 DNA binding and activation domain interactions to examine whether interactions between regions of Dnm1l could be altered by the Python mutation. We used regions of the protein that have been used by others in similar assays [17–22] and examined all possible reciprocal interactions of bait (in pDEST32) and prey (in pDEST22) proteins for regions of Dnm1l: full-length, N-terminal region, C-terminal region, M domain and GED (GTPase Effector Domain) (Figure 3C). On the basis of ability to grow on medium lacking histidine and b-galactosidase activity, the only strong interactions we identified were interactions between the full-length proteins, the N terminal and C-terminal regions of the proteins as reported by Zhu *et al.* [20], and the N-terminal region and the GED (Figure 3D). We found that while the Python mutation had negligible influence on the ability of the full-length proteins to interact (Figure 3D and 3E), it abrogated the ability of the N-terminal region to interact with both the C-terminal region and the GED alone (Figure 3D). Quantitative assays for b-galactosidase activity confirmed the substantial effect the Python mutation had on these interactions (Figure 3E).

The *Dnm1l*^{Py} mutation results in the impairment of mitochondrial and peroxisomal dynamics

Given that the Python mutation occurs in a highly conserved domain of the Dnm1l protein and alters protein interaction *in vitro*, its effect on *in vivo* functions associated with Dnm1l were examined. Protein levels of Dnm1l were not altered in either heart or brain (Figure 4A) suggesting that there is no haploinsufficiency (i.e. the Python protein is assumed to be present). Dnm1l was distributed diffusely within the cell in both Python and wild type cultured skin fibroblasts (Figure 4B) suggesting that introduction of the Python protein did not drastically alter trafficking of Dnm1l. As Dnm1l function is involved in mitochondrial and peroxisomal dynamics, cultured neonatal skin fibroblasts were examined for morphology of both these organelles. Mitochondrial morphology was altered. Python mitochondria were highly elongated compared to wild type controls (Figure 4C), as were peroxisomes (Figure 4D). To determine if mitochondrial volume was altered, we utilized a novel assay where cells were loaded with a fluorescent mitochondrial marker and analyzed by flow cytometry. Intensity of fluorescence should reflect mitochondrial volume in the cell. As shown in Figure 4E, there was no difference in overall mitochondrial volume between Python and wild type fibroblasts, despite the significant changes in mitochondrial shape. This indicates that the Python mutation affects the *in vivo* functional activity of Dnm1l, thereby impairing mitochondrial fission.

Homozygosity for the Python mutation is embryonic lethal; heterozygosity for Python modifies mitochondrial structure

To discern the functional effects of the Python mutation, we intercrossed heterozygotes to obtain homozygous animals. Genotyping of embryos demonstrated that no homozygous Python embryos could be recovered from E12.5 onwards (Figure 5A). Homozygous embryos appear to be normal up to approximately E9.5. At E11.5, *Py/Py* embryos were severely retarded in growth and exhibited a posterior truncation (Figure 5B). The homozygous embryonic phenotype is very similar to that recently reported for the *Dnm1l*-null mutation [23–24]. Embryos die at a similar stage and their morphology is similar. Mouse Embryonic Fibroblasts (MEFs) cultured from homozygous E9.5 embryos survived poorly in culture. Few cells attached and there was no proliferation (Figure 5C). Mitochondria of *Py*/+ MEFs were abnormal with numerous long tubular mitochondria (Figure 5C), similar to *Py*/+ skin fibroblasts. In contrast, homozygous Python MEFs had grossly abnormal mitochondria. Whereas a tubular mitochondrial network evenly distributed throughout the cytoplasm characterized mitochondria in +/+ and *Py*/+ MEFs, some mitochondria of *Py/Py* MEFs appeared to be spherical and aggregated (Figure 5C). This could reflect Dnm1l dysfunction alone though it may reflect a general dysfunction of these cells. As mentioned earlier, these cells fail to proliferate. Over several weeks in culture they slowly die. The nuclei staining with Hoechst 33342 demonstrated evidence of chromatin condensation in homozygous Python cells (Figure 5C), suggesting the cells could be dying by necrosis.

The *Dnm1l*^{Py} mutation results in the impairment of energy metabolism in the heart

The observation that Python fibroblasts exhibit abnormal mitochondria coupled with the well-recognized role of *DNM1L* in mitochondrial fission [25] and the critical role of mitochondria in both the normal function and the death of cardiomyocytes [26], led us to examine the mitochondrial and energetic phenotype of Python heterozygous mice in greater detail. Aside from the development of CHF, the Python mice did not exhibit any features prominently recognized in mitochondrial cytopathies, such as metabolic, neurological and skeletal muscle defects. They exhibited a normal general behavioral and functional profile as defined by the SHIRPA series of tests (Table S2) [27], which would reveal any major neurological abnormalities. Grip strength (a reflection of muscle strength) was normal, as was muscle histology as assessed from H&E-stained sections (data not shown). Plasma lactate levels, an indicator of general metabolic dysfunction, were not elevated in Python mice aged 5–9 weeks compared to wild type littermate controls (Figure 6A).

Given that the Python phenotype at a gross pathological level appeared to be restricted to the heart, we examined the mitochondrial phenotype of Python cardiomyocytes. There was

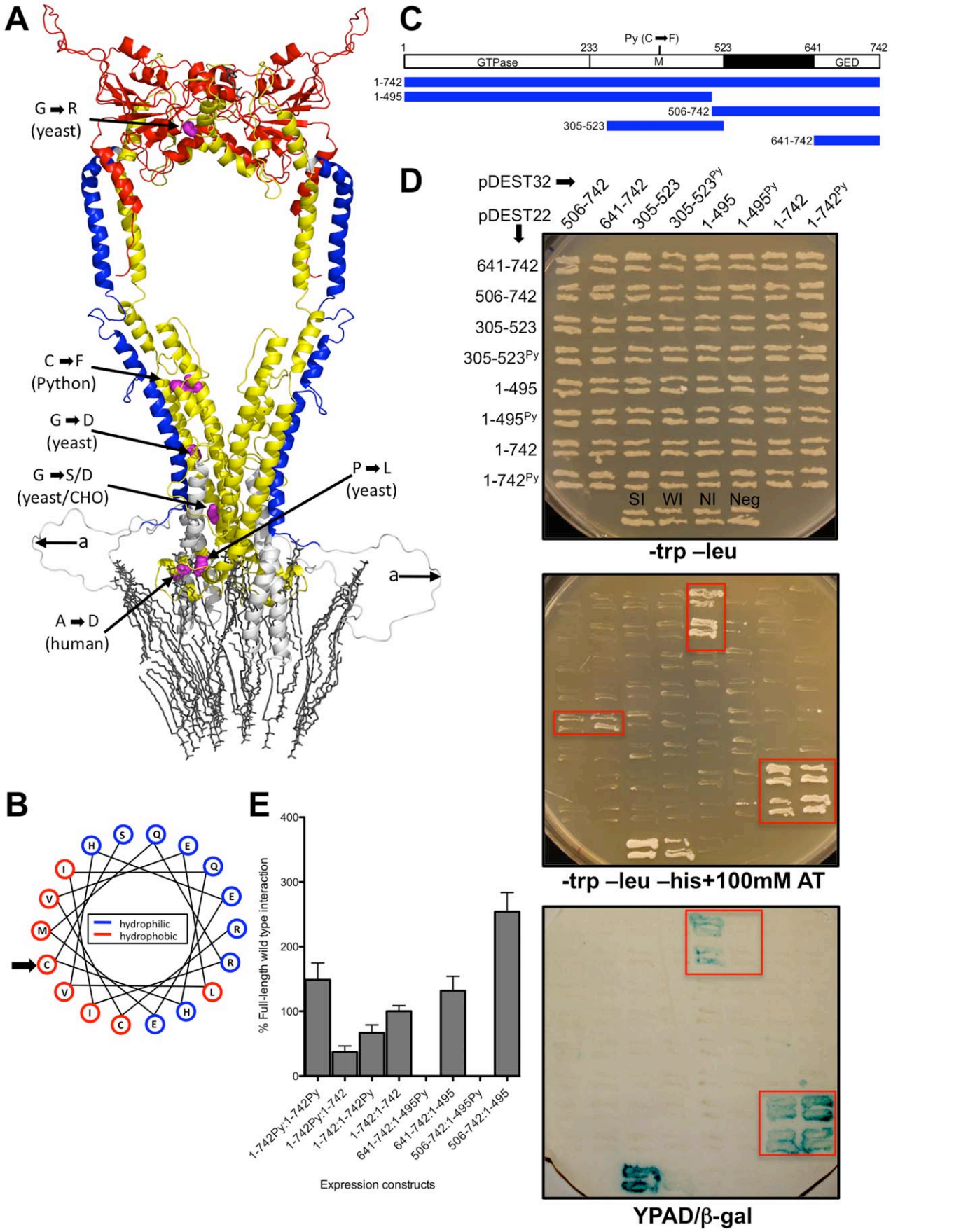
A
G ➡ R
(yeast)
C ➡ F
(Python)
G ➡ D
(yeast)
G ➡ S/D
(yeast/CHO)
P ➡ L
(yeast)
a
a
A ➡ D
(human)
B
hydrophilic
hydrophobic
C
Py (C ➡ F)
1
233
523
641
742
GTPase
M
GED
1-742
1-495
506-742
305-523
641-742
D
pDEST32 ➡
pDEST22
506-742
641-742
305-523
305-523Py
1-495
1-495Py
1-742
1-742Py
641-742
506-742
305-523
305-523Py
1-495
1-495Py
1-742
1-742Py
SI
WI
NI
Neg
-trp –leu
-trp –leu –his+100mM AT
YPAD/β-gal
E
% Full-length wild type interaction
400
300
200
100
0
1-742Py:1-742Py
1-742Py:1-742
1-742:1-742Py
1-742:1-742
641-742:1-495Py
641-742:1-495
506-742:1-495Py
506-742:1-495
Expression constructs

Figure 3. Effect of the Python mutation on the Dnm1l protein. (A) Ribbon representation of the homology model of the dimeric form of Dnm1l protein in the extended conformation and embedded in a lipid membrane. The dimeric conformation model and coordinates of the lipid membrane were generated by the superposition of the structural model of human Dnm1l onto the structure of bacterial dynamin-like protein Bdlp2 [13]. The positions of amino acid mutations reported in yeast Dnm1 and mammalian Dnm1l are shown as sphere representations in pink. A region that could not be modelled because of lack of a homologous region in BDLP is labelled with 'a'. Colours indicate protein domains: GTPase (red), M domain (yellow) and GED (blue). (B) A helix wheel projection of the mutation-containing region of the Dnm1l protein. The hydropathy indices of the amino acids have been divided into relatively hydrophilic (blue) and relatively hydrophobic (red). An arrow indicates the cysteine that is substituted in the *Py* allele. Note how this face of the alpha-helix is relatively hydrophobic. (C) The locations within Dnm1l of the protein sequences used in the yeast two-hybrid analysis. (D) Yeast two hybrid analysis of all combinations of protein sequences as either bait (GAL4 DNA binding domain in pDEST32) and prey (GAL4 activation domain in pDEST22). Duplicate yeast colonies from each transfection grown on a –trp-leu plate (top), –trp-leu-his +100 mM AT (middle, colonies exhibiting growth are boxed in red) and a filter lift from the –trp-leu plate assayed for b-galactosidase activity (bottom). (E) Level of b-galactosidase in liquid cultures from interactors detected in (D) along with comparison to those with introduced Python mutation. Levels shown are relative to average of full-length wild type interaction. Each assay is the mean ± SEM of 6 independent measurements from 6 individual colonies for each combination.
doi:10.1371/journal.pgen.1001000.g003

little evidence of morphological change in Python cardiomyocyte mitochondria. For example, we examined the nuclear:mitochondrial DNA ratio in Python hearts as mtDNA is lost when *DNM1L* is down-regulated and mitochondrial fission impaired [28], However, there was no alteration in the nuclear:mitochondrial DNA ratio in Python hearts at any stage before the development of overt CHF and even at this stage only some Python hearts showed an increased ratio (Figure 6B). This suggests that a major derangement of nuclear:mitochondrial DNA ratios was not a generalized effect of the Python mutation.

There was evidence of mitochondrial function changes in hearts of Python mice suffering from overt CHF. Examination by enzyme immunohistochemistry for succinate dehydrogenase (SDH) and cytochrome c oxidase (Complex IV) activities revealed a reduction for both enzymes in Python hearts (Figure 6C). In the case of SDH there is evidence of diminished myocellular enzyme activity as indicated by less-intense staining. However for Complex IV, the enzyme immunohistochemistry suggests that in the failing heart, the change in Complex IV enzyme levels may be due to the substantial fibrosis that occurs late in the disease process rather than a change in enzyme activity. *In vitro* measurement of Complex IV activity and quantity showed that both were proportionately reduced by similar amounts in ailing Python hearts (Figure 6D), indicating that the enzyme remains fully active but is less abundant at 12 weeks of age. This reduction in overall levels at this age most likely reflects the considerable fibrosis and loss of cells that occurs in late-stage Python hearts.

Defects in mitochondrial enzyme activity are recognized as a general phenomenon in CHF [29] and, therefore, the differences observed in failing Python hearts might be secondary to the primary cause of heart failure. To determine if the Python mutation was affecting mitochondrial function prior to major changes in heart structure, we examined heart samples from Python and wild type littermates at 10 weeks of age. This is before there are any overt signs of CHF though the cardiovascular data above (Table 1) indicates that heart function is abnormal at this stage. Electron micrographs of heart samples were examined. Morphometric analysis of the proportional area occupied by mitochondria (a reflection of overall volume per cell) revealed no difference between Python hearts and controls (Figure 6E). This in agreement with the flow cytometry findings in Python skin fibroblasts (Figure 4E). Nor were myofibre widths significantly different between Python hearts and controls (data not shown). There was no evidence of the membrane pinching reported in the *Dnm1l*-null mouse fibroblasts [Ishihara2009], nor was there evidence of large aggregates as has been reported for *in vitro* cultured *DNM1L* mutants [30]. However, the average size of a mitochondrion was slightly smaller in Python hearts than wild type hearts (Figure 6E). Smaller cardiomyocyte mitochondria have been previously reported in some cases of heart failure [31–33]. In the case of Python, if mitochondrial volume is not altered but mitochondrial tubules are extended in length, then a smaller cross-sectional transverse area of mitochondria would be consistent with this.

If Dnm1l affects mitochondrial dynamics, we predicted that the end point of this would be impairment of respiratory chain function. Examination of mitochondrial enzyme complex activities normalized to citrate synthase activity in heart samples from 10-week-old mice revealed no differences (Figure 6F and 6G). There was a slight reduction in the overall level of mitochondrial citrate synthase activity in Python hearts at this age but it was not statistically significant (Student's t test, $P = 0.11$) (Figure 6G) also suggesting that the total mitochondrial volume in Python hearts was not reduced. As the end-point of respiratory chain function is ATP synthesis, and given that down-regulation of *DNM1L* results in a reduced rate of ATP synthesis [28,34], myocardial ATP and total adenine nucleotide (TAN) levels were measured using HPLC. Python hearts exhibited a dramatic, approximately 50%, reduction in ATP and TAN levels (Figure 6H and 6I) compared to hearts from littermate controls. In liver and brain at the same age, ATP and TAN levels were similar in Python mice and controls (Figure 6H and 6I), indicating that the defect in ATP generation was not a general one. These results were confirmed by using complementary quantitative bioluminescence assays (Figure S2).

A range of metabolites in the heart was examined using high-resolution ^{1}H NMR spectroscopy and Gas Chromatography Mass Spectrometry (GC-MS)-based metabolomic approaches [35] on Python and control mice. The metabolite changes identified are summarized in Table 2. Significant reductions in Python hearts were noted in mitochondrial metabolic intermediates or accessory molecules e.g. succinate, malate, fumarate, pyruvate (all associated with the citric acid cycle), creatine, glucose, AMP and adenosine. Two notable increases were in the amino acids glycine and proline. These account for approximately 50% of the amino acids in collagen, possibly reflecting the fibrosis in Python hearts.

Discussion

We report the identification, through ENU mutagenesis, of a novel genetic cause of cardiomyopathy. Our principal finding is that a missense mutation in the middle domain of *Dnm1l*, whose product is critically involved in mitochondrial fission, results in DCM. The resulting defect in mitochondrial remodelling renders the Python hearts progressively energy deficient potentially contributing to the phenotype [36].

The fundamental importance of mitochondrial remodelling in mammalian pathophysiology has been underlined by *in utero* lethality and cerebellar degeneration in mice with homozygous

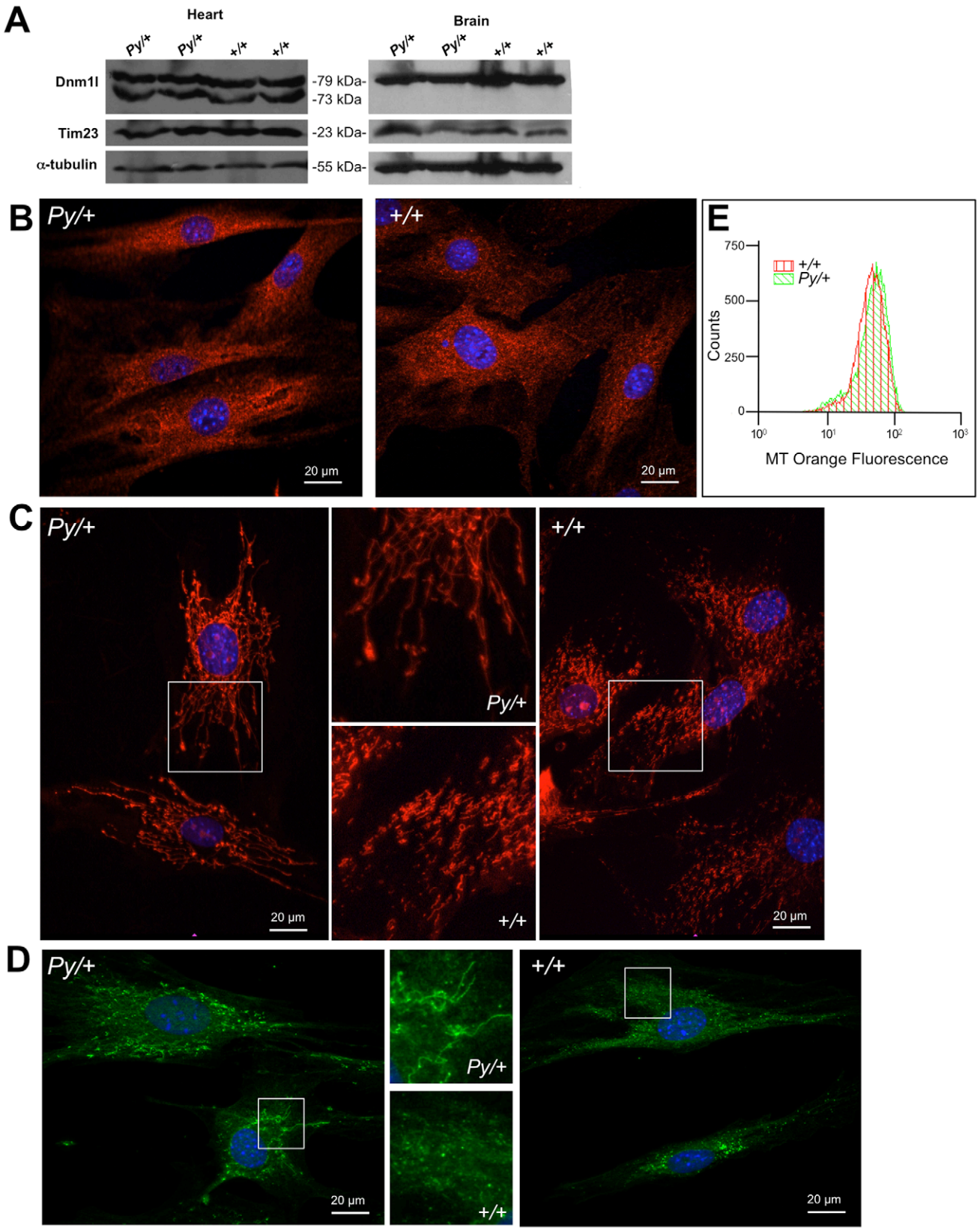

Figure 4. Mitochondrial and peroxisomal morphology is altered by the Python mutation. (A) Western blot analysis of total heart and liver protein extracts from 5-week-old male mice of the indicated genotypes demonstrating that Dnm1l protein levels are not altered. Western blots were re-examined using an anti-Tim23 antibody, an inner mitochondrial membrane protein, which demonstrate that the level of this mitochondrial protein is also not altered in Python mutants. After stripping, a-tubulin was detected to demonstrate loading levels of protein extracts. (B) Typical example of immunocytochemistry in neonatal mouse skin fibroblasts using an anti-DRP1 antibody. There was no appreciable difference between Python

fibroblasts and wild type littermate controls. (C) Typical example of mitochondria (shown in red after staining with Mitotracker Orange) from cultured Python neonatal skin fibroblasts compared to littermate controls. (D) Typical example of peroxisomes (shown in green after incubation with an anti-catalase antibody and FITC-labelled secondary antibody) from cultured Python neonatal skin fibroblasts compared to littermate controls. The areas in C and D bounded by white squares are magnified and shown in the middle frames. Nuclei are stained with Hoechst 33258. (E) Typical example of FACS analysis of early passage skin fibroblasts from a Python neonate and littermate control after labelling with Mitotracker Orange. The histogram of fluorescence for both cells types is similar.
doi:10.1371/journal.pgen.1001000.g004

mutations in *Dnm1l* itself, as well as *Mfn1*, *Mfn2*, or *Opa1* [23,37,38]. Given the heart's manifest dependency on mitochondria [39] as evidenced by its frequent involvement in mitochondrial disorders [40], mitochondrial remodelling defects might be expected to occur in some forms of myocardial disease. Recently it has been reported that mitochondria are smaller in failing hearts and DNM1L protein levels were increased in DCM heart samples [33] but until now, there has been no direct evidence that genes involved in regulating mitochondrial dynamics might be involved in heart failure. Python is the first such example.

DNM1L is a member of the dynamin superfamily. In the higher order spirals formed by dynamin, the basic repeating unit appears to be a dimer [41]. The association between the GED and M domains forms a 'stalk' conformation through which strong intermolecular interactions of the dimers occur [41]. Mutations in the M domain have accordingly been shown to adversely affect self-assembly into a higher order oligomeric structures that are critical to Dnm1l function [22] and conformational changes within this region are associated with the constriction of dynamin tubes that facilitates fission [42]. It is not difficult to envisage how the substitution of a bulky hydrophobic phenylalanine residue into a helix-rich region of the M domain (Figure 3A) has the potential to modify interactions necessary for Dnm1l's effective function. As a corollary, our yeast two hybrid analysis showed Python's capacity to abrogate Dnm1l's N-terminal region interacting with the C-terminal region (and GED), while leaving the interaction between Dnm1l monomers unaffected. A similar effect was reported when the S637D mutation was introduced into Dnm1l [43]. This effect of the mutation on Dnm1l higher order structure is consistent with a dominant-negative mode of action. Since there appears to be no change in overall Dnm1l protein levels, we propose that the Python monomer is readily incorporated into dimers with the wild type protein but fails to function effectively within that dimer due to defective intramolecular interactions. If this model is accurate, only 1 in 4 Dnm1l dimers might be expected to be fully functional.

This study cannot exclude a systemic (i.e. non-cardiac) impact of the C452F mutation, though from a clinical perspective, most tissues and organ functions appeared to be grossly spared. The liver was the one organ that did show evidence of extra-cardiac involvement but this might reflect congestive cardiac hepatopathy caused by heart disease. The predominant cardiac phenotype in the Python heterozygotes contrasts with the marked skeletal muscle and metabolic abnormalities in the infant with a dominant mutation in *DNM1L* [15]. It is unclear why the Python mutation manifests an overt phenotype only in heart. The reported human mutation in domain M, a dominantly acting alanine to aspartic acid mutation, appears to be much more severe than the Python mutation appeared to have a widespread metabolic defect. This may be related to the location of the amino acid within the structure and/or the chemical nature of the amino acid substitutions involved. An inter-species difference in DNM1l functionality is possible but unlikely given the extremely high degree of inter-species conservation. All 7 mutations identified in the M domain that affect mitochondrial dynamics are conserved not only in the M domain of DNM1L orthologues across multiple species (Figure S1), but are also conserved across the M domain of DNM1, DNM2, DNM3 and DNM1L (Figure 2E). The human alanine to aspartate mutation occurs in a region of the protein that might interact with the membrane (Figure 3A). When overall compatibility of the amino acid replacements are compared the Python amino acid replacement scores significantly higher in compatibility with its original amino acid in terms of hydrophobicity, size and charge compatibility (15.8, 9.4, 18.17 for the Python mutation compared to 12.8, 8.6 and 12.82 for the A400D human DNM1L mutation) [44]. Given that there is no evidence that this cysteine is involved in disulphide bonding in DNM1L, and its effect in the yeast two-hybrid system on intramolecular but not intermolecular Dnm1l interactions, its effect on Dnm1l function may be relative mild, still enabling the formation of dimers but with reduced functionality.

Although the gross impact of the heterozygous C452F Dnm1l mutation on cardiac morphology was relatively subtle at ~70 days, the corresponding functional and, even more so, the biochemical phenotypes were apparent. This was reflected in uniform lethality shortly thereafter. The degree of ATP deficiency in the Python hearts at this age is, to the best of our knowledge, unprecedented. The apparent fall of ATP levels to 44% of wild type levels in hearts from 10-week-old mice (15.1 vs. 6.6 nmol ATP/mg/protein in +/+ and *Py*/+ hearts at 10 weeks of age confirmed by two independent means) may have been exaggerated by increased fibrosis, yet still seems beyond the range by which it is thought that cardiac [ATP] is allowed to diminish (~25% to 30%) even in CHF [39]. We used an exacting method involving HPLC to measure these levels to ensure they were as accurate as possible. However a major caveat to these observations, is that the degree of difference in ATP levels observed herein will inevitably be exaggerated by the technical limitations associated with measuring ATP levels in tissue samples after excision from the body. The resulting rapid depletion of ATP pools may have precluded accurate measurements. However, a difference in ATP levels between Python and control hearts (that is not found in liver and brains) may indicate that the Python mutation does espouse an aberrant and progressive impact on myocardial energetics.

One possible explanation for the Dnm1l-mediated cardiomyopathy is cardiac energy deficiency. It is recognized that CHF is associated with, and in many cases exacerbated by, cardiac energy deficiency [36,39,45,46]. Indeed, the commonality of CHF to numerous primary mitochondrial diseases represents an excellent source of evidence that primary energy deficiency can and does cause CHF [36,47]. As reduction of Dnm1l function is known to impair cellular energetics [28,34] and as this pattern of cellular energetic impairment is profoundly and progressively manifested in Python hearts even in advance of gross cardiac dysfunction, cardiac energy deficiency may contribute to the phenotype of Python hearts and may be the proximate cause.

Detailed questions remain regarding the impact of the C452F substitution. Further biochemical and cellular studies are needed to investigate the hypothesis that such M domain mutations alter the intra/inter-molecular interactions and alter the homo-oligomerisation properties of Dnm1l [48]. Such studies will have to explain why in the context of the subtle reticular mitochondrial changes in Python, there is a discrepancy between the lack of an

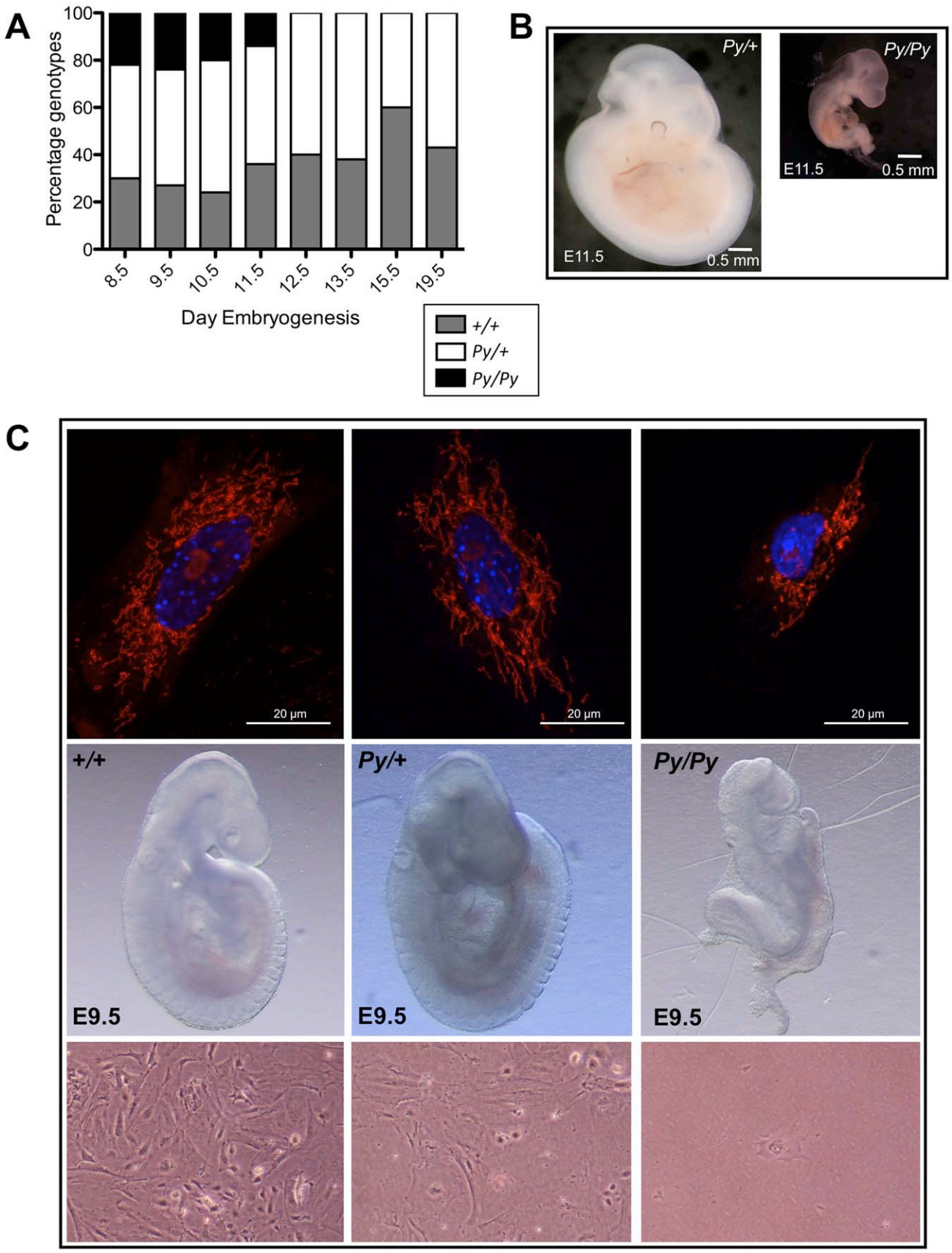

Figure 5. Homozygosity for the *Py* allele results in embryonic lethality. (A) Distribution of genotypes of embryos recovered from *Py*/+ x *Py*/+ intercrosses. Embryo numbers genotyped at each time point were: E8.5–26, E9.5–48, E10.5–20, E11.5–19, E12.5 20, E13.5–21, E15.5–10 and E19.5–14.

(B) Comparison of day 11.5 embryos heterozygous and homozygous for the *Py* allele. Homozygous embryos are growth retarded and have a severe posterior truncation. (C) Comparison of day 9.5 +/+, *Py*/+ and *Py*/*Py* embryos. Typical examples of individual fibroblasts obtained from culturing these embryos and stained with MitoTracker Orange are shown above. Below, typical examples of E9.5 embryonic fibroblasts in culture three days after embryo harvest. Note that the *Py*/*Py* cells have failed to proliferate and only a single cell is visible in this field.
doi:10.1371/journal.pgen.1001000.g005

overall decrease in mitochondrial volume or function and the degree of ATP depletion. There are a number of other metabolic and cellular processes that could be altered by the Python mutation. Calcium cycling, for example, is altered in cells lacking the mitochondrial fission protein Mitofusin 2, reflecting its role in endoplasmic reticulum (ER)-mitochondria tethering [49]. Inhibition of *Dnm1l* alters ER structure [50], though we could find no alteration in the morphological appearance of the ER in Python fibroblasts (data not shown). Nevertheless, further investigation of Ca^{2+} uptake into mitochondria and release from ER is warranted. An energy defect not reflected in altered respiratory complex enzyme activity might also result from other disturbances such as uncoupling of electron transport and ATP production, perturbation of supercomplexes [51], cell cycling [52] organelle quality control through autophagy, or generation of reactive oxygen species [28]. It is possible that Python has effects on Dnm1l function, unrelated to mitochondrial dynamics.

The tissue specificity of the Python defect warrants further investigation. This may reflect unique properties of cardiomyocytes, their mitochondria, or a unique role for *Dnm1l* in cardiomyocytes. For example, a role for DNM1L in the heart has been inferred by Ong *et al.* who observed that mitochondrial fission protects the heart against ischemia/reperfusion [53]. One strategy to address this question would be to effect conditional inactivation of *Dnm1l* in cardiomyocytes, in a similar manner to mitochondrial fusion factor elimination in skeletal muscle [54]. In conclusion, we report the first model of mitochondrial remodeling to be associated with cardiomyopathy. It is likely that the C452F substitution in the M domain of Dnm1l alters the balance of mitochondrial fission and fusion. The impairments in mitochondrial remodeling and function result in a relatively tissue specific disease as manifested by rapidly progressive cardiomyopathy. It is plausible that mutations in *Dnm1l* that are similarly subtle and hence do not represent a barrier to viability, will be identified and prove to be of importance in human disease.

Materials And Methods

Mice

Mice were maintained in high health status facilities with access to food and water *ad libidum*. All work was approved by the Animal Ethical Review Committees of MRC Harwell, University of Sheffield and University of Leeds, and the UK Home Office, and conducted with the highest quality of animal care and in accordance with the 3Rs.

ENU mutagenesis

Adult BALB/cAnNCrl mice aged 10 weeks were mutagenized by intraperitoneal injection of two weekly doses of 100 mg/kg ENU, mated with C3H/HeH and F_1 offspring screened for abnormalities. Python mice were further backcrossed to C3H/HeN and C57BL/6J. All tissue samples used for metabolic and cellular analysis were derived from a line generated by inbreeding of an N_{11} backcross to C3H/HeN.

Genetic mapping

Genome-wide low-resolution mapping was performed using DNA samples from 15 N_2 C3H/HeH backcross animals that were identified as carriers based on the development of congestive heart failure. Genomic DNA samples isolated from tail biopsies of these animals were screened by PCR amplification and gel electrophoresis with 53 microsatellite markers spaced at regular intervals across the genome. Samples were genotyped as either homozygous C3H or heterozygous BALB/c-C3H for each marker. For finer mapping, crosses of Python mice with both C3H and C57BL/6J were used, and further microsatellite markers polymorphic between either BALB/c and C3H or BALB/c and C57BL/6J were used to identify Python mice that were recombinant in the critical region. Single nucleotide polymorphisms (SNPs) were genotyped by sequencing of PCR products amplified with primers flanking the SNP site. Sequencing of candidate genes involved designing primer pairs to amplify individual exons as well as flanking splice donor/acceptor sequences. All exons and splice sites in the critical region were sequenced using homozygous as well as heterozygous Python DNA, ensuring that no base changes were missed.

Measurement of blood lactate

A small drop of blood was obtained from the lateral tail vein and processed using a Lactate Pro analyzer (HabDirect, Southam, UK).

Histology and TEM

Tissues for light microscopy were emersion fixed in 10% neutral buffered formalin and wax-embedded 3 μm sections were stained with haematoxylin and eosin or Mauritius Scarlet Blue (MSB). Mice were perfusion fixed for TEM. *In situ* staining for succinate dehydrogenase and Complex IV activities were a previously described [47,55,56].

In vivo cardiac phenotyping

Conscious ECG measurements were obtained in unrestrained male Python mice and littermate controls (n = 6 of each) at 10 weeks of age using the non-invasive AnonyMOUSE ECG screening tool (Mouse Specifics Inc). One week after, at 75±2 days of age, the same mice were anaesthetised with isoflurane and placed on a homeothermic blanket. Parasternal short- and long-axis views were obtained under 1.25% isoflurane anaesthesia using an Agilent Sonos 5500 with 15 MHz transducer. The LV was cannulated via the right carotid artery with a 1.4F Mikro-tip conductance cannula (SPR-839, Millar Instruments). The superior vena cava was cannulated with a second 1.4F Millar cannula (SPR-671) to measure central venous pressure. Mice were allowed at least 15 minutes equilibration before baseline aortic and ventricular pressure measurements were obtained. Dobutamine was given by intraperitoneal injection (1.5 μg/g body weight) and pressure measurements obtained under maximal b-adrenergic stimulation. Mice were then killed by cervical dislocation and organs washed in heparinised saline, blotted and weighed. Two experiments were performed daily, alternating between genotypes for morning and afternoon experiments.

Enzymatic assays

All activities were determined at 30°C. Prior to analysis cells were subjected to three cycles of freezing and thawing to lyse

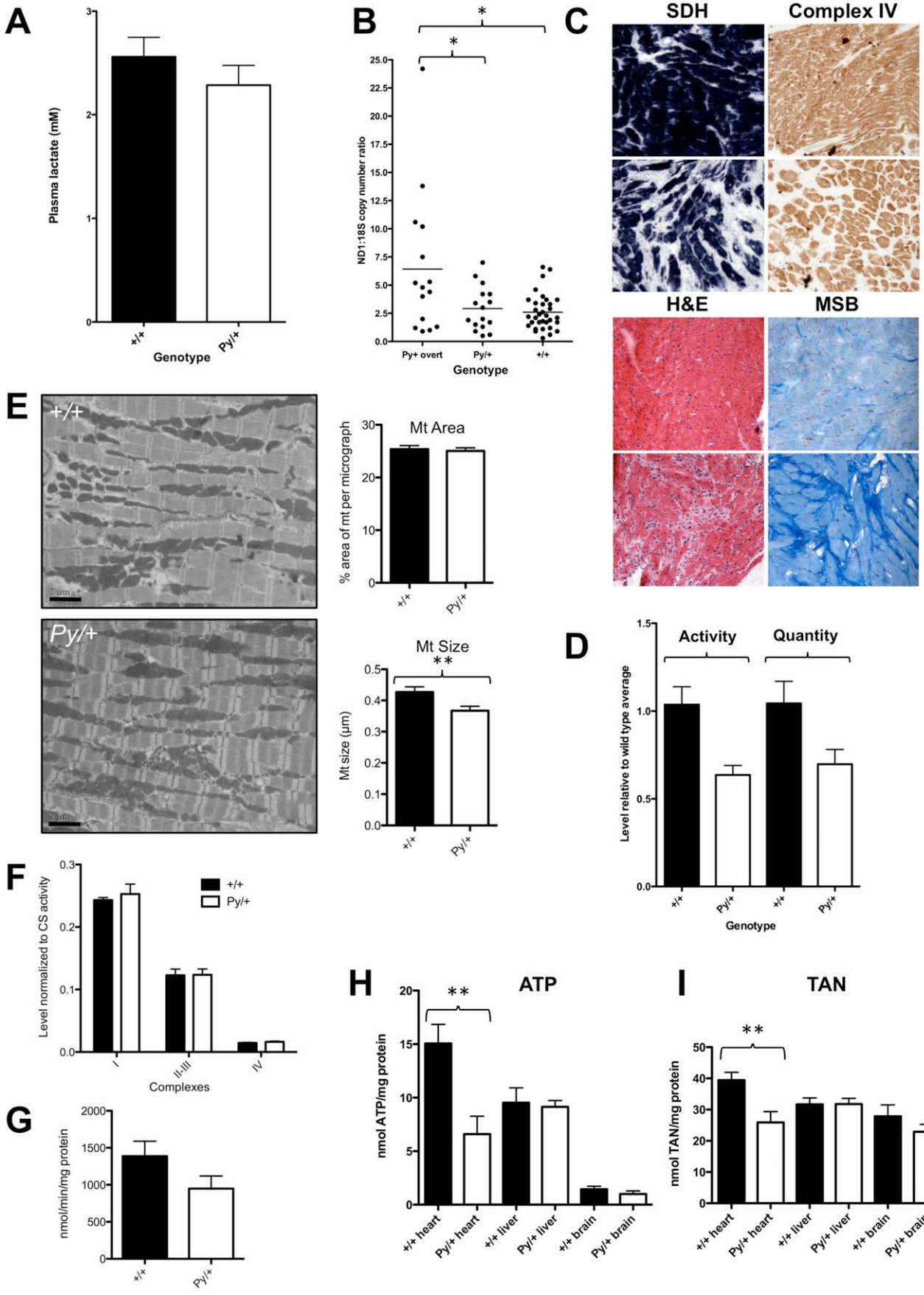
A
Plasma lactate (mM)
Genotype
+/+
Py/+
B
ND1:18S copy number ratio
Py+ overt
Py/+
+/+
Genotype
C
SDH
Complex IV
H&E
MSB
D
Activity
Quantity
Level relative to wild type average
Genotype
E
+/+
Py/+
Mt Area
% area of mt per micrograph
Mt Size
Mt size (μm)
F
Level normalized to CS activity
Complexes
I
II-III
IV
G
nmol/min/mg protein
H
ATP
nmol ATP/mg protein
+/+ heart
Py/+ heart
+/+ liver
Py/+ liver
+/+ brain
Py/+ brain
I
TAN
nmol TAN/mg protein

Figure 6. Cardiomyocyte energy metabolism is altered in Python mice. (A) Plasma lactate levels (mean ± SEM) in adult Python (n = 29) and wild type (n = 33) mice aged between 5 and 9 weeks and in mice. Sexes have been pooled. (B) The relative mitochondrial:nuclear DNA levels in heart samples from Python and control mice as assessed using Q-PCR. '*Py/+* overt' refers to heart samples taken from Python mice at the time of overt symptoms of heart failure. All other mice were aged between 5 and 7 weeks at time of sampling. *$P<0.05$, 1-way Anova with Bonferroni's Multiple Comparison Post-Test. (C) Typical example of enzyme histochemical staining for succinate dehydrogenase (SDH) and Complex IV from hearts of Python males suffering from overt CHF (aged 93 days) and an age-matched littermate control. Typical sections stained with Haematoxylin and Eosin (H&E) and Martius/Scarlet Blue (MSB) to stain connective tissue are shown for comparison. Note the scarring and loss of myocytes in Python hearts. (D) Comparison of Complex IV activity and quantity (mean ± SEM) measured in extracts from hearts of Python mice showing overt signs of CHF and wild type controls aged 91–103 days (n = 7 Python, n = 7 controls). (E) Representative transmission electron micrographs of Python and control hearts from mice aged 9–10 weeks. Scale bar = 2 μm. The graphs on the right summarizes the morphometric measurements (mean ± SEM) of mitochondrial area (reflecting volume per cell) and mitochondrial size in Python (4 mice; n = 75 micrographs) and wild type (4 mice; n = 55 micrographs) heart EM images. **$P<0.01$. (F) Mitochondrial respiratory complex enzyme activities (mean ± SEM measured in extracts of heart tissue from Python (n = 8) and control mice (n = 8) aged 10 weeks and normalized to level of citrate synthase activity. All activities expressed as nmol/min/mg total protein except complex IV which is expressed as k/min/mg. Complex I: NADH: Ubiquinone reductase, Complex II–III: Succinate: Cytochrome c reductase, Complex IV: Cytochrome c oxidase. (G) Overall citrate synthase activity (mean ± SEM nmol/min/mg total protein) in heart extracts from H (n = 8 Python and n = 8 wild type, Student's t test $P = 0.12$). (H) ATP level (mean ± SEM) after normalization to total protein level in extracts of tissue from Python and control mice at age 10 weeks. Student's t test *P* values are: heart +/+ (n = 7) vs. *Py/+* (n = 6): $P = 0.006$; liver +/+ (n = 6) vs. *Py/+* (n = 6): $P = 0.80$; brain +/+ (n = 6) vs. *Py/+* (n = 5): $P = 0.29$. (I) Total adenine nucleotide pool (TAN) in extracts of tissue from Python and control mice at age 10 weeks. Values shown are mean ± SEM nmol ATP + ADP + AMP normalized to mg protein. Student's t test *P* values are: heart +/+ (n = 7) vs. *Py/+* (n = 6): $P = 0.008$; liver +/+ (n = 6) vs. *Py/+* (n = 6): $P = 0.97$; brain +/+ (n = 6) vs. *Py/+* (n = 5): $P = 0.31$.
doi:10.1371/journal.pgen.1001000.g006

membranes. Enzyme activities were assessed were assessed using a Uvikon 940 spectrophotometer (Kontron Instruments Ltd, Watford, UK). Complex I activity was measured according to the method of Ragan *et al.* [57]. Complex II-III activity was measured according to the method of King [58]. Complex IV activity was measured according to the method of Wharton and Tzagoloff [59]. Citrate synthase (CS; EC 1.1.1.27) activity was determined by the method of Shepherd and Garland [60]. Enzyme activities were expressed as a ratio to citrate synthase to compensate for mitochondrial enrichment in cell samples [61]. Measurement of Complex IV activity and quantity in terminal heart samples used a Complex IV Mouse Duplexing (Activity + Quantity) Microplate Assay Kit (Mitosciences, Eugene, OR) according to the manufacturer's instructions.

NMR and mass spectroscopy

Tissues were extracted using a methanol: chloroform: water extraction procedure to separate aqueous soluble metabolites from lipids as previously described [62]. Briefly, ~100 mg tissue were pulverised with dry ice. 600 μl methanol: chloroform (2:1) was added and the samples were sonicated for 15 min. Water and chloroform were added (200 μl of each). The resulting aqueous and organic layers were separated from the protein pellet. The organic layer was dried overnight in a fume hood whilst the aqueous extracts were evaporated to dryness using an evacuated centrifuge (Eppendorf, Hamburg, Germany).

NMR spectroscopy. The aqueous extracts were rehydrated in 600 μl D_2O, buffered in 0.24 M sodium phosphate (pH 7.0) containing 1 mM (sodium-3-(tri-methylsilyl)-2, 2, 3, 3-tetradeuteriopropionate (TSP) (Cambridge Isotope Laboratories Inc., Andover, MA, USA). The samples were analysed using an AVANCE II+ NMR spectrometer operating at 500.3 MHz for the ^1H frequency (Bruker Gmbh, Germany) using a 5 mm ATMA TXI probe. Spectra were collected using a solvent suppression pulse sequence to saturate the residual ^1H water proton signal (noesypr1d pulse sequence; relaxation delay = 2 s, $t_1 = 3$ μs, mixing time = 150 ms, solvent presaturation applied during the relaxation time and the mixing time). 128 transients were collected into 16 K data points over a spectral width of 12 ppm at 27°C.

GC-MS. Aqueous samples were derivatised using the procedure reported [63]. 150 μl of the D_2O sample used for ^1H NMR spectroscopy was evaporated to dryness in an evacuated centrifuge and 30 μl methoxyamine hydrochloride (20 mg ml^{-1} in pyridine) was added. The samples were vortex mixed for 1 minute, and derivatised at room temperature for 17 hours. Samples were then silylated with 30 μl of *N*-methyl-*N*-trimethylsilyltrifluoroacetamide (MSTFA) for 1 hour at room temperature. The derivatised samples were diluted (1:10) with hexane prior to GC-MS analysis. Organic phase metabolites were derivatised by acid catalyzed esterification [64]. Lipids were dissolved in 0.25 ml of chloroform/methanol (1:1 v/v). 0.10 ml BF_3/methanol (Sigma-Aldrich) was added and the vials were incubated at 80°C for 90 minutes. Once cool 0.3 ml H_2O (mQ) and 0.6 ml hexane was added and each vial vortex mixed for one minute. The aqueous layer was discarded and the remaining organic layer was evaporated to dryness before reconstitution in 200 μl hexane for analysis. The derivatised aqueous samples were injected into a Thermo Electron Trace GC Ultra equipped with a 30 m×0.25 mm ID 5% phenyl polysilphenylene- siloxane column with a chemically bonded 25 μm TR-5MS stationary phase (Thermo Electron Corporation; Injector temperature = 220°C, helium carrier gas flow rate = 1.2 ml min^{-1}). The initial column temperature was 70°C; this was held for 2 min then increased by 5°C min^{-1} to 310°C and was held for 20 min. The derivatised organic metabolites were injected onto a ZB-WAX column (30 m×0.25 mm ID×0.25 μm df; 100% polyethylene glycol). The initial column temperature was 60°C; this was held for 2 min then increased by 10°C min^{-1} to 150°C and then by 4°C min^{-1} up to a temperature of 230°C where it was held for 7 min. The column eluent was introduced into a DSQ quadrupole mass spectrometer (Thermo Electron Corporation) (transfer line temperature = 310°C for aqueous metabolites and 240°C for lipid metabolites, ion source temperature = 250°C, electron beam = 70 eV). The detector was turned on after a solvent delay of 240 s and data was collected in full scan mode using 3 scans s^{-1} across a mass range of 50–650 m/z.

Data Analysis. NMR spectra were processed using ACD SpecManager 1D NMR processor (version 8, ACD, Toronto, Canada). Spectra were Fourier transformed following multiplication by a line broadening of 1 Hz, and referenced to TSP at 0.0 ppm. Spectra were phased and baseline corrected manually. Each spectrum was integrated using 0.04 ppm. integral regions between 0.5–4.5, and 5.1–10.0 ppm. To account for any difference in concentration between samples each spectral region was normalised to a total integral value of 10000. GC-MS chromatograms were analysed using Xcalibur, (v. 2.0, Thermo Fisher Corp), integrating each peak individually. Peaks were normalised so that the total sum of peaks was set to 10000.

Table 2. Changes in metabolite levels measured in hearts from Python mice and littermate controls.[1]

^{1}H NMR spectra	Metabolite	Python: wt ratio	*P* value (t test)
Increased in Python	Aspartate	2.11	4.2×10^{-9}
	Glutamate	1.15	5.1×10^{-4}
	Glycine	1.67	4.8×10^{-15}
	Proline	1.24	1.4×10^{-8}
	Valine/leucine/isoleucine	1.69	6.3×10^{-10}
Decreased in Python	Choline	0.80	1.6×10^{-4}
	Creatine	0.69	2.3×10^{-11}
	Lactate	0.80	2.6×10^{-5}
	Succinate	0.58	3.2×10^{-8}
	Taurine	0.92	1.1×10^{-3}
Gas chromatography-mass spectrometry			
Increased in Python	Asparagine	1.62	2.3×10^{-4}
	Glycine	1.57	1.3×10^{-8}
	Proline	2.35	3.1×10^{-5}
	Threonine	1.82	3.3×10^{-6}
	Uric acid	1.65	4.4×10^{-4}
Decreased in Python	α-glycerophosphoric acid	0.69	3.5×10^{-7}
	Adenosine	0.37	7.0×10^{-7}
	AMP	0.27	5.7×10^{-7}
	Creatine	0.44	1.5×10^{-5}
	Fumarate	0.55	5.9×10^{-5}
	Glucose	0.42	$1.1.\times10^{-4}$
	^{1}H-Indole-2,3-dione	0.37	2.1×10^{-6}
	^{9}H-Purine-6-amine	0.66	5.0×10^{-4}
	Malate	0.59	2.5×10^{-6}
	Myo-inositol	0.66	1.1×10^{-5}
	Pyruvate	0.47	3.8×10^{-7}
	Ribose	0.40	1.4×10^{-3}
	Succinate	0.54	5.9×10^{-5}

[1]Mice were on a C3H/HeN genetic background. Average of individual measurements from each heart sample of mice aged 10–11 weeks (n = 10 *Py*/+; n = 10 +/+).

doi:10.1371/journal.pgen.1001000.t002

Deconvolution of overlapping peaks was achieved by generating traces of selected ions. A 0.1 minute threshold window was used for the deviation of peaks away from the predicted retention time across the data set. Structures were assigned using both the NIST database of mass spectra and analysis of standard compounds. Datasets were imported into SIMCA-P 10.0 (Umetrics, Umeå, Sweden) for processing using PCA, PLS (Partial least squares, a regression extension of PCA used to separate out a trend from other variation in the data set) and PLS-DA (a regression extension of PCA used for classification). Identification of major metabolic perturbations within the pattern recognition models was achieved by analysis of corresponding loadings plots. Additionally, R^2 and Q^2 were used as measures for the robustness of a pattern recognition model. R^2 is the fraction of variance explained by a component, and cross validation of R^2 gives Q^2 which reveals the fraction of the total variation predicted by a component. Both values are indicative of how good the overall model is. Typically a robust model has $R^2>0.50$ and $Q^2>0.40$. Coefficient scores rank the observations according to their contribution to the model. In order to confirm which metabolites contributed significantly to each model, each variable was assessed by a jack-knifing routine to assess its contribution to a given component. Only variables deemed to have a coefficient significantly different from zero were included.

Quantification of mtDNA and 18S rRNA by Q-PCR

100,000 cells were resuspended in 100 µl extraction solution (0.2 mg/ml proteinase K, 0.2% SDS and 5 mM EDTA in PBS) and incubated at 50°C for 3 h. Total DNA was then precipitated by addition of 10 µl of 3 M sodium acetate (pH 5.2), 110 µl isopropanol and incubation for 20 minutes on ice before centrifugation at 12,000 rpm at 4°C. The DNA-pellet was washed once with cold 70% ethanol, air dried for 15 min and resuspended in 100 µl TE buffer at 4°C overnight. Realtime PCR amplification was performed on 10 ng of total DNA using a iCycler (Bio Rad) and iQ SYBR Green Supermix (BioRad) following the manufacturer's instructions. A 211 bp fragment of the mtDNA 12S RNA gene was amplified between nucleotide 1095 and nucleotide 1305 (Forward primer: 5′ GCTCGCCA-GAACACTACGAG 3′, reverse primer: 5′ CAGGGTTTGCT-GAAGATGGCG 3′). Elongation translation factor 1 gene (EEF1A1) was used as an endogenous reference across all experimental conditions (Forward primer: 5′ GGATTGCCA-CACGGCTCACATT 3′, reverse primer: 5′ GGTGGA-TAGTCTGAGAAGCTCTC 3′).

Yeast two-hybrid analysis

Regions of *Dnm1l* were amplified from a mouse IMAGE cDNA clone plasmid and cloned into the vectors pDEST22 (prey) and pDEST32 (bait) (Invitrogen Ltd., Paisley, UK) according to the manufacturer's instructions. The two hybrid tests were performed in the yeast strain MaV203, which contains a HIS3 promoter driving expression of *HIS3* and a *GAL1* promoter to drive expression of *LACZ* as chromosomally integrated reporter genes. Interactions were initially tested by plating on yeast dropout medium agar without leucine, tryptophan and histidine and with increasing amounts of 3-amino-1,2,4-triazole (10, 25, 50 and 100 mM). Interactions were then further tested using a semi-quantitative b-glactosidase filter lift assay followed by a quantitative b-galactosidase liquid culture assay according to the Pro-Quest instruction manual (Invitrogen Ltd., Paisley, UK).

Isolation of embryonic fibroblasts

For skin fibroblasts, 2–4-day-old pups were humanely culled, and a portion of the skin removed, washed in PBS and finely minced using a razor blade. A small piece of tissue was retained for genotyping purposes. Numerous small segments of tissue approximately 1 mm^3 were placed well spaced on 10 cm Petri dishes and allowed to air dry for 10 minutes, DMEM containing Glutamax and 10% FCS (Invitrogen Ltd., Paisley, UK) was then carefully added to the dish so as to avoid dislodging the tissue pieces. Plates were cultured for 7 days at 37°C, 5% CO_2, then outgrowing cells were harvested with trypsin and passaged in the same medium. For embryonic fibroblasts, embryos were dissected from the uterus and the yolk sacs were removed for use in genotyping the embryos. The embryos were placed in 50 µl 0.05% trypsin and macerated using a 20 µl disposable pipette tip. After incubation for 15 minutes at 37°C, the cells were counted and plated in one well of a 6-well plate in DMEM containing Glutamax and 10% FCS and cultured at 37°C, 5% CO_2.

Labeling of mitochondria in fibroblasts

For microscopy, fibroblasts were cultured on glass coverslips in 50–200 nM Mitotracker Orange CM-H_2TMRos in DMEM containing Glutamax and 10% FCS for 45 minutes at 37°C. Cells were washed in PBS, then fixed in 4% paraformaldehyde for 20 minutes at room temperature. Cover slips were mounted on glass slides in a drop of ProLong Gold mounting medium (Invitrogen Ltd., Paisley, UK) containing 10 µg/mL Hoechst 33258. For FACS analysis, cells were harvested by trypsinization, washed with PBS, then fixed for 20 minutes at 4°C in 4% paraformaldehyde. Cells were subsequently centrifuged and resuspended in PBS.

Western blot analysis

Brain and heart samples from 5-week-old mice were snap frozen in liquid nitrogen then homogenized in RIPA (50 mM Tris-HCl pH 8, 150 mM NaCl, 1% NP-40, 0.5% sodium deoxycholate, 0.1% SDS) containing 1× protease inhibitor cocktail (P8340; Sigma-Aldrich, Dorset, UK). Equal amounts of protein were separated by Laemmli stacking/separating SDS PAGE and blotted to Hybond-P (GE Healthcare, Little Chalfont, UK), then individual proteins were detected using antibodies to Drp1 (Clone 8; BD Biosciences, Oxford, UK), Tim23 (Clone 32; BD Biosciences, Oxford, UK), and a-tubulin (T6074; Sigma-Aldrich, Dorset, UK). An anti-mouse HRP-conjugated antibody (7076; Cell Signaling, NEB, Hitchin, UK), was used for detection in combination with ECL Western Blotting Detection Reagents (GE Healthcare, Little Chalfont, UK).

Immunocytochemistry

For peroxisome labeling, a primary rabbit anti-catalase IgG (ab16731, Abcam) was used with a goat anti-rabbit FITC-conjugated IgG (ab6717, Abcam). For examining Dnm1l distribution in fibroblasts, an anti-Drp1 primary antibody (Clone 8; BD Biosciences, Oxford, UK) with a Daylight549-conjugated anti-mouse Ig was used.

Fluorescent imaging

All images were taken on a Zeiss AxioCam MRc5 microscope using Axiovision Release 4.7.2 software. For imaging mitochondria with Mitotracker Orange and Dnm1l using a Daylight549-labelled secondary antibody, a filter with excitation 530–585 nm, emission 600–660 nm was used. For Imaging peroxisomes with a FITC-labeled secondary antibody, a filter with an excitation of 450–490 nm, emission 510–560 nm was used. For FACS analysis, cells were incubated in 200 nM Mitotracker Orange CM-H_2TMRos in DMEM containing Glutamax and 10% FCS for 45 minutes at 37°C, harvested using trypsin, washed with PBS and fixed by incubation in 4% paraformaldehyde for 20 minutes at 4oC. Cells were washed in PBS and resuspended in PBS containing 1% FCS and analyzed for fluorescence on a CyAnADP O2 flow cytometer (Dako). The gate for Mitotracker Orange-positive cells was set using control cells that were not labelled.

ATP and total adenine nucleotide pool measurements

Hearts were excised, washed in heparinised normal saline, blotted and weighed, before being snap frozen in liquid nitrogen and stored at −80°C. Total adenine nucleotide (TAN) content and myocardial adenosine triphosphate (ATP) were measured by High Performance Liquid Chromatography (HPLC) as previously described [65]. For the purpose of calculating activity per mg of protein, the Lowry method was used.

Homology modelling

The structure of the human DNMlL protein (Uniprot [66] accession number O00429) was predicted by homology modelling as follows. The structure of the bacterial dynamin-like protein BDLP [13] (PDB [67] identification code 2w6d) was used as template. Given the low sequence identity (around 12%), the alignment between target sequence and template was performed using a profile-to-profile alignment method implemented in the FFAS03 server [68] (http://ffas.ljcrf.edu). Profile-to-profile alignments are superior in terms of sensitivity and alignment quality compared to traditional pair wise alignments (and in particular at low sequence identity). The FFAS03 score for the alignment was −33.5 implying significant similarity (FFAS03 scores below −9.5 reported less than 3% false positive under benchmarking conditions [68]). The alignment was manually inspected and the structural model was derived using MODELLER [69] as previously described [70]. Structure representations were prepared using the molecular visualization program PyMOL (http://www.pymol.org).

Software and databases

DNA sequence alignments for detecting mutations were performed using DNASTAR (DNASTAR Inc. Madison, WI). Protein alignments were performed using CLUSTALW2 and ALIGN software available online from the European Bioinformatics Institute (www.ebi.ac.uk). Prism software (GraphPad Software, Inc., La Jolla, CA) was used throughout for statistical analysis. Morphometric analysis used ImageJ [71]. For measurement of mitochondrial area and size, contrast of micrographs was enhanced by 0.5%. After setting the scale, the threshold was altered such that only mitochondria were marked. The thresholded image was then analyzed for area, and area fraction for particles greater than 50 pixels. For measurement of area stained in MSB sections, the image type was set to RGB stack and the threshold set to detect areas positive for collagen. The thresholded image was then analyzed for area above threshold.

Supporting Information

Figure S1 Alignment of domain M in multiple species and mutations found in Dnm1l protein homologues that have an effect on mitochondrial morphology. Identical or functionally very similar amino acids are shown grouped together by colour on the basis of size and hydrophobicity. Reported mutations that result in amino acid substitutions are 1, G269R yeast [14]; 2, G385D yeast [14]; 3, G398S yeast [14]; 4, G369D hamster CHO cell line [16]; 5, A400D human [15]; 6, P444L yeast [14]; 7, C452F mouse (Python).
Found at: doi:10.1371/journal.pgen.1001000.s001 (9.96 MB TIF)

Figure S2 ATP measurements (mean plus/minus SD) in heart and brain samples expressed as level relative to wild type mean, measured using a quantitative bioluminescent method. Tissue samples were minced and then digested for 45 minutes in 10 mM Tris pH 8.0 and 100 µg/ml proteinase K at 55°C. Protein concentrations were estimated using a Bio-Rad DC Protein Assay kit according to the manufacturers instructions. Samples were then normalized based on total protein. ATP was measured using an ATP Luminescence Assay Kit (Invitrogen Corp.) according to the manufacturers instructions.
Found at: doi:10.1371/journal.pgen.1001000.s002 (0.71 MB TIF)

Table S1 Degree of similarity of domain M of mouse dynamin proteins.
Found at: doi:10.1371/journal.pgen.1001000.s003 (0.03 MB DOC)

Table S2 SHIRPA Assessment of Python mice.
Found at: doi:10.1371/journal.pgen.1001000.s004 (0.04 MB DOC)

Acknowledgments

We are thankful to Sarah Perry, Gill Hawcroft, and Jack Leek for assistance with imaging and to Mark Jones for assistance with flow cytometry analysis. We also thank the Histology and Sequencing Services of the University of Sheffield and the MRC Harwell Histology Laboratory for provision of technical services, Elaine Whitehill for initial identification of the founder Python mouse, and Clare McCartney, Jan Bilton, Lynne Williams, and the staff of St James Biological Services, University of Leeds, Mary Lyon Centre, Harwell and Field Labs, University of Sheffield, for maintenance of the Python colony.

Author Contributions

Conceived and designed the experiments: HA CAL JL PD JLG IH NFF MC HW TND. Performed the experiments: HA LD VL CT MN VS CAL TH ST DW SW DN SGJ JL IB ZL DS SB IH NFF TND. Analyzed the data: HA CAL IB JLG IH MC TND. Wrote the paper: HA HW TND.

References

1. Maron BJ, Towbin JA, Thiene G, Antzelevitch C, Corrado D, et al. (2006) Contemporary definitions and classification of the cardiomyopathies. Circulation 113: 1807–1816.
2. Dec GW, Fuster V (1994) Idiopathic dilated cardiomyopathy. N Engl J Med 331: 1564–1575.
3. Burkett EL, Hershberger RE (2005) Clinical and genetic issues in familial dilated cardiomyopathy. J Am Coll Cardiol 45: 969–981.
4. Seidman JG, Seidman C (2001) The genetic basis for cardiomyopathy: from mutation identification to mechanistic paradigms. Cell 104: 557–567.
5. Kärkkäinen S, Peuhkurinen K (2007) Genetics of dilated cardiomyopathy. Ann Med 39: 91–107.
6. Acevedo-Arozena A, Wells S, Potter P, Kelly M, Cox RD, et al. (2008) ENU mutagenesis, a way forward to understand gene function. Annu Rev Genomics Hum Genet 9: 49–69.
7. Quwailid MM, Hugill A, Dear N, Vizor L, Wells S, et al. (2004) A gene-driven ENU-based approach to generating an allelic series in any gene. Mamm Genome 15: 585–591.
8. Keays DA, Clark TG, Campbell TG, Broxholme J, Valdar W (2007) Estimating the number of coding mutations in genotypic and phenotypic driven N-ethyl-N-nitrosourea (ENU) screens: revisited. Mamm Genome 18: 123–124.
9. Gerull B, Heuser A, Wichter T, Paul M, Basson CT, et al. (2004) Mutations in the desmosomal protein plakophilin-2 are common in arrhythmogenic right ventricular cardiomyopathy. Nat Genet 36: 1162–1164.
10. Grossmann KS, Grund C, Huelsken J, Behrend M, Erdmann B, et al. (2004) Requirement of plakophilin 2 for heart morphogenesis and cardiac junction formation. J Cell Biol 167: 149–160.
11. Papathanasiou P, Goodnow CC (2005) Connecting mammalian genome with phenome by ENU mouse mutagenesis: gene combinations specifying the immune system. Annu Rev Genet 39: 241–262.
12. Low HH, Löwe J (2006) A bacterial dynamin-like protein. Nature 444: 766–769.
13. Low HH, Sachse C, Amos LA, Löwe J (2009) Structure of a bacterial dynamin-like protein lipid tube provides a mechanism for assembly and membrane curving. Cell 139: 1342–1352.
14. Jensen RE, Hobbs AE, Cerveny KL, Sesaki H (2000) Yeast mitochondrial dynamics: fusion, division, segregation, and shape. Microsc Res Tech 51: 573–583.
15. Waterham HR, Koster J, van Roermund CW, Mooyer PA, Wanders RJ, et al. (2007) A lethal defect of mitochondrial and peroxisomal fission. N Engl J Med 356: 1736–1741.
16. Tanaka A, Kobayashi S, Fujiki Y (2006) Peroxisome division is impaired in a CHO cell mutant with an inactivating point-mutation in dynamin-like protein 1 gene. Exp Cell Res 312: 1671–1684.
17. Shin HW, Takatsu H, Mukai H, Munekata E, Murakami K, et al. (1999) Intermolecular and interdomain interactions of a dynamin-related GTP-binding protein, Dnm1p/Vps1p-like protein. J Biol Chem 274: 2780–2785.
18. Smirnova E, Shurland DL, Newman-Smith ED, Pishvaee B, van der Bliek AM (1999) A model for dynamin self-assembly based on binding between three different protein domains. J Biol Chem 274: 14942–14947.
19. Fukushima NH, Brisch E, Keegan BR, Bleazard W, Shaw JM (2001) The GTPase effector domain sequence of the Dnm1p GTPase regulates self-assembly and controls a rate-limiting step in mitochondrial fission. Mol Biol Cell 12: 2756–2766.
20. Zhu PP, Patterson A, Stadler J, Seeburg DP, Sheng M, et al. (2004) Intra- and intermolecular domain interactions of the C-terminal GTPase effector domain of the multimeric dynamin-like GTPase Drp1. J Biol Chem 279: 35967–35974.
21. Chang CR, Blackstone C (2007) Cyclic AMP-dependent protein kinase phosphorylation of Drp1 regulates its GTPase activity and mitochondrial morphology. J Biol Chem 282: 21583–21587.
22. Ramachandran R, Surka M, Chappie JS, Fowler DM, Foss TR, et al. (2007) The dynamin middle domain is critical for tetramerization and higher-order self-assembly. EMBO J 26: 559–566.
23. Ishihara N, Nomura M, Jofuku A, Kato H, Suzuki SO, et al. (2009) Mitochondrial fission factor Drp1 is essential for embryonic development and synapse formation in mice. Nat Cell Biol 11: 958–966.
24. Wakabayashi J, Zhang Z, Wakabayashi N, Tamura Y, Fukaya M, et al. (2009) The dynamin-related GTPase Drp1 is required for embryonic and brain development in mice. J Cell Biol 186: 805–816.
25. Suen DF, Norris KL, Youle RJ (2008) Mitochondrial dynamics and apoptosis. Genes Dev 22: 1577–1590.
26. Gustafsson AB, Gottlieb RA (2008) Heart mitochondria: gates of life and death. Cardiovasc Res 77: 334–343.
27. Rogers DC, Fisher EM, Brown SD, Peters J, Hunter AJ, et al. (1997) Behavioral and functional analysis of mouse phenotype: SHIRPA, a proposed protocol for comprehensive phenotype assessment. Mamm Genome 8: 711–713.
28. Parone PA, Da Cruz S, Tondera D, Mattenberger Y, James DI, et al. (2008) Preventing mitochondrial fission impairs mitochondrial function and leads to loss of mitochondrial DNA. PLoS ONE 3: e3257. doi:10.1371/journal.pone.0003257.
29. Quigley AF, Kapsa RM, Esmore D, Hale G, Byrne E (2000) Mitochondrial respiratory chain activity in idiopathic dilated cardiomyopathy. J Card Fail 6: 47–55.
30. Smirnova E, Shurland DL, Ryazantsev SN, van der Bliek AM (1998) A human dynamin-related protein controls the distribution of mitochondria. J Cell Biol 143: 351–358.
31. Sabbah HN, Sharov V, Riddle JM, Kono T, Lesch M, et al. (1992) Mitochondrial abnormalities in myocardium of dogs with chronic heart failure. J Mol Cell Cardiol 24: 1333–1347.
32. Sharov VG, Goussev A, Lesch M, Goldstein S, Sabbah HN (1998) Abnormal mitochondrial function in myocardium of dogs with chronic heart failure. Journal of molecular and cellular cardiology 30: 1757–1762.
33. Chen L, Gong Q, Stice JP, Knowlton AA (2009) Mitochondrial OPA1, apoptosis, and heart failure. Cardiovascular Res 84: 91–99.
34. Benard G, Bellance N, James D, Parrone P, Fernandez H, et al. (2007) Mitochondrial bioenergetics and structural network organization. J Cell Sci 2007 120: 838–848.
35. Griffin JL (2006) Understanding mouse models of disease through metabolomics. Curr Opin Chem Biol 10: 309–315.
36. Ashrafian H, Redwood C, Blair E, Watkins H (2003) Hypertrophic cardiomyopathy: a paradigm for myocardial energy depletion. Trends Genet 19: 263–268.
37. Chen H, Detmer SA, Ewald AJ, Griffin EE, Fraser SE, et al. (2003) Mitofusins Mfn1 and Mfn2 coordinately regulate mitochondrial fusion and are essential for embryonic development. J Cell Biol 160: 189–200.
38. Chen H, McCaffery JM, Chan DC (2007) Mitochondrial fusion protects against neurodegeneration in the cerebellum. Cell 130: 548–562.
39. Ingwall JS, Weiss RG (2004) Is the failing heart energy starved? On using chemical energy to support cardiac function. Circ Res 95: 135–145.
40. Finsterer J (2004) Mitochondriopathies. Eur J Neurol 11: 163–186.
41. Zhang P, Hinshaw JE (2001) Three-dimensional reconstruction of dynamin in the constricted state. Nat Cell Biol 3: 922–926.
42. Mears JA, Ray P, Hinshaw JE (2007) A corkscrew model for dynamin constriction. Structure 15: 1190–1202.
43. Chang CR, Blackstone C (2007) Cyclic AMP-dependent protein kinase phosphorylatiopn of Drp1 regulates its GTPase activity and mitochondrial morphology. J Biol Chem 282: 21583–21587.
44. Biro JC (2006) Amino acid size, charge, hydropathy indices and matrices for protein structure analysis. Theor Biol Med Model 3: 15–26.
45. Ashrafian H, Watkins H (2007) Reviews of translational medicine and genomics in cardiovascular disease: new disease taxonomy and therapeutic implications cardiomyopathies: therapeutics based on molecular phenotype. J Am Coll Cardiol 49: 1251–1264.
46. Neubauer S (2007) The failing heart—an engine out of fuel. N Engl J Med 356: 1140–1151.
47. Graham BH, Waymire KG, Cottrell B, Trounce IA, MacGregor GR, et al. (1997) A mouse model for mitochondrial myopathy and cardiomyopathy resulting from a deficiency in the heart/muscle isoform of the adenine nucleotide translocator. Nat Genet 16: 226–234.
48. Bhar D, Karren MA, Babst M, Shaw JM (2006) Dimeric Dnm1-G385D interacts with Mdv1 on mitochondria and can be stimulated to assemble into fission complexes containing Mdv1 and Fis1. J Biol Chem 281: 17312–17320.
49. de Brito OM, Scorrano L (2008) Mitofusin 2 tethers endoplasmic reticulum to mitochondria. Nature 456: 605–610.

50. Pitts KR, Yoon Y, Krueger EW, McNiven MA (1999) The dynamin-like protein DLP1 is essential for normal distribution and morphology of the endoplasmic reticulum and mitochondria in mammalian cells. Mol Biol Cell 10: 4403–4417.
51. Acín-Pérez R, Fernández-Silva P, Peleato ML, Pérez-Martos A, Enriquez JA (2008) Respiratory active mitochondrial supercomplexes. Mol Cell 32: 529–539.
52. Mitra K, Wunder C, Roysam B, Lin G, Lippincott-Schwartz J (2009) A hyperfused mitochondrial state achieved at G1-S regulates cyclin E buildup and entry into S phase. Proc Natl Acad Sci USA 106: 11960–11965.
53. Ong S-B, Subrayan S, Lim SY, Yellon DM, Davidson SM, et al. (2010) Inhibiting Mitochondrial Fission Protects the Heart Against Ischemia/Reperfusion Injury. Circulation 121: 2012–2022.
54. Chen H, Vermulst M, Wang YE, Chomyn A, Prolla TA, et al. (2010) Mitochondrial fusion is required for mtDNA stability in skeletal muscle and tolerance of mtDNA mutations. Cell 141: 280–289.
55. Wang J, Wilhelmsson H, Graff C, Li H, Oldfors A, et al. (1997) Dilated cardiomyopathy and atrioventricular conduction blocks induced by heart-specific inactivation of mitochondrial DNA gene expression. Nat Genet 21: 133–137.
56. Hayashi M, Imanaka-Yoshida K, Yoshida T, Wood M, Fearns C, et al. (2006) A crucial role of mitochondrial Hsp40 in preventing dilated cardiomyopathy. Nat Med 12: 128–132.
57. Ragan CI, Wilson MY, Darley-Usman VM (1988) Subfractionation of mitochondria and isolation of proteins of oxidative phosphorylation. In Darley VM, Rickwood D, Wilson MT, eds. Mitochondria: A Practical Approach. Oxford: IRL Press. pp 79–113.
58. King TE (1967) Preparation of succinate cytochrome c reductase and cytochrome b-c1 particle and reconstruction of Succinate cytochrome c reductase. Methods Enzymol 10: 446–451.
59. Wharton DC, Tzagoloff A (1967) Cytochrome oxidase from beef heart mitochondria. Methods Enzymol 10: 245–250.
60. Shepherd JA, Garland PB (1969) Citrate synthase activity from rat liver. Methods Enzymol 13: 11–19.
61. Heales SJR, Hargreaves IP, Olpin SE (1996) Diagnosis of mitochondrial electron transport chain defects in small muscle biopsies. J Inher Metab Dis 19 (Supplement 1): 151.
62. Atherton HJ, Bailey NJ, Zhang W, Taylor J, Major H, et al. (2006) A combined 1H-NMR spectroscopy- and mass spectrometry-based metabolomic study of the PPAR-alpha null mutant mouse defines profound systemic changes in metabolism linked to the metabolic syndrome. Physiol Genomics 27: 178–186.
63. Gullberg J, Jonsson P, Nordstrom A, Sjostrom M, Moritz T (2004) Design of experiments: an efficient strategy to identify factors influencing extraction and derivatization of Arabidopsis thaliana samples in metabolomic studies with gas chromatography/mass spectrometry. Anal Biochem 331: 283–295.
64. Morrison WR, Smith LM (1964) Preparation of Fatty Acid Methyl Esters and Dimethylacetals from Lipids with Boron Fluoride—Methanol. J Lipid Res 5: 600–608.
65. Neubauer S, Horn M, Naumann A, Tian R, Hu K, et al. (1995) Impairment of energy metabolism in intact residual myocardium of rat hearts with chronic myocardial infarction. J Clin Invest 95: 1092–1100.
66. Wu CH, Apweiler R, Bairoch A, Natale DA, Barker WC, et al. (2006) The Universal Protein Resource (UniProt): an expanding universe of protein information. Nucleic Acids Res 34: D187–191.
67. Berman HM, Bhat TN, Bourne PE, Feng Z, Gilliland G, Weissig H, Westbrook J (2000) The Protein Data Bank and the challenge of structural genomics. Nat Struct Biol 7 Suppl: 957–959.
68. Jaroszewski L, Rychlewski L, Li Z, Li W, Godzik A (2005) FFAS03: a server for profile—profile sequence alignments. Nucleic Acids Res 33: W284–288.
69. Sali A, Blundell TL (1993) Comparative protein modelling by satisfaction of spatial restraints. J Mol Biol 234: 779–815.
70. Fernandez-Fuentes N, Madrid-Aliste CJ, Rai BK, Fajardo JE, Fiser (2007) M4T: a comparative protein structure modeling server. Nucleic Acids Res 35: W363–368.
71. Abramoff M, Magelhaes P, Ram SJ (2004) Image Processing with ImageJ. Biophotonics Int 11: 36–42.